Experimental Investigations of Airflow in the Human Upper Airways During Natural and Assisted Breathing

Callum J. T. Spence

A thesis presented for the degree of
Doctor of Philosophy
in
Mechanical Engineering
at the
University of Canterbury,
Christchurch, New Zealand.
2011

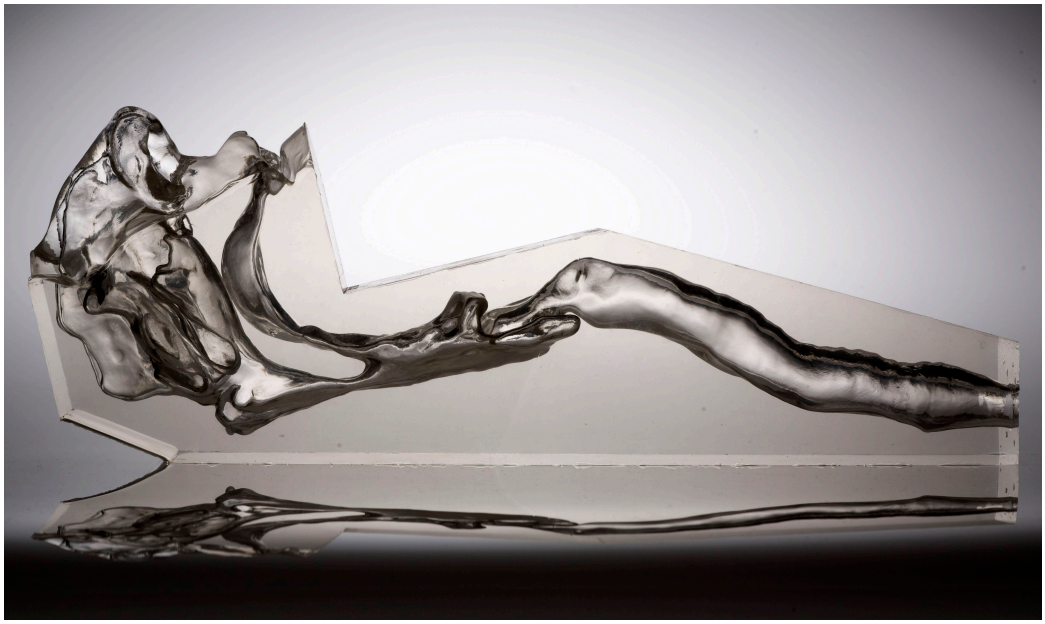

To
my family, friends, teachers and colleagues, from whom
I have learnt so much

Acknowledgments

In this short note, I would like to attempt to show my appreciation to the people who have made the research presented in this thesis possible and as enjoyable as I have found it.

First of all I would like to thank my primary supervisors and friends Dr. Mark Jermy and Mr. Craig White, both for the wonderful opportunity to undertake this research and for your guidance and support. Our interesting discussions and your advice have been invaluable.

Of my colleagues and friends in the bioengineering centre, I would like to give particular thanks to Nicolas Buchmann. I have learnt a great deal from you and our intellectual discussions. Wenn ich ein wenig weiter gesehen haben ist es durch Stehen auf den Schultern von Riesen. Thanks also to Steve Moore, Patrick Geoghagan, and Zulkhairi Zainol Abidin for your inputs to this research.

To Clare Stevens and Scott Wells from St. George's radiology for giving their time and providing the CT scan data necessary to conduct this research. To the mechanical engineering department, with special thanks to the contributions of Graeme Harris, Julian Phillips, Eric Cox and workshop staff. To the support and hospitality of Fisher & Paykel Healthcare.

The funding provided by Fisher & Paykel Healthcare, the Tertiary Education Commission's Bright Futures Enterprise scholarship, the Royal Society of New Zealand's R.H.T Bates Postgraduate Scholarship and travel grants, UC "Ph.D. in 3", and the Department of Mechanical Engineering.

I would like to give my sincerest thanks to the Bright family. You made Christchurch my home away from home. My dear friend Angel; to you I give my deepest gratitude.

Finally, and most of all, I would like to thank my parents. You have given me strong foundations in all aspects of life and have been a great source of motivation and support in all my undertakings. You have taught me the importance and value of a strong education, and given me a passion for learning and discovering.

Abstract

Nasal high flow (NHF) cannulae are used to deliver heated and humidified air to patients at steady flows ranging from 5-50 l/min. Knowledge of the airflow characteristics within the nasal cavity with NHF and during natural breathing is essential to understand the treatment's efficacy. In this thesis, the distribution and velocity of the airflow in the human nasal cavity have been mapped during natural and NHF assisted breathing with planar- and stereo-PIV in both steady and oscillatory flow conditions. Anatomically accurate transparent silicone models of the human nasal cavity were constructed using CT scan data and rapid prototyping. Breathing flowrates and waveforms were measured in vivo and dimensionally scaled by Reynolds and Womersley number matching to reproduce physiological conditions in vitro. Velocities of 2.8 and 3.8 m/s occurred in the nasal valve during natural breathing at peak expiration and inspiration, respectively; however on expiration the maximum velocity of 4.2 m/s occurred in the nasopharynx. Velocity magnitudes differed appreciably between the left and right sides of the nasal cavity, which were asymmetric. NHF modifies nasal cavity flow patterns significantly, altering the proportion of inspiration and expiration through each passageway and producing jets with in vivo velocities up to 20.8 m/s for 40 l/min cannula flow. The main flow stream passed through the middle airway and along the septal wall during both natural inspiration and expiration, whereas NHF inspired and expired flows remained high through the nasal cavity. Strong recirculating features are created above and below the cannula jet. Results are presented that suggest the quasi-steady flow assumption is invalid in the nasal cavity during both natural and NHF assisted breathing. The importance of using a three-component measurement technique when investigating nasal flows has been highlighted. Cannula flow has been found to continuously flush the nasopharyngeal dead space, which may enhance carbon dioxide removal and increase oxygen fraction. Close agreement was found between numerical and experimental results performed in identical conditions and geometries.

Publications Arising from this Research

Journal Papers

Published

1. **Spence C.J.T.**, Buchmann N.A., & Jermy M.C. (2011) Unsteady flow in the nasal cavity with high flow therapy measured by stereoscopic PIV. *Experiments in Fluids*:1-11 DOI 10.1007/s00348-011-1044-z.

2. **Spence C.J.T.**, Buchmann N.A., Jermy M.C., & Moore S.M. (2010) Stereoscopic PIV measurements of flow in the nasal cavity with high flow therapy. *Experiments in Fluids*:1-13 DOI 10.1007/s00348-010-0984-z.

In Review

3. Geoghegan P.H., Buchmann N.A., Jermy M.C., Nobes D., **Spence C.J.T.**, & Docherty P.D. SPIV and Image Correlation Measurements of Surface Displacement During Pulsatile Flow in Models of Compliant, Stenosed Arteries. *Invited to Experiments in Fluids: 15th International Symposium on Laser Applications to Fluid Mechanics Special Issue.*

Current

4. **Spence C.J.T.**, Buchmann N.A., Geoghegan P.H., Moore S.M., & Jermy M.C. Fabrication and Implementation of In vitro Models for Optical Measurement. Planned for *Journal of Visualization.*

5. **Spence C.J.T.**, Stringer N., Jermy M.C., Cater J.E. Comparison of Experimental and Computational Investigations of the Airflow in a Realistic Human Nasal Cavity. Planned for *Journal of Biomechanics.*

6. **Spence C.J.T.**, Jermy M.C., & White C. Mechanisms of nasal high flow therapy. Planned for *Respiratory Medicine.*

7. **Spence C.J.T.**, Geoghegan P.H., X.B. Lu., Jermy M.C., Hunter P.J., & Cater J.E. Stereoscopic Particle Image Velocimetry Measurement of Articulatory Airflow for Validation of a Computer Model of Speech. Planned for *International Journal of Experimental and Computational Biomechanics.*

8. **Spence C.J.T.**, Doorly, D.J., & Jermy M.C. Experimental investigation of nasal airflow variance. Planned for *Respiratory Physiology & Neurobiology*.

9. Jermy M.C., **Spence C.J.T.**, Abidin Z.Z., Dougherty R,. Ecclestone M., Al-Tiay Y., White C. High speed photography to determine the presence or absence of airborne droplets in the exhaled air of subjects wearing high flow nasal cannulae (Optiflow™) with calculations of trajectory and drying time. Planned for *Respiratory Medicine*

Conference Proceedings

1. **Spence C.J.T.**, Geoghegan P.H., X.B. Lu., Jermy M.C., Hunter P.J., & Cater J.E. (2010) Stereoscopic particle image velocimetry measurement of articulatory airflow for validation of a computer model of speech. In *Proceedings of the 17th Australasian Fluid Mechanics Conference*, Auckland, New Zealand, 5–9 December.

2. Jermy M.C., **Spence C.J.T.**, Collingwood R., Wenborn T., Green A., Lei M.X., & Eaton-Evans. J (2010) Pressure losses in neonate breathing. Abstract accepted for *17th Australasian Fluid Mechanics Conference*, Auckland, New Zealand, 5–9 December.

3. **Spence C.J.T.**, Buchmann N.A., & Jermy M.C. (2010) Pulsatile flow in the nasal cavity with high flow therapy measured by stereoscopic PIV. In *Proceedings of the 15th International Symposium on Applications of Laser Techniques to Fluid Mechanics*. Lisbon, Portugal, 5–8 July.

4. Geoghegan P.H., Buchmann N.A., Jermy M.C., Nobes D., **Spence C.J.T.**, & Docherty P.D. (2010) SPIV and image correlation measurements of surface displacement during pulsatile flow in models of compliant, stenosed arteries. In *Proceedings of the 15th International Symposium on Applications of Laser Techniques to Fluid Mechanics*. Lisbon, Portugal, 5–8 July.

5. **Spence C.J.T.**, Buchmann N.A., & Jermy M.C. (2009) Flow field in the human nasal cavity with nasal high flow therapy from stereoscopic PIV measurements. In *Proceedings of the 8th International Symposium On Particle Image Velocimetry*. Melbourne, Australia, 25–28 August.

6. Geoghegan P.H., Jermy M.C., Buchmann N.A., **Spence C.J.T.**, & Freitag T. (2009) Experimental investigation of flow in a compliant tube using particle image velocimetry. In *Proceedings of the 8th International Symposium On Particle Image Velocimetry*. Melbourne, Australia, 25–28 August.

7. **Spence C.J.T.**, Buchmann N.A., & Jermy M.C. (2009) Upper airway stereoscopic particle image velocimetry measurements with high-flow nasal cannula. In *Proceedings of the 4th Asian Pacific Conference on Biomechanics*. Christchurch, 14–17 April.

8. Geoghegan P.H., Jermy M.C., Buchmann N.A., & **Spence C.J.T.** (2009) Experimental investigation of flow in compliant tubes to validate numerical models of aneurysms. In *Proceedings of the 4th Asian Pacific Conference on Biomechanics*. Christchurch, 14–17 April.

9. Jermy M.C., Buchmann N.A., **Spence C.J.T.**, Nguyen C.V., & David T. (2008) PIV measurements of human Human Blood and Upper Airway flows Flow in scaled Scaled Models. In *Proceedings of the 5th Australian Conference on Laser Diagnostics in Fluid Mechanics and Combustion*. Perth, 3–4 December.

10. **Spence C.J.T.**, Buchmann N.A., & Jermy M.C. (2008) Particle image velocimetry measurements of nasal cavity flow with high flow humidified nasal interface. In *Proceedings of the 13th International Symposium Flow Visualization*. Nice, 1–4 July.

11. Buchmann N.A., **Spence C.J.T.**, & Jermy M.C. (2008) PIV Measurements of the Flow Field in a Domestic Kitchen Oven as a Function of Temperature. In *Proceedings of the 13th International Symposium Flow Visualization*. Nice, 1–4 July.

12. Buchmann N.A., Jermy M.C., & **Spence C.J.T.** (2008) In vitro Imaging of Blood Flow in Human Carotid Arteries. In *Proceedings of the 13th International Symposium Flow Visualization*, Nice, 1–4 July.

13. **Spence C.J.T.**, Buchmann N.A., & Jermy M.C. (2007) Airflow in a Domestic Kitchen Oven measured by Particle Image Velocimetry. In *Proceedings of the 16th Australasian Fluid Mechanics Conference*. Gold Coast, 2–7 December.

Table of Contents

List of Figures

List of Tables

Nomenclature

List of Symbols

c	Maximum permissible circle of confusion [m]
C	Cunningham correction factor
C_d	Drag coefficient [m]
d_H	Hydraulic diameter [m]
d_p	Particle diameter [m]
D	Laser beam diameter [m]
F	Lens focal length [m]
f_1, f_2	Interrogation regions from exposures one and two
$\overline{f}_1, \overline{f}_2$	Mean pixel intensity values
g	Acceleration due to gravity [m/s^2]
Gr	Grashof number
I	Turbulence Intensity
L	Characteristic length scale [m]
n	Refractive index
N	Lens f-number
p	Fluid pressure [Pa]
Q	Flowrate [m^3/s]
R	Radius of curvature of a streamline [m]
Re	Reynolds number
Ri	Richardson number
St	Strouhal number
Stk	Stokes number
[u, v, w]	Cartesian velocities [m/s]
$\bar{u}$	Mean velocity [m/s]

u’	Fluctuating velocity component [m/s]
t	Depth of field [m]
T	Period [s]
T_{ref}	Bulk temperature [°C]
T_S	Surface temperature [°C]
α	Womersley number
β	Volumetric thermal expansion coefficient [1/°C]
δ	Curvature ratio
θ	Angle [°]
κ	Dean number
μ	Dynamic viscosity [Pa.s]
ν	Kinematic viscosity [m^2/s]
ρ	Fluid density [kg/m^3]
ρ_p	Particle density [kg/m^3]
$\Delta X,\Delta Y$	Particle displacements [m]

1 Introduction

1.1 Anatomy and Physiology of Respiration

It is first necessary to introduce the anatomy, physiology and terminology of the respiratory tract. The terminology of anatomical orientations adopted throughout the text is illustrated in Figure 1. The respiratory tract can be segmented into two parts commonly referred to as the lower airways and the upper airways. Although there are variations in the literature regarding the boundary of the lower and the upper airways, here I will consider the lower airways to begin at larynx as shown in Figure 2. At the bottom of the trachea the airway bifurcates into the primary bronchi, which is followed by 20–23 bifurcations in each lung (Weibel 1989). At the end of the bronchioles, small pockets called alveoli separate air from blood by a thin membrane and allow the diffusion of oxygen from the air into blood and the reverse for carbon dioxide. Although alveolar only have a diameter of approximately 200 μm, because they number in the order of 500×10^6 (Ochs et al. 2004), they form a large surface area almost equal to a tennis court for which diffusion to occur over.

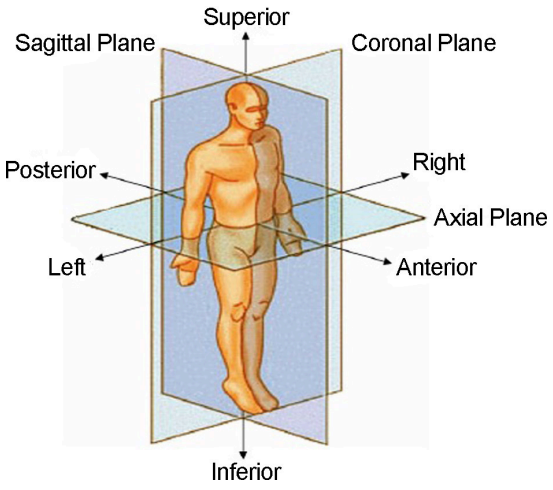

Figure 1. An illustration of the terminology used to describe anatomical orientations (adapted from Moore, 2007).

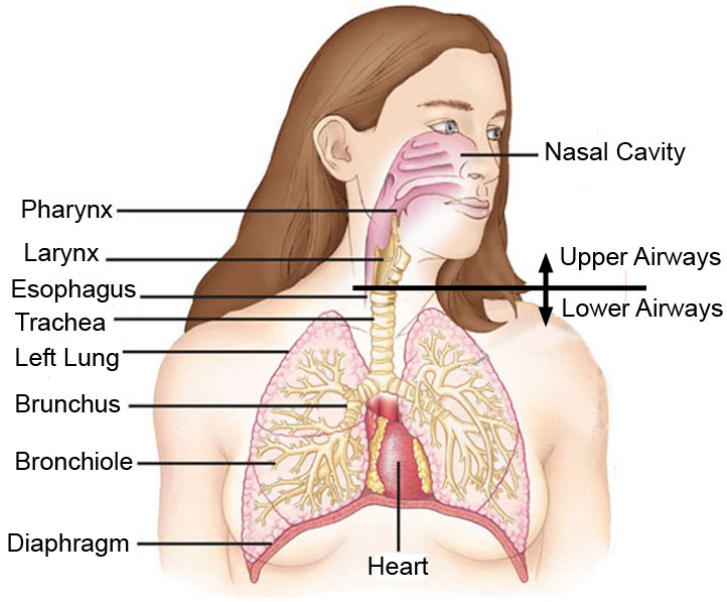

Figure 2. Respiratory System (adapted from http://kvhs.nbed.nb.ca)

A typical adult male has a total lung capacity of 6 litres and a resting tidal volume of 500 ml as shown in Figure 3. The functional residual volume is the volume of gas contained in the lungs at the end of a normal expiration, which continues to undergo gaseous exchange. Air is drawn into the lungs on inspiration when the diaphragm and respiratory muscles actively contract and expand the chest cavity. Expiration is normally a passive process where the lungs and associated muscles recoil naturally. The upper airways, also known as the conducting airways, consist of the nasal cavity, the pharynx, and the larynx. Focus of the current work will be on the upper airways and more specifically on the nasal cavity. Figure 4 shows a typical change in cross-sectional area throughout the respiratory tract within one person. Note, however, that just as there is a wide range of sized people, variation in the size of the airways also vary widely.

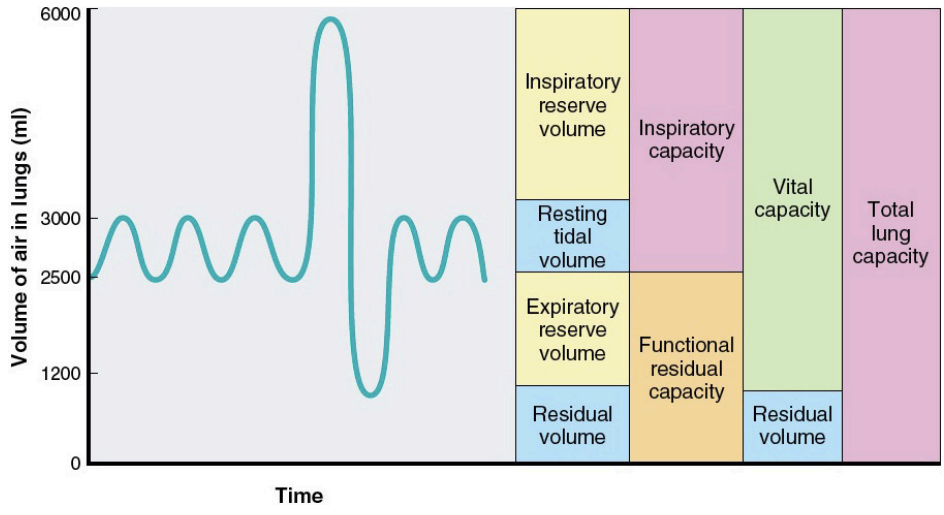

Figure 3. Typical lung volumes for an adult male (adapted from Vander et al., 2001)

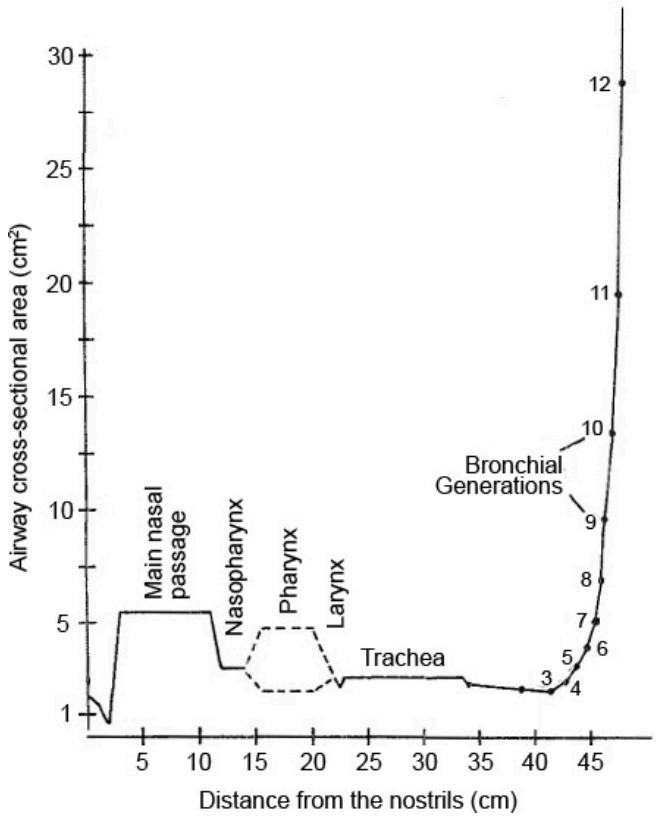

Figure 4. Change in total cross-scetional area along the airway (adapted from Swift, 1977)

1.1.1 The Upper Airways

The nasal cavity begins at the nostrils (external nares) and extends backward as two separate airways partitioned by the nasal septum (Figure 5), until the nasopharynx where the airways merge. Each side of the nasal cavity is called a choana. The nasal vestibule is the area enclosed by the external cartilages of the nose and is lined with small, filtering hairs (vibrissae). Posterior of the nasal vestibule the cross-sectional area narrows to a minimum called the nasal valve (ostium internum). The left and right nasal valves are labeled as 1L and 1R, respectively, in Figure 5 and correspond to the minimum in Figure 4. The size of the nasal valves are not static but constantly changing with surrounding erectile tissues (P. Cole 2000) inflating and deflating out of phase in each nostril over a period of normally 3–4 hours (Eccles 1978). This process is called the nasal cycle, and it causes an alternation of airflow from one nasal passage to another with a flow bias through either nostril as great as 80% (Swift & Proctor 1977). Following the nasal valve is an abrupt expansion into the main nasal passageways both in height and in cross-sectional area. The turbinates (or concha) are long, narrow and curled bone shelves that protrude into the nasal cavity, creating a large surface area and forming the inferior, middle and superior airways and meatus

passageways. The olfactory receptors, responsible for the sense of smell, are located in the olfactory slit on the nasal cavity roof. Although each side of the nasal cavity shares common features, they are asymmetric. It is worth mentioning now that the geometry depicted in Figure 5 is that created by and used in the current work.

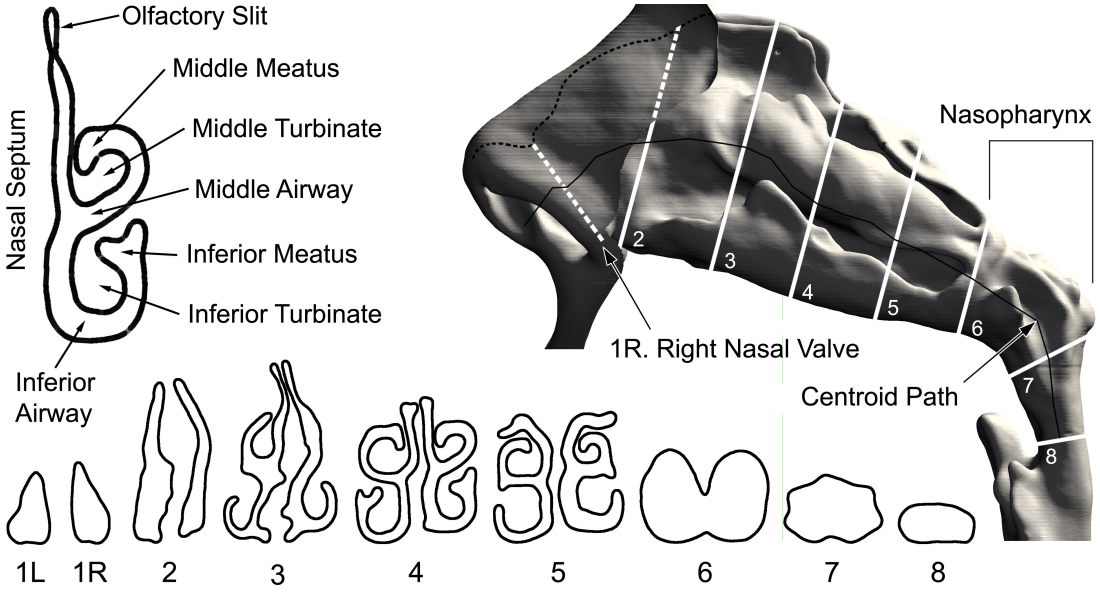

Figure 5. Coronal cross-sections of a 44-year-old male's nasal cavity with respective locations illustrated on the sagittal view.

The two choanae merge in the nasopharynx and the cross-sectional area narrows, as illustrated in Figure 4. From the nasopharynx to the tracheal bifurcation there is a single airway. The nasopharynx, oropharynx and laryngopharynx together make up what is known as the pharynx, as illustrated in Figure 6. The size of the nasopharynx and oropharynx is dependent on the position of the soft palette (velum palate), which is the muscle tissue that forms the back roof of the mouth and changes location depending on the mode of breathing. The soft palette can for example be closing off the mouth during nasal breathing, closing off the nasal passages during mouth breathing, or be in a neutral position. The narrow constriction formed by the soft palate at location 8 in Figure 5 is termed the velopharynx. Following the pharynx, the larynx forms the entrance to the trachea, contains the vocal folds and prevents food or liquid from entering the trachea and lungs during swallowing. The anatomy, physiology and function of the nose is described in further detail in several works including those by Proctor (1982) and Mygind and Dahl (1998).

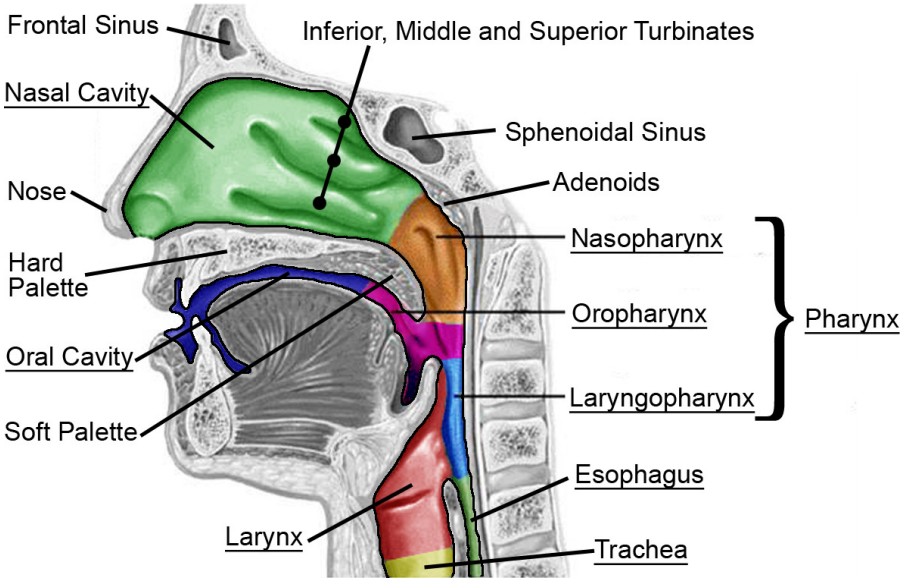

Figure 6. Anatomy of the upper airways

1.1.2 Air-Conditioning in the Nasal Cavity

The nose and nasal breathing has been known to be of importance since the Bible mentioned that it was specifically through the nostrils and not the mouth that the 'breath of life' was given.

> Genesis 2:7 - *"Then the Lord God… breathed life-giving breath into his nostrils and the man began to live"* (*Good News Bible: Today's English Version* 1976)

It is now known that the primary function of the nasal cavity is to warm, humidify and filter inspired air before it reaches the lungs (Elad et al. 2008; Mygind & Dahl 1998; Naftali et al. 2005). Although conditioning of inspired air continues throughout the respiratory tract, the nasal cavity is designed to perform the vast majority of this function as well as providing the sense of smell (olfaction). The nasal cavity's tortuous passages form a large surface area and are lined with mucosa. These moist surfaces are extensively vascularised (Ritter 1970) and facilitate the mechanism for heat transfer and evaporation of water from mucus (Jackson 1999; Naftali et al. 1998; Nunn 1993). Elad et al. (2008) reviewed 31–34°C temperatures and 90–95% relative humidities in the nasopharynx during inspiration of dry air at room temperature. Even when breathing very cool air (7°C), Swift and Proctor (1977) reported that the air had reached 28°C by the nasopharynx. The nasal cavity is also able to recover moisture and humidity from expired air (Churchill et al. 2004; Keck et al. 2000). Airborne particles are filtered by the nasal hairs and

caught by nasal mucosa, providing significant defense against particles as small as 2–4 μm (Elad et al. 2008).

The complex geometry of the nasal cavity imposes a significant resistance to breathing in comparison to mouth breathing. Nasal airway resistance is known to account for 42–60% of the total respiratory tract resistance (Butler 1960; Craig et al. 1965; Swift & Proctor 1977) and Bridger and Proctor (1970) showed that almost all of the nasal resistance to airflow is produced in the anterior 2-3cm. When mouth breathing on the other hand, the oral cavity accounts for only about one-fifth of the total respiratory resistance and thus requires approximately 50% less effort than nose breathing (Swift & Proctor 1977). Despite this, healthy humans will normally breathe through their nose. Breathing through the mouth bypasses the air-conditioning function of the nose, however, reduced resistance allows greater flowrates of air during exercise. The importance of nasal breathing and air-conditioning is thought to be a reason why infants to the age of 6 months are obligatory nose breathers (Swift & Proctor 1977). The nasal cycle is thought to share the burden of air-conditioning between the two choana so that one side can rest while flow prevails through the other (Eccles 1978). Churchill et al. (2004) reviews literature to support that different nasal air-conditioning requirements is the reason why populations adapted to cold/dry climates tend to be characterized by having larger more protrusive noses with downwardly directed nares and larger turbinates, whereas in hot/humid environments flatter, smaller noses with more anteriorly directed nares are prevalent. Elad et al. (2008), Cole et al. (2000) and Scherer et al. (1989) provide further reviews of the air-conditioning characteristics and biophysics of nasal airflow.

1.2 Particle Image Velocimetry

Particle Image Velocimetry (PIV) is an optical flow measurement technique that provides a near instantaneous velocity map of a cross-section through a gas or liquid flow. A close relation to PIV is Particle Tracking Velocimetry (PTV), which tracks individual particles moving with a fluid. PTV in its simplest form has been around for many years and can consist of merely dropping a piece of wood or a ball of paper in a river and measuring the time the object takes to travel a certain distance, not unlike Joseph Bazalgette's flow speed measurements of the river Thames in the 19th century. PTV uses a very low tracer particle concentration because the distance between particle neighbours must be greater than the distance a particle moves in a time, t so that confusion is not created between particles. PIV on the other hand uses

higher particle concentrations, and measures the displacement and subsequently the velocities of groups of particles.

A typical and basic planar-PIV system configuration is illustrated in Figure 7. A high power laser passes through an optical arrangement to produce a light sheet, which illuminates tracer particles that are added to the flow. The tracer particles are selected to be small enough to follow the flow faithfully and cause negligible distortion to the flow, whilst being large enough to scatter sufficient light. The light scattered by the tracer particles is recorded via a digital camera that is mounted perpendicularly to the light sheet. The laser acts as a photographic flash that pulses twice to capture two images that are separated by a short time delay and called an image pair. 'Successive images' will be used to refer to images within an image pair, notwithstanding continuous image pair acquisition frame rates of 10-15 Hz by standard modem PIV cameras. The time delay controls the particle displacement between successive images and is determined by the maximum flow velocity and imaging magnification. Image pairs are divided into a grid of small subareas called interrogation windows. The local displacement of the particles contained within each interrogation window between the first and second exposures is calculated using a statistical computer processing method known as a cross-correlation (COR) algorithm. By also knowing the time delay and image magnification, the velocity vector for each interrogation window can be calculated by $U=d/t$ and plotted on a velocity map.

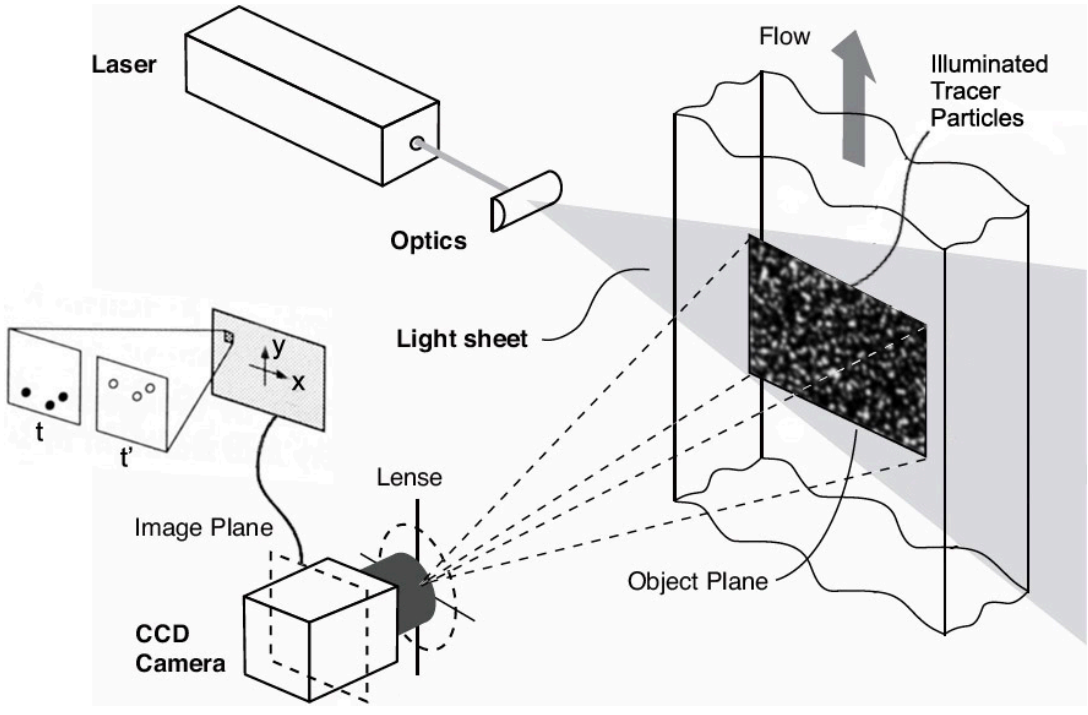

Figure 7. Basic configuration of a Particle Image Velocimetry system (adapted from (Buchmann 2010))

Since PIV was developed in the 1980's (Adrian 2005) and digitized in the early 1990's (Westerweel 1993; Willert & Gharib 1991) it has been employed in a multitude of applications, and to a growing extent in physiological flows. PIV was the flow measurement technique of choice for the current work for its ability to measure whole velocity fields instantaneously in complex flows, such as in the case of the nasal cavity. Being optically based, PIV is non-intrusive and works without the need for pressure probes or hot-wires that can disturb flow patterns, and only measure the velocity of the flow at a single point. In contrast, the spatial resolution of PIV is high and velocities across large parts of flow fields can be measured at thousands of locations simultaneously. As well as being quantitative in both space and velocity, PIV like flow visualisations provides a picture of the flow and enables the detection of large- and small-scale spatial structures in the flow.

The basic PIV configuration presented in Figure 7 is known as planar PIV and is limited to one camera and measuring the two velocity components parallel with the light sheet. Several variants of PIV exist to measure the three-dimensional (3D) flow velocity fields: stereoscopic PIV (SPIV) (Arroyo & Greated 1991), defocusing PIV (DDPIV) (Pereira & Gharib 2002; Willert & Gharib 1992), tomographic PIV (TPIV) (Elsinga et al. 2006), and holographic PIV (HPIV) (Meng & Hussain 1991). The current work will be limited to the use of planar and stereoscopic PIV, and a detailed description of each technique is given in Chapter 3.

1.3 Nasal Airflow Studies

The efficacies of the nasal cavity's air-conditioning and olfaction functions are strongly dependent on the flow field in the nasal cavity where heat and moisture transfer rates vary locally with flow velocity and turbulence intensity. Numerous studies have been conducted to date to build an understanding of the basic principles of nasal airflow patterns and gain insight into the function of the nasal cavity and its complex form. Motivations for other nasal airflow pattern studies also include assessing the impact of surgical interventions of diseases of the nose (Hentschel et al. 2006; S. K. Kim & Chung 2004) and investigating particle transport and deposition in the nasal cavity with applications to the delivery of drugs (Y. Cheng et al. 1988; Versteeg & Hargrave 2001) and pollutant retention (Zwartz & Guilmette 2001). Research of human nasal airflow dates back until the late 19th century and have since employed in vivo, in vitro and numerical methods. The purpose for this section is to review the airflow studies in the adult human nasal cavity performed to date and to outline the current knowledge.

1.3.1 In Vivo Experimental Measurements

The ideal conditions to measure the airflow pattern within the nasal cavity would be to take direct measurements on a subject in vivo. The narrowness and complexity of the nasal geometry, however, poses significant limitations. Any currently available flow measurement device introduced into the airway would alter the flow pattern and interfere with the analysis. Furthermore, intruding devices are likely to cause a reflex response from the sensitive nasal mucosa and a deviation from a natural breathing pattern due to both discomfort and an awareness of breathing, which is normally spontaneous. Mlynski et al. (2000) conclude "…in vivo investigations [with] sufficient visualisation of air flow appears to be impossible". Nonetheless, a small number of in vivo studies of nasal airflow patterns have been undertaken. Early investigations by Goodale (1896) and Parker (1901) attempted to infer the internal airflow patterns by observing the external distributions of inhaled airborne powder and exhaled smoke. Shevrygin (1973) explored the flow pattern within the nasal cavity by lining the internal passages with litmus paper and having subjects inhale dilute ammonia gas. It is likely that the ammonia gas produced a vasomotor reaction in the nasal mucosa (Hornung et al. 1987) and the results influenced by mucosal swelling. Shevrygin also measured the direction and distribution of inspired flow by measuring the regional cooling caused by incoming air with electro-thermometer probes.

1.3.2 In Vitro Experimental Measurements

The limitations surrounding in vivo measurements of the airflow pattern in the nasal cavity have turned researchers to in vitro studies using artificial models of the nasal geometry. For over a century researches have constructed artificial models of the nasal cavity to investigate the flow pattern using techniques such as flow visualization, Pitot probes, hot wire anemometry, laser Doppler anemometry and more recently PIV. Here the applications of the various methodologies employed are reviewed. A detailed discussion on the artificial models themselves and their construction will be given in Chapter 2. Pertinent findings from studies will be discussed here to help describe the history of in vitro experiments, however, a comprehensive overview of the current knowledge of the airflow pattern in the nasal cavity is given in section 1.3.5.

Flow Visualisations

The earliest experiments were flow visualisations conducted using steady flows through anatomical specimens harvested from cadavers. Paulsen (1882) divided a head in half and distributed red litmus paper throughout a nasal cavity specimen. The head was then placed back together and air saturated with ammonia inhaled through the nostrils using a pump connected to the trachea. Paulsen noted the regions in which the red litmus paper turned blue. In 1893, Francke (1893) divided a head in line with the septum and replaced the septal wall with a glass plate. Flow visualisations were conducted with smoke as air was drawn through the model by a pump connected to the trachea. In 1922 Takahashi (1922) attempted to infer the course of airstreams by looking at the areas of powder deposition in the nasal cavity, however, was criticized (Dawes 1952) because the sites of deposition were said to indicate obstruction to the airflow rather than areas of higher flow. Schiedeler's measurements (1938), which passed a corrosive gas through a model of the nose, were critiqued for a similar reason. Using a specimen with a glass septum similar to that of Francke, Proetz (1941) used a rheostat-controlled pump to simulate steady flowrates typical of normal breathing, forced breathing, sniffing and talking, and visualised the associated flow fields with streams of smoke.

In 1951, Proetz was the first to construct an artificial model of the nasal cavity by taking a cast of a cadaver. Proetz describes specimen models to be difficult to work with and needed to be returned to a pickling solution after each measurement. Casts of the airway geometry were therefore undertaken to enable a larger number of flow visualisations that could be repeated and continued as long as required. After careful inspection of the flow characteristics, Proetz concluded that to simulate inspiration it made no difference whether a positive pressure was applied at the nose or a negative pressure was applied at the trachea, as long as the same differential existed. The same held true for expiration. A water manometer was used to measure the positive and negative pressures at the trachea and the nose. Proetz generally agreed with inspiratory patterns presented by the pioneering investigations, however, the need for more research was highlighted by contradictions that arose, such as whether the main flow stream was through the middle or inferior meatus, whether the flow in different sections of the nasal cavity are turbulent or laminar, or whether or not vortices in specific regions exist. Proetz suggested that there is a basic flow pattern in the nasal cavity for inspiration and expiration and that different currents to some extent are dependent on an individual's anatomy.

Flow visualisations with dye trails by Masing (1967a) revealed that the flow patterns in a nose model were dependent on the location where the dye was released. Several other flow visualisation studies have been conducted in artificial models from nasal casts with transparent nasal septums using both liquids (Fischer 1969; Hess et al. 1992; Konno 1969; Mlynski et al. 1993; Müller-Wittig et al. 2002; Stuiver 1958) and gases (Masing 1967b; Simmen et al. 1999; Tonndorf 1939). Hess et al. (1992) recorded on a camera the motion of 0.2 mm polystyrene particles and die injections from several needles and demonstrated that flow existed throughout the nasal cavity to some extent because the entire surface of his model could be stained with dye. Flow visualisations by Simmen et al. (1999) were the first to use an unsteady flow to simulate physiological conditions. Peak airflow rates of 10, 20 and 30 l/min were created with a piston pump, with inspiration and expiration durations of 2 and 3 seconds, respectively.

Mlynski et al. (2000), and Churchill et al. (2004) have carried out more recent visualisations of steady flows through nasal casts of cadavers. Mlynski et al. carried out flow visualisations in flat, transparent boxes (Mink 1920) and nasal casts using inks, coloured solutions and hydrogen bubbles. The featureless boxes allowed Mlynski et al. to investigate the effect of different physiologically relevant inflow and outflow conditions independently from the complex geometry of the nasal cavity. A concavely curved inflow opening, for example, represented a nostril and produced a more dispersed and turbulent flow stream in the main cavity compared with a straight inflow opening. Also, an anterior wall that was inclined to represent the downward curve of the nasopharynx encouraged the flow stream towards the roof of the main cavity, whereas the flow was more horizontal with a vertical anterior wall. Flow interference from the small tubes used to apply the coloured solutions was overcome by delivering the coloured solutions perpendicularly to the water flow through small holes in the model wall. Mlynski had previously (Mlynski et al. 1993) used air as the working fluid and visualised streamlines with ammonium chloride, titan-(4)-chloride, tobacco smoke, and smoke from fumigating candles; however, abandoned air as the working fluid in favour of water due to difficulties with clouding of the models' inner walls, irritations in the investigator's airways due to the airborne chemicals, and producing a steady and reproducible stream line.

Churchill et al. (2004) studied inspiratory airflow patterns and flow regimes in half nasal models derived from six male and four female Caucasians. In undertaking these measurements Churchill et al. were attempting to elucidate the impact of anatomical variation between individuals and justify the contradictions in the literature at the time. In four models, principal flow was equally divided between the inferior and middle meati, whilst in three models the main flow was along the septum and did not enter the meati. The flow was exclusively through the middle meatus in two models, and in the final model the flow

was relatively uniform throughout the nasal cavity. At flowrates as low as 1.3 l/min (in vivo scale) all the models exhibited either turbulent or transitional flow characteristics. In no cases were laminar flows present throughout the nasal cavity; however, in two models streamlines persisted up until the nasal valve at 35 and 41 l/min. The large differences between results from each model suggest a large inter-individual variation amongst the population and provide justification for the discrepancies in principal flow paths reported in the literature. Churchill et al. performed an analysis of variance (ANOVA) and found no statistically significant correlations between the airflow characteristics and any of the morphological features assessed, such as nares angle, height of the nasal cavity, nasal valve area relative to internal chamber cross-sectional area, and projection of the inferior and middle turbinates. This suggests that the features influencing the flow regime are yet to be identified or that the sample size of 10 models was simply too small considering the large variation exhibited between each.

One Dimensional Quantitative Methods

Stepping back in time from Churchill et al.'s measurements, it was in 1977 that Swift and Proctor conducted the first quantitative measurement of a nasal velocity field using a miniature Pitot probe device. The tests were made in conjunction with flow visualisation experiments in a clear polyester resin cadaver cast of one choanae. Swift and Proctor give a detailed description of the inspiratory flow pattern at a half nasal flowrate of 12.5 l/min (representative of a total 25 l/min). In 1983 Girardin et al. claimed the first noninvasive, quantitative study of nasal airflow patterns by using laser Doppler Velocimetry (LDV). These measurements were a precursory study to those by Arbour et al. (1985). Optical access was achieved by replacing the septal wall from a cadaver cast with a viewing window. The experimental apparatus consisted of a 15mW ThermoSystems (TSI 900-2) laser (He-Ne) Doppler velocimeter and a ThermoSystems TSI 3060 particle generator to produce seeding particles of water in air. Measurements were conducted across five coronal cross-sections. Four years later, Hornung et al. (1987) quantified the distribution of the inspiratory airflows in a plastic model of the left choanae using a scintillation camera to detect gamma rays released by radioactive xenon 133 gas. The radioactive gas was infused into the flow through needle catheters and the distribution of radioactivity throughout the nasal cavity analysed for 5 release locations. The catheter position had a significant but reproducible effect on the distribution of the radioactivity in the model.

Scherer et al. (1989) and Schreck et al. (1993) constructed the first scaled up nasal models from computated tomography (CT) and magnetic resonance imaging (MRI) scan data, respectively. In order

to achieve a more detailed view of nasal airflow patterns and reduce the relative size and intrusiveness of measurement devices, Scherer et al. (1989) and Hahn et al. (1993) both conducted hot wire anemometry measurements in their ×20 scale model (~1.69 × 0.61 × 1.22 m) of the right choana. An expiratory flow of 66 l/min and inspiratory flows of 10.8, 33.6 and 66 l/min, which represented an average inspiration rate, medium sniff, and a forced sniff, were driven through the large-scale test facility by a brushless direct current fan connected to 0.45 m diameter ducting. Schreck et al. (1993) conducted local flow velocity measurements with hot-wire anemometry to complement their flow visualisation measurements in a 3 times scale model at flowrates representative of 3 and 90 l/min. With interpersonal variations know to be wide Schreck et al. also simulated natural congestion and mucosa swelling to assess intrapersonal flow patterns.

Particle Image Velocimetry

Since Park et al. first successfully employed PIV to measure nasal flow patterns in 1997, there has been a growing, yet limited number studies undertaken. Table 1 gives an overview of the PIV measurements conducted in other studies to date. Although PIV has become a widely used experimental flow measurement technique, PIV measurements of nasal flows have been limited largely because of the difficulties associated with replicating the nasal geometry in an optically transparent material. Much of the detail on the methodologies implemented in other studies is reserved for Chapter 2 where discussion is made in context with the techniques employed and developed in the current work. Only an overview is given here in order to outline the extent to which PIV has been performed by other researchers to date.

Each study has constructed an optically clear model of the nasal geometry using a method employing CT scan data and rapid prototyping. A liquid that matched the refractive index of the model was used as the working fluid to allow undistorted optical access through the models' curved internal surfaces. To date only planar-PIV has been employed to measure the flow through both sagittal and coronal cross-sections of the nasal cavity. Models have been limited to only one side of the nasal cavity, with the exception of Garcia et al. (2007) who constructed a bilateral model of a subject suffering from atrophic rhinitis (chronic inflammation of the nasal mucosa). Almost all the studies have simulated nasal flows by employing steady flows either assuming the respiratory cycle time is very long compared with the mean transit time for a flow through the nose (Doorly et al. 2008a), that nasal flows are quasi-steady (Chung & Kim 2008; Horschler et al. 2006a) or have not offered justification (Garcia et al. 2007; J. T. Kelly et al. 2000; J. K. Kim et al. 2006; Park et al. 1997), presumably because the simplification has been common place in nasal flow

investigations. Flowrates investigated ranged from 5–12 l/min and in three of the studies shown in Table 1 only inspiration was investigated. Chung et al. (2006) conducted the first and only time-resolved planar-PIV measurements in the nasal cavity using a piston pump driven by a cam to simulate respiration at rest. Common to each study has been shortcomings in the boundary condition applied at the nose, which will be discussed in detail in Chapter 2.

The available camera resolution has increased over the years and enabled higher spatial resolutions. Park et al. (1997) constructed time averaged full field velocity maps through the nasal cavity by stitching together results from five overlapping regions in order to increase the spatial resolution obtainable with a 785 × 512 pixel^2 resolution camera. The use of dual cavity, pulsed Nd:YAG lasers has been prevalent, although Doorly et al. (2008a) used a diode laser, which allowed high repetition rates and enabled measurements to be captured at the maximum frame rate of their CMOS camera (462 fps). Diode lasers are relatively cheap, however, the pulse power is low. Kelly et al. (2000) captured results on 46 sagittal planes through the nasal flow domain spaced by 1 mm increments and presented each as a 2D plot. Chung et al. (2006) reconstructed flow volumes and coronal cross-sections from data obtained over 33 sagittal planes. In 2008, Doorly et al. provided a review of PIV studies in the nasal cavity, which is still up-to-date excluding the current work. PIV has also been applied to measure the flow field in idealized models of the human oropharynx and larynx (Heenan et al. 2003; Triep et al. 2005; Versteeg & Hargrave 2001).

Table 1. Experimental parameters for PIV measurements of nasal flows conducted to date

Study	Scale	In Vivo Flow Conditions	Liquid	Seeding	Camera	Laser	Light Sheet Orientation
Park et al. 1997 Brücker & Park 1999	3:1	Steady Inspiration: 5 l/min Expiration: 5 l/min	Tetraline	N.A.	CCD-video camera connected to a S-VHS recorder 768 × 512 pix^2 (25 Hz)	Not specified	Sagittal: 18 planes, 2 mm intervals
Hopkins et al. 2000; Kelly et al. 2000	2:1	Steady Inspiration: 7.5 l/min	Aqueous glycerol	60 μm hollow glass spheres	CCD (Kodak ES1.0) 1008x1018 pix^2	Dual cavity 300 mJ pulsed Nd:YAG	Sagittal: 46 planes, 1 mm intervals
Horschler et al. 2006	1.5:1	Steady Inspiration: 9.5 l/min Expiration: 7.6 l/min	Aqueous glycerol	Air bubbles	CCD	Dual cavity pulsed Nd:YAG	Sagittal: 20 planes, 1 mm intervals Coronal:10 planes
Kim et al. 2004 Kim et al. 2006	N.A.	Steady Inspiration: 7.5 l/min Expiration: 7.5 l/min	Aqueous glycerol	80 μm polyvinyl spheres	CCD 1280 × 1024 pix^2	Dual cavity 150 mJ pulsed Nd:YAG	Sagittal
Chung et al. 2006	2:1	Unsteady Period: 3 s Tidal volume: 500 ml	Aqueous glycerol	80 μm polyvinyl spheres	CCD 1280 × 1024 pix^2	Dual cavity 150 mJ pulsed Nd:YAG	Sagittal: 33 planes, 1 mm intervals
Garcia et al. 2007	1:1	Steady Inspiration: 12 l/min	Aqueous glycerol	9-13 μm hollow glass spheres	CCD (Flowmaster 2S) 2048 × 2048 pix^2	Dual cavity pulsed Nd:YAG	18 planes total Sagittal: 2 mm intervals Coronal: 5 mm intervals
Doorly et al. 2008	2:1	Steady Inspiration: 6 l/min	Aqueous sodium benzoate	10 μm hollow glass spheres	CMOS (VDS Vosshuler HCC-1000) 1024 ×1024 pix^2 (462 fps)	200 W diode laser, 16mJ/pulse, (HSI 5000)	Sagittal

N.A. Not available

1.3.3 Pressure Measurements

In vivo

Rhinomanometry is a widely employed clinical method that attempts to quantify nasal airflows and pressures, contribute to the diagnosis of a patient's condition, and determine the degree of nasal obstruction before and after pharmaceutical or surgical interventions (K. Naito & Iwata 1997; Rappai et al. 2003; Sulsenti & Palma 1996). Rhinomanometry dates back to the 19th century when Zwaardemaker (1889) was the first to investigate nasal flow by placing a cold mirror under a subject's nose and measuring the area of condensed vapour that formed from each nostril. A similar method is described by Gertner et al. (1984) and illustrated in Figure 8. Modern rhinomanometry involves obtaining trans-nasal pressures with a nasal catheter and can be conducted using active or passive rhinomanometry in either anterior or posterior configurations. Active rhinomanometry relies on the subject generating the airflow through their nose by their own effort, whilst passive rhinomanometry uses a constant flow of air from an external pressure source. In posterior rhinomanometry, the nasal catheter is located in the oropharynx, and in anterior rhinomanometry, the catheter is held in and sealed with tape in one nostril. Although rhinomanometry is unable to measure the airflow pattern through the nasal cavity, it is a very useful tool for measuring nasal resistance, from which the identification of areas of high viscous losses and velocity regions can be inferred.

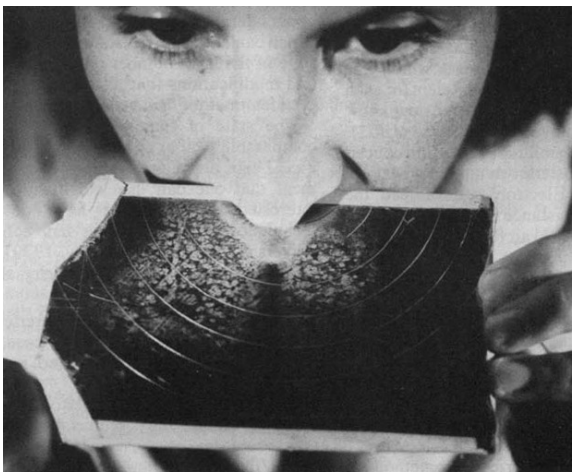

Figure 8 - Measurements by Gertner et al. (1984)

A large number of in vivo investigations have been undertaken to measure nasal pressures at various locations and the resistances of the different nasal compartments and passageways. Although

disagreements in the airflow pattern have been described to occur in the literature, the distribution of pressures and sites of high pressure losses in the nasal cavity are more consistent. The significant resistance and pressure drop across the nasal valve has already been discussed. A number of studies have measured the pressure drop across the anterior portion of the nasal cavity and attempted to decrease its resistance during exercise and for obstructive sleep apnea sufferers with the use of mechanical dilators and splinting of the nares (Gehring et al. 2000; Meissner et al. 1999; Petruson 1988). Pressure measurements by Verin et al. (2002) reported that obstructive sleep apnea sufferers had a higher upper airway resistance than normal subjects, which gave them a predisposition to airway collapse during negative inspiratory pressures. Swift and Proctor's (1977) pressure measurements on a normal volunteer showed that there is relatively very little pressure change in the 8–10 cm beyond the anterior 1.5 cm of the main nasal chamber. The flow leading up to the nasal valve is described to be 'accelerative' and the flow past the constriction 'dissipative' such that little of the pressure drop is recoverable following the nasal valve as the mean velocity decreases. A venturi meter for example behaves differently and is designed to restore the outlet pressure to the inlet pressure as much as possible. The reduced pressure at the constriction (by Bernouilli's law) has been shown empirically to promote nasal airway obstruction by collapsing the nasal valve in subjects with nasal deformity and inadequate cartilaginous support (Santiago-Diez de Bonilla et al. 1986). The magnitude of the pressure drop across the nasal valve not only varies considerably from person to person but also from time to time over the course of the nasal cycle. Pressure measurements by Hasegawa et al. (1978), Knight et al. (1991) and Principato and Ozenberger (Principato & Ozenberger 1970) showed that although the resistance of each choana changes with the nasal cycle, the total nasal resistance stays relatively constant. Laine et al. (1994) showed that breathing cold air increases nasal resistance by causing a reduction in the nasal cavity's cross-sectional area, which subsequently reduces air flowrates. Weber et al. (1981) found that there was no association between head posture and resistance to nasal airflow.

In Vitro

In vivo pressure measurements inherently include a large number of uncontrollable variables because they are taken on a non-static living subject. The catheters used as pressure probes also include measurement uncertainties. On expiration, for example, a simple open-ended catheter positioned in the airway pointing towards the lungs will only give an accurate measure of the dynamic pressure if it is orientated in the direction of the flow at that point. Furthermore, the same catheter on inspiration will measure a mixture of static and dynamic pressures. Different catheter designs have been implemented to improve the reliability

of pressure sampling, however, the desire for more repeatable and accurate measurements of airway pressures have encouraged the use of pressure tapped in vitro models.

Mylavarapu et al. (2009) conducted pressure measurements in a twice scale model of the nasal cavity built in stereo-lithography resin. Static pressure measurements were obtained at 16 pressure taps distributed along the walls of the model at an expiration flowrate of 200 l/min. It is unclear from the manuscript whether this was the flowrate applied in vitro or the represented in vivo flowrate. Presumably it was the in vitro flowrate and was representative of a 100 l/min in vivo flowrate; however, this flowrate is still above a normal physiological range for nasal flows and is even higher than the maximum nasal flowrate of approximately 60 l/min measured during exercise by Gehring et al. (2000). Such high flowrates were used because the measured static wall pressure values at lower flowrates were below the sensitivity range of the pressure sensors used. Despite subsequently impractical absolute pressures, value is obtained from the pressure trends through the nasal cavity. Mylavarapu's results show that there is very little pressure drop through the main nasal passages posterior to the nasal valve on expiration, complementing Swift and Proctor's (1977) results on inspiration. Mylavarapu's measurements uniquely included pressure measurements in the oropharynx, reporting the largest pressure drop was found to occur across the velopharynx, where the pressure was negative at the narrowest point. The pressure largely recovered as the cross-sectional area increased again towards the nasopharynx, unlike the unrecoverable pressure loss following the nasal valve on inspiration described by Swift and Proctor.

In a three times scaled model, Schreck et al. (1993) measured the pressure drop across three sections of the nasal cavity over a 6–66 l/min range of expiration and inspiration flowrates. As a fraction of the total nasal cavity pressure loss, the contribution of the nasal valve rose dramatically between a flowrate of 6 and 12 l/min due to the onset of turbulence, which was observed in parallel visualisation experiments. Over a flowrate of 12 l/min the pressure loss contribution of the nasal valve remained relatively constant, as did the pressure loss across the main nasal cavity and the nasopharynx. To examine the influence of geometry on the pressure losses, the cross-section at various locations was reduced with modeling clay. A reduction in nasal valve cross-sectional area from 1.2 cm^2 to 0.50 cm^2 (~50%) almost quadrupled its flow resistance. A partial enlargement of the inferior turbinate that narrowed the inferior and middle airways resulted in a more pronounced increase in resistance than a complete blockage of the upper meatus and the olfactory slit. Pressure measurements by Naito et al. (1989), in assessing 18 different simulated pathological nasal conditions, similarly found that swelling of the inferior turbinate produced the greatest increase in nasal resistance, particularly when combined with other minor abnormalities such as a polyp in the middle

airway. It can therefore be inferred from Schreck et al.'s and Naito et al.'s results that there was a preference of flow towards the inferior and middle airways. Mylavarapu et al. (2009) and Schreck et al. (1993) reported significant pressure variations around a given location's perimeter due to local acceleration and deceleration amongst the convoluted surfaces.

1.3.4 Computational Modeling

Difficulties in constructing laboratory models and developments in the fields of computational methods and computer technology over the past two decades have enabled a large growth in the number of computational studies modeling physiological flows. Recently there has been a growing interest in the application of computational fluid dynamics (CFD) to respiratory flows for it's non-invasive nature and the ease in which multiple variables, such as inspiratory and expiratory flowrates, breathing patterns, geometries, and lung pressure can be altered and their respective influence on the flow characteristics assessed. A goal proposed by Horschler et al. (2006a) was to be able to use CFD to determine the potential value of surgery prior to operation by conducting virtual nose surgery. Although a large number of numerical studies of nasal airflows have been performed, because the focus of the current study is experimental, rather than discussing numerical methodologies in detail, the findings of the numerical studies will be included in the following section and the methodologies only discussed where relevant. Suffice it to say that the vast majority of the numerical works conducted to date have used steady flows through simplified geometries derived from CT or MRI scan data and employed a RANS (Reynolds-averaged Navier-Stokes) based solver (Elad et al. 1993; Ishikawa et al. 2006; Keyhani et al. 1995; Lindemann et al. 2006; Schroeter et al. 2006; Subramaniam et al. 1998; Taylor et al. 2010; Wen et al. 2008; Yu et al. 2008; Zhang et al. 2008). Large eddy simulations (LES) (Lee et al. 2010; Liu et al. 2010; Mylavarapu et al. 2009) and Lattice Boltzmann methods (LBM) (Ball et al. 2008; Finck et al. 2007; Mosges et al. 2010) have also been implemented, whilst the complex geometry and flow within the nasal cavity has to date prohibited the use of Direct Numerical Simulations (DNS). Early works were limited to idealised two-dimensional models (Daviskas et al. 1990; Farley & Patel 1988; Schroter & Watkins 1989) and investigations of only one side of the nasal cavity (Elad et al. 1993; Keyhani et al. 1995). Bailie et al. (2006) provides a review of the general issues in applying CFD techniques to modeling nasal airflow.

1.3.5 Nasal Airflow Patterns

This section provides a detailed overview of the current knowledge on the airflow pattern through the human nasal cavity, drawing on the aforementioned in vivo, in vitro and numerical studies conducted by researchers to date. Inspiration and expiration will be reviewed separately because the flow pattern is dependent of the flow's direction, behaving differently around the various nasal cavity structures. To aid visualisation and understanding, the flow pattern will be described by stepping through the various regions of the nasal cavity sequentially for both inspiration and expiration. Surveys of knowledge at the time on the flow characteristics in the nasal cavity obtained from experimental and computational methods include those provided by Eccles et al. (2000), Wolf et al. (2004), Bailie et al. (2006), and Doorly et al. (2008b).

Inspiration

Numerical simulations by Doorly et al. (2008c) show that flow inspired into the nostrils is drawn in from the entire hemisphere in front of the face. The inspired air enters the nostrils at an angle of approximately 60° relative to the horizontal floor of the nose (Swift & Proctor 1977) and flows in towards the septum at approximately 20° for the first 10 mm after entering the nostrils (Proetz 1951). Proetz (1951) described the size and shape of the nostrils not to cause a deviation from a standard flow distribution throughout the nasal cavity so long as the initial stream enters generally upward. On the other hand, Churchill et al. (2004) described correlations in nostril size and orientation with populations' different air-conditioning requirements as mentioned in section 1.1.2. It is now thought that both the flow in the nasal cavity and overall resistance is largely determined by the size and orientation of the nasal valve (Doorly et al. 2008c; Schreck et al. 1993; Taylor et al. 2010). Results from all studies to date have been consistent in showing stable acceleration of the flow up to and large pressure drop across the nasal valve. The ubiquity of this phenomena is supported by numerical simulations by Yu et al. (2008) and Zhang (2008) who respectively investigated the flow pattern in 24 and 30 adult nasal geometries, and found the nasal valve and nasal vestibule to consistently account for more than half and up to 78.3% of the overall upper airway resistance. Unanimous agreement on inspiratory flow patterns, however, ends downstream of the nasal valve where there is an abrupt expansion in both cross-sectional area and height entering the main cavity.

Wolf et al. (2004) reviewed maximum velocities of 6–18 m/s in the nasal valve, and described inspired air to rise vertically towards the anterior end of the middle turbinate and decrease to 2 m/s as it entered the main cavity. Doorly et al. (2008c) described the emergence of an inspired jet from the internal nasal valve into the main cavity on inspiration. Several researchers (Doorly et al. 2008c; Hopkins et al. 2000; Schreck

et al. 1993; Swift & Proctor 1977) have described a large recirculation in the upper anterior region and flow separation above the inspired jet caused by the adverse pressure gradient along the abrupt expansion in cross-sectional area. Schreck et al. also reports a second smaller yet distinct vortex below the stream of inspired air. Schreck et al. visualised the vortex circulation to increase with flowrate, yet remain relatively constant in size. Dye injected into the lower vortex was immediately washed downstream, whereas dye injected into the upper vortex was recycled and took a time-span equivalent to an inspiration period to be replaced by fresh air.

The main inspiratory flow stream has commonly been reported to pass through the middle airway (Doorly et al. 2008b; Francke 1893; Hornung et al. 1987; J. K. Kim et al. 2006; Masing 1967a; Paulsen 1882; Swift & Proctor 1977). This conclusion has required careful analysis of the literature because the terminology used to describe the various pathways in the nasal cavity is inconsistent. The regions defined in the current work to be the middle airway and the middle meatus have in some instances been referred together as the middle meatus (J. K. Kim et al. 2006; Parker 1901; Proetz 1951). This is misleading because the middle airway is a region of high flow, whilst low flowrates have been reported in each of the inferior, middle and superior meati (J. T. Kelly et al. 2000; Schreck et al. 1993; Wen et al. 2008). Swift and Proctor (1977) describe a small amount of air passing through the middle airway to be directed towards the floor of the chamber. Kim et al. (2006) measured the flow distribution passing through the superior, middle and inferior superior airways as 14.7, 53.2, and 32.1%, respectively, at a flowrate of 7.5 l/min. Contrastingly, the majority of inspired flow has been reported to pass through the inferior airway by Hess et al. (1992), Kelly et al. (2000), Keyhani et al. (1995) and Elad et al. (1993). Scherer et al.'s (1989) results showed that approximately 50 % of inspiratory flow passes through the combined middle and inferior airways and 14% of the flow passes through the olfactory region regardless of flowrates. Churchill et al. (2004) described the olfactory area as "effectively a dead space" with very little flow in each of the models they investigated. Stuiver (1958) reported that 5–20% of inspired air passed through the olfactory slit. Hahn et al. (1993) reported that nasal airflow distributions were very similar for all inspiratory flowrates measured (10.8, 33.6 and 66 l/min), which differs to the findings of Stuiver et al. who suggested the percentage flowrate through the different passageways varied with flowrate. The distribution of flows between the various nasal passageways becomes more even towards the posterior (Girardin et al. 1983) and the flow exits the nasal cavity following the roof of the nasopharynx downwards (Parker 1901). Numerical investigations that included the pharynx by Jeong et al. (2007) showed that the constriction at the velopharynx causes an accelerated jet that extends down into the larynx attached to the posterior

pharyngeal wall. Jeong et al. suggested the size and strength of the jet (and hence magnitude of the reduced velopharynx pressure) to be dependent on a subject's individual anatomy and the main reason for pharyngeal occlusion in some OSA patients.

Although Proetz (1951) said the turbinates have little to do with the direction of inspiratory currents because they are streamlined in this direction, my opinion after an exhaustive survey of the literature is that the apparent disagreement on the flow pattern and distribution through the main cavity is dependent on the relative orientation and dimensions of the nasal valve and the inferior turbinate. It appears that if the inspired stream from the nasal valve impinges on the upper side of the inferior turbinate the flow is directed through the middle airway, whilst if the flow hits the under side the flow is deflected through the inferior airway. I also think that this can be flowrate dependent, i.e. at what point the flow separates from the nasal valve.

Expiration

There is less literature available regarding the expiratory flow pattern than on inspiration because a significant fraction of researchers have focused on the flow phenomena associated with air-conditioning of inspired air alone (Doorly et al. 2008a; Garcia et al. 2007; Jeong et al. 2007; J. T. Kelly et al. 2000; Scherer et al. 1989; Swift & Proctor 1977). On expiration, Proetz (1951) described a single stream to flow rapidly upwards from the velopharynx and be deflected sharply forward along the roof of the nasopharynx. Proetz observed a region of little air movement on the floor of the nasopharynx below the high-speed air stream. Girardin et al. (1983) reports a maximum velocity of 2 m/s along the nasopharynx roof on expiration, whilst only 1 m/s occurred on inspiration. Other studies found the geometry at this location induced a stagnation point and flow separation (Park et al. 1997) as well as flow recirculation (Chung & Kim 2008). Although not named in the manuscript as Dean vortices (Dean 1928), Schreck et al. (1993) described secondary flows consisting of two counter-rotating streamwise vortices formed in the bend of the nasopharynx in an analogous manner to those formed in curved pipes. The strength of these vortices increased with flowrate and caused the flow to enter into the main nasal cavity with a swirling motion.

The flow is bifurcated into each choana by the posterior end of the septum and subsequently divided by the posterior ends of the turbinates. Again flow through the middle airway appears to predominate (Francke 1893; Park et al. 1997; Simmen et al. 1999). Kim et al. (2006) measured the flow distribution passing through the superior, middle and inferior superior airways as 13.9, 43.8, and 42.3%, respectively, at a flowrate of 7.5 l/min. Although the main flow was again through the middle airway, the amount of flow

through the inferior airways was larger than during inspiration. Contrasting results that show the main expiratory flow stream through the inferior airway are again present in the literature (Elad et al. 1993; Ishikawa et al. 2006; Keyhani et al. 1995; Parker 1901); however, it is generally agreed the flow is lower though the nasal cavity on expiration than on inspiration (Chung & Kim 2008; Parker 1901; Swift & Proctor 1977) and the flow more evenly distributed (Ishikawa et al. 2006; Keyhani et al. 1995; Simmen et al. 1999). Furthermore, the flow becomes more evenly distributed towards the anterior (Girardin et al. 1983), which in the current author's opinion is due to the large resistance imposed by the nasal valve upstream. Parker et al. (1901) reported the main flow stream to be constantly in the inferior airway, although an increasing percentage passed through the middle airway at increased flowrates. This is perhaps because the higher the flowrate, the higher the tendency of the flow to concentrate high on the roof of the nasopharynx as it turns into the main nasal cavity due to centripetal acceleration. Like on inspiration, low flowrates in the olfactory region are unanimously agreed. Wolf et al. (2004) surveyed maximum velocities of 3–6 m/s in the nasal valve and velocities of 1–2 m/s throughout the main cavity. Also noteworthy on expiration is a small eddy located in the sphenoethmoidal recess (Proetz 1951) (the region formed by the protrusion of the sphenoidal sinus illustrated in Figure 6) and a flushing of the anterior vortices present on inspiration (Schreck et al. 1993).

Flow Regime

Opinion on whether the flow is laminar, turbulent or disturbed laminar in different regions of the nasal cavity is also divided for both inspiration and expiration. Doorly et al. (2008c) states that even minor laminar flow disturbances in the complex geometry of the nasal cavity can induce rapid dispersion, which can be confused with turbulent mixing. It is clear from surveying the literature that the Reynolds number is not the sole criterion for predicting the onset of flow instability. Schreck et al. (1993) for example reported a transition to turbulence posterior of the nasal valve at a Reynolds number of only 600 and a flowrate of 15 l/min. Despite Girardin et al's (1983) calculations estimating the flow regime to be laminar, the flow within the anterior main cavity was reported to contain "strong local turbulence".

Swift and Proctor (1977) and Churchill et al. (2004) found the flow through the nostril and nasal valve to be laminar and was predicted to remain as such at higher flows because of the favourable pressure gradient and stability of the flow converging up to the nasal valve constriction. The abrupt expansion from the high-velocity, low pressure conditions of the nasal valve to the low-velocity, high pressure region of the main cavity was said to cause turbulence from the sudden decrease in velocity and viscous retardation of the air.

Swift and Proctor reported a transition at 7.5 l/min where the streamlines did not break up immediately downstream of the nasal valve at lower flowrates. Flowrates at which flow instability onset occurred have also been reported as 10.2 l/min (Doorly et al. 2008c), 10.8 l/min (Hahn et al. 1993), 12 l/min (Keyhani et al. 1995) and 9.8 l/min (Churchill et al. 2004). Kim et al. (2006) calculated the root mean square (RMS) velocity fluctuation intensities from data obtained with PIV. Although values were not presented, the highest levels were found to occur where the inspiratory jet entered the main cavity from the nasal valve, indicating that this was the region with the greatest velocity gradient and flow instability.

Swift and Proctor describe turbulence to persist throughout the remainder of the nasal cavity without the geometry introducing further flow instability. The projection of the turbinate bones into the nasal cavity have been said to laminate the flow (Churchill et al. 2004; Elad et al. 1993; Girardin et al. 1983; Scherer et al. 1989), or in other words create regions of laminar flow within an otherwise turbulent regime. In contrast, Courtiss and Goldwyn (1983) and Proetz (1951) have suggested the role of the turbinates is to induce turbulence. On analysis of hot wire anemometry measurements, Hahn et al. (1993) reported the airflow in the nasal cavity to be mostly turbulent at 33.6 and 66 l/min, and laminar at 10.8 l/min. Turbulence intensities, *I*, were calculated to be highest near the nasal valve (2.3-3.7%) and in the nasopharynx (3.1-5.1%), as defined by Equation 1, where $\bar{u}$ is the mean velocity and u' is the fluctuating component. Although Hahn et al. and several other researchers (Arbour et al. 1985; Hornung et al. 1987; Masing 1967a; Schreck et al. 1993; Simmen et al. 1999) report the flow in the nasal cavity to be fully turbulent, based on these turbulence intensity values and review of the literature it appears more likely that the flow is laminar with unsteady flow features. Empirical turbulence intensities of 5% or less are unlikely to be indicative of fully turbulent flow and in the current author's opinion merely show a level of flow variance and include measurement error. Flow instability and transient behaviour is thought to be advantageous for air-conditioning because particle impact on the mucosal surfaces is increased and the boundary layer is destabilised, keeping thermal and moisture gradients high, and preventing an insulating laminar boundary layer (Churchill et al. 2004; P. Cole 1982). Literature concerning the effect of time varying breathing flowrates will be reviewed in Chapter 6.

$$I = 100\frac{\sqrt{(u')^2}}{\bar{u}}\% \qquad \textbf{Equation 1}$$

1.4 Nasal High Flow Therapy

The use of nasal cannulae to deliver supplemental oxygen to patients at flowrates in the order of 1–6 litres per minute became common practice in hospitals since the first cannula was invented and patented by Wilfred Jones in 1949. Cannula therapy until recently has been limited to low flowrates due to the discomfort and irritation caused by delivering dry, cold gas to the nasal passages (Campbell et al. 1988). Campbell et al. noted that even at these low flowrates, over 40% of patients complained of a dry nose and throat while receiving the therapy. Exposing the air-conditioning tissues in the nasal cavity to higher than normal ventilation flows can overload these tissues and cause significant dysfunction, drying and damage to nasal mucosa (M. G. Kelly et al. 2001; Robertson et al. 1996; R. Williams et al. 1996). A relatively new breathing therapy known as nasal high flow (NHF) delivers heated and humidified air at body temperature pressure saturated (BTPS) to patients at steady flows ranging from 5–50 l/min via a nasal cannula. BTPS air is 37°C, has a relative humidity of 100% and an absolute humidity of 43.9 mg H_2O/l. NHF flows are coined high flow because they are not only significantly higher than what had been used previously but also because cannula flowrates can exceed patients' peak inspiratory flowrates. NHF is used in hospitals worldwide as well as in home settings. The Optiflow™ nasal cannulae (Figure 9) investigated in this study are produced by Fisher & Paykel Healthcare, Auckland, New Zealand. Optiflow™ consists of a manifold that rests on the upper lip and two elliptical cross-section prongs that protrude into each nostril

Figure 9. Optiflow™ nasal cannula (medium size) produced by Fisher & Paykel Healthcare

by approximately 10 mm. The dimensions of the three available sized cannulae, which vary in prong diameter, are given in Table 2.

Table 2. Dimensions of cannulae prongs

Prong Dimensions (mm)	Small	Medium	Large
Internal major and minor axis	4.5, 3.0	5.5, 3.5	6.0, 6.0
Wall thickness	0.4	0.4	0.5
Separation distance	14	15	18

NHF has been introduced as a potential alternative to more established non-invasive ventilation methods such as nasal and full-face continuous positive airway pressure (CPAP) masks, non re-breather masks, and venturi masks. Tight fitting masks are often poorly tolerated by patients, which can result in a need for invasive ventilation (Demoule et al. 2006). Non-invasive ventilation is desirable where possible because intubation and mechanical ventilation require a more intensive level of care and pose considerable risk of airway trauma (Ursella et al. 2007). It has been reported that patients are more willing to comply with NHF because it is more comfortable and allows patients to drink, eat and communicate without interruption of the therapy (Sreenan et al. 2001), as well as reducing the number of patients requiring intubation (Groves & Tobin 2007). Although NHF has several advantages over traditional non-invasive ventilation methods, more of which will be described in the following paragraphs, because NHF is still in its infancy as a breathing therapy it is not yet seen as a replacement for current methods, but is proposed to fit along a continuum of respiratory care as shown in Figure 10.

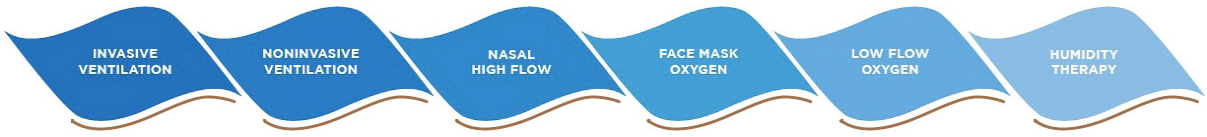

Figure 10. Continuim of respiratory care proposed by Fisher & Paykel Healthcare

NHF can provide ventilation with or without supplemental oxygen to treat hypoxemic patients in mild to moderate respiratory distress. The flexibility of delivering a broad range of flowrates and oxygen concentrations allows the therapy to be titrated as a patient's condition improves and is weaned off respiratory support or becomes more acute. The most common patient conditions for which NHF is currently employed are chronic obstructive pulmonary disease (COPD) and hypoxic pneumonia. COPD refers to a progressive disease that creates breathing difficulties such as in the case of chronic bronchitis

and emphysema. In 2007, COPD was the 4th leading cause of death in the United States of America and resulted in US$42.6 billion in health care costs and lost productivity (*Morbidity & Mortality: 2007 Chart Book on Cadiovascular, Lung, and Blood Diseases* 2007). NHF is also used to treat patients undergoing head and neck cancer radiotherapy with impaired saliva glands or in postoperative recovery because the humidification prevents dehydration and thickening of secretions (Conway et al. 1992) and subsequent irritation of the nasal mucosa. The metabolic energy cost associated with warming and humidifying inspired gas during normal breathing is thought to be reduced with NHF because air is delivered already at BTPS (Dysart et al. 2009). Saslow et al. (2006) found that the mechanical work of breathing was similar between NHF and nasal CPAP. It has been demonstrated that improved ventilation is achieved with NHF compared with a traditional Hudson CPAP mask (Lund et al. 1996) or a non-rebreather mask (Tiep & Barnett 2002) at equivalent flowrates. A key mechanism by which NHF is thought to improve ventilation is the production of elevated airway pressures.

Artificially elevating the pressure in the airways with the use of masks that seal to the face is widespread in intensive care units. There are a number of measures of the level of elevated airway pressure, including maximum and minimum pressure, positive end expiratory pressure (PEEP) and the mean airway pressure. The maximum pressure in the airway occurs at the height of expiration and the minimum at the maximum inspiratory flowrate. PEEP pressure is defined as the airway pressure (usually measured in the oropharynx) at the end of expiration when there is no flow. Positive airways pressure (PAP) was initially used for the treatment of obstructive sleep apnea. The increased pressure effectively splints the airway, which prevents the soft palette from collapsing as it relaxes during sleep and causing a pause in breathing (an apnea) by blocking the airway. Today PAP is also known to improve ventilation through alveoli recruitment and increase the functional residual capacity of the lung. In some cases of respiratory failure the alveolar can collapse during inspiration (negative lung pressure), which not only renders them ineffective but also requires significant work and pressure to re-expand them on expiration. PAP holds open regions of the lung that would otherwise collapse. This is a process is called lung recruitment. Whether or not alveolar have collapsed, the distending pressure from PAP expands the chest and lung and increases the functional residual capacity. There is therefore more gas in the lung that is constantly undergoing gaseous exchange, improving the effectiveness of the lungs.

NHF has also been found to produce elevated airway pressures in both adults (Chatila et al. 2004; Groves & Tobin 2007; A. B. Williams et al. 2006) and neonates (Kubicka et al. 2008; Lampland et al. 2008; Saslow et al. 2006; K. L. Spence et al. 2007; Sreenan et al. 2001; Wilkinson et al. 2008). Although the two

therapies are functionally similar, the cannula design, anatomy and breathing mechanics differ significantly between adult and neonate NHF systems. The current work will consider only NHF in adults. Groves et al. (2007) measured pharyngeal pressures in five male and five female healthy adult subjects aged 29–41 years with a 3.3 mm (French gauge 10) catheter passed via the nose into the oropharynx. While breathing with the mouth closed and 40 l/min cannula flow, the average pharyngeal PEEP over the 10 subjects was 5.5 cm H_2O. Groves et al. reported that pressures were in general higher in the females, because of their noticeably more 'petite' facial features despite higher body mass indexes than the male volunteers. The mean pharyngeal pressures reported by Williams et al. (2006) at cannula flows of 10 and 50 l/min in 10 healthy subject of 0.51 cm H_2O (± SD of 0.35 cm H_2O) and 5.13 cm H_2O (± SD of 1.32 cm H_2O), respectively, compared well with Groves et al's results. Chatila et al's (2004) values of tracheal PEEP of 2.5–3 cm H_2O measured in one subject with a cannula flow of 36 l/min were slightly lower than that of Groves et al. It should be noted that the measurement location of Chatile et al. (trachea) and Groves et al. (pharynx) differed; however, given that both were measuring PEEP pressure, which by definition occurs when the flow is zero, this discrepancy should have no or negligible effect because at zero flow the resistance between the trachea and pharynx should be zero. Groves et al. also measured PEEP during mouth-open breathing and found that the pharyngeal pressures were approximately half the mouth-closed results.

Despite the very limited number of studies measuring airway pressure during NHF, and the small sample size of healthy volunteers of each, it is clear that there is a large interpersonal range of airway pressures for a given cannula flowrate. This seems reasonable given a large range in different people's anatomy and physiology, for example nare size and breathing pattern. A clinician administering NHF therefore can't be sure what level of therapy is being given. This is the difficulty of NHF being an open system, where the prongs do not seal around the nares and the patient is free to open their mouth, as opposed to the more easily controlled closed system nature of a CPAP mask. Although NHF has been shown to produce elevated airway pressures and is currently used in hospitals with this intention, the therapy is not marketed as a pressure delivery therapy because the pressure is unregulated. The key parameters that determine the delivered pressure are thought to be the cannula flowrate, breathing flowrates and nare size. With a smaller nare size there is less area for expiratory and cannula flows to escape between the cannula's prongs and the nostrils, creating a high resistance on expiration. The only current guidelines for controlling the pressure in which NHF delivers are based on feedback where possible from the patient on what flowrate seems comfortable or tolerable, and that the cannula occludes no more than 50% of the patient's nostril area.

NHF is instead marketed to deliver high flows of conditioned breathing gases for increased oxygenation and benefits of humidification.

1.5 Conclusions

The nasal cavity geometry is complex and comprises two separate and asymmetric choana that extend backward from the nostrils until the nasopharynx where the airways merge. The primary function of the nasal cavity is to warm, humidify and filter inspired air before it reaches the lungs. The nasal cavity's tortuous passages form a large surface area and are lined with mucosa. These moist surfaces are extensively vascularised and facilitate the mechanism for heat transfer and evaporation of water from mucus. The nasal cavity accounts for approximately half of the total respiratory tract airflow resistance and the majority of the resistance is attributed to the nasal valve constriction.

Detailed flow measurements in the nasal cavity in vivo are prohibited by the narrowness and complexity of the nasal geometry, necessitating the construction of transparent artificial models for in vitro flow studies. PIV is a non-intrusive, high resolution and accurate optical flow measurement technique that provides a near-instantaneous whole field velocity map through a cross-section of a gas or liquid flow. PIV is well suited to measuring complex flow patterns and was chosen for the current work on this basis for measuring the flow field in the nasal cavity. Only a small number of PIV studies of nasal flows are present in the literature and all have been limited to planar-PIV and varying degrees of geometry simplification. All studies have also employed only steady flows and unilateral nasal models of one choana with only one exception for each. The most important finding from surveying the literature on nasal airflow patterns is perhaps that the flow distribution through the nasal cavity is not uniform and is dependent on a particular nasal geometry and flowrate. Although there is variation in reports on the principal direction of flow in the nasal cavity, there is agreement on the gross flow features, which appear to be common to the entire population. These features include high velocities in the nasal valve and nasopharynx, low velocities in the olfactory region and in each meatus and a more even distribution of flowrates through the various passageways on expiration compared with inspiration, where the flow is higher through the nasal cavity. The relationship between morphology and variations in the characteristics of nasal airflow remains to be identified, although the size and orientation of the nasal valve is thought to have a significant influence on flow distribution and magnitude. Although a number of studies have reported turbulent flow and referred to turbulent flow features in various regions, the term turbulence will be avoided until the flow can be

proven as truly turbulent on a wide range of scales. Instead, flow features such as recirculation regions and flow expansion will be described as transient behaviour or flow instability. It is important not to confuse flow variance with turbulence.

Nasal high flow cannulae are used to deliver heated and humidified air to patients at steady flows ranging from 5-50 l/min. NHF generates elevated airway pressures to help treat a variety of patient conditions and has a number of advantages over more traditional therapies. The difficulty, however, is that because the system is open to the atmosphere and everyone's anatomy is different, interpersonal variations in delivered airway pressure and therefore level of therapy for a given cannula flowrate are large. The mechanisms by which NHF generates elevated airway pressures are not yet understood. Current clinical selection of NHF flowrates is based simply on patient feedback (where possible) and experience with what has proven successful for previous patients.

To better understand the therapy and allow clinicians to make informed decisions on cannula flowrates, it is necessary to understand the effect of NHF on nasal flow phenomena, distributions and velocities, and how elevated pressures are generated. In this thesis, the flow velocities in the nasal cavity during natural breathing and NHF assisted breathing have been mapped in vitro using PIV. Investigations are focused on the nasal cavity because this is thought to be the principal site in which NHF generates positive airway pressures and where the NHF flow pattern deviates most from natural breathing conditions. As well as elucidating the effect of NHF flow in the nasal cavity, the results contribute to the understanding of the flow in the nasal cavity during natural breathing by providing the flow pattern in another unique geometry. Interpersonal variation of nasal cavity geometry is wide, and it is important to confirm that results from the limited number of geometries investigated in other studies are applicable to the general population.

The thesis is structured in the following way. Chapter 2 describes the manufacturing procedure developed to produce accurate replica models of the nasal cavity that are suitable for optical flow measurement. Chapter 3 discusses PIV techniques and introduces the necessary soft- and hardware components to perform planar and stereoscopic PIV measurements in complex nasal models. Section 3.4, which discusses the stereo-PIV apparatus, software and performance employed in the current work has been published in *Experiments in Fluids* (C. J. T. Spence et al. 2010). Chapters 4, 5 and 6 implement the constructed transparent nasal models in a series of three PIV measurement campaigns that are performed and developed with increasing complexity, measurement accuracy and physiological realism. The steady flow, planar-PIV measurements presented in Chapter 4 were published in the proceedings of the 13th

International Symposium on Flow Visualisation held in Nice, France (C. J. T. Spence et al. 2008). The steady flow, stereo-PIV measurements presented in Chapter 5 have been published in *Experiments in Fluids* (C. J. T. Spence et al. 2010). The oscillatory flow, stereo measurements presented in Chapter 6 have also been published in *Experiments in Fluids* (C. J. T. Spence et al. 2011). Each journal article published thus far are available online (http://www.springerlink.com/). Chapter 7 outlines a series of investigations conducted to supplement the knowledge obtained from previous chapters. Finally, Chapter 8 concludes the key aspects of this thesis and presents possible future developments and applications for this research.

2 Experimental Model Creation

In order to conduct PIV measurements in the nasal cavity, an optically clear physical model that accurately represents the internal geometry must first be created. These models, also referred to as flow phantoms, will be used to pass a fluid representative of air. In the current work, three anatomically accurate flow phantoms of the adult nasal cavity and upper airways were produced. In each, progressive developments were made to the modeling process, however, here only the final procedure for constructing the models is discussed. The three models are designated model 1, 2 and 3, and each was intended for a particular purpose. The construction of model 1, the first and most simplified model of half the nasal cavity, served as a pilot model on which to develop model manufacture and PIV methods. Model 2 encompassed the complete upper airways down to the bottom of the larynx and simulated mouth-closed breathing, which was the focus of the current work. Model 3 was representative of mouth-open breathing with NHF and was a culmination of developed model manufacturing techniques.

The first part of this chapter is a background of previous laboratory nasal cavity models and construction methods. The second part describes in detail the manufacture method developed and employed in the current work. A discussion on each of the three models produced is then given, followed by an outline of the various modeling assumptions. It is more traditional to discuss modeling assumptions at the beginning of a chapter; however, the intention of this chapter was to create nasal models as detailed and physiologically accurate as possible without first limiting freethinking and new developments to a set of pre-defined assumptions. The shortcomings and necessary assumptions employed are therefore adjourned, not because they are ancillary, but because this was the design process approached. Lastly, the models are compared to in vitro nasal replicas produced in previous studies and conclusions drawn.

2.1 Background

The complex re-entrant surfaces of the nasal cavity formed by the protrusion of the turbinates pose a significant challenge to replicating the complex geometry. The first artificial models of the nasal cavity were made from casts of cadavers, and then as new technologies such as medical imaging and rapid prototyping techniques became available, new techniques emerged. Proetz (1951) was the first to create an artificial model of the nasal cavity and did so by undergoing a lengthy casting procedure. A master cast of one nasal passage was first taken by injecting plaster of paris into a cadaver's nostril. For the current research such a model of the airways will be referred to as a negative, because a solid geometry has been created from what is normally the shape of the airspace. The negative model was then cast in Duroc, a hard cement-like compound used by dentists, and the plaster of Paris destructively removed to form a positive Duroc model. Silicone rubber was then poured inside the positive model to create a pliable model that could be removed intact from the undercut regions of the mold without destruction of the positive model. A number of silicone negative models were produced and modified from what was considered the original geometry to allow a range of viewing and measurement configurations. The modified silicone negatives were then cast again using Duroc to form multiple different solid positive models on which measurements were performed. Optical access was achieved by replacing the septal wall with a glass plate. Although the flat surface of the glass plate did not represent the contours of the septum, Proetz attempted to reproduce various ridges and thickenings by applying molded rubber pads. Similar methods of constructing artificial models from cadavers that incorporate some form of optical access have been employed in numerous studies (K. Cheng et al. 1995; Churchill et al. 2004; Girardin et al. 1983; Hess et al. 1992; Hornung et al. 1987; Konno 1969; Masing 1967a; Mlynski et al. 1993; K. Naito et al. 1989; Park et al. 1997; Proetz 1951; Simmen et al. 1999; Swift & Proctor 1977). Levine et al. (1986) provides a detailed description on methodology for constructing an artificial model from a cadaver.

Models constructed from a cadaver accurately replicate the form and configuration of the nasal passages; however, suffer from a number of limitations and inaccuracies. Shrinkage of the nasal mucosa due to the effects of embalming and dehydration causes the nasal casts to represent a larger nasal cavity in a hyper-decongested condition (K. Cheng et al. 1995). Injecting the casting compound is also likely to cause local deformities and distend the airway, creating a larger than normal nasal cavity that is potentially deformed. Mlynski et al. (2000), however, did state their casting material to have "outstanding cold-flowing properties" and assumed a one to one copy of the inner nasal cavity. Uniquely, Churchill et al. (2004) used

a low melting point alloy (Cerrolow 147) with a melting point of 60°C, which was assumed not to sear the nasal mucosa. The alloy was melted out of the acrylic block in boiling water and the models rinsed in dilute hydrochloric acid to remove any residue. Gravitational forces can also affect the shape of the mucosal lining post-mortem (Churchill et al. 2004). Casts from cadavers are restricted to 1:1 scale, however, Park et al. (1997) used sections of Mlynski et al.'s (1993) cadaver geometry to create a 3:1 scale model, although they did not divulge details of their methods. Simmen et al. (1999) used modeling paste to enlarge the turbinates to simulate a congested state and partially resected the turbinates to assess the effect of a turbinectomy. Naito et al. (1989) employed a model purchased commercially from Kohken Co., Ltd., Tokyo.

With the advent of medical imaging techniques such as magnetic resonance imaging (MRI) and computated tomography (CT) scans, the nasal geometry could be obtained from live subjects, avoiding the complications of obtaining a cast geometry post-mortem. Schreck et al. (1993) constructed a model of an adult male's left choana from hard copies of MRI images. The images were digitised by hand on a digitising board used to make 27 coronal templates that were cut into 12 mm acrylic cross-sections and laminated together. Although this model was the first of its kind, because of the relatively thick Perspex sheeting, the nasal contours were coarsely discretised. The subject was treated with 0.05% oxymetazoline (decongestant) for 30 minutes prior to the scan. Using a similar methodology of sections, Scherer et al. (1989) and Hahn et al. (1993) constructed a colossal 20:1 scale model of one adult male nasal choana using CT scan data (2 mm slices) to investigate finer details of the nasal flow patterns. The cross-section outlines were enlarged using photographic and pantographic techniques and were traced and cut in Styrofoam slabs that were 0.61 m wide, 1.22 m high and 40 mm thick. The sections were laminated together to form a block measuring 0.61 × 1.22 × 1.69 m that contained the internal nasal passages. The block was cut into several sections to allow the model to be disassembled and access gained to coat each internal surface with smooth casting plaster and position measuring equipment.

Rapid prototyping is a broad term used to describe a range of techniques in which a CAD model can be constructed or 3D printed in a solid material. Hopkins et al. (2000) was the first to use rapid prototyping to build a transparent model of the nasal cavity for PIV measurement. The general procedure of which is described below.

1. Segment (extract) the nasal airway geometry from medical imaging data and create a solid computer model of the nasal airspace

2. Rapid prototype the negative in a water dissoluble material
3. Cast the negative in transparent silicone
4. Dissolve the negative, leaving the positive nasal airway replicate model.

This method not only allows larger than life-size artificial models to be produced from geometries of live subjects but also in much higher resolution than the method of sections of Schreck et al. and Hahn et al. A number of nasal models have since been constructed for PIV measurement using Hopkins et al's method and these are outlined in Table 3. Each was made in transparent silicone and each uses a negative rapid prototyped in a water dissolvable material. Hopkins et al. specifically identify their transparent silicone to be Sylgard 184 (Dow Corning) and each study identifies their rapid prototyping material as cornstarch, except Garcia et al. (2007), who do not mention the material of their negative model. Although not suitable for the current work because it is opaque, noteworthy is the acrylonitrile-butadiene-styrene (ABS) plastic rapid prototyped extrathoracic model of Grgic et al. (2004) who employed boroscopic PIV.

Physical models of the nasal cavity to date have all had the shortcoming of restricting the boundary conditions of the flow domain. Modifications such as truncations before the nose and/or throat to facilitate connection of flow conduits force inflow and outflow boundary conditions that deviate from a physiological situation. The boundary condition at the nose is normally free and a fully developed profile typically applied to the nasopharynx does not accurately replace the flow profile from the lower airways. The inflow and outflow channels used in the models by Doorly et al. (2008a), Horschler et al. (2006a), and Park et al. (1997) are visible in Figures 11a–c. Images of all the models created in other studies (where available) are provided in Appendix A. The issue of over defined boundary conditions also extends to computational simulations with few exceptions (Croce et al. 2006; Doorly et al. 2008b). Numerical simulations by Taylor et al. (2010) have showed inflow geometry truncation to affect flow predictions throughout the nasal cavity significantly. Doorly et al. has also shown that the external shape of the nose influences flow entering the nares. To attempt more physiological conditions, Garcia et al. (2007) incorporated an 'air box' around the external shape of the nose, as shown in Figure 11d. Although this was an improvement on previous models, the inflow would have still been unnaturally directed upwards. Horschler et al. (2006a) immersed their model in a reservoir to create a freer boundary condition at the nostril; however, the shape of their nostril was not physiologically accurate and did not include the shape of the external nose. Each model (with the exception of Garcia et al.) has considered only one half of the

Table 3. Overview of transparent silicone nasal cavity models constructed from CT Scan data

Study	Scale	CT Scan Parameters		Segmentation Software	Subject	Comments
		No# of Images	Spacing (mm)			
Hopkins et al. 2000 Kelly et al. 2000	2:1	26	1.5	Voxel-Q and IDEAS Master Series	25 year old male	Left choana only Nostril to the start of the nasopharynx
Kim et al. 2004 Kim et al. 2006	N.A.	166	0.6	N.A.	Healthy Korean adult	Left choana only Nostril to the end of the nasopharynx
Horschler et al. 2006	1.5:1	300	1	N.A.	N.A.	Left choana only Nostril to the end of the nasopharynx (heavily simplified)
Chung et al. 2006 Chung et al. 2008	2:1	N.A.	1.25	Vworks 4.0 (CyberMed, Inc.)	Healthy Korean adult	Right choana only Nostril to the end of the nasopharynx
Garcia et al. 2007	1:1	N.A.	0.6	Mimics	26 year old Caucasian male, Atrophic Rhinitis	Both choanae External nose to the end of the nasopharynx
Doorly et al. 2008	2:1	82	0.7	Amira	N.A.	Left choana only Nostril to the end of the nasopharynx

N.A. Not available

nasal cavity, where the septum is falsely extended into the nasopharynx and/or a semi-realistic bend used to replicate missing nasopharynx geometry. In these models, the flow in the nasopharynx can therefore not be regarded as accurate.

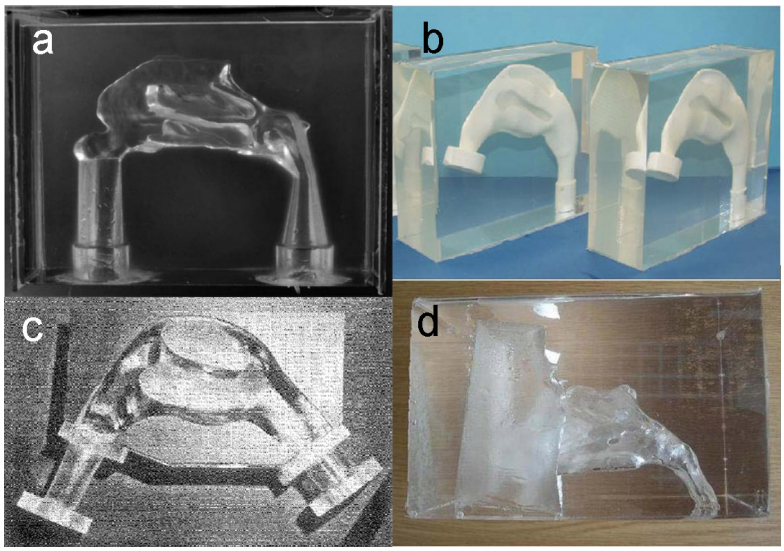

Figure 11. Experimental nasal flow models by a) Doorly et al. (2008), b) Horschler et al. (2006), c) Park et al. (1997), and d) Garcia et al. (2007).

2.2 Casting Procedure

The construction of the nasal models in the current work is based largely on the method outlined by Hopkins et al. (2000), which follows a procedure commonly known as investment casting or lost-wax casting. Hopkins et al. and subsequent papers by other researchers have omitted the necessary detail in the manufacturing process to enable construction of models from a recipe. The method of construction used in the current work therefore required significant development. Developments over a period of two years optimised all aspects of the model. Each step employed in the current work is described in detail below.

2.2.1 Solid Computer Model

The starting point for creating a replica of the nasal cavity is to define the in vivo geometry, which can be obtained from medical imaging tools such as computer tomography (CT) or magnetic resonance imaging (MRI) scans. CT scans are preferable because MRI scans have a poor contrast at the tissue/air interface due the inherent function of an MRI scan and the low concentration of hydrogen atoms in air. MRI scans

also take upwards of ten minutes to perform and even slight movements from the patient, which are inevitable for the respiratory system, can cause distorted images and a loss of contrast at interfacial surfaces. CT scans effectively measure differences in density (absorption of x-rays) and therefore provide a relatively distinct boundary between tissue and air. An example data set is shown in Figure 12. The anonymised patient CT data used in the current work were obtained from St George's Radiology, Christchurch by both retrospective examination of clinical records and prior arrangement with specific criteria. The subjects were given a stop swallowing instruction and asked to hold their breath for the approximate 15-second duration of the scan. The geometries obtained and models produced are therefore representative of a mid tidal breathing phase. Holding the breath was not expected to alter the resting position of the soft palate because given a mode of either nasal or mouth breathing this does not normally change between inspiration and expiration. The distensibility of nasal tissues will be addressed in section 2.5.1.

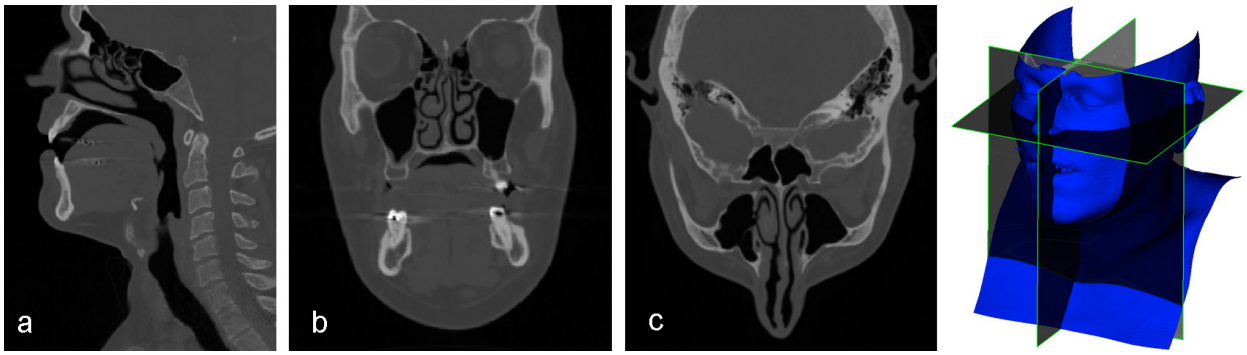

Figure 12. CT scan data set of the upper airways: (a) sagittal view (b) coronal view (c) axial view

In order to extract the airway geometry from the CT scan data a process referred to as segmentation is performed using a combination of manual user intervention and thresholding. Significant manual manipulation of the images is required to exclude the sinuses and their connecting passageways (ostia). The tissue/air interface of the sinuses and ostia is practically identical to that within the main nasal passageways, rendering delineation of the model domain impossible by simple thresholding techniques alone. Fine structures, particularly in the superior sections of the nasal cavity, can also suffer from partial volume effects necessitating manual smoothing of the boundary. Each axial image and reconstructed coronal and sagittal slices were reviewed and edited using software developed by Moore (2007) and written in Matlab (http://www.mathworks.com/). In the case of model 1, the segmentation was already performed and the geometry used as provided by Hopkins et al. (2000).

The airspace within the nasal cavity is produced as a negative solid body. The Matlab software creates a 3D airway geometry from the edited axial slices using a 'vtkContourFilter' surface extraction algorithm, which is analogous to the marching cubes algorithm of William and Harvey (1987). The airspace in front of the face was also modeled as a solid body so as to incorporate the shape of the external nose to the model. A circular cross-section lofted to the termination of the trachea at no greater angle than 7° in all three models facilitated the smooth connection of flow conduits to the model. The models were all scaled larger than life-size to increase the effective spatial accuracy in model construction and in setting-up and aligning the laser sheet with the narrow nasal passageways. A larger scale also increased temporal resolution because dimensional scaling resulted in slower flow velocities and breath periods than in a real nose. The computer models of the segmented airway geometries for models 1–3 are shown in Figure 13.

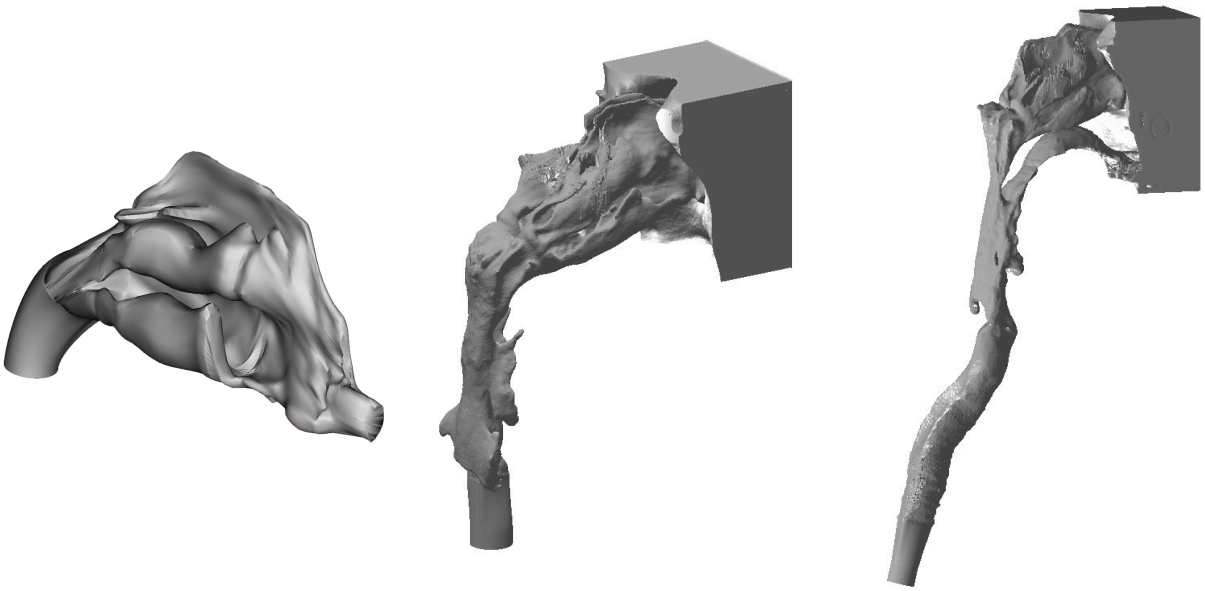

Figure 13. Computer models of the airway geometries for models 1–3

2.2.2 Rapid Prototyping and Negative Model Preparation

Each airway geometry was exported to a stereo-lithography (STL) file, which is a standard 3D graphics format compatible with rapid prototyping machines. The negative airway geometries were rapid prototyped at Auckland University of Technology's, Creative Industries Research Institute using a Z-Corporation 'ZPrinter 310 Plus'. The models were constructed in ZP130 powder and binder, which results in a plaster like material that is brittle, porous and becomes macerated in water. For typical applications the plaster is soaked in epoxy resin to increase the model's strength, however, this renders the model insoluble. The ZPrinter 310 Plus and ZP130 have since been superseded by the Spectrum Z510

rapid prototyper and ZP150 powder and binder, which I have found when making models for other airway studies to produce a smoother surface and is more readily dissoluble in water. The specifications for the rapid prototyping machines are given in Table 4. Although the accuracy of the printers has not been quantified, it is comparable to one layer thickness. The models were charged at cost price with the build time and labour expenses waived. The costs of materials were \$0.30/cm^3 for the powder and \$0.40/ml for the binder. The rapid prototyped negatives for models 1, 2, and 3 cost \$84, \$155 and \$466, respectively.

Table 4. Specifications for the rapid prototyping machines used

	ZPrinter 310 Plus	Spectrum Z510
Max Build Size (mm)	203×254×203	254×356×203
Layer thickness (mm)	0.089–0.203	0.089–0.203
Resolution (dpi)	300×450	600×540
Number of print heads	1	4
Number of jets	304	1216
Build Speed	2–4 layers per minute	2–4 layers per minute

The ZP130 and ZP150 powders are stronger than the cornstarch used in previous studies. This has enabled the complex form of the nasal cavity to be rapid prototyped without simplification of the geometry. This material also allows researchers who do not have suitable rapid prototyping facilities in their immediate vicinity access to resources elsewhere because the material is strong enough to survive shipment and any breakages can normally be easily repaired with polyvinyl acetate (PVA) glue. The models in this study were sent from Auckland to Christchurch in a rigid box lined with foam and filled with polystyrene beads. For added protection of particularly fragile models, an encompassing box can be modeled around the component. The model will then be printed inside the protecting box and supported by the unbound powder within. The structural integrity of a box with an appropriate wall thickness is much greater than that of the geometry. The additional cost of the powder and binder in the box as well as the cost of the powder in the contained volume must of course be considered.

The surface of the negative model must be sealed prior to casting because of the porous nature of the plaster. If the silicone is allowed to seep into the plaster the surface quality will be compromised or even render a section of the model irremovable. PVA glue was used to seal the models, which is dissolvable in water and has a high surface tension. The high surface tension creates a smooth, glossy surface despite the porosity of the plaster. Prior to coating the surface, the models were lightly sanded with 400-grit

sandpaper. PVA was brushed on the exposed surfaces with a soft bristled brush taking care to stroke over an area only once because the PVA itself would dissolve the plaster and subsequent brush strokes would roughen the surface. The PVA dissolving the plaster would also weaken the model so only a small area was painted at a time and allowed to dry before continuing in order to maintain structural integrity. With the exposed surfaces coated with a layer of PVA, which significantly strengthened the model, the reentrant surfaces were coated with PVA by momentarily immersing the model in bath of 70% PVA, 30% water. The PVA was diluted to reduce its viscosity and allow the excess PVA to flow more freely through and off of the model. The model was drip dried and rotated to ensure a homogeneous coating. Full strength PVA was used for the initial painting to minimise the absorption of the PVA into the surface and the weakening of the plaster during the early stages. Dunking the plaster was only possible after the model had been given its initial strengthening coats in order for the model to support its own weight in any orientation. When purchasing the PVA, because a large quantity is required to fill a bath and most large quantities are sold for industrial purposes, it is important to ensure the PVA does not contain any water resistant stabilisers, which will make removing the negative model more difficult. The rapid prototyped geometry of model 2 is illustrated in Figure 14 with surface preparation completed.

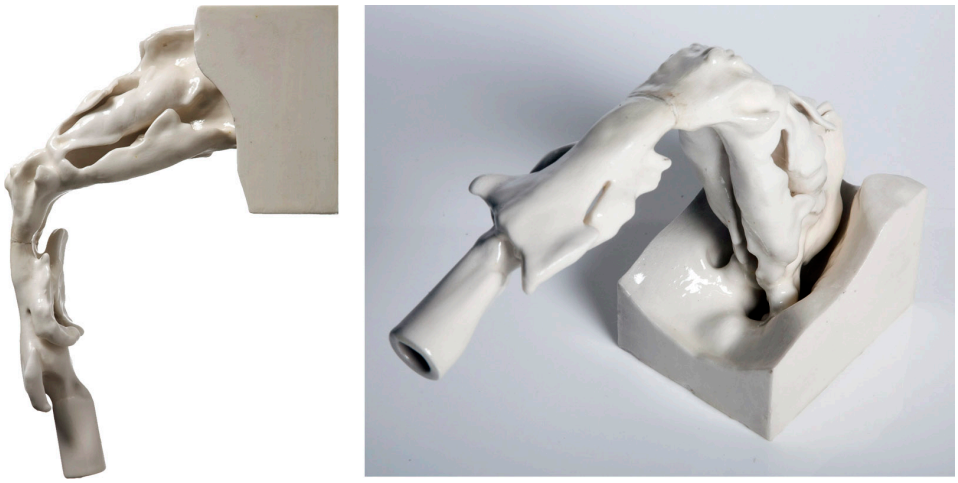

Figure 14. Rapid prototyped model with surface prepared

2.2.3 Casting

A casting box was designed and constructed around each model out of 8 mm acrylic, and fastened and sealed with pan-machine screws and PVA glue. An optically transparent silicone elastomer (Sylgard 184, Dow Corning, $108 per 0.5 kg) was chosen as the material for the final flow phantoms because it had a low refractive index that could be matched by an aqueous glycerol solution, had a proven track record

(Hopkins et al. 2000) and was already in use by a concurrent project (Buchmann 2010). Refractive index matching will be discussed in detail in Chapter 4. The casting box fitted around the negative such that the resulting model minimum wall thickness was 12 mm, which was considered sufficient to assume the internal geometry was rigid. The silicone elastomer was a two-part mix, requiring 10% hardener. Judicious mixing of the hardener is required not only to ensure correct curing of the silicone, but also because even small changes in hardener concentration change the refractive index of the silicone. To ensure a homogeneous refractive index throughout the flow phantom it is vital to mix the hardener thoroughly and prepare sufficient silicone for the model to be cast using a single batch. Mixing the silicone and hardener introduces air bubbles that must be removed by placing the silicone in a vacuum chamber. The air bubbles would otherwise corrupt the clarity of the model and result in a large amount of reflective noise due to the large refractive index mismatch of the silicone and the encapsulated air. A basic water aspirator connected to a faucet was used to create a vacuum in a plastic desiccator and degas the silicone at a gauge pressure of -75 kPa. Air bubbles rose out of the mixture and burst on the surface upon release of the desiccator's pressure. Four cycles were sufficient to completely degas the silicone up to a depth of 150 mm. The first cycle resulted in a large volume of bubbles that needed to be burst after approximately 3 minutes and before the desiccator reached its minimum pressure to avoid the silicone overflowing. In the fourth cycle the silicone was held at the minimum pressure for approximately 15 minutes until the last air bubble reached the surface. In total the degassing procedure took approximately 45 minutes.

Pouring the silicone into the casting box around the negative required care so as not to entrain further air bubbles. Some new air bubbles and air pockets around the concave down surfaces of the model are inevitable. These were drawn out using a length of shaped 2 mm tube attached to a syringe. After initially mixing the hardener, approximately four hours is available to work with the silicone. After 24 hours at 23°C the silicone will have cured sufficiently to be handled, however, full strength is achieved after 7 days. Although the silicone can be cured more quickly at elevated temperatures (4 hours at 65°C, 1 hour at 100°C, 15 minutes at 150°C), being a plastic, the PVA loses its strength and the negative can deform within the casting box due to its own weight or buoyancy. The air in the porous plaster also expands at elevated temperatures and can escape through the softened PVA, and hence corrupting the model with air bubbles. The negative geometry of model 3 mounted within a casting box and encapsulated in silicone is shown in Figure 15.

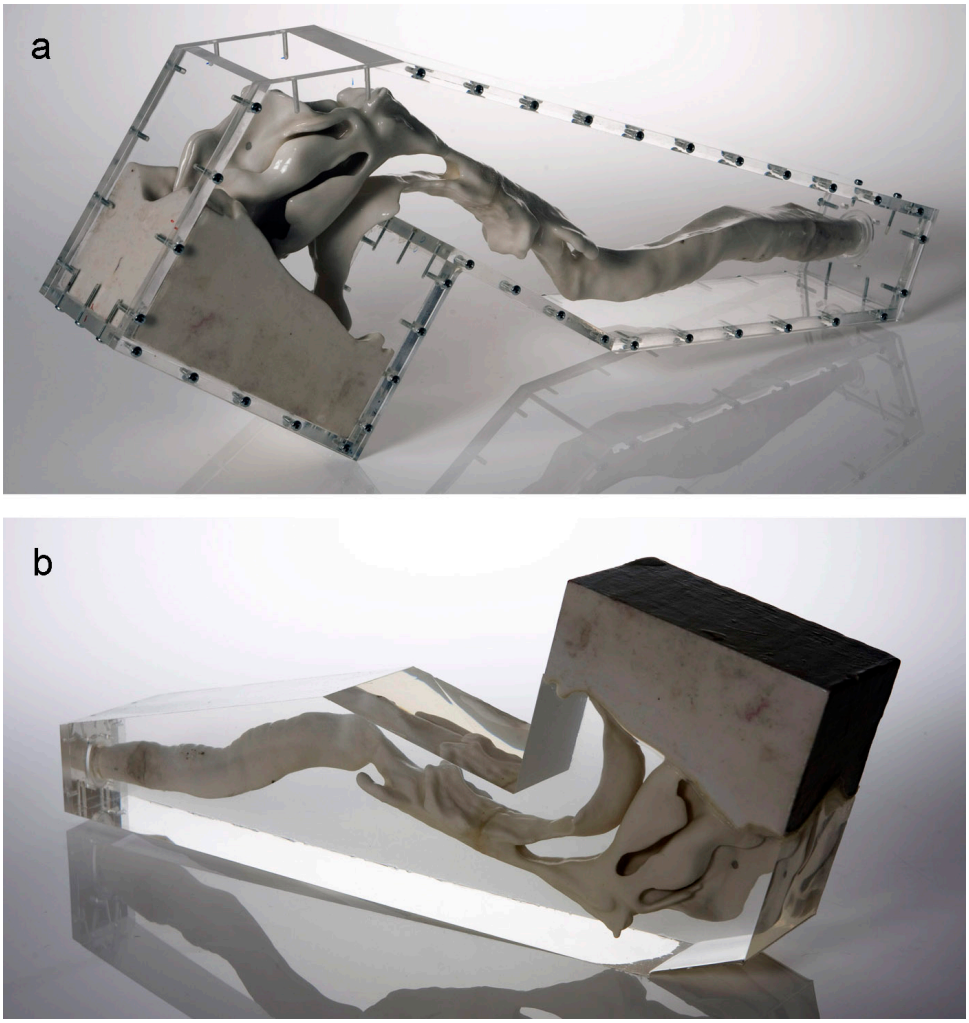

Figure 15. The rapid prototyped geometry of model 3 (a) mounted in it's casting box and (b) encapusulated in silicone.

2.2.4 Removing Negative

The rapid prototyping plaster becomes soft and breaks up when soaked in water; however, considerable mechanical effort is required to fully remove the negative. The plaster is effectively chemically inert and a variety of chemicals (hydrochloric acid, sulfuric acid, sodium hydroxide) proved to be no more effective in dissolving the material than water. A chemical formula for the proprietary material was not available to objectively assess the most effective solvent. A 3 mm stainless steel tube was connected via flexible plastic tubing to a faucet at mains pressure (approximately 500 kPa) and used to water blast and erode the plaster while the model was immersed in water. Once a narrow passageway through the model was open, a pump was connected to the throat to drive flows through the model in alternate directions to erode the plaster over a period of approximately three days. Noteworthy is the fact that the plaster could not be removed by running steady flows through the model from regions of the nasal cavity where previous studies had found

low velocities such as in the olfactory slit and the meatus passageways. To remove the plaster in these regions the water blaster tube was aimed directly at these regions and adjusted in position as necessary over a period of hours. Once the plaster had been completely removed the final model remained. The silicone absorbs water when immersed and the surface turns cloudy; however, this can be rectified by placing the model in an oven at 100°C for approximately 30 minutes, which does not harm the silicone. Models 2 and 3 are illustrated in Figure 16.

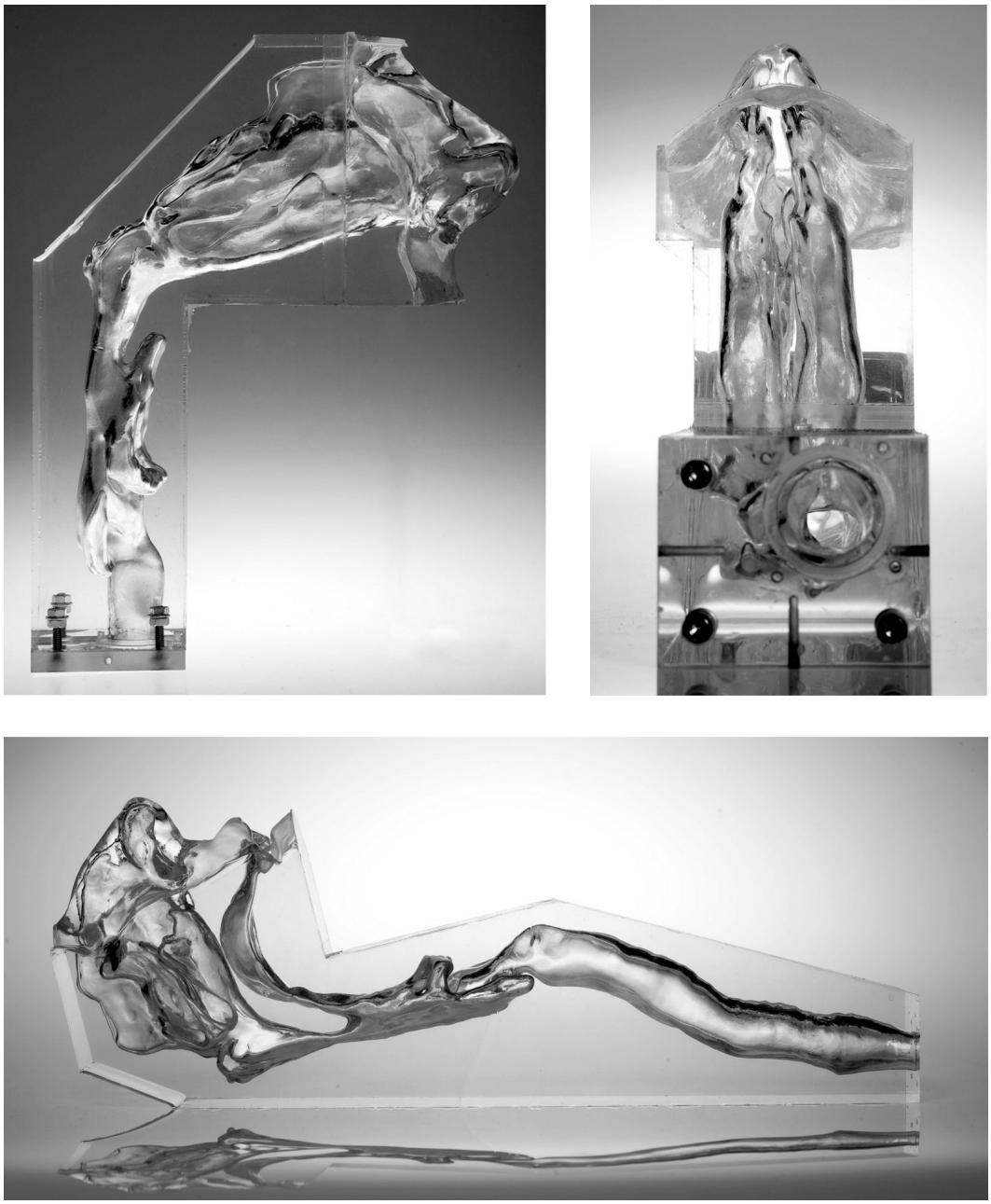

Figure 16. Completed models 2 and 3.

2.3 Nasal Geometries

2.3.1 Model 1: Simplified Choana

The initial model was based on the geometry of Hopkins et al. (2000) and was obtained by contacting the authors. The geometry was of the left choana and was constructed from twenty-six CT images of a normal 25-year-old male. The geometry as received terminated at the beginning of the nasopharynx. A bend was lofted onto the geometry (evident in Figure 17a) to simulate the nasopharynx and provide a semi-realistic inflow pattern to the nasal cavity on expiration. The bend was terminated at a diameter of 23.3 mm, which was the hydraulic diameter of the model's nasopharynx. The flow phantom was constructed at 2× scale as it had been in Hopkins et al.'s study. The shape of the external nose was not available. The nostril was simulated by a blunt opening, which was thought prior and later shown to be a shortcoming of the model on inspiration by other researchers (Doorly et al. 2008b; Taylor et al. 2010) who highlighted the importance of the inflow opening and the external shape of the nose. Nevertheless, model 1 had served its purpose for preliminary measurements by the time this research was published and further investigations on more detailed geometries were underway. Further details on this geometry are given in both Hopkins et al. (2000) and Kelly et al. (2000). The final model is illustrated in Figure 17.

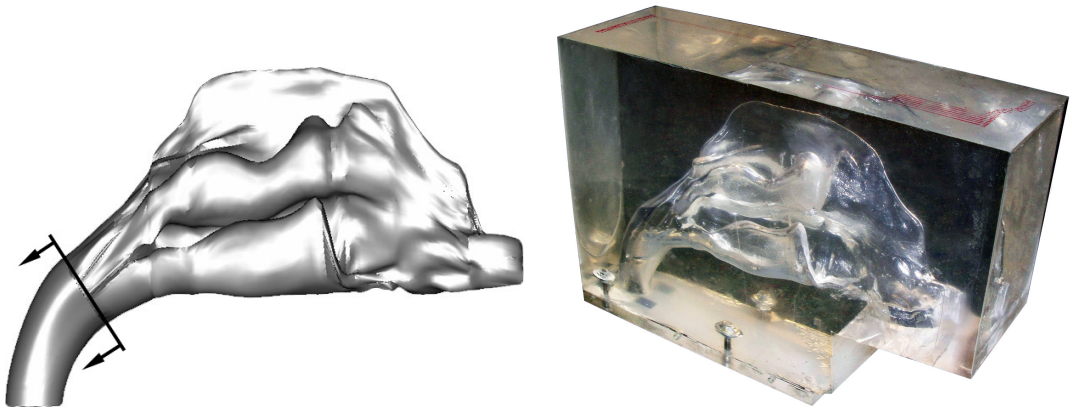

Figure 17. (a) The geometry of the left nasal choana obtained from Hopkins et al. (2000) and (b) the final silicone model

2.3.2 Model 2: Mouth Closed

The second model was constructed from a CT data set of a 44-year-old male and comprised 452 axially acquired 512 × 512 pixel^2 resolution images with a 0.6 mm slice spacing and thickness. The in-plane pixel

size was 0.42 × 0.42 mm. Although the subject was scanned for suspected lymphoma, a radiologist declared the nasal cavity free from any visible abnormalities. Model 2 included a number of improvements compared with the first model. Firstly, the model included both sides of the nasal cavity, which negated the assumption that each choana and their respective flowrates are symmetrical, and allowed a total flowrate to be applied through the throat. The respective flowrates through each choana were therefore determined by the geometry alone and information regarding the effect of differences between the morphology of either choana could be gained. Secondly, the model included a physiologically accurate geometry down to the beginning of the trachea to provide an accurate flow profile into the nasal cavity on expiration. When the CT scan was taken the soft palette was in a position such that the soft palette occluded the oral cavity. This was one reason this particular data set was selected from the database because the objective for this model was to investigate nasal breathing with the mouth closed. Furthermore, the model incorporated the external nose and a local portion of the face to ensure a physiologically accurate inflow pattern to the nostrils on inspiration. The model was constructed at 1.55× life-size because this was the largest size that could be rapid prototyped in one piece.

The variation of the cross-sectional area through the nasal cavity versus distance along a centroid path (Figure 5) measured from the external naris to the oropharynx is shown in vivo scaled in Figure 18. Although each side of the nasal cavity shares common features, they are asymmetric. The cross-sectional area of the right nasal cavity 7.2 cm posterior of the nostrils was 30% larger than on the left. Liu et al. (2009) in pursuing an average geometry of the human nasal cavity obtained CT scans of 30 healthy subjects that had been confirmed to have nasal anatomy within normal limits and found the internal volume of the middle region of the left and right nasal cavities to vary by up to 65 percent. A high degree of asymmetry in the left and right passages of healthy adults was therefore considered to be normal. The left and right nasal valves can be seen as the curve minima labeled as 1L and 1R in Figures 5 and 18 and have cross-sectional areas of 1.11 and 1.15 cm^2 respectively. These cross-sectional areas lie within the 0.54–1.21 cm^2 range measured by Çakmak et al. (2003) using CT data from 25 healthy adults. Beyond the nasal cavity, the cross-sectional area narrows through the nasopharynx before reaching a minimum cross-sectional area of 1.1 cm^2 at the velopharynx, which is shown as location 8 in Figures 5 (page 4) and 18. The soft palette in the current study's geometry created a notably smaller airway than the combined cross-sections of the two nasal valves.

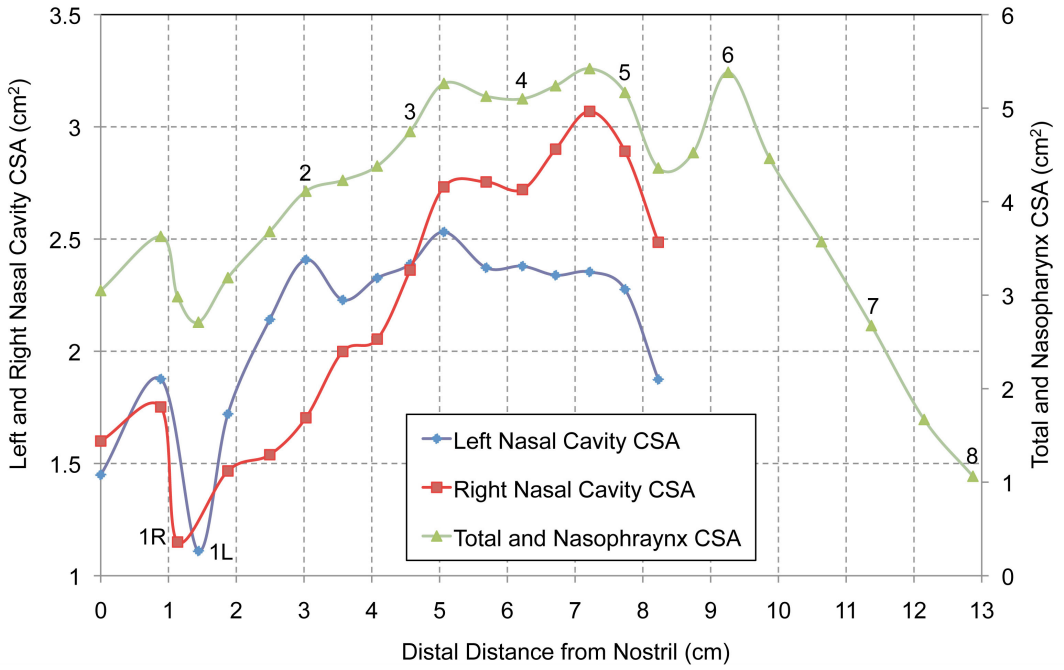

Figure 18. Variations of the cross-sectional area (CSA) through the nasal cavity versus distance along a centroid path (Figure 5) measured from the external naris. The numbered locations correspond to those illustrated in Figure 5.

Model Fidelity

The final silicone itself was CT scanned to quantify deviations from the original geometry due to the rapid prototyping and casting procedures, and to allow a detailed analysis of the actual flow phantom geometry. The CT images (762 images) were performed with a 512 × 512 pixel^2 resolution and a slice spacing and thickness of 0.4 mm, providing a pixel size of 0.43 × 0.43 mm. The distinct and uniform contrast between the silicone and air, and the increased effective spatial resolution of the scaled model, facilitated precise and automatic segmentation of the fabricated geometry. Cross-sections of the original and fabricated geometries were compared at a number of locations, and the surface of the flow phantom found to deviate by a mean of 0.32 mm on a 1:1 scale. This was comparable to mean magnitude of 0.29 mm reported by Doorly et al. (2008a). These values represent the accumulation of errors of the various fabrication stages and in both cases were less than a pixel size of the original data set. The deviation is largely due to coating the geometry in PVA, which adds girth to the negative. Despite the small deviation, because the surface area is very large cross-sectional areas were found to be up to 16% larger in the flow phantom. The largest discrepancy occurred in the cross-section shown in Figure 19 where the perimeter to area ratio is the largest. Although this error could be corrected for by estimating the PVA coating thickness and appropriately downsizing the negative geometry, the error was accepted because the objective of this study

did not require a patient specific geometry and interpersonal anatomical variations in cross-sectional area within the nasal cavity can be as large as 124% (Çakmak et al. 2003).

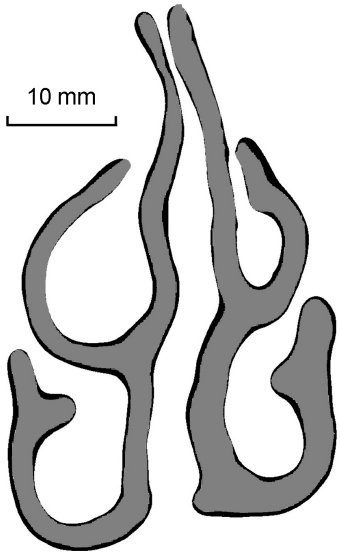

Figure 19. Cross-section of the original geometry overlayed in grey on the reproduced geometry in black.

2.3.3 Model 3: Mouth Open

The primary purpose for constructing model 3 was to investigate the effect of mouth-open breathing when receiving NHF. With the mouth open, cannula flow holds the soft palette in a neutral position such that inspiratory and expiratory flows can pass both through the nasal or oral passageways. This does not normally occur naturally. In order to obtain an accurate airway geometry with the mouth open and the soft palette in a neutral position, it was necessary to administer a subject with a nasal cannula flowrate of 30 l/min while a CT scan was being taken. This was arranged in advance with consent from a patient who had a scheduled CT for medical purposes. The CT data set comprised 462 images acquired axially with a resolution of 512 × 512 pixel^2 and a 0.6 mm slice spacing and thickness. The in-plane pixel size was 0.52 × 0.52 mm. Although the patient was diagnosed with a small thyroglossal duct cyst this was deemed to have negligible effect on the airway geometry because it was anterior of the hyoid bone.

Model 3 is a complete model of the human upper airways. The model extends from the nose and external nares down to the bottom of the trachea in the lower airways, just above the first bifurcation into the bronchi. Physiological details such as the ribbed tracheal wall and facial features including the lips are visible in Figures 20 a and b. The main advantage of incorporating the entire respiratory geometry was the ease with which physiological boundary conditions in the oral and nasal cavities on both inspiration and

expiration could be granted. The model was constructed at 1.55× life-size because the experimental rig was designed for this scale during the measurements of model 2. Due to the model's size, the negative needed to be rapid prototyped in two halves and joined together with a dowel and filler made from ZP130 powder and PVA glue. A CT scan of the final flow phantom and fidelity analysis was performed as with model 2, and deviations found to be of the same magnitude. An overview of the notable characteristics of each nasal model constructed during the current work is given in Table 5.

Figure 20. Close ups of model 3 showing a) the ribbed tracheal wall and b) facial features

Table 5. Overview of the parameters for each model.

	Model 1	Model 2	Model 3
Notes	Simplified choana	Mouth closed	Mouth open
Scale	2:1	1.55:1	1.55:1
Number of CT images	26	452	462
Image resolution (pixel^2)	N.A	512 × 512	512 × 512
Pixel size (mm)	N.A.	0.42	0.53
Slice spacing / thickness (mm)	N.A.	0.6	0.6
Subject	25 year-old male	44 year-old male	60 year-old male
Dimensions (mm)	240 × 160 × 80	250 × 190 × 70	490 × 175 × 85
Volume of Negative (cm^3)	131.5	253.6	982.0
Volume of Silicone (ml)	2530	1640	3940
Total materials cost ($NZ)	$631	$510	$1320

2.4 Cannula Models

Models of each of the small, medium and large cannulae were rapid prototyped at 1.55 times scale in clear stereo-lithography resin. Although the models were translucent and had a refractive index of 1.51, laser reflections were minimised by painting the cannulae matt black. A modeled fitting was merged with the manifold of each cannula geometry such that, once scaled a ¾" BSP tapered hose tail could be securely fitted to facilitate connection to the flow circuit. The laboratory model of the medium cannula is shown in Figure 21.

Figure 21. Rapid prototyped 1.55 times scale model of the medium cannula

2.5 Model Assumptions

Although each silicone model is anatomically accurate, and in the case of model's 2 and 3 show a high level of detail, the models are imperfect replicas of the nasal passageways. When attempting to reproduce physiological conditions in vitro a number of assumptions need to be made. Here the various assumptions made on the physical parameters of the nasal cavity are discussed.

2.5.1 Nasal Geometry

The silicone models have been constructed with walls that are effectively rigid; however, a real nasal cavity is made up of different regions that are both rigid and made from soft distensible tissue. The turbinates for example are rigid bone shelves, whereas compliance of the nasopharynx and cartilaginous external nose is thought to cause a slight narrowing on inspiration and an increased resistance relative to expiration

(Schreck et al. 1993; Shepard & Burger 1990). Neglecting the effects of nasal compliance during normal quiet breathing is, however, commonplace and each in vitro nasal flow study to date has made this assumption. Modeling the effects of nasal compliance on flow patterns is also a feat yet to be attempted with computational simulations. The effects of distensibility are neglected for two reasons. Firstly, the global flow structure within the nasal cavity during both natural and NHF assisted breathing was assumed to remain unchanged with or without compliant walls and a rigid model offered a constant geometry for which to compare the two breathing patterns despite variations in airway pressure. Secondly, the difficulties and complexity in constructing rigid walls was something that also needed to be overcome before attempting to produce a yet more challenging model with compliant walls in the correct regions. It should be noted that this assumption does not mean to diminish the importance of nasal compliance or its effect on the pressure-flow relationship, and that future studies should address this issue.

The geometry of the nasal cavity is not static but alters with the nasal cycle. The models lack the vasomotor responses of the mucosa in living noses and have been assumed to provide a snap shot in time of the nasal geometry. The time scale of NHF treatments measured in days or weeks is far longer than the time scale of fluctuations in the nasal geometry. A rigid geometry was therefore considered reasonable for assessing time averaged flow patterns and also helps to eliminate the effects of changing physiological factors so as to be able to compare natural and NHF nasal flow patterns more clearly. The influence of the nasal cycle is of less importance with models 2 and 3, because they include both sides of the nasal cavity. Although Hopkins et al. did not discuss the nasal cycle, it was assumed that the model 1 geometry was representative of a neutral point in the nasal cycle where the flowrates would be equally shared between each choana. Model 1 also assumes that both sides of the nasal cavity are symmetrical and otherwise have an equal resistance. Model 1 was a simplified geometry, which although had advantages for manufacture and perhaps gave the geometry wider applicability amongst inter-individual variations, models 2 and 3 represented patient specific geometries so as not to risk neglecting certain significant attributes by making arbitrary simplifications.

2.5.2 Surface Characteristics

The silicone phantoms do not have the same surface properties as the moist, sticky mucosa lining the internal nasal cavity. Mlynski et al. (2000), however, showed experimentally that the roughness of the nasal walls did not exhibit a significant influence on flow patterns. Differences in surface characteristics were therefore neglected and the global flow structure assumed to be independent of surface roughness.

2.5.3 Boundary Conditions

The flow profile from the lungs on expiration was not known, nor was an attempt made to replicate it. The length of physiologically accurate geometry upstream was assumed to create a realistic flow profile entering the area of interest. In model 2 for example, the region of interest was the nasal cavity and nasopharynx, and the effect of the rather convoluted oropharynx and larynx geometries on the flow profile entering the nasopharynx was assumed to dominate any flow profile entering at the trachea. Nevertheless, a length of straight tube was connected to the throat of each model. This assumption was weakest in model 1, where it was only the simplified bend of the nasopharynx that determined the flow profile entering the nasopharynx. The inclusion of the external nose and a local portion of the face provided a physiological situation on inspiration in models 2 and 3.

2.5.4 Paranasal Sinuses

The sinuses surrounding the nasal cavity were disregarded to reduce optical noise and the complexity of constructing the phantom. This simplification has been made on the justification that the sinuses have negligible effect on the flow pattern in the nasal cavity. The ostia that connect the sinuses to the nasal cavity are small with a diameter in the order of 2 mm. Although there is a pressure lag in the sinuses and with each inspiration some air from the sinuses joins the nasal stream and the reverse on expiration (Drettner 1965), this air exchange occurs slowly (Drettner 1982; Mlynski et al. 2000). Churchill et al. (2004) observed that dye did not enter the sinuses in models with ostia.

2.5.5 Nasal Vibrissae

By experiment, Mlynski et al. (1993), Fischer et al. (1969) and Girardin et al. (1983) have each concluded that the vibrissae have no measureable effect on the flow pattern. Hahn et al.'s (1993) measurements in their 20× scale model simulated scaled nasal hairs with 1 mm diameter copper rods and reported that the addition of nasal hairs increased turbulence in the area of the nares only, but had no effect of flow downstream in their model. The considerable effort to include vibrissae in the current study's models was therefore not undertaken.

2.5.6 Heat and Mass Transfer Effects

The silicone models do not replicate the heating of inspired air from the warm, moist nasal tissues and measurements are carried out in isothermal conditions. The effect of thermal buoyancy on velocity profiles in a real nose, however, can be shown to be negligible and dominated by breathing driven flows through an examination of the Richardson number. Although this analysis is unique amongst the literature it is nonetheless convincing. The Richardson number, *Ri* (Equation 2) can be represented by the ratio of the Grashof number, *Gr* and the square of the Reynolds number, *Re* (in this form, the Richardson number is also known as the Archimedes number). The Grashof number (Equation 3) represents the ratio of buoyancy to viscosity, where β is the volumetric thermal expansion coefficient, T_S is the surface temperature, T_{ref} is the bulk temperature, g is the acceleration due to gravity, L is a characteristic length scale, ρ is the density and μ is the dynamic viscosity. The Reynolds number (Equation 4) represents the ratio of inertial forces to viscous forces, where V is the mean fluid velocity. The Richardson number therefore expresses the relative strengths of buoyancy to inertial forces, or in other words the relative importance of natural and forced convection. When $Ri < 0.1$, natural convection is negligible and when $Ri > 10$, forced convection is negligible. At cross-section 4 in Figures 5 (page 4) and 18 (page 48) the Richardson number was estimated to be 0.018 using a hydraulic diameter of 5.6 mm (371 mm perimeter, 5.24 cm^2 area) as the characteristic length scale, a nasal wall and ambient temperature of 34°C and 20°C, and a typical average breathing flowrate of 12 l/min. The properties of air were taken at 27°C (β = 3.33×10^{-3} /°C, ρ = 1.18 kg/m^3, μ = 18.56×10^{-6} kg/m^3). The Grashof and Reynolds numbers were 325 and 136, respectively. Thermal buoyancy effects in a real nose are therefore negligible and no bias was expected by using the silicone models in isothermal conditions. Similarly, differences in density due to the effects of water evaporation and humidity gradients in the real nose are also assumed to be negligible.

$$Ri = \frac{Gr}{Re^2}$$ **Equation 2**

$$Gr = \frac{\beta\left(T_S - T_{ref}\right)gL^3\rho^2}{\mu^2}$$ **Equation 3**

$$Re = \frac{\rho VL}{\mu}$$ **Equation 4**

2.6 Model Comparison

Models 2 and 3 are compared across a number of facets in Table 6 with all the transparent models of the nasal cavity fabricated for PIV measurement in previous studies. It is clear from reviewing Table 6 and the images in Appendix A that models 2 and 3 are superior. The model by Garcia et al. (2007) had a number of advantages over previous models, however, erroneous holes are visible in the model geometry where perhaps the signal was low in the CT Scan or an incorrect threshold was selected during segmentation. Similarly, the olfactory region in the model by Kim et al. (2006; 2004) is abnormal. Model's 2 and 3 are the only reported models to include the entire nasal cavity, provide a free boundary condition through the

Table 6. Comparison of models 2 and 3 with nasal models constructed in previous studies for PIV measurement

		Model 2	Model 3	(Brücker & Park 1999	Hopkins et al. 2000 Kelly et al. 2000	Kim et al. 2004 Kim et al. 2006	Horschler et al. 2006	Chung et al. 2006 Chung et al. 2008	Garcia et al. 2007	Doorly et al. 2008
CT Scans	Number of images	452	462	N.A	26	166	300	N.A.	N.A.	82
	CT slice thickness (mm)	0.6	0.6	N.A	1.5	0.6	1	1.25	0.6	0.7
	Accurate segmentation	✓	✓	✓	✓	×	✓	✓	×	✓
Model Geometry	Scale (× life-size)	1.55	1.55	3	2	N.A.	1.5	2	1	2
	Non-simplified	✓	✓	×	×	✓	×	✓	✓	✓
	Both choana	✓	✓	×	×	×	×	×	✓	×
	External nose	✓	✓	×	×	×	×	×	✓	×
	Nasopharynx*	✓	✓	×	×	✓	✓	×	✓	✓
	Larynx	✓	✓	×	×	×	×	×	×	×
	Trachea	×	✓	×	×	×	×	×	×	×
	Oral cavity	×	✓	×	×	×	×	×	×	×
	Physiological inlet profiles	✓	✓	×	×	×	×	×	×	×
	Fidelity Assessed	✓	✓	×	×	×	×	×	×	✓

N.A. Not Available

* Rudimentary bends are not considered here to have modeled the nasopharynx faithfully

nostrils with the external shape of the nose, and extend as far as the larynx. Furthermore, model 3 is the only model to include the trachea and both the nasal and oral passageways. The only other study that has reported performing a fidelity assessment of the fabricated geometry with respect to the original geometry has been than of Doorly et al. (2008a). The deviation from the original geometry was found to be comparable to that reported by Doorly et al. who used a similar construction method.

2.7 Conclusions

Artificial replicas of the nasal cavity constructed from cadavers suffer from a number of limitations and inaccuracies associated with nasal tissue shrinkage and deformation, being restricted to life scale, and in some cases a large number of casting steps that result in an accumulated deviation from the original geometry. In the current work a method employing CT scan data and rapid prototyping was developed. Three optically clear silicone models of the nasal cavity were constructed sequentially with increasing complexity and physiological realism at enlarged scales. Scaled nasal cannulae models were also produced using rapid prototyping. Assumptions made on nasal geometry, surface characteristics, boundary conditions, paranasal sinuses, nasal vibrissae and heat and mass transfer effects have all been justified. Models 2 and 3 have been shown to be uniquely superior to previous nasal replicas across a number of facets. Despite in vitro models being inevitably deficient of all in vivo parameters, the models were considered suitable for investigating the flow field in the nasal cavity during natural and NHF assisted breathing.

3 Particle Image Velocimetry Techniques

In this chapter the fundamental aspects of PIV flow measurements and the techniques employed in the current work are described. One of the fundamental assumptions of PIV is that the seeding particles flow the flow faithfully, because it is not the motion of the fluid that is being measured, but the particles'. It therefore makes sense to begin with a description on seeding selection criteria. The chapter goes on to describe the PIV apparatus employed and the cross correlation and image processing methods found to be pertinent for nasal flows. The chapter concludes with descriptions on the sources of invalid vectors and an analysis of the methodology and performance of the stereo-PIV apparatus and software implemented in the current work.

3.1 Experimental Apparatus

3.1.1 Tracer Particles

In contrast to flow visualisations where tracer particles (dye, smoke) are injected at specific points in a flow to mark certain features, a homogenous distribution of tracer particles is desired in PIV. Tracer particles (also called seeding) must be small enough so that they do not deviate from the motion of the fluid due to inertial or gravitational forces or interact with the flow. The seeding particles must also, however, be large enough to scatter a sufficient amount of light. It is clear that a compromise is necessary in any experiment and extensive discussions have been made on this topic (Melling 1997; Raffel et al. 1998). The Stokes number (Equation 5) can be calculated to give a measure on a particles ability to track the flow. The Stokes number (Stk) is a dimensionless number and is a ratio of particle momentum to viscous forces on the particle. For $Stk >> 1$, particles will continue in a straight line as the fluid turns. For PIV the Stokes number for seeding must be less than 0.1, but preferably less than 0.01, so that the viscous forces on the particles dominate particle momentum and the error induced by particle inertia is less than 0.7% (Dring 1982).

$$Stk = \frac{\rho_p d_p^2 UC}{18\mu R}$$ **Equation 5**

Flows were seeded with hollow glass spheres with a mean diameter of 16.2 μm (Buchmann 2010) and a density of 1.1 g/cm^3. They offered good light scattering efficiency, had a low Stokes number, and closely matched the fluid density (1.15 g/cm^3). The highest velocities in the nasal cavity were expected to occur at the exit of the cannula's prong at the highest NHF flowrate. With a cannula flowrate of 50 l/min the average velocity exiting a prong was estimated to be 14.7 m/s. The worst case Stokes number for these seeding particles was hence approximated to be 0.017, where ρ_p is the particle density, d_p is the particle diameter, U is the flow velocity, C is a Cunningham correction factor (C=1) and R is the radius of curvature of a stream line, which was taken to be the half the radius of the cannula prong. The fluid properties were taken at 25°C. The seeding particles were therefore assumed to follow the flow sufficiently well, whilst being large enough to scatter a sufficient amount of light to enable a magnification such that the entire nasal cavity could be imaged in one frame.

The drag coefficient (Equation 6) provides a ratio of gravitational or buoyancy forces to inertial forces, where g is the acceleration due to gravity, ρ_f is the fluid density and L is a characteristic length scale (taken as the 45 mm height of the nasal cavity). To assess the effect of the density mismatch between the particles and the fluid, an analysis of the drag coefficient was performed. In this case a lower velocity in the olfactory region gave the worst-case scenario; therefore a value of 0.2 m/s (Doorly et al. 2008a) was used for U. The drag coefficient was hence calculated to be 0.5, which shows that inertial forces dominate gravitational or buoyancy forces on the particles in even lowest flow velocity regions. Larger seeding particles would have scattered more light, improving the signal to the cameras, and likely have a higher stokes drag; however, larger particles such as Mecofill (SG2-30128) with a mean diameter of 30 μm had a density of only 600 kg/m^3 would not have been appropriate due to buoyancy forces. An overview of the tracer particles considered is given in Table 7. Particles were rejected either due to cost, a mismatch with the fluid density or size.

$$C_d = \frac{g(\rho_p - \rho_f)L}{\rho_f U^2}$$ **Equation 6**

Table 7. Overview of tracer particles considered for use in experiments

Tracer Particles	Diameter (μm)	Density (g/cm^3)	Reference
Sphericel 110P8	**16.2**	**1.1**	**Potters Industries Inc., http://www.pottersbeads.com/**
Polyamide	5, 20, 50	1.03	Dantec Dynamics, http://www.dantecdynamics.com
Silver-coated hollow glass spheres (HGS), €208/100g	10	1.4	
Fluorescent polymer	10, 30, 75	1.5	
Fluostar	15	1.1	EBM Corp., www.ebm.vc
Mecofill, silver-coated HGS	30	0.6	Brazel Technology, www.brazel.com
Isospheres, titania-coated HGS, £150/100g	5–20	~	Microsphere technology, www.microspheretechnology.com
Conifer pollen	50–60	1.0	(Gallagher & McEwan 1996)
Polystyrene	500	1.05	(Khoo et al. 1992)
Polyvinyl	80	1.02	(Chung et al. 2006; J. K. Kim et al. 2006)
Hollow glass spheres	60	0.6	(Hopkins et al. 2000; J. T. Kelly et al. 2000)

3.1.2 Laser

A dual cavity Nd:YAG laser (New Wave Solo 120XT) was used as the light source and is a common choice for PIV applications. Nd:YAG is an acronym for the neodymium-doped yttrium aluminium garnet ($Nd:Y_3Al_5O_{12}$) crystal that is used as the lasing medium. The crystal rod is doped with the active medium, Nd^{3+} ions and placed within an unstable oscillator cavity that has mirrors at each end and is pumped with a flash lamp. Through stimulated emission, energised photons build up and after multiple reflections are released via the Q-switch. The beam exits the cavity as a tightly collimated light beam of constant wavelength (monochromatic) through one of the cavity mirrors that is partially transmissive. In the case of a dual cavity laser, there are two independent cavities and the beams from each are optically combined onto a concentric path. The beam has a wavelength of 1064 nm, which is invisible to the human eye (yet very dangerous) and to digital cameras that have been optimized to the visible band of 400–700nm. The beam is therefore converted with the use of a KDP (Potassium Dihydrogen Phosphate) frequency doubling crystal into a useful wavelength of 532 nm, a lime green colour. The pulse intensity from each cavity was relatively constant, however, varied between cavities. The image exposed by the first laser cavity

was always slightly brighter than that of the second. The specifications for the New Wave laser are given in Table 8.

Table 8. Specifications for the New Wave Solo 120XT, Nd:YAG laser

Specification	
Repetition Rate per cavity (Hz)	1–15
Max. pulse energy (mJ)	120
Pulse width (ns)	3-5
Energy stability (±%)	4
Beam diameter at laser output (mm)	5
Divergency (m-rad)	< 3

A strong light source is required for PIV in liquid flows for two reasons. The light scattered by the particles is inconveniently subject to the Lorenz-Mie regime (Hulst 1957) where most of the light is scattered in the forward and backward directions and the least amount of light intensity is scattered perpendicularly to the camera, as shown in Figure 22. Additionally, the small difference in refractive index between the seeding and the liquid also diminishes scattering efficiency. This is not such an issue with gas flows. Pulse lasers are commonly used for PIV for their ability to discharge a large amount of light in a short amount of time (3–5 ns), which gives high light intensity and eliminates motion blurring in the particle images. Dual cavity lasers are typical of modern PIV systems and allow the pulses to be separated by an infinite range. Dual cavity lasers therefore open up PIV to the application and measurement of very fast flows.

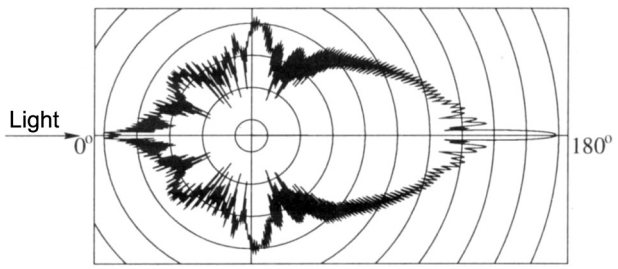

Figure 22. Light scattering pattern by a 10 μm glass particle in water (adapted from Raffel et al. (1998))

3.1.3 Optics

In order to create the required light sheet for PIV measurement a series of optics was required. The optics performed two basic functions; 1) reduce the beam diameter to in turn reduce the light sheet's thickness

and 2), diverge the beam into a sheet. A pair of convex lenses in a reverse Galilean telescope arrangement as shown in Figure 23 was used to reduce the laser beam diameter from 5 mm. The focal lengths of the lenses were 150 and 50 mm, which by Equation 7 gave a beam diameter of approximately 2 mm. A negative cylindrical lens with a back focal length of 20 mm was placed immediately after the second convex lens to diverge the beam into a sheet. Even though the optical arrangement included a focal point, ionization of the air close to the focal point was not observed and the optics were covered to avoid dust particles from disturbing the beam properties.

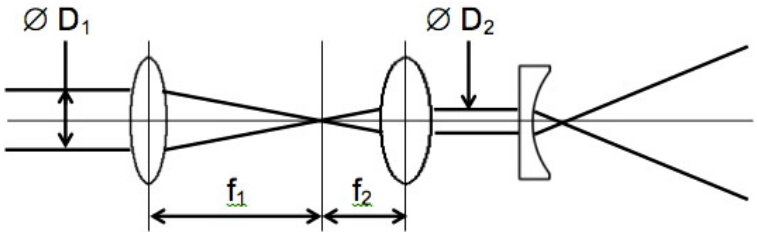

Figure 23 Schematic of the optical system

$$\frac{D_2}{D_1} = \frac{f_2}{f_1}$$ **Equation 7**

3.1.4 Cameras

Digital cameras typically of a CCD (Charged Couple Device) or CMOS (Complementary Metal-Oxide-Semiconductor) architecture are used for PIV image recording. The cameras used in the current work were Dantec Flow Sense 2M cameras, which have a CCD array dimension of 1200 × 1600 pixels (specifications given in Table 9), and were fitted with 60 mm lenses (Nikon Micro-Nikkor). A CCD camera is able to capture two images in rapid succession and the Flow Sense cameras could do this at a maximum of 17.17 Hz. After the first image is exposed onto the photo diode array, the data is transferred to a CCD array on the CCD chip. Once the data from the first image has been transferred to the CCD array, the second image can be exposed onto the photo diode array. While the second image is being exposed, the first image's data on the CCD array is transferred to memory buffers via the camera's first frame grabber. With the first image's data downloaded off of the CCD array, the second image on the photo diode array is transferred to the CCD array and then to memory buffers via the camera's second frame grabber. The time to transfer the data from the photo diode to the CCD array is known as the transfer pulse width (TPW) and is far smaller than the time to transfer data from the CCD array to

memory. The time between images within an image pair is therefore limited by the time it takes to transfer data from the photo array to the CCD chip, which for the Flow Sense cameras is 1.5 μs. The camera lenses used had a diameter and focal length of 60 mm, and an allowable aperture range from a f-number of 2.8 to 32. Larger apertures (smaller f-number) allow more light to the CCD sensor and create brighter particles; however, lead to an increase in lens aberration and a decrease in depth of field. In the current work, the light scattered by the particles was sufficient that the largest aperture used was a f-number of 8.

Table 9. Dantec Flow Sense 2M digital camera specifications

Specification	Dantec Flow Sense 2M
Sensor type	CCD, progressive scan monochrome
Pixel linear size (mm)	7.4 μm
Sensing area	11.8 × 9.8 mm
Effective pixels	1600 × 1200
Maximum frame rate	17.17 frames/sec
Output quantisation	8 or 10 bit
Frame separation	1.5 μs
Lens mount	C-mount
Lens focal length / diameter	60 mm / 60 mm

Synchronisation of the cameras and laser was controlled with TTL signals from a BNC 565 pulse/delay generator as illustrated in Figure 24. The Q-switch delay, QSD (182 μs), is the time a laser cavity takes to fire once triggered and is a fixed characteristic of the laser cavities' charge time. Similarly, the camera delay was 4 μs. The trigger for the first exposure was therefore offset from the laser trigger by 176 μs, so that the first laser pulse occurred in the centre of the first exposure. The duration of the first exposure was fixed at 4 μs. The second exposure began after the TPW and continued until the camera received the next trigger signal. The duration of the second exposure was therefore dependent on the acquisition frequency. Consequently, it was important to conduct measurements in a dark environment because the second exposure time was long enough for a continuous light source to expose the background. The second laser pulse was triggered at the desired PIV time delay, which inevitably fell within the second exposure.

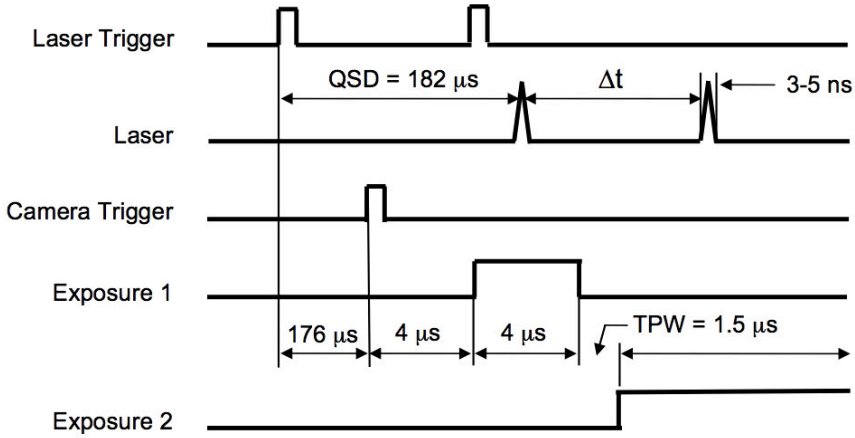

Figure 24. Schematic ilustrating the synchronisation of the cameras and laser

3.2 Cross-Correlation

This section describes the evaluation of the tracer particle displacement within an image pair using a cross-correlation (COR) algorithm. Although other methods exist, such as the minimum quadratic differences (MQD) algorithm (http://www.oceanwave.jp/softwares/mpiv/), discussion will be limited to the more conventional COR algorithm. Although improvements to processing code were made over the duration of the current work, development of a cross-correlation algorithm was not an objective. The fundamentals of a COR algorithm are demonstrated here to facilitate the understanding of certain technical solutions later on. Detailed mathematical formulations of the PIV method are given and reviewed by Westerweel (1997) and Raffel et al. (1998) respectively. The COR algorithm specific to the current work was constructed largely by Buchmann (2010). Parts of the algorithm are developed in C++ language (i.e. cross-correlation, image interpolation) and the overall implementation conducted in Matlab.

The cross-correlation procedure is illustrated in Figure 25. The particle images are first divided into a uniform rectangular grid of interrogation windows, typically with an initial size of 64 × 64 pixel^2. It is assumed that the interrogation window size is sufficiently small that the particles contained are subject to a uniform displacement between the two exposure times. Although this may not be the case for the initial window size, a process called iterative window refinement will be introduced later that can alleviate this issue. The light (pixel) intensity distribution within an interrogation window is compared between exposures one (t) and two (t + Δt) using the normalised cross-correlation function, Equation 8. $C(\Delta X,\Delta Y)$ is the correlation magnitude for a particle displacement vector components ΔX and ΔY, f_1, f_2

are the interrogation regions from exposures one and two, $\overline{f}_1, \overline{f}_2$ are the mean pixel intensity values of f_1, f_2, N is the length in pixels of one side of the interrogation window (i.e. the array matrix size), and X_i, Y_j is the position of pixel *i, j* in the interrogation window. The numerator locates the intensity peaks for each interrogation region by analysing the intensity of each array coordinate (pixel) between exposure one and two. The denominator is a normalisation factor, confining the magnitude of correlation to a set range of 0 to 1. Effectively, the correlation function moves the interrogation window in exposure two and returns the highest value when the unique particle patterns are overlaid with the closest possible match to exposure one. The correlation function results in a correlation map where the distance from the peak of the correlation (i.e. where the best match was found) to the centre of the interrogation window is the particle displacement between exposures. Displacements are initially evaluated at discrete values and if further processing is not performed or if each particle occupies too few pixels, peak locking can occur where particle displacements are biased toward integer values. In the current work, a two-dimensional (elliptical) Gaussian interpolation function was used to estimate the centroid of the correlation peak to sub-pixel accuracy (Nobach & Honkanen 2005). Each vector produced is the statistical average displacement for all the particles within an interrogation region. The cross-correlation is repeated for each interrogation window and the resulting displacement vectors plotted on the original grid. A velocity map is obtained by simply dividing by the time delay between exposures and multiplying by the magnification. The density of the velocity fields in the current work was increased by using a grid of interrogation windows with 50% overlap, effectively quadrupling the number of sampled vectors, however, not increasing the number of independent vectors.

$$C(\Delta X,\Delta Y) = \frac{\sum_{i=1}^{N}\sum_{j=1}^{N}\left[f_1(X_i,Y_j)-\overline{f}_1\right]\left[f_2(X_i+\Delta X,Y_j+\Delta Y)-\overline{f}_2\right]}{\sqrt{\sum_{i=1}^{N}\sum_{j=1}^{N}\left[f_1(X_{i,},Y_j)-\overline{f}_1\right]^2}\sqrt{\sum_{i=1}^{N}\sum_{j=1}^{N}\left[f_2(X_{i,}+\Delta X,Y_j+\Delta Y)-\overline{f}_2\right]^2}} \qquad \textbf{Equation 8}$$

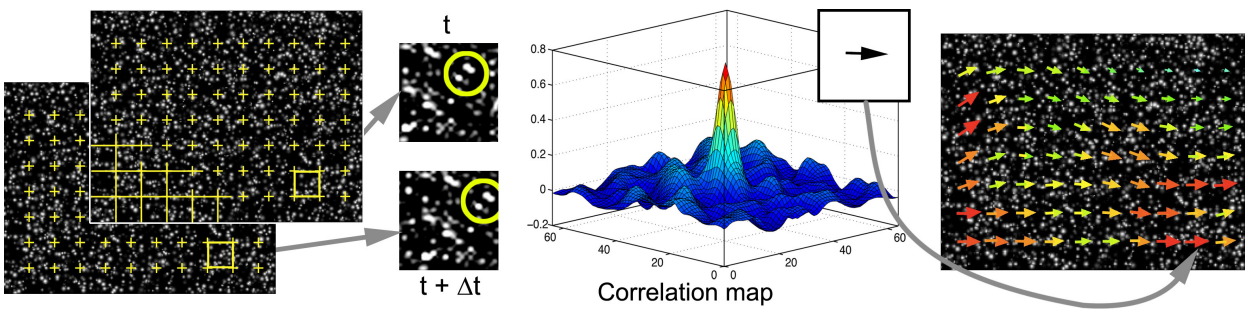

Figure 25. Schematic illustrating the cross-correlation proceedure

3.2.1 Ensemble Correlation Averaging

When the signal to noise ratio is poor, the correlation peak can be indistinguishable from the surrounding spurious peaks and the correlation algorithm can fail and give an erroneous velocity estimate. Low seeding density, high image noise due to light reflections, particles entering and leaving the light sheet, CCD noise, and high velocity gradients can all degrade the signal to noise ratio. The best solution for a poor signal to noise ratio is to take good experimental data in the first case; however, ensemble correlation averaging can be used to improve signal strength when time averaged results are desirable. Ensemble correlation averaging computes the mean correlation map over any number of image pairs for each interrogation window. Since the noise is often random and the correct correlation peak repeated, a distinct peak is strengthened. Ensemble correlation averaging was employed in the current work to increase the signal to noise ratio and produce time averaged velocity maps. Mean velocity maps can also be produced by averaging a series of instantaneous velocity fields, however, in areas of low signal to noise ratio can fail to converge to correct mean velocities.

3.2.2 Vector Validation and Filtering

A velocity estimate was retained as a valid vector only if the ratio of the values of the highest peak to the mean correlation value (averaged over the interrogation area) exceeded a preset threshold value. This is termed the signal-to-mean ratio (SMR) and is typically set between 1.5 and 2.0. A more common approach is to use the ratio of the highest to the second highest peak as a validation criterion (Keane & Adrian 1990), however, this was not used in the current work because during ensemble averaging a second correlation peak may be absent. Occasionally, in areas of particularly low signal to noise ratios, the highest peak can correspond to a noise spike that passes the SMR criteria. A second validation criterion was therefore implemented called the normalised median test (NMT). The NMT test was developed by Westerweel and Scarano (2005) and effectively compares the displacement vector under consideration with the displacements of the surrounding eight windows. Spurious vectors are detected based on a threshold of the allowable local variations in velocity. If a non-valid vector was obtained it was omitted and the resulting space on the vector plot filled with a linear interpolated result (Westerweel 1994). It is possible to store the locations of the next three highest correlation peaks and try them as alternatives to the noise spike before making simple interpolations. Kelly et al. (2000) reported 14% invalid vectors in their nasal flow measurements and replaced approximately 57% of these (8% of the total) with the vector corresponding to the second, third or fourth strongest correlation signal peak. The remaining 43% (6% of

the total) were interpolated from neighbouring data. In the current work less than 5% invalid vectors were obtained for each measurement without using subsidiary peaks and these were replaced by interpolation. The technique of trying subsidiary peaks could be added to the cross-correlation algorithm in later studies to further improve the quality of the results.

3.2.3 Window Refinement and Shifting

The magnitude of the particle displacements is critical to the successful application of the cross-correlation algorithm; therefore, the time delay between successive images most be chosen appropriately. The time delay must be long enough to be able to determine the displacement of the particles between exposures with sufficient resolution to avoid peak locking, yet short enough to minimise the number of particles with an orthogonal velocity component entering or exiting the light sheet. Also, if the time delay is too long, in-plane particle displacements will be too large for the cross-correlation windows to contain enough corresponding particle information to achieve an acceptable correlation. The time delay is typically chosen such that the largest displacement of any particle contained within an interrogation window is no more than one quarter of the window's dimensions. The time delays used in the current work ranged from 100–4000 μs.

Cross-correlation based PIV algorithms are limited in spatial resolution mainly by the size of the interrogation window and the final smallest window size limited by seeding density. The smallest possible window size is therefore desirable, which will also reduce the averaging effect of the interrogation region. Iterative window refinement and window shifting is a method introduced by Westerweel et al. (1997) to enable the use of smaller interrogation windows whilst maintaining the dynamic resolution associated with larger particle displacements. The cross-correlation is initially performed on a large window following the one-quarter rule. The resulting displacement field is then used as a predictor for a subsequent iteration where the window size is reduced by a factor of two and translated to follow the motion of the particles as illustrated in Figure 26. The dynamic range and spatial resolution are consequently decoupled. The increase in spatial resolution clearly evident in Figure 26. Moreover, the strength of the cross-correlation is improved because of the higher number of matched particles. A further iteration at the final window size gives an additional increase in signal to noise ratio by using a more accurate displacement predictor. This maximises the number of matched particles and the displacement bias approaches zero (Scarano & Riethmuller 2000), which centers the correlation peak on the correlation plane and improves the fit of the

Gaussian sub-pixel peak estimator. The correlation window can typically be progressively refined until about 9 particles are contained within the window. Increasing the seeding density can allow further refinement, however, unless the resolution of the camera is increased accordingly this can lead to speckle imaging where large numbers of particles overlap and the cross-correlation strength degraded. The window refinement and shifting techniques were particularly important in the current study because of the particularly large dynamic range of velocities in the nasal cavity. The velocities in the cannula jet were for example two orders of magnitude larger than the slow velocities in the meatus passageways.

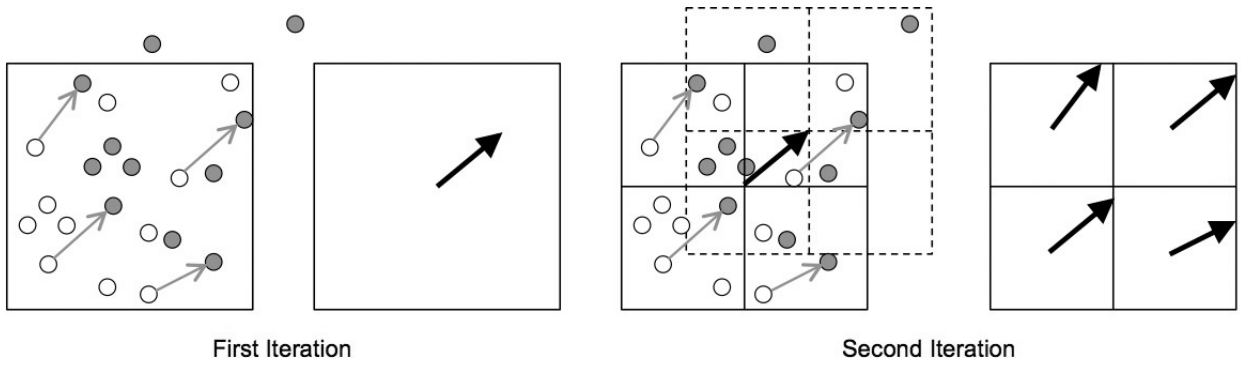

Figure 26. Schematic illustrating window refinement and shifting. The grey particles represent the particle locations in the second exposure.

3.2.4 Window Distortion

As already mentioned, the cross-correlation method assumes that the motion of the tracer particles within an interrogation window is uniform. In regions of high velocity gradients this assumption leads to a significant reduction in the signal to noise ratio by broadening or splitting the correlation peak (Westerweel 2008). The window distortion method first introduced by Huang et al. (1993) was implemented in the current work to improve accuracy and combat the high velocity gradients around the NHF jet and near the ubiquitous nasal cavity walls. Figure 27 illustrates the basic principle of distorting a correlation window in the second exposure to encompass all the seeding particles from the first exposure by accounting for velocity gradients across the window. The distorted correlation window grid is interpolated based on the velocity gradient calculated from a displacement predictor field. Figure 28 gives an example of a correlation grid fitted to the cross-sectional velocity gradients of a flow through a pipe with secondary flows. There is more to the actual implementation of the distortion method than Figure 26 demonstrates. In practice, the correlation windows between exposures must be of equal shape and size. The particle images contained within the skewed correlation windows are therefore deformed and mapped

onto a grid of equal dimensions to the original. Instead of deforming each interrogation region individually, deformation was applied to the entire PIV recording; otherwise window overlaps of 50% would result in repeated deformations of overlapping regions and come at significant and unnecessary computational expense. The mathematical formulation of the distortion method is given in Huang et al. (1993) and reviewed by Scarano (2002).

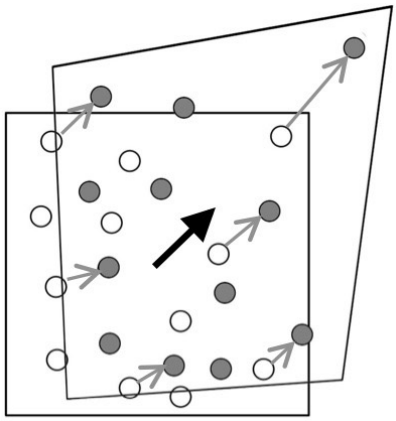

Figure 27. Schematic illustrating the basic principle of the window distortion method

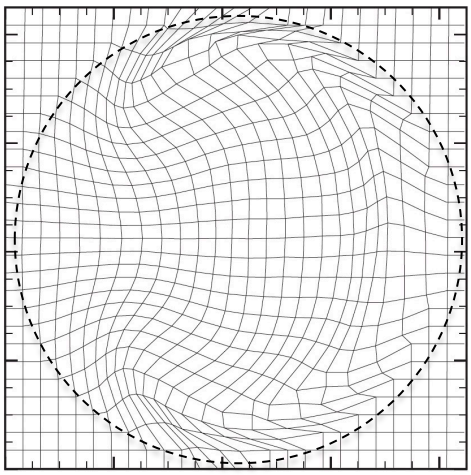

Figure 28. Distorted correlation window grid for a flow through a pipe with secondary flows (adapted from Buchmann 2010))

The cross-correlation algorithm employed in the current work was assessed with synthetic particle images with known displacement properties. For typical imaging and processing conditions with 2 mm particle diameters, 1/32 particles per pixel, 10% background noise, moderate (0.05–0.15 pixel/pixel) velocity gradient, 32 × 32 pixel^2 interrogation window and discrete window shifting, the expected total measurement uncertainty is approximately 0.05–0.1 pixel.

3.3 Image Preprocessing

The main objective of image preprocessing is to increase the signal to noise ratio for cross-correlation by enhancing the contrast of the particle images and reducing image noise. The cross-correlation algorithm is heavily dependent on the image intensity of particles, where brighter particles have a greater influence on the cross-correlation than duller particles. Stationary objects in images such as light reflections from boundaries must be removed from each image because these will create a bias error towards zero displacement. Some image preprocessing methods employed by other studies include background subtraction; image intensity thresholding, clipping and stretching; and low and or high-pass filtering (Honkanen & Nobach 2005; Raffel et al. 1998; Stitou & Reithmuller 2001; Westerweel 1993).

Although a high level of optical clarity was achieved in flow phantom construction and the working liquid was precisely refractive index matched, illumination of the background and stray reflections were unavoidable due to deposition of tracer particles on internal interfacial surfaces, air bubbles trapped irremovably in inaccessible regions of the nasal cavity, clouding of the silicone model surface due to absorption of water, and model imperfections such as small imbedded dust particles. To avoid over exposing the CCD sensor and associated image artifacts or even sensor damage, the aperture size was limited by the brightest reflection. Since the reflections were brighter than most of the seeding particles, the signal to noise ratio was affected. Reflections and the subsequent illumination of the background is evident in the raw image shown in Figure 29a. In a test case, an ensemble cross-correlation of 10 raw image pairs resulted in 26% invalid vectors.

Numerous background removal methods were explored and developed during the current work. Background images that could be subtracted from each recording were created using two methods: averaging over the entire data set and taking the minimum pixel intensity from each recording. Since the background in each image was static and the particle locations unique in each image, averaging over a large number of images (>100) produced a mean image of the noise. Similarly, taking the minimum (darkest) pixel intensity for each image element from across a series of images produced a minimum image that included only noise. Minimum background images tended to be more conservative than average background images, such that less useful information was subtracted along with the background. Cross-correlations of background subtracted images using the average and minimum methods resulted in 13% and 12% invalid vectors, respectively. In each case, a gain was applied to the resulting images to bring the maximum pixel intensity to 255 (intensity stretching). The background images were created from 200

image pairs. It was necessary to make a background image for each exposure individually because the two laser cavities produced slightly different light intensities.

Due to the nature of the nasal cavity geometry, at any measurement location, the light sheet was near to a parallel wall within some region. This illuminated stationary particles adhered to the wall that appeared to be in plane. These surfaces were also parallel with the flow and on inspection of the particle images, it was evident that particles would become adhered to and dislodge from the surfaces at random intervals. The aforementioned background subtraction technique failed to remove these particles because they were only present for a fraction of the data set. Sliding minimum background images created from the three corresponding exposures either side of the image in question were attempted. Although this reduced the number of invalid vectors to 8%, because a stationary particle would only be removed if it were present for all six images, the technique was not considered optimal. The background extraction method presented by Honkanen et al. (2005) where the second frame was subtracted from the first frame and vice versa, although it would have removed particles that were stationary for even the briefest of moments, was not practical in the current work for two reasons: the light intensities of each exposure were different and legitimate particles in low velocity regions were partially or completely eliminated due near zero displacements. Instead, background noise was removed by subtracting the corresponding exposure of either the previous or following image pair from each image, whichever gave the minimum image. This technique removed any particles that had momentarily adhered to the internal surface of the model or had dislodged within any period longer than 0.1 s (image pairs taken at 10 Hz). Although Honkanen et al.'s method would have caused a loss of information in the low velocity regions, because the time between image pairs is significantly longer than the time delay between successive images, particles had moved a sufficient distance to not cancel each other out. The number of invalid vectors was reduced to 7%.

A 3×3 pixel^2 Gaussian filter kernel was passed over the background subtracted images for two reasons. Firstly, the magnification was less than ideal in order to have the entire flow domain in one frame and avoid complications of stitching results from two half frames together. Most particles therefore only occupied approximately one pixel, which restricted the sub pixel estimation of the exact location of the signal (peak interpolation). The Gaussian filter increased the size of each particle, resulting in a wider correlation peak and improving the sub-pixel fitting and peak locking that is normally associated with under sampled images (Raffel et al. 1998). The Gaussian filter also acted as a low pass filter and removed high frequency noise such as CCD noise. A gain was applied to each image to bring the particle intensity to a value of 255. Finally a binary mask image that followed the contour of the nasal cavity cross-section was applied to

define the flow region, impose a zero flow condition at the fluid-wall interface and to suppress wall reflections. Application of a mask image also reduced computation time by excluding non-flow regions from cross-correlation. An example of a preprocessed image with the mask applied is given in Figure 29b. The final preprocessed images for the same test data set resulted in only 2% invalid vectors.

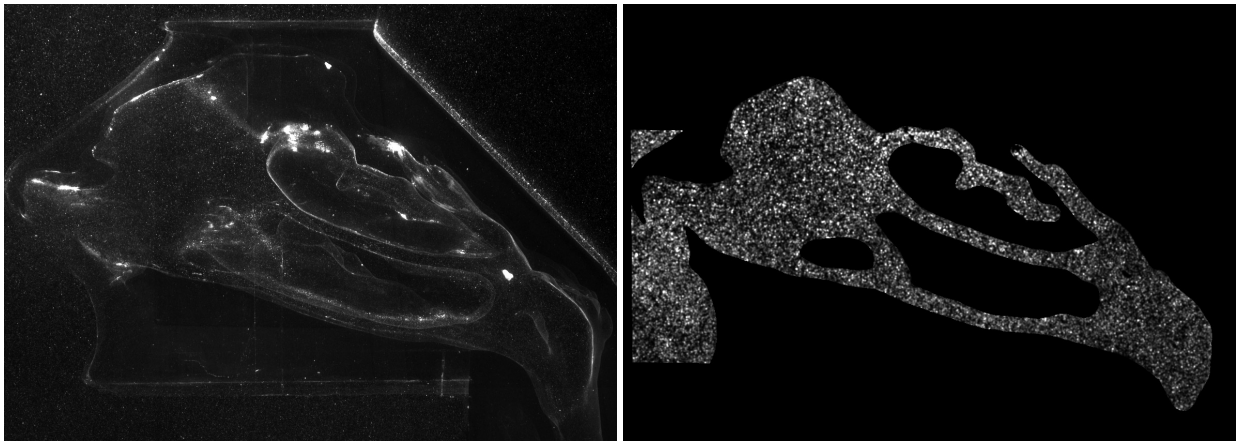

Figure 29. Examples of a a) raw image and b) a pre-processed image

Another image preprocessing tool developed over the course of the current work was image oversampling. Image oversampling was the term used to describe adding images from corresponding exposures together to artificially increase seeding concentrations. Pixel intensities below 5 (8 bit images) were not added to limit the accumulation of noise. This method was explored to increase the cross-correlation strength in regions of the nasal cavity with low seeding concentrations due to limited convective mixing and low velocities such as in the meatus passageways. The technique was not, however, utilised because a stronger correlation was found by ensemble averaging over the same number of images. Ensemble averaging was likely better able to deal with the high image noise because false peaks are averaged away over multiple correlation maps, whereas the number of false peaks increases linearly with oversampling. Samarage et al. (2010) have investigated in detail the advantages, disadvantages and applicability of temporal averaging processes including oversampling, ensemble and vector averaging.

In summary, the best PIV results were obtained using the image preprocessing methods outlined below and the techniques subsequently adopted for each PIV measurement presented.

- Subtract corresponding exposure from preceding or following image pair
- Intensity stretching
- Filter each image with a 3×3 pixel^2 Gaussian kernel

- Masking

3.3.1 Mask Creation

In order to create mask images that accurately represented the complex contours of each measurement location's cross-sectional profile, the laser sheet locations were measured relative to a known reference point on each model and cross-sectional profiles at the same location extracted from computer geometries obtained by CT scanning the flow phantoms themselves. Cross-sections were extracted using the freeware visualisation software Paraview (http://www.paraview.org/) and aligned with maximum images created by accumulation of the bright in-plane pixels from each image. As well as being far quicker than manually tracing the flow domain from a maximum image, this method was also more accurate because the extracted contour was infinitely thin. Manual tracing from a maximum image is unable to locate the exact location of the intended flow domain because the 2 mm thick light sheet can illuminate a large band of the wall where the two are near parallel, resulting in systematically oversized masks. A maximum image is overlaid with a contour obtained from Paraview in Figure 30 to illustrate the precise fit achieved. Since the computer geometry was obtained from the phantom itself, once the reference point was aligned, contours could be generated automatically throughout the geometry at the same spacing as traversed measurements. Any discrepancies were under 2 pixels deviation, which corresponds to 0.29 mm in vitro or 0.19 mm in vivo. This technique, to the author's knowledge, has not been reported elsewhere.

Figure 30. Contour of the nasal cavity obtained from a CT scan of the flow phantom overlaid on a maximum image.

3.4 Stereoscopic PIV

In traditional planar-PIV, where the axis of a single camera is perpendicular to the area of interest, particle velocities are projected onto the plane of the light sheet and the out of plane velocity component is lost. In flows that are largely two-dimensional this gives reliable results, however, in complex flows, when the orthogonal velocity component is significant, perspective error contaminates in-plane velocities (Prasad 2000). The perspective error is proportional to the relative magnitudes of the out-of plane velocity component to the in-plane components, as well as the distance in the image from the camera axis. In-plane velocity errors of about 10% have been estimated when the in and out of plane velocity magnitudes are similar (Prasad 2000).

An extension of the basic planar-PIV method is stereoscopic PIV, which uses two cameras viewing along different directions to enable the resolution of the out-of plane velocity component and elimination of perspective error. A typical stereoscopic imaging configuration is illustrated in Figure 31. This method was chosen over the translation method (Raffel et al. 1998), in which both cameras are orthogonal to the light sheet, because it is more flexible and allows a larger common area between the two cameras. The stereo-PIV system involves the simultaneous acquisition of particle images from each stereo camera. The two-dimensional, two velocity components (2D-2C) vector fields are computed separately for each camera and the two-dimensional, three velocity components (2D-3C) velocity field subsequently obtained by stereo-reconstruction via a three-dimensional camera calibration. A user defined regular grid in object space is projected onto each camera such that the resulting vectors are located at the desired object space positions. Typically, a grid spacing that provides an effective interrogation window overlapping factor of 0.5 is applied to increase the spatial sampling. Stereo angles (θ_1, θ_2) are typically 15–45°, with the theoretical optimum accuracy in the orthogonal direction when the angles are 45°. Viewing the laser sheet at an angle presents the difficulty of a varied magnification and focus across the width of the image. The Scheimpflug condition solves this problem by tilting the image plane relative to the lens plane (as evident in Figure 31) to provide equally good focus over the image width (Prasad & Jensen 1995).

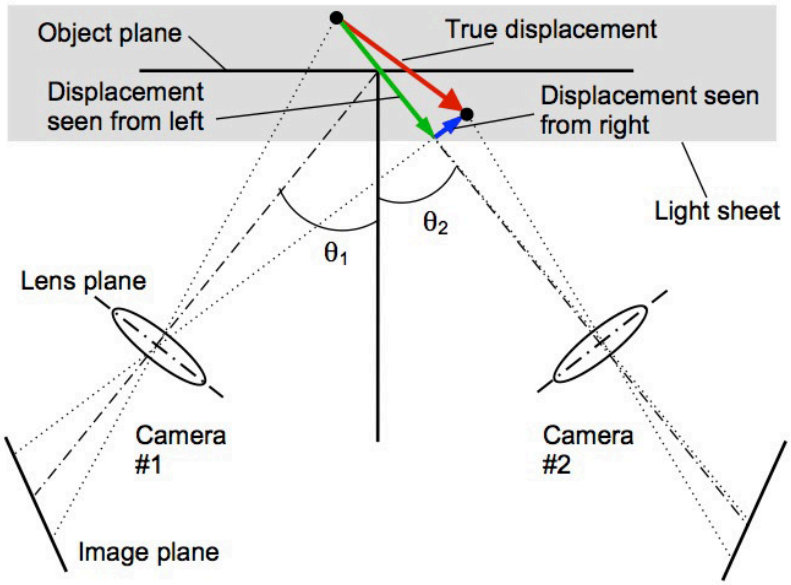

Figure 31. Basic stereoscopic imaging configuration with the Scheimpflug condition

The Scheimpflug arrangement does not remove perspective distortion. Transformation of the velocity vectors from distorted image space into non-distorted object space was conducted using the in-situ three-dimensional calibration-based reconstruction method described by Soloff et al. (1997). This technique does not rely on an accurate knowledge of the geometry of the stereo camera set-up and is able to account for any known and unknown distortion encountered in the real experiment. The cameras are calibrated by imaging a calibration plate with a Cartesian grid pattern, which was aligned with the light sheet and traversed through the measurement volume at a minimum of three different z locations. The locations of the calibration markers are identified via local pattern matching (i.e. cross-correlation) and used to calculate the coefficients of an image space mapping function (Equation 9) by least squares. Each calibration marker was mapped to the third-order polynomial to typically within an accuracy of 0.5 pixels as shown in Figure 32 (i.e. mapping error). According to Soloff et al. (1997), a third-order polynomial mapping function is sufficient to account for linear distortions. The linear terms account for perspective error and the higher order terms compensate for non-linear distortions such as barrel and pincushion radial distortions. Others studies (Prasad 2000) have used higher orders and have found little or no significant increase in the accuracy of the reconstructed velocity field.

$$\begin{aligned} F(x,y,z) = {} & a_0 + a_1 x + a_2 y + a_3 z + a_4 x^2 + a_5 xy + a_6 y^2 + a_7 xz \\ & + a_8 yz + a_9 z^2 + a_{10} x^3 + a_{11} x^2 y + a_{12} xy^2 + a_{13} y^3 \\ & + a_{14} x^2 z + a_{15} xyz + a_{16} y^2 z + a_{17} xz^2 + a_{18} yz^2 \end{aligned} \qquad \textbf{Equation 9}$$

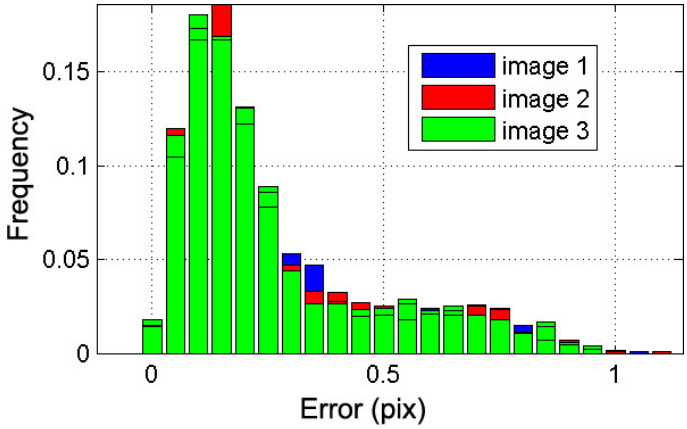

Figure 32. Histogram showing a typical distrbution of mapping errors for each calibration marker

The calibration plate was a 38 × 38 array of 2.5 mm diameter white dots at 5 mm spacing on a black background. The dots, or calibration markers were CNC machined into a 200 × 200 x 10 mm black anodized aluminium plate and filled with white polyfill flush with the surface. The array of calibration markers was large enough to fill the entire image frame and dense enough to provide over 500 calibration points in each field of view investigated. In the centre of the plate was a larger dot (3 mm diameter) surrounded by 4 smaller dots (1.5 mm), which defined the origin (0, 0, Z) of the coordinate system. The cameras and calibration plate were positioned such that the origin was in the centre of both images to maximise the common area seen from the two cameras and gain a common frame of reference. Example calibration images for the left and right cameras are given in Figure 33. The calibration plate was mounted on a micrometer screw operated linear traverse, aligned with the centre of the light sheet at Z = 0, and traversed half the light sheet thickness (1 mm) in the positive (away from the cameras) and negative (towards the cameras) directions. Code that was developed by Brown (2008) that used a camera calibration method called *resection* was implemented into the current work's camera calibration code to give the exact camera orientations and positions.

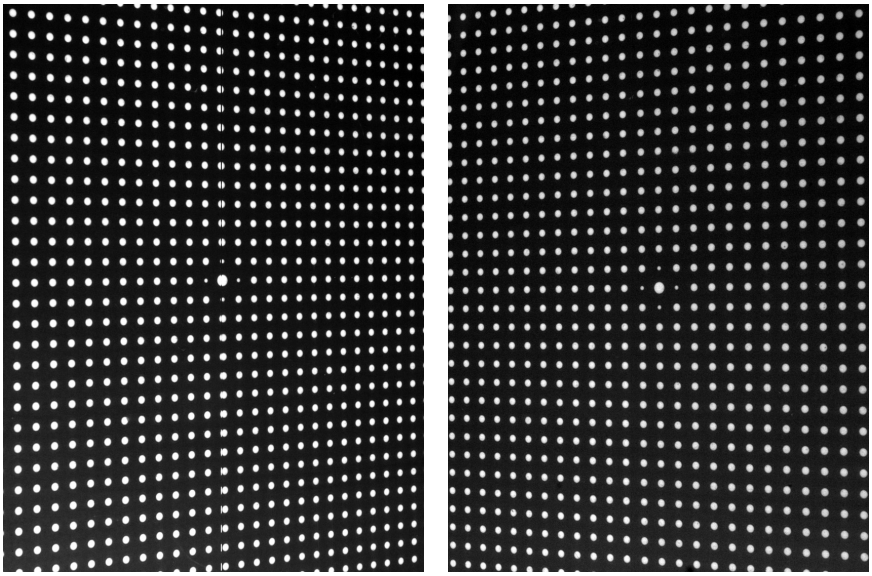

Figure 33. Left and right calibration images

The reconstruction method assumes that the calibration target is aligned with the centre of the light sheet plane. In practice, however, this alignment is difficult and a slight out-of-plane shift or rotation can introduce significant errors in the image to object mapping (Wieneke 2005; Willert 1997). A method for the alignment correction as proposed by Wieneke is also implemented into the current stereo-PIV procedure. This is generally referred to as self-calibration or disparity correction. If the calibration target were to be perfectly aligned with the light sheet and the image mapping function entirely accurate, the particle images from the left and right cameras for corresponding exposures when mapped into object space would match perfectly because they were taken simultaneously. Disparity correction was made by iteratively updating the mapping function coefficients based on the disparity obtained from cross-correlating corresponding left and right camera particle images that have been de-warped into object space.

For creating the mask images, an additional code was written to map the cross-section contour obtained from the computer model in object space into image space for each camera using an inverse of the camera calibration function. A flowchart of the stereo-PIV cross-correlation algorithm (SPIVCC) implemented in the current study is given in Figure 34.

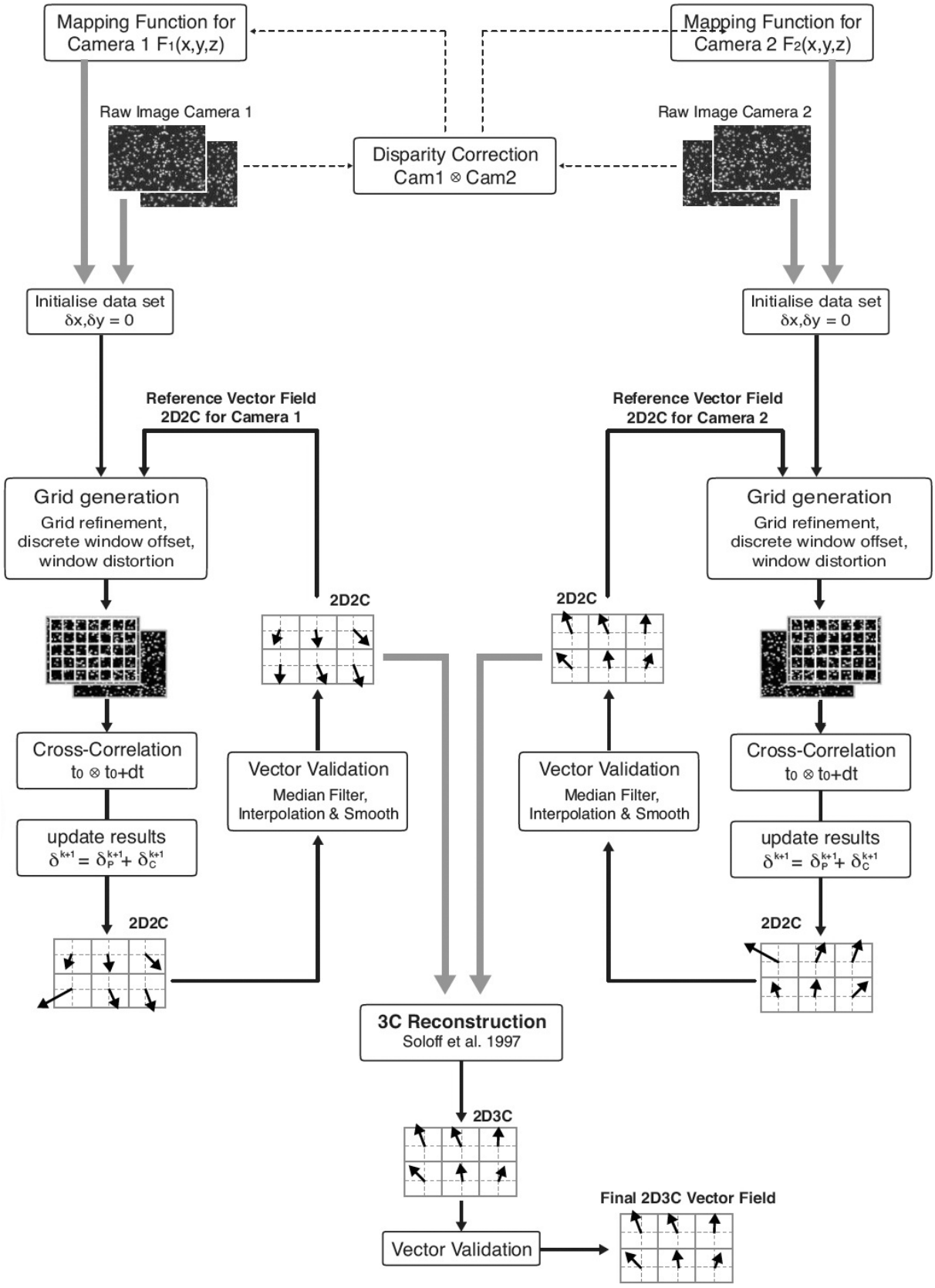

Figure 34. SPIVCC algorithm: flow chart for stereo-PIV vector calculation.

3.4.1 Measurement Accuracy

The performance and accuracy of the stereo-PIV apparatus and software implemented in the current work was assessed using a simple solid body translation experiment that involved the recording of a particle image pattern with known displacements and subsequent analysis. Seeding particles were simulated by a sheet of 150-grit sandpaper illuminated with diffused light to provide excellent contrast and signal to noise. The cameras were separated by 45° symmetrically and an acrylic panel placed between the cameras and the object plane to simulate optical distortion similar to that of the real experiment. The same lenses, apertures and a similar magnification to that shown in later flow measurements were each employed here. The particle pattern was displaced by 1 mm ± 5 μm in the x and z directions (i.e. 13–14 pixels) with a micrometer driven traverse. The displacement field was computed using a 64 × 64 pixel^2 interrogation window with a 50% overlap and no vector validation or filtering.

The statistical results from the resolved displacement in the three principle directions are shown in Table 10. The mean and RMS errors are calculated from a total of 10 measurements and averaged over the entire measurement plane. The RMS error in the x, y and z displacement is a function of the direction of motion and includes the PIV displacement error, interpolation errors, camera calibration errors, target grid spacing errors and traversing errors. For the 1 mm displacement, the measurement results show a total error of 0.4% and 0.5% or 3.9 μm and 5 μm in the x and z directions, respectively. The errors due to a displacement in y direction were not assessed, which are typically of the same order as the x direction (Willert 1997). The ratio between in-plane and out-of-plane error was approximately one and consistent with the theoretical $1/\tan(\alpha)$ relation (Lawson and Wu, 1997). The RMS errors for Δx, Δy, and Δz are low for the 0 mm displacement and range between 1.2 and 4.2 μm in the case of the 1 mm displacement. The largest error in Table 10 was 5.2 μm and the shortest time delay used in the current work's PIV measurements was 100 μs. The largest velocity error was therefore estimated to be ±0.05 m/s, which for typical nasal velocities of 2–3 m/s corresponds to percentage errors of ±1.6–2.5%.

Table 10. Resolved displacements for the three independent traverses investigated.

Traversed Displacements	Resolved Displacements Mean (μm)			RMS (μm)		
	Δx	Δy	Δz	Δx	Δy	Δz
0 mm	0.28	0.25	0.32	0.36	0.29	0.42
1 mm in x	999.2	1.5	5.2	3.1	1.2	4.2
1 mm in z-	1.6	1.5	997.2	2.1	1.9	2.2

3.5 Conclusions

The experimental apparatus and methodologies of the PIV measurement system employed in the current work have been described. Ensemble correlation averaging was employed to increase the signal to noise ratio and produce time averaged velocity maps. Window refinement, shifting and distortion were also used to increase the strength of the cross-correlation and increase the accuracy of measurements by accounting for the large dynamic range and velocity gradients that occurred in the nasal cavity, particularly with NHF. A number of unique contributions to image preprocessing techniques were made including original background subtraction and PIV image mask creation methods. Both of these techniques would prove useful to any PIV measurements in complex internal geometries. The stereo-PIV system was outlined in detail and showed to measure velocities to within ± 0.05 m/s for the current work's flow conditions.

4 Steady Flow by Planar-PIV

This chapter presents the first of three sets of PIV measurement campaigns conducted in the current work. Here planar-PIV has been used to measure steady flows in one half of the nasal cavity (model 1) during simulated natural and NHF assisted breathing. To the author's knowledge the results were the first reported PIV velocity fields in the nasal cavity with assisted breathing,. This work served largely as a feasibility study and building block for later more complex measurements. The experimental methodology that formed the basis for each measurement campaign is described in detail, including justification for using steady flows.

4.1 Introduction

4.1.1 Nasal Flow Modeling Considerations

Air is classified as a Newtonian fluid having constant viscosity, which is not to be confused with an ideal fluid that flows without viscosity or a perfect fluid that flows without viscosity and compressibility. Airflow in the nasal cavity can be considered incompressible because flow velocities are low compared to the speed of sound in air (Ishikawa et al. 2006) and peak airway pressures as high as 6 cm H_2O (gauge) during nasal breathing at rest (Proctor 1982) have negligible effect on density. Peak oral cavity pressures were measured in the current work up to 12 cm H_2O with 50 l/min cannula flow by holding a probe between the lips. By using the form of the ideal gas law given in Equation 10, it can be shown that even at these pressures there is only a 0.7 % change in the density of air. Air in the nasal cavity will also be assumed to be homogeneous and isothermal.

$$p = \rho RT \qquad \textbf{Equation 10}$$

Airflow in the nasal cavity is not steady and decelerates and accelerates in either direction during inspiration and expiration. Although breathing is a cyclical process with a time varying flowrate, most

studies of nasal airflows to date have used steady flow conditions based on a quasi-steady flow assumption. A quasi-steady flow assumption supposes that a fluid flow responds instantaneously to a change in pressure gradient. In other words, and in the case of nasal flows, the time scale of a breath has been considered sufficiently long that inertial effects on the flow pattern are negligible. The Strouhal (St) and Womersley (α) numbers (Equations 11 and 12) are dimensionless parameters used to classify oscillating flows, where for nasal flows L is equivalent to airway length, d_H the hydraulic diameter, f the breathing frequency, U the mean velocity, and ν the kinematic viscosity of air. In biofluid mechanics, the Womersley number is often preferred over the Strouhal number. The two are related by the Reynolds number in Equation 13. Flow in pipes will follow a Poiseuille velocity profile closely when α <1 and can be assumed to be quasi-steady (Womersley 1955) because viscous forces dominate inertial forces. Above α = 1 the phase lag between flow and pressure increases sharply and the velocity profile flattens (as seen in Figure 35), until at α = 10 the phase lag is approximately 80° and the amplitude of the oscillatory pressure gradient produces only about one-fifteenth of the flowrate as in a Poiseuille flow case where the same pressure gradient is applied to both flows (Womersley 1955). For quiet breathing at a frequency of 15 breaths per minute the Womersley and Strouhal numbers were estimated by Doorly et al. (2008a) to be less than 3 and 0.25 respectively. A similar analysis by Hahn et al. (1993) predicted values of 4 and 0.01. Although these Womersley number estimates are greater than one, the low value for St suggests that the flow may be assumed to be quasi-steady (Hahn et al. 1993). The flow and pressure relationship in the nasal cavity will after all be different to that in pipes as measured by Womersley. Isabey and Chang (1981) showed experimentally that oscillatory effects are not present in the lower airways until α > 4. The quasi-steady flow assumption is commonplace in both experimental and numerical nasal flow research (Horschler et al. 2006b), and was made for this campaign of measurements. Preliminary in vivo breathing flowrate measurements tested later in section 4.2.3 showed that breath period increased proportionally with increasing cannula flow, reducing the Womersley number. Quasi-steady flow was therefore assumed to hold true with NHF.

$$St = \frac{2\pi f L}{U} \qquad \textbf{Equation 11}$$

$$\alpha = \frac{d_H}{2}\sqrt{\frac{2\pi f}{\upsilon}} \qquad \textbf{Equation 12}$$

$$\alpha = \frac{1}{2}\sqrt{\mathrm{Re}St} \qquad \textbf{Equation 13}$$

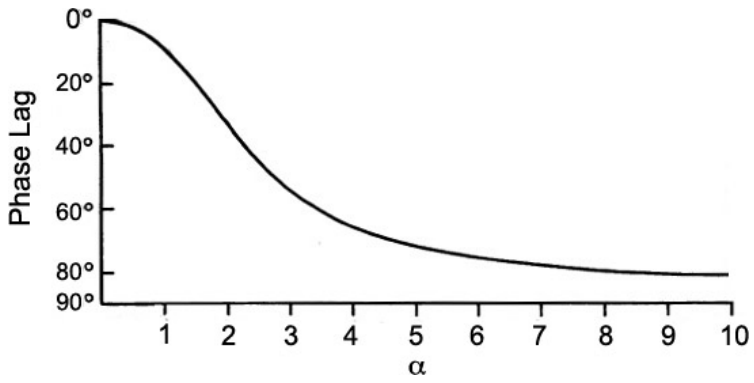

Figure 35. The effect of the Womersley number (α) on the phase lag between oscillating pressure and the flow generated in a pipe (adapted from (Womersley 1955))

4.2 Experimental Setup

4.2.1 Flow Circuit

The nasal cavity phantom model 1 was installed in a recirculating flow system as shown in Figure 36, with the side face of the model parallel to the reservoir wall and at a separation of 2 mm. A constant pressure header tank supplied steady expiration and cannula flows, and steady flow was pumped in reverse for inspiration. A straight tube of length L = 40D (D = 25.4 mm) was installed at the throat to ensure a fully developed inlet profile. Two electromagnetic flow meters (Tigermag FM626, Krohne IFC 010D) and valves were used to adjust the individual cannula and throat flowrates. Repeatability of the electromagnetic flow meter readings was improved by adding 0.1 g/l of salt to the working fluid. Linear calibrations of the flow meter readings and the actual flowrate were made with repeated bucket and stopwatch measurements. Return and overflow lines connected the reservoir and header tank to ensure flow over the weir and constant head. The phantom was immersed in the reservoir to a depth such that the free surface remained flat at the highest flowrate, effectively providing a constant static pressure at the nostrils. The reservoir measured 0.6 × 0.6 × 0.8 m (Figure 36 is not to scale). The orientation of the nasal cavity in the reservoir was regarded as inconsequential because inertial forces were shown to dominate buoyancy forces in the real nose in section 2.5.6 and on the seeding particles in section 3.1.1. Measurements by Hahn et al. (1993) were even conducted with the nasal cavity upside down. The model was placed in the reservoir in a

supine position (horizontal throat and nose upwards). Although model 1 did not include the external shape of the nose, a physiologically accurate inlet profile on inspiration was maximised by immersing the model in the reservoir to provide a free boundary condition at the nostrils, unlike in the other studies that used truncated inlets. A medium size nasal cannula prong was modeled with a length of clear PVC plastic tubing that matched the scaled diameter and wall thickness of the cannula and was molded to a mimicked contour. A mirror was placed behind the cannula and aligned perpendicularly with the laser sheet to illuminate the particles in the cannula's shadow. A matt black steel sheet was placed behind the model to maximise the contrast in the particle images.

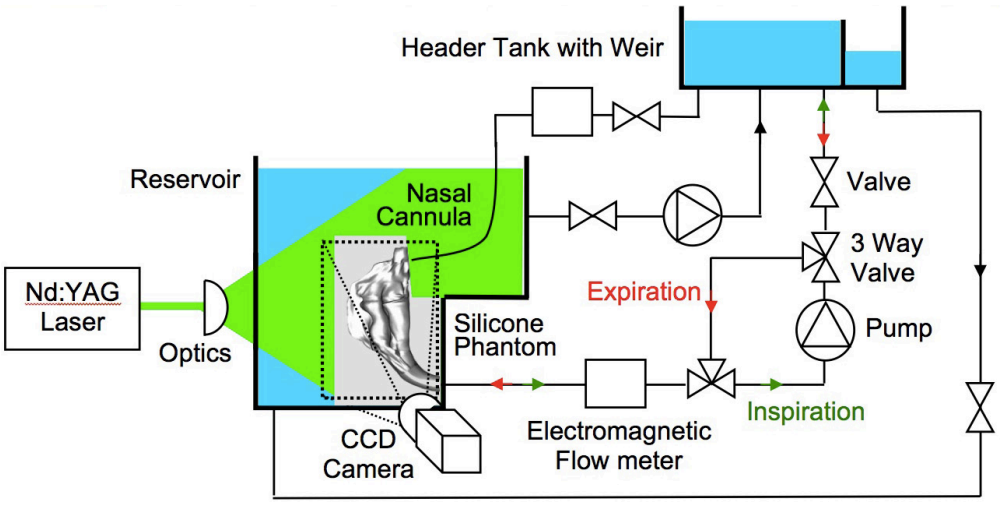

Figure 36. Schematic of the experimental facility

A temperature control system was constructed to maintain a constant temperature during measurements. Heating was supplied with a standard mains power residential hot water cylinder element connected to a transformer (variac). Water was cooled in an external closed loop circuit by immersing the evaporation coils of a dehumidifier in a bucket. The water from the bucket was then pumped through copper coils placed inside the main reservoir to provide constant cooling. Equilibrium was maintained at 25°C by selecting the appropriate voltage to the heating element. A submersible pump with both inlet and outlet open to the reservoir was placed within the reservoir to both pass a steady flow over the heating and cooling elements and maintain a homogenous and constant seeding concentration by agitating the seeding and preventing it from settling.

4.2.2 Working Liquid

The refraction of light passing through a liquid-solid or gas-solid interface, and subsequent image distortion, poses a difficulty common to optical diagnostic techniques in complex geometries. The change of direction and wavelength of the light occurs at the media interface as the light travels from one medium with a given refractive index *n* to a medium with a different refractive index. The ratio of the speed of light in a vacuum to the speed of light in the material defines the refractive index *n* for that material. Snell's law (Equation 14) describes the relationship between the angles of incidence and refraction for two materials with different refractive indices. The working fluid needs to match the refractive index of the flow phantoms in order to avoid optical distortion in the PIV images.

$$\frac{\sin\theta_1}{\sin\theta_2} = \frac{n_2}{n_1} \qquad \textbf{Equation 14}$$

In this study a mixture of glycerol and water was used as the carrier medium to simulate airflow and match the refractive index of the flow phantoms. Differences in the compressibility of air and the liquid were considered inconsequential because air was assumed incompressible. Glycerol has a refractive index of approximately 1.47 and when mixed with water, which has a refractive index of 1.33, the refractive index of the mixture can be tuned to that of the silicone. The refractive index of the silicone rubber used for the phantom construction is specified as 1.43 by the manufacturer, but varies due to differences in mixing and curing from model to model. The studies shown in Table 11 have matched the refractive index of their silicone flow phantoms for PIV measurement with glycerol/water mixtures ranging from 48/52% to 59/41%. Each of the three models constructed in the current work were carefully prepared in the same manner and consistently had a refractive index of 1.42. The optimum mixture was found to be 61% glycerol and 39% water by volume at the working temperature of 25°C.

Tetraline (1,2,3,4-tetrahydronaphthalene) (Park et al. 1997) and aqueous sodium benzoate (Doorly et al. 2008a) have been used in other studies, which are overviewed in Table 11. Park et al. reported difficulties when working with tetraline due to chemical attack within the flow circuits' materials causing stress cracking and deformation. Tetraline irritates skin, inhalation of vapour is particularly irritating to the respiratory tract and it must be considered as a hazardous waste for disposal. Tetraline was also not a suitable option because it's refractive index is too high for the silicone and is insoluble in water. Glycerol on the other hand is soluble in water and is very safe to work with, being used in a large number of food and

cosmetic products. Glycerol is comparatively very cheap to sodium benzoate and 40 litres can be obtained for approximately NZ$100.

Table 11. Properties of refractive index matching liquids at 20°C

	n	ρ (kg/m^3)	μ (kg/m s) $\times 10^{-3}$	Matching Material
Glycerol/Water: 48/52% (S. K. Kim & Haw 2004), 54/46% (Garcia et al. 2007), 55/45% (Horschler et al. 2006a) (Chung et al. 2006), 59/41% (Hopkins et al. 2000)	~1.38-1.43	1140	10.0	Silicone (Sylgard 184)
1,2,3,4-tetrahydronaphthaline (tetraline): (Park et al. 1997)	1.55	970	2.2	Epoxy-based casting resin
Aqueous sodium benzoate: (Doorly et al. 2008a)	1.41	1145	4.9	Silicone

The refractive index matching ratio of glycerol to water was found by immersing the silicone models in a bath of glycerol and progressively adding water to the solution until a laser beam passed perfectly straight through the flow phantom. The laser beam was first passed through the bath without the model and a mark made on a target that was approximately 3 metres away. The flow phantom was then immersed in the bath so that the laser beam passed through multiple convoluted internal surfaces of the phantom. Water was continuously added and mixed until the laser beam aligned with the original target mark. In another method, a grid of white and black squares was placed behind the model and water added until the grid was undistorted. The laser beam method was, however, more accurate because it was difficult to see distortion in the grid when fine-tuning was required. With the laser beam method, a small refractive index mismatch still created a distinct displacement of the point on the wall. By Snell's law and using an angle of incidence on one of the internal surfaces of the phantom of 30°, a refractive index discrepancy of 1% corresponds to a distance of 17.1 mm between the laser beam and the target mark. For each model the mixture was tuned such that this distance was less than 5 mm. Errors introduced by this level of refractive index mismatch were considered to be negligible. Further precision required significant time to achieve and the refractive index needed to be regularly monitored due to the evaporation of water from the mixture.

The refractive index of the 61/39% glycerol/water mixture was measured with a refractometer at four temperatures (Figure 37), and found to decrease approximately linearly with temperature. The mixture's density was measured across the same 20–35 °C temperature range, using a volumetric flask (200 ml), a

thermocouple, heated plate and electronic scales. The results are shown in Figure 38. Shear stress, τ was measured using a Haake RV20/RC20 viscometer across 50–2700 s^{-1} shear rate, γ and 16–36 °C temperature ranges. The results in Figure 39 at each temperature map to linear trend lines that have R^2 values within 0.05% of 1. The linear relationship between shear stress and shear rate demonstrates the mixture to be Newtonian as in the case of air. The dynamic viscosity, μ at each shear rate was calculated ($\mu = \gamma/\tau$) and averaged at each temperature. The variation in dynamic viscosity of the mixture across a 16–36 °C temperature range is shown in Figure 40. At 25°C the working fluid had a refractive index of 1.422, a density of 1154 kg/m^3, and a dynamic viscosity of 9.02 × 10^{-3} kg/ms.

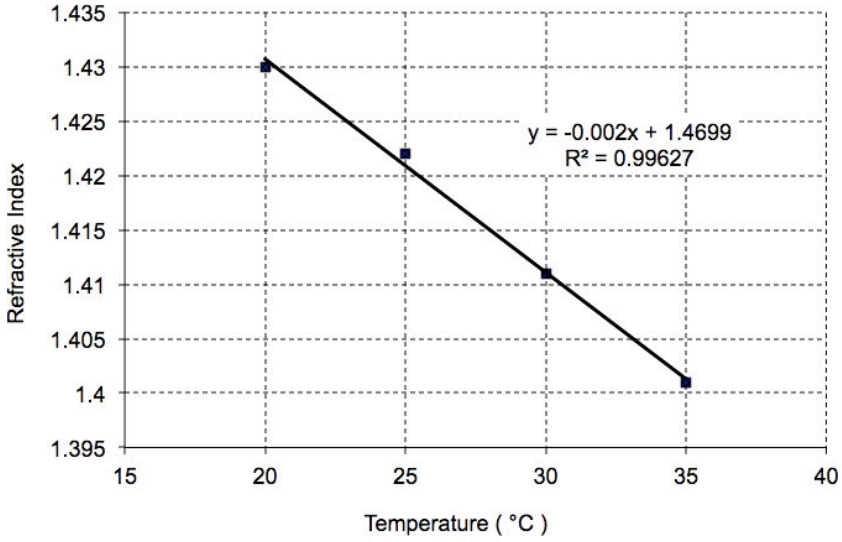

Figure 37. Refractive index versus temperature for a 61/39% glycerol/water mixture

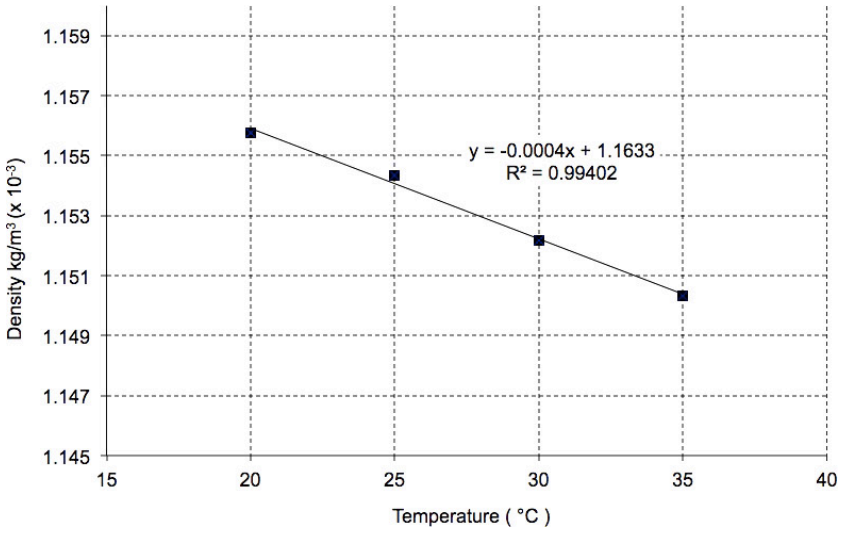

Figure 38. Density versus temperature for a 61/39% glycerol/water mixture

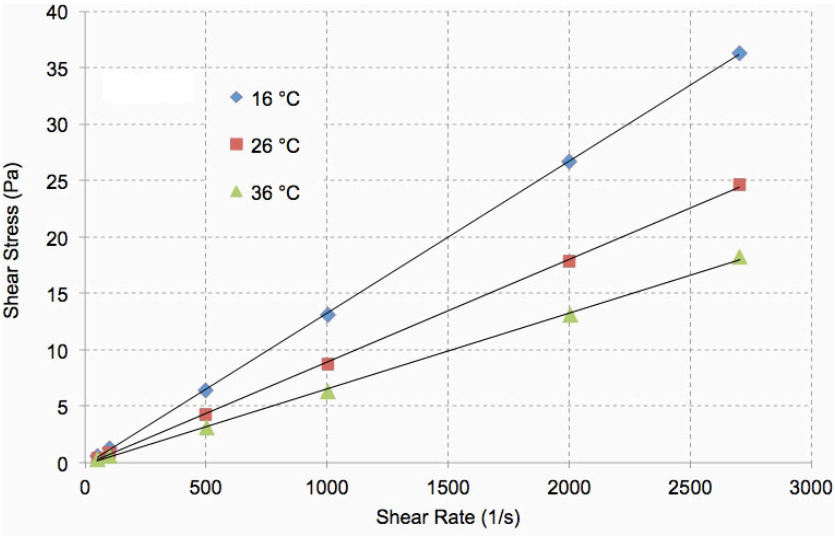

Figure 39. Shear rate versus temperature for a 61/39% glycerol/water mixture

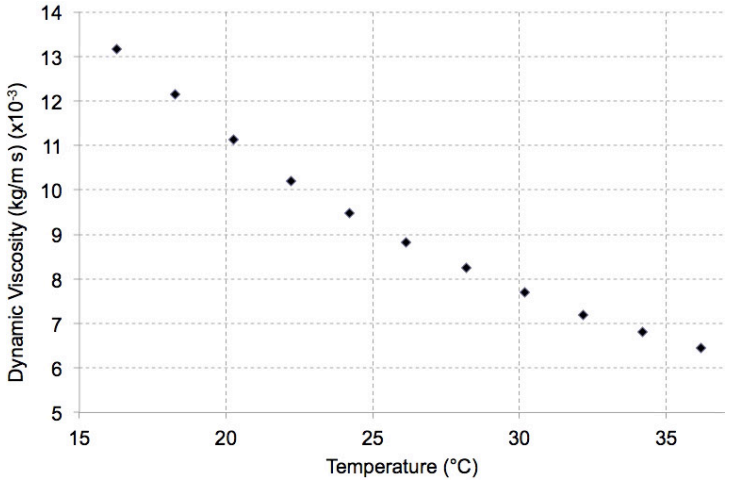

Figure 40. Dynamic viscosity versus temperature for a 61/39% glycerol/water mixture

4.2.3 Preliminary In Vivo Flow Measurements

To ensure physiologically accurate flowrates were reproduced in vitro, preliminary in vivo measurements were conducted and subsequently dynamically scaled. Lung flowrates with and without NHF were measured in vivo on a healthy 23-year-old male with height 184 cm and weight 85 kg. To measure natural breathing flows, a mask sealed around the face was worn and connected to a TSI-4040 flow meter that exhausted to the atmosphere. The resistance to flow imposed by the mask and flow meter was neglected and assumed not to disturb the natural breathing pattern. To quantify the lung flowrate with NHF, the same mask was worn over a cannula and a second TSI-4040 flow meter used to measure the cannula flowrate. The cannula flowrate was subtracted from the simultaneously measured mask flowrate to yield

lung flowrates for cannula flows over a 10–50 l/min range in increments of 10 l/min. The subject was relaxed during measurements. The results displayed in Figure 41 show that NHF modifies natural inspiratory and expiratory flowrates and breathing frequencies by assisting inspiration and providing resistance on expiration. Positive relationships existed between cannula flowrate and both the peak inspired flowrate and breath period. The increase in breath period with increasing cannula flow is largely due to the increased resistance and duration of expiration. Expiration is a passive process and the natural recoil of the lungs produced an expiratory flowrate relatively independent of cannula flow. Although tidal volume was not calculated, it can be inferred that there is also a positive relationship between cannula flowrate and tidal volume because expirations at higher cannula flows occur at approximately the same flowrate yet have a longer duration.

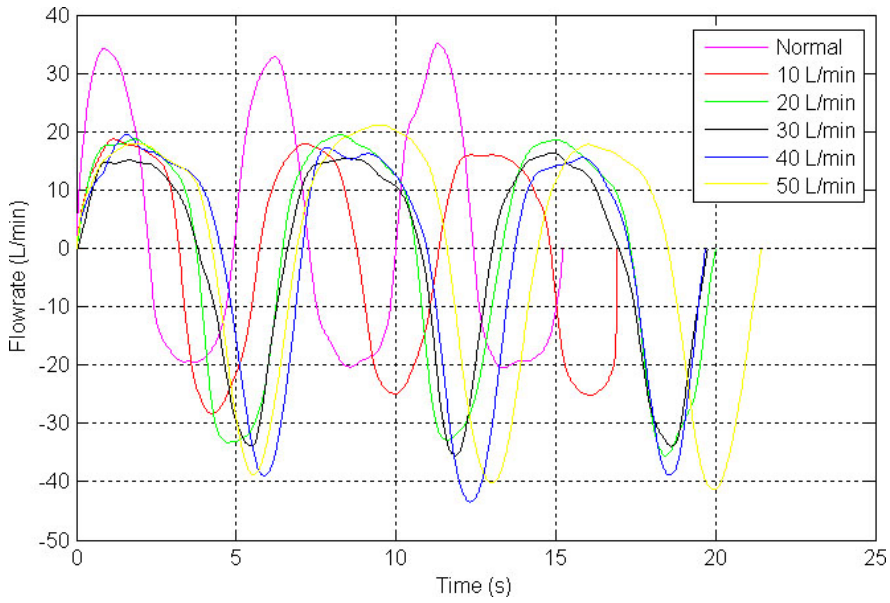

Figure 41. Lung flowrates during normal breathing and with 10-50 l/min cannula flowrates (expiration positive)

Although the nasal cavity geometry and in vivo flowrates were obtained from two different healthy adult males, Tobin et al. (1983) measured the breathing pattern of 65 normal subjects from 20 to 81 years of age and found no effect of age on the mean values of various breathing pattern components or any significant correlation with body height. Both subjects were therefore assumed to be sufficiently similar for any differences in their breathing patterns to fall within a normal range of interpersonal variability (Tobin et al. 1983). The subjects' weight and height statistics were not available with any of the geometries used.

4.3 Description of the Measurements

Studies to date have investigated inspiration and expiration flowrates that are assumed to be representative of the average conditions over the respiratory cycle. Peak flowrates were chosen for investigation in the current work because maximum and minimum airway pressures are key indicators to breathing therapy and occur at peak expiration and inspiration, respectively. The peak in vivo flowrates averaged over 10 breaths used in experiments are given in Table 12. The expiration flowrates when averaged were all within ±1 l/min and no correlation with cannula flowrate was found so 18 l/min was used for each cannula flow. Dimensional similarity between in vivo and in vitro conditions was obtained by matching the Reynolds number in the nasopharynx for lung flows and at the prong exit for cannula flows by Equation 15, where $\overline{u}$ is the mean velocity. An air flowrate of 22 l/min for example corresponded to a flow of 19.8 l/min for the water and glycerol mixture at 25°C in the 2× scale model. As with Hopkins et al.'s measurements, it was assumed that the nasal cavity geometry represented a mid nasal cycle state where breathing flowrates were equally shared between the two nasal cavities. Since only one choana was investigated, flowrates half of the full physiological flowrates shown in Table 12 were therefore applied. The Reynolds numbers are based on the hydraulic diameter of the half nasopharynx (23.3 mm) and the mean internal diameter of the cannula prong (4.5 mm). The density and dynamic viscosity of saturated air at 37°C were taken as 1.068 kg/m^3 and 18.8×10^{-6} kg/ms, respectively. Only the medium sized cannula was investigated because at the time that was the only size available. Fisher & Paykel Healthcare developed the small and large cannula sizes over the duration of the current work.

$$\overline{u}_{in\ vivo} = 2\frac{\upsilon_{in\ vivo}}{\upsilon_{in\ vitro}}\overline{u}_{in\ vitro} \qquad \textbf{Equation 15}$$

Table 12. In vivo flowrates (l/min) for the 12 conditions investigated with nasopharynx Reynolds numbers in parentheses

		Cannula flowrate				
	Natural breathing	10 (1700)	20 (2680)	30 (4010)	40 (5350)	50 (6690)
Inspiration,	22 (2130)	26 (2520)	30 (2900)	34 (3280)	38 (3680)	42 (4060)
Expiration,	32 (3100)	18 (1750)	18 (1750)	18 (1750)	18 (1750)	18 (1750)

Planar-PIV was used to measure nasal flow velocities on a single sagittal cross-section plane that bisected the left nostril as indicated in Figure 42. This single slice was measured because it contained the strongest flow and bisected the cannula's prong, which gave the most information on the behaviour of the jet. Further cross-sections to build a more complet view of the flow in the nasal cavity will be investigated in Chapters 5 and 6. Measurements were made at peak expiration and inspiration flows, simulating both natural breathing and NHF flowrates over a 10–50 l/min range in 10 l/min increments. The 12 measurement conditions are those presented in Table 12. Time delays ranged from 400 μs during natural inspiration to 110 μs with 50 l/min cannula flow on inspiration, to give a maximum pixel displacement of approximately 10 pixels in each image. A total of 200 image pairs were acquired at a frequency of 10 Hz. Ensemble correlation averaging was performed over 100 image pairs. Although 200 image pairs were available, there was no appreciable difference in the results when correlating more than 100 image pairs and thus computation time was saved. Time averaged measurements were of interest because the time scale of one breath (approximately 4 seconds) is significantly shorter than NHF treatment durations. Mean flow fields also served as the basis for comparing natural and assisted breathing flow patterns without the results being clouded with any time dependent fluctuations. The particle images were divided into 64 × 64 pixel^2 interrogation regions and the area average displacement calculated by locally cross-correlating the particle image intensities between two subsequent recordings. An overlapping factor of 50% and iterative window refinement was applied with a final interrogation window size was of 32 × 32 pixel^2. A table of the measurement parameters is provided in Table 13.

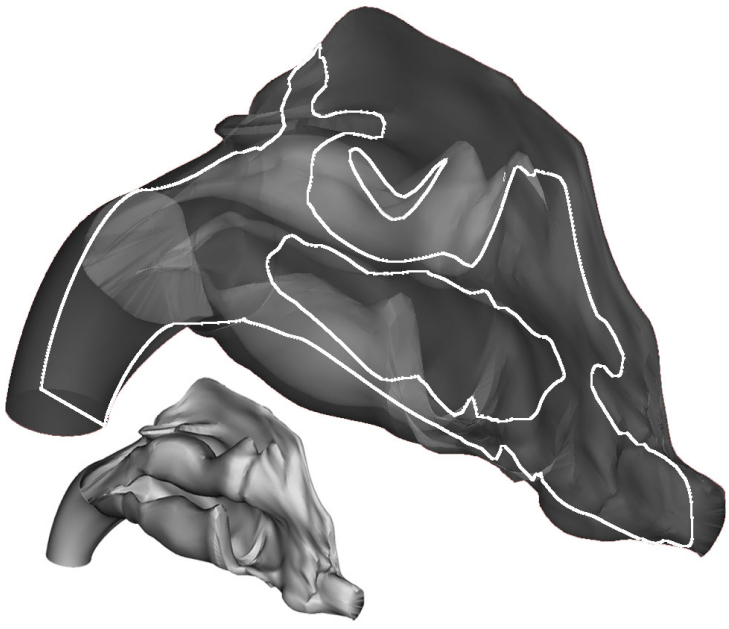

Figure 42. Measurement plane bisecting the left nostril

Table 13. Table of measurement parameters

Nasal cavity model	Scale	2 : 1
	Dimensions (H × W × D)	240 × 160 × 80 mm
	Material	Silicone (Sylgard 184)
Flow	Liquid	61% glycerin, 39% water
	Properties at 25°C	η = 1.422, μ = 9.27x10^{-3} kg/ms, ρ = 1154 kg/m^3
	U_{max}	17.3 m/s
Seeding	Type	Hollow glass spheres
	Mean Diameter	16 μm
	Density	1.1 g/cm^3
Laser	Type	Nd:YAG, dual cavity
	Max Power	120 mJ
	Pulse width	9 ns
	Thickness	2 mm
Camera	Type	CCD
	Resolution	1600 × 1200, 8 bit
	Pixel Size	7.4 × 7.4 μm
Image Properties	Lens focal length	60 mm
	Lens aperture	f = 11
	Magnification	0.113 mm/pixel
	Region of interest	180 mm × 135 mm
	Maximum particle displacement	10 pix
PIV analysis	Spatial Resolution	32 × 32 $pixel^2$ (3.6 × 3.6 mm^2)
	Overlap	50%

4.4 Results and Discussions

Figures 43–49 are two dimensional, time averaged velocity maps through one sagittal cross-section of the left nasal cavity that bisects the nostril. All velocities shown are in vivo scaled and where applicable, only every fifth vector is displayed for clarity. The vector lengths denote in-plane velocity magnitude and the colour contour shows absolute velocity calculated from the two in-plane velocity components. Streamlines are drawn for visualisation purposes and are plotted with respect to only the in-plane velocities. In Figures

45–49 the velocity contour is capped at 6.0 m/s to aid visualisation of lower velocities. Data is unavailable in the small grey region at the nostril.

The velocity distributions through the nasal cavity during natural inspiration and expiration are shown in Figures 43a and b. Maximum in vivo inspiration and expiration velocities of 2.3 m/s and 3.2 m/s respectively were measured as the flow accelerates through the nasal valve. The nasal valve has been described to account for the majority of the total respiratory resistance to airflow. The concentration of high velocities in this narrow area on inspiration and expiration creates high levels of viscous shear resulting in such a high resistance to flow. On inspiration, the flow enters the main cavity on a steep vertical trajectory, which corroborates findings from several other studies in the literature (Proetz 1951; Wolf et al. 2004) both in magnitude and direction. Proctor for example stated "air passes vertically upwards through the anterior naris at a velocity of 2–3 m/s". Interestingly, a small current of air evident in Figure 43a detaches from the main flow stream and follows the anterior wall of the nasal cavity before separating and causing a small low velocity counter-rotating eddy in the superior anterior region. Flow separation and recirculation posterior of the nasal valve is common in the literature (J. T. Kelly et al. 2000; Park et al. 1997), however, the small detached current appears to be unique to this geometry. The main flow stream passes through the middle airway.

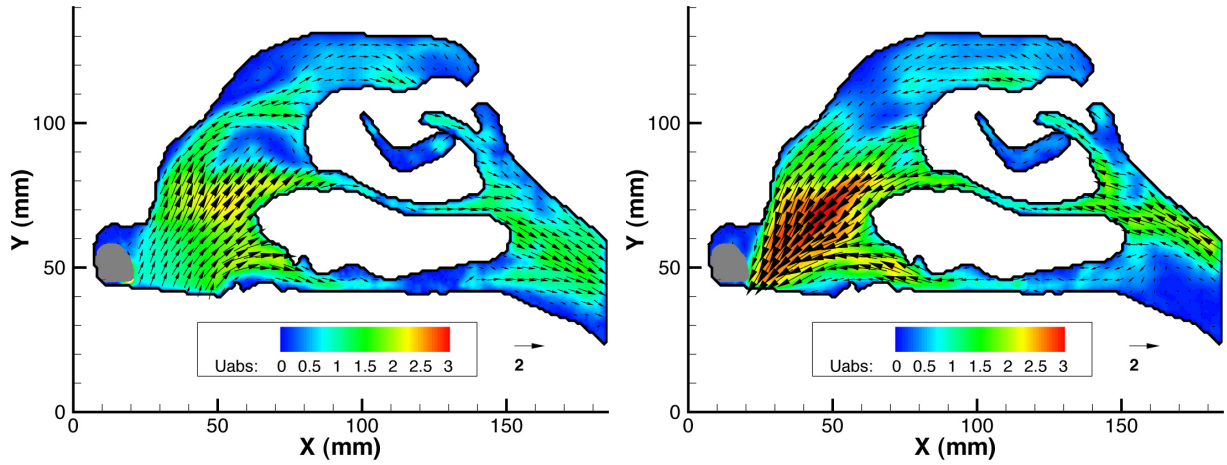

Figure 43. Velocity (m/s) maps during natural breathing (a) inspiration, (b) expiration

On expiration, the flow rising from the throat of the model converges on the roof of the nasopharynx, turning through the near 90° bend into the nasal cavity. Velocities reach 2.2 m/s and concentrate on the outside of the bend, whereas the flow through the nasopharynx on inspiration was more evenly distributed and contained a maximum velocity of 1.7 m/s. A spanwise vortex rotating in an anticlockwise direction is located on the floor of the nasopharynx in the low velocity region underneath the fast flowing stream. As

on inspiration, the main flow stream appears to pass through the middle airway. Also common to both inspiration and expiration are low velocities in the olfactory slit at the top of the nasal cavity. Low velocities in the olfactory region would suggest that odorant molecules are not delivered efficiently to receptors and olfactory response is hindered. Low velocities and recirculating of odorant molecules may actually improve olfactory response through increased residence time. Purging of the olfactory region is evident on expiration. Although a portion of the flow is not seen, flow separation evidently persisted in the nasal vestibule.

The results are not comparable with the results of Hopkins et al. (2000) and Kelly et al. (2000) from whom the geometry was obtained because it is the current author's opinion that the accuracy of the boundary condition imposed at the nostril in their measurements was questionable. Figure 44 shows a result from Kelly et al. with the contour of the face as it was interpreted in the current work overlaid in grey. It can be seen that the flow in Kelly et al.'s measurements originates from the anterior wall of the nasal vestibule instead of at the nostril. This inflow boundary condition directs inspiratory flow on a strongly horizontal path and is contrary to all other reports of inspired flow trajectories in the literature. Parallel and adjacent slices taken by Kelly et al. show the same horizontal trajectory in the nasal vestibule, giving evidence that flow was not directed on a natural path into the nostril and there is not simply a strong out of plane velocity component in Figure 44. A critique of the work by Hopkins et al. and Kelly et al. has not been found in the literature. Churchill et al. (2004) do, however, highlight that a general lack of consideration to physiological conditions is likely to be a large reason for inconsistent results reported by different studies. Nevertheless, the results in the current work are well supported by findings in the literature (Churchill et al. 2004; Doorly et al. 2008a; Wolf et al. 2004).

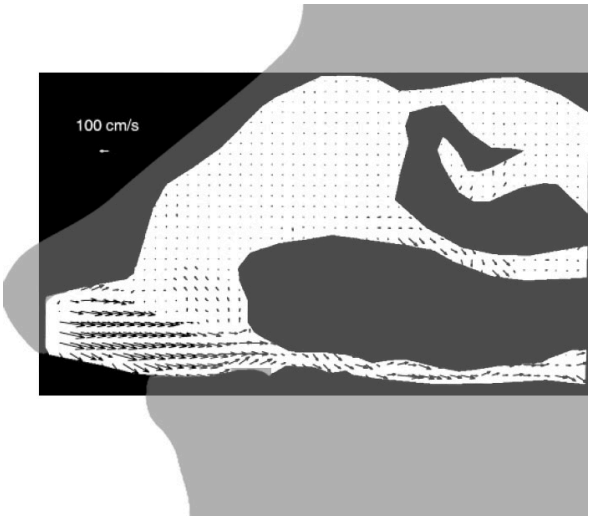

Figure 44. Velocity vector map from Kelly et al. (2000)

Figures 45–49 show the nasal cavity velocity maps with NHF cannula flows from 10–50 l/min. On inspiration, maximum velocities were consistently located in the cannula jet and ranged from 7.3 m/s at 10 l/min to 17.3 m/s at 50 l/min as shown in Table 14. Maximum measured velocities (m/s). At 10 l/min the inspired flow pattern is very similar to that of natural breathing, with the exception of the higher velocities in the jet and nasopharynx due to an increased lung flowrate. At 20 l/min an anticlockwise recirculating feature forms above the cannula jet, which grows in size and strength with increasing cannula flowrate. Even though cannula flowrates of 40 and 50 l/min (Figures 48 and 49) exceeded inspiratory demand, flow can still be seen to enter the nostril underneath the cannula by a means thought to be analogous to a jet pump. Excess flow is ejected from the eddy above the jet and exits over the prong. The main flow stream rises vertically as during natural breathing, but to a lesser extent. The angle of the cannula is such that the main flow stream is more concentrated through the middle airway. Low velocities in the olfactory region and on the nasopharynx floor persist. Separation occurs off the nasopharynx floor due a strong horizontal velocity component towards the posterior of the nasal cavity. Separation is less pronounced in this region at 40 and 50 l/min possibly because of larger static pressures in the nasopharynx due to increased flowrates, or perhaps a turbulent boundary layer forms and delays separation. The later hypothesis is fitting with the nasopharynx Reynolds numbers shown in Table 12. At 40 and 50 l/min cannula flow the Reynolds numbers were 3680 and 4060, respectively.

Table 14. Maximum measured velocities (m/s)

	Natural breathing	Total cannula flowrate (l/min)				
		10	20	30	40	50
Inspiration,	2.32	7.26	9.40	12.01	14.80	17.32
Expiration,	3.21	5.88	7.52	8.76	9.41	10.44

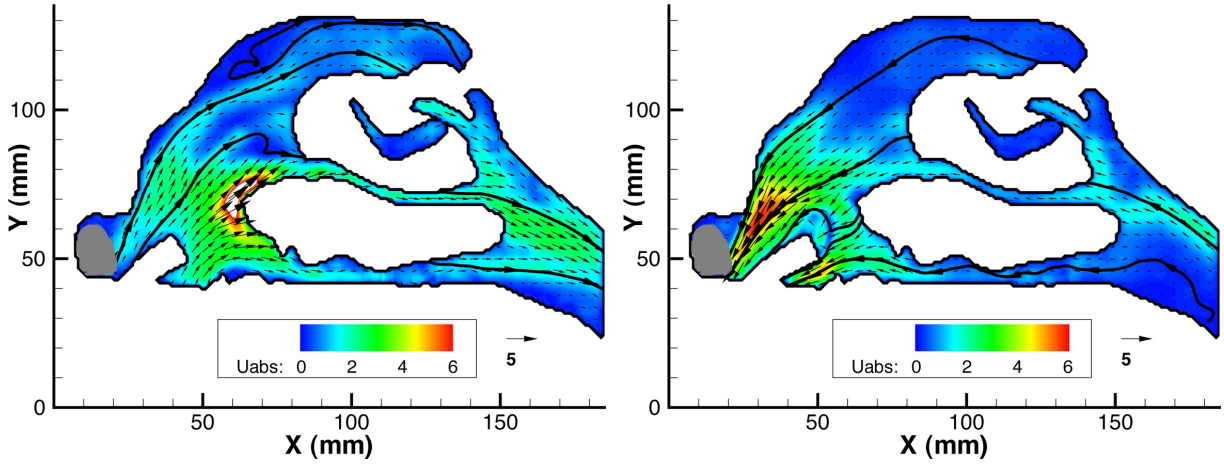

Figure 45. Velocity (m/s) maps with 10 l/min NHF flow (a) inspiration, (b) expiration

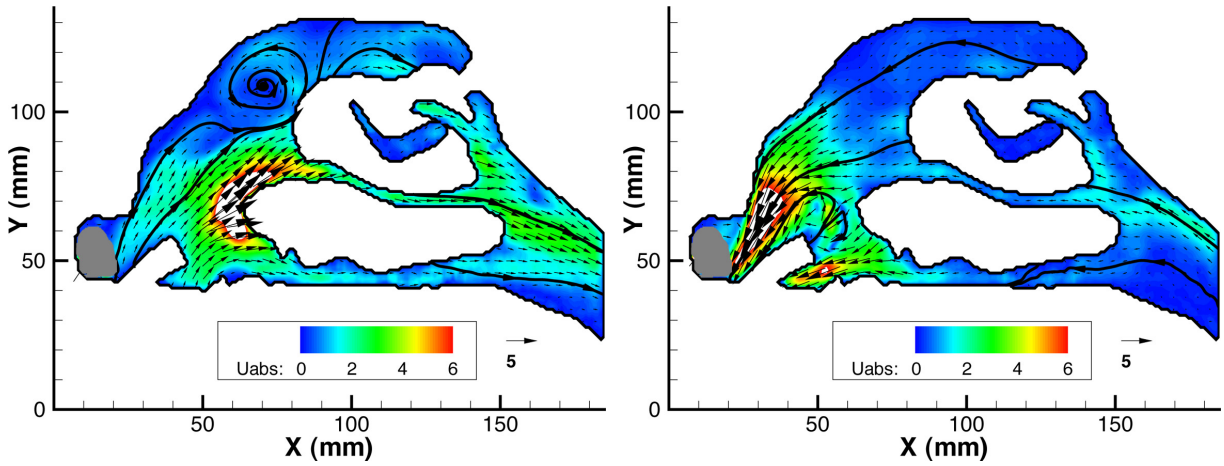

Figure 46. Velocity (m/s) maps with 20 l/min NHF flow (a) inspiration, (b) expiration

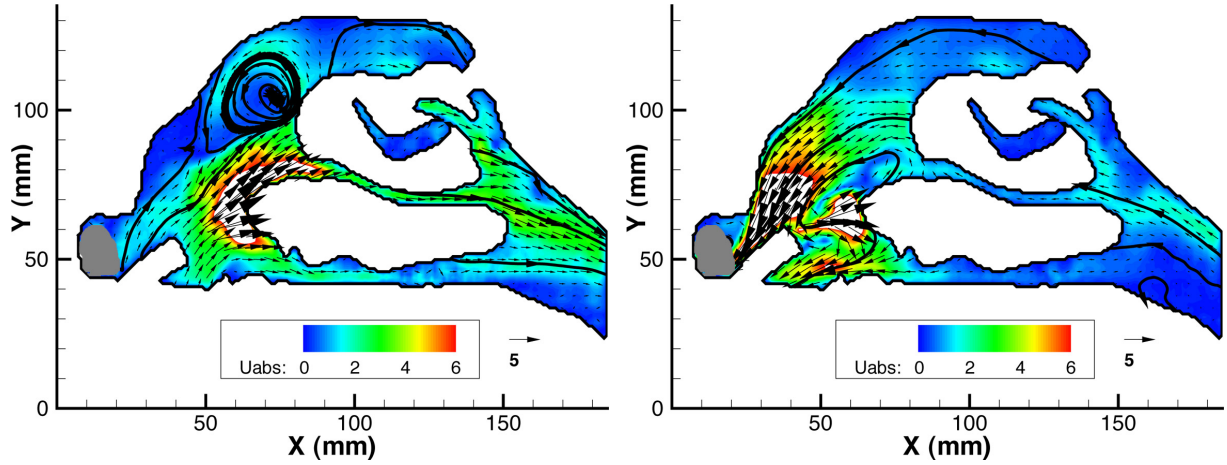

Figure 47. Velocity (m/s) maps with 30 l/min NHF flow (a) inspiration, (b) expiration

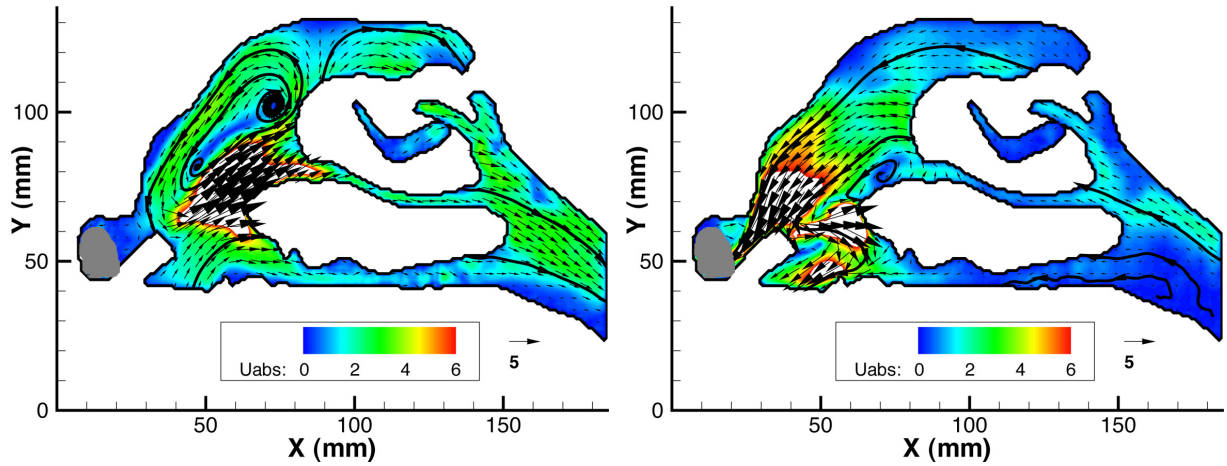

Figure 48. Velocity (m/s) maps with 40 l/min NHF flow (a) inspiration, (b) expiration

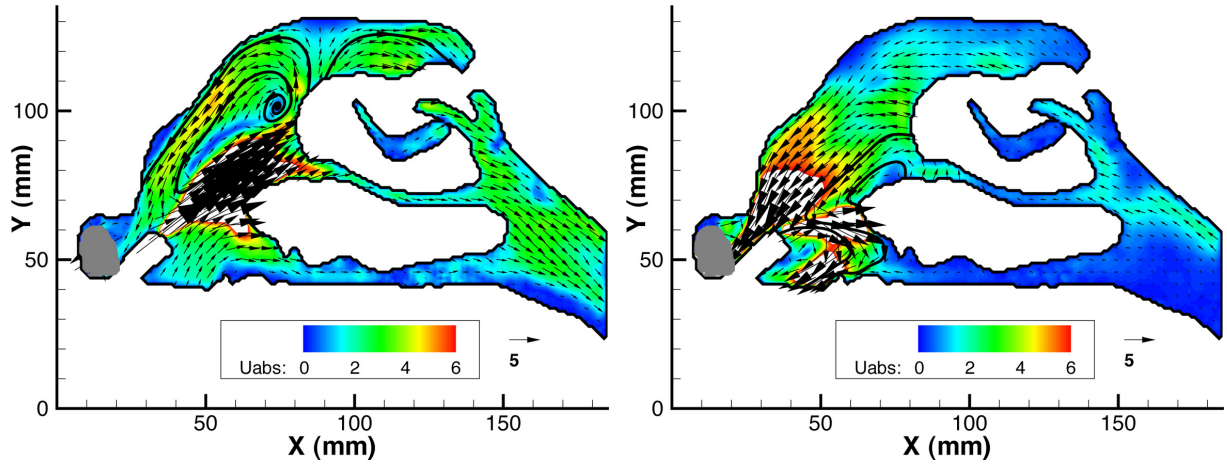

Figure 49. Velocity (m/s) maps with 50 l/min NHF flow (a) inspiration, (b) expiration

On expiration with NHF, the flow distribution through the nasopharynx and main cavity appear to be very similar to natural breathing regardless of cannula flowrate. Low velocities on the nasopharynx and main

cavity floors, and in the olfactory region remain, as well as high velocities on the nasopharynx roof and predominating flow through the middle airway. It will be shown in Chapter 5 that there are differences in the distribution of flow through each passageway; however, it is difficult to discern here through only one sagittal slice. The flow pattern in the anterior region of the nasal cavity is altered significantly with NHF. High velocities are concentrated in the nasal valve and nostril, where cannula flow is forced to turn 180 degrees by the expired volume to also exit through the area available between the cannula prong and nostril. The momentum required to turn the jet, narrowness of the passageways, and large velocity gradients creating high shear suggest there is a large pressure drop across the nasal valve with NHF. This resistance is thought to be largely responsible for the elevated airway pressures experienced clinically. At cannula flowrates of 10 and 20 l/min (Figures 45 and 46) the cannula jet turns upward, whilst at higher cannula flowrates the jet is turned in a clockwise direction to exit beneath the prong and a counter-rotating vortex above the jet is formed on the anterior end of the inferior and middle turbinates

4.5 Conclusions

This chapter presents the first PIV measurements in the nasal cavity with NHF and reveals for the first time the effect of NHF on nasal flow patterns. Planar-PIV measurements were successfully taken at steady flowrates representing peak expiration and inspiration during natural and NHF assisted breathing with cannula flowrates ranging from 10–50 l/min. Physiologically accurate flowrates were measured in vivo and applied in vitro using dimensional analysis and Reynolds number matching. A positive relationship was found between cannula and peak inspiratory flowrates, whilst peak expiratory flowrate was relatively independent of cannula flowrate. An anatomically accurate transparent silicone flow phantom was created from a ready-segmented nasal geometry obtained from CT images. Physiologically realistic conditions were replicated as closely as possible with the available nasal geometry by immersing the model in a reservoir to provide a free inflow boundary condition at the nostril on inspiration. A bend was lofted onto the nasopharynx to provide a semi-realistic flow profile into the nasal cavity on expiration.

Natural breathing flow patterns and magnitudes were corroborated by findings of other studies, such as: high velocities in the nasal valve; prevailing flow through the middle airway; low velocities in the olfactory region, and along the main cavity and nasopharynx floors; vertically rising inspired flow that separates off the anterior wall of the nasal cavity; and flow concentration on the roof of the nasopharynx during expiration. NHF was found to alter the flow magnitudes and patterns in the nasal cavity significantly.

Maximum inspiration and expiration velocities increased from 2.3 m/s and 3.2 m/s during natural breathing to 17.3 m/s and 10.4 m/s with a NHF flowrate of 50 l/min, respectively. Strong jetting from the cannula creates recirculating features that dominate the anterior flow pattern on both inspiration and expiration. Reversal of the jet's momentum on expiration and regions of high shear stress are expected to contribute to elevated airway pressures. The effect of cannula flow was less pronounced towards the posterior.

The methodologies and findings arising from this preliminary study formed the basis for and gave confidence to progressively more complex models of the nasal cavity and PIV measurements.

5 Steady Flow by Stereo-PIV

This chapter presents the second of three PIV measurement campaigns conducted in the current work. The methodologies developed in Chapter 4 are again implemented yet significantly developed. To avoid repetition, the reader is advised to consider all the methods and assumptions made in Chapter 4 to also be implemented here unless otherwise stated. Developments include: the use of stereo-PIV; model 2, which is more complete was implemented; the light sheet was traversed throughout the model to capture a full flow field, and additional measurements with the large size cannula.

5.1 Introduction

To date only planar-PIV had been used to measure flow patterns in transparent models of the nasal cavity. This chapter describes the first reported stereo-PIV nasal cavity velocity maps, with or without assisted ventilation flows. As discussed in section 3.4, planar-PIV is unable to resolve the out-of-plane velocity component and introduces perspective errors when projecting three-dimensional vectors onto a two-dimensional plane. The nasal cavity geometry is complex and thus the flow field was thought to be equally complex and three-dimensional. Stereoscopic PIV (stereo-PIV) was therefore implemented in order to resolve the transverse velocity component, which has in the past been assumed to be negligible with respect to velocities contained in a sagittal plane. Unlike in Chapter 4 where only one sagittal plane was investigated, in this campaign of measurements the light sheet is traversed through the entire nasal cavity to build a 3D picture of the flow. Model 2 superseded model 1 and offered improved boundary conditions and optical clarity. Again mouth-closed breathing was the focus of the current measurement campaign.

Measurements in steady flow conditions representing peak natural inspiration and expiration are repeated with stereo-PIV to capture the transverse velocity component, assess normal breathing patterns in another unique geometry, and provide a baseline for comparison with further flow pattern measurements with NHF. When the current campaign of measurements was undertaken in 2009, the large size cannula had

been recently made available and there was interest regarding the effect of the size of the prong on the flow pattern.

5.2 Experimental Setup

5.2.1 Flow Circuit

The nasal cavity phantom was installed in a recirculating flow system as shown in Figure 50, which is identical to the previous chapter but with the addition of a second camera in a stereoscopic arrangement. The reservoir was mounted on a translation stage consisting of two linear slides driven by a 1 mm pitch ballscrew and ballnut system connected to a digital caliper slide. With the cameras and laser securely fixed, this allowed the flow phantom within the reservoir to be traversed through the light sheet with a precision of ±5 μm. Traversing the laser and cameras with a stationary flow phantom was considered; however, was rejected because stereo-PIV is highly sensitive to the alignment of the light sheet and cameras, which would need to have been traversed independently resulting in an accumulation of uncertainties.

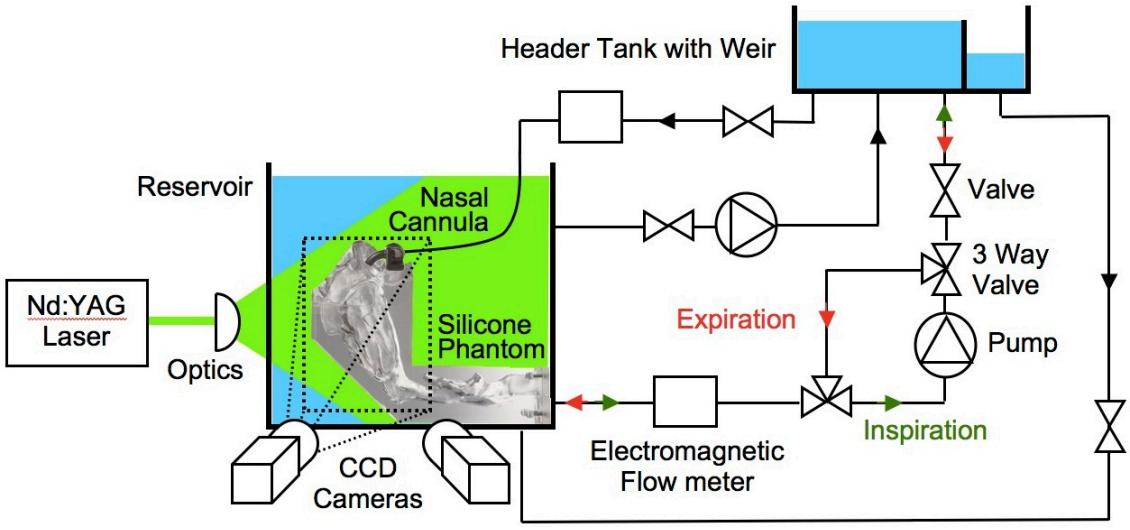

Figure 50. Schmatic of the experimental facility

Since model 2 included both sides of the nasal cavity, unlike in the case of model 1, it was unnecessary to make any assumptions on the flowrates through either side of the nasal cavity and at what location of the nasal cycle the nasal geometry represented. Full physiological flowrates were applied at the throat and the flowrates through each nostril governed simply by the respective resistances imposed by the geometry

itself as in a real nose. Model 2 provided the most physiologically realistic inflow conditions to the nasal cavity of any experiment conducted to date. On inspiration, the shape of the external nose and a local contour of the face were included, which gave a physiologically accurate free boundary condition at the nostrils when immersed in the reservoir. On expiration, the upstream pharynx and larynx geometries included in the model created a realistic entry profile to the nasopharynx. Nevertheless, a fully developed profile was applied to the throat of the model using the same length of straight pipe used previously ($L = 40D$). Instead of the simplified cannula prong molded from plastic tubing employed in Chapter 4, scaled rapid prototyped models of the nasal cannulae (see Figure 21 on page 51) were now used. The abrupt changes in flow direction within the cannula manifold negated the use of fully developed inlets.

5.2.2 Particle Image Velocimetry

The left and right cameras were positioned at angles of 20.5° and 19.5° (separated by 40.0°), respectively, and had an average magnification of 0.145 mm/pix. The left camera was set with a f-number of 8, whilst the right camera in forward scatter afforded a smaller aperture with an f-number of 11. Nevertheless, each camera was treated with a Scheimpflug angle such that focus was maintained across the width of each image. The camera calibrations were performed using the method described in section 3.4. Although the distance between the cameras and laser plane was constant, the distance between the 8 mm thick acrylic reservoir wall ($n = 1.49$) and the cameras was unique for each traverse. Because the cameras viewed through the acrylic at an angle without the use of viewing prisms (Prasad & Jensen 1995), the optical distortion at each traverse location was unique, necessitating discrete camera calibrations. Three calibration images were taken at 1 mm spacing for each camera and traversed measurement location. Self-calibrations were performed to correct for small misalignments of the target plate with the laser sheet. Mask images were created using the method described in section 3.3 and 3.4. A sagittal laser plane was anticipated to contain the highest two velocity components and was therefore used to minimise the loss of seeding particles.

The particle images were divided into 80×80 pixel^2 interrogation regions and ensemble correlation averaging performed across 100 image pairs to yield time averaged, mean velocity fields. A grid spacing of 0.75 mm was used, giving an average overlapping factor of 75%, and iterative window refinement was applied with a final interrogation window size was of 40 × 40 pixel^2. Window displacement and deformation based on the local velocity gradient was also applied. The maximum velocity for each

traversed measurement plane was unique and required time delays ranging between 80 and 1,900 μs to maintain a maximum in-plane displacement of approximately 10 pixels. An overview of the relative PIV parameters is given in Table 15.

Table 15. Table of PIV Parameters for steady flow stereo-PIV measurements

Nasal cavity model	Scale	1.55 : 1
	Dimensions (H × W × D)	250 × 190 × 70 mm
	Material	Silicone (Sylgard 184)
Flow	Liquid	61% glycerin, 39% water
	Properties at 25°C	η = 1.422, μ = 9.27×10^{-3} kg/ms, ρ = 1154 kg/m^3
	U_{max}	20.8 m/s
Calibration target	Dimensions (H × W × D)	200 × 200 × 10 mm
	Grid spacing	5 × 5 mm
	Marker diameter	2.5 mm
Seeding	Type	Hollow glass spheres
	Diameter	20 μm
	Density	1.1 g/cm^3
Laser	Type	Nd:YAG, dual cavity
	Max power	120 mJ
	Pulse width	9 ns
	Thickness	2 mm
Cameras	Type	CCD
	Resolution	1600 × 1200, 8 bit
	Pixel size	7.4 × 7.4 μm
Image Properties	Lens focal length	60 mm
	Viewing angles	-20.5° & 19.5° (left & right)
	Lens aperture	f = 8 & 11
	Average magnification	0.145 mm/pixel
	Region of interest	125 mm × 170 mm
	Maximum particle displacement	12 pix
Stereo PIV analysis	Spatial resolution	40 × 40 pixel^2
		5.8 × 5.8 mm^2
	Grid spacing	1.5 mm
		10 pixel

Volume Resolution (full nasal cavity)	Number of vectors	114 x 84 x 19
	Rectangular domain dimensions	20 × 168 × 54 (I × J × K)
	Number of sagittal planes	19
	Sampling resolution	1.9 × 1.9 × 0.83 mm (X × Y × Z)

5.3 Description of the Measurements

The same physiological flowrates obtained from preliminary in vivo flow measurements in the Chapter 4 and presented in Table 12 on page 90 were also implemented in this chapter at an equilibrium temperature of 25°C. The range of conditions and regions of interest (ROI) for which 65 stereo-PIV measurement planes were acquired are overviewed in Figure 51. For natural breathing, the phantom was traversed to capture measurements on 19 sagittal slices throughout the entire nasal cavity at 2.5 mm increments during both inspiration and expiration as illustrated in Figure 52. The series of traversed 2D-3C time-averaged velocity maps obtained were reconstructed into three-dimensional, three velocity component (3D-3C) volumes using a kriging interpolation algorithm (Davis 1986) (Davis 1986). This enabled comparison of the 3D flow fields between the two choanae.

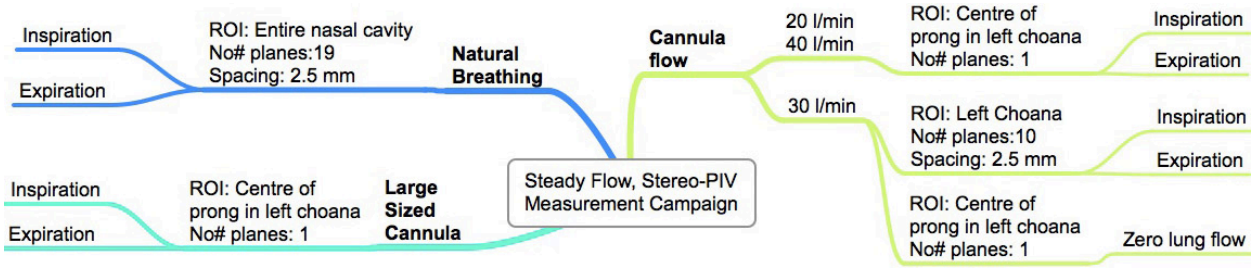

Figure 51. Overview of conditions measured by stereo-PIV and their respective regions of interest (ROI).

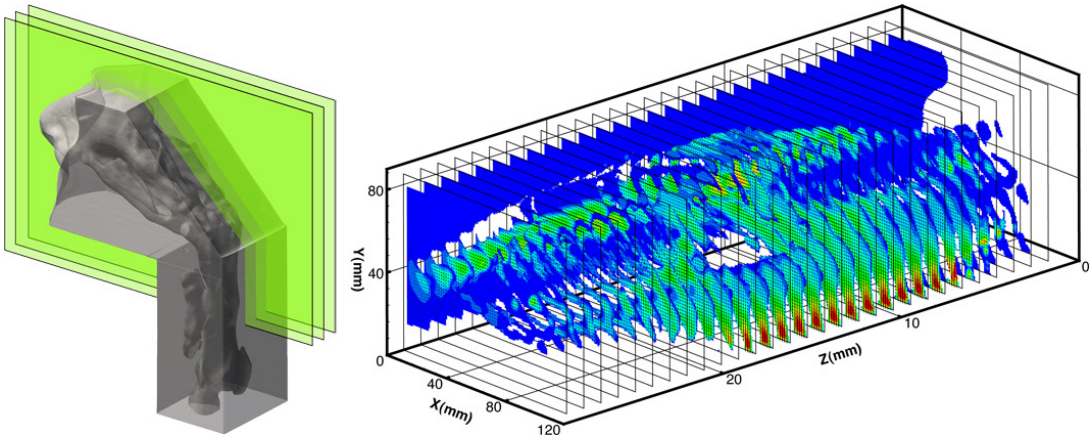

Figure 52. Schematic showing (a) the orientation of parallel sagittal measurement planes and (b) their distribution throughout the nasal cavity

The effect of cannula flowrates on the flow field was investigated at 20, 30 and 40 l/min. A cannula flowrate of 30 l/min is a typical clinical setting and was selected as the point of reference for which the flow fields of other flowrates and NHF conditions could be compared. The medium sized cannula was also considered as neutral point of reference The cannula was positioned with the cannula's manifold resting flat on the upper lip and sitting against the base of the nose such that the prongs protrude into the nares as much as possible. At 30 l/min, 10 measurement planes spanning the left choana at 2.5 mm spacing were acquired during peak inspiration and expiration. Comparisons between the natural and NHF assisted breathing flow fields could therefore be made over the reconstructed volume of the left choana. The remaining measurement conditions were limited to the sagittal plane that coincided with the centre of the prong and left choana because the greatest region of interest included the jet exiting from the prong. Recordings were captured with zero lung flow and with the large cannula during both inspiration and expiration. The measurement conducted with zero lung flow simulated the flow pattern in the nasal cavity produced by NHF at the zero flow transitions during tidal breathing.

5.4 Results and Discussions

All velocities shown are in vivo scaled and where applicable, only every third vector is displayed for clarity. The vector lengths denote in-plane velocity magnitude and unless otherwise stated the colour contour shows absolute velocity calculated from all three components by Equation 16. Figures 53 and 60 are reconstructed velocity volumes of the entire nasal cavity and left choana, respectively. Figures 54, 55, 61, and 63–69 are velocity maps through one sagittal cross-section of the left nasal cavity that bisects the

nostril and cannula. Velocities over 6 m/s have been omitted to enhance the visualisation of lower velocities. Streamlines shown in Figure 53 are of the measured 3D flow, whereas the streamlines in the 2D velocity maps shown in Figures 61, 63, 65–69 are 2D projections from the only the in-plane components to aid visualisation of the flow direction in low velocity regions where the vectors are short.

$$u_{abs} = \sqrt{u^2 + v^2 + w^2}$$ **Equation 16**

5.4.1 Natural Breathing

Figure 53 shows the distribution of velocities throughout the nasal cavity for natural inspiration and expiration. For both conditions, the maximum velocity was located in the small cross-sectional area of the nasal valve. Maximum velocities of 2.1 m/s and 2.8 m/s were obtained in the left and right nasal valves, respectively, on inspiration and 3.2 m/s and 3.8 m/s on expiration. These values compared well with the maximum inspiration and expiration velocities of 2.3 m/s and 3.2 m/s measured in model 1. The highest velocities occurred in the slightly larger right nasal valve, revealing a bias of flow through the right nasal cavity. Both nasal cavities were exposed to the same inlet and outlet pressures, so the cumulative resistance of the left nasal cavity must have been higher. There are three notable explanations for the higher resistance in the left nasal cavity. First, the smaller cross-sectional area of the left nasal valve poses a greater resistance. Secondly, Figure 18 on page 48 shows a rapid expansion into the main cavity following the left nasal valve and a much more gradual gradient for the right. On inspiration, this rapid expansion created a separation region that is prominent in Figure 54a and is visibly larger in the left nasal cavity in the second anterior cross-section of Figure 53a. It can therefore be suggested that the pressure loss associated with this flow separation is larger in the left nasal cavity. The rapid change in cross-sectional area in the left nasal cavity will also create a higher resistance on expiration, however, to a lesser extent due to the favourable pressure gradient. Indeed the difference in maximum velocity between the left and right cavity on expiration (0.6 m/s) is less than the difference on inspiration (0.7 m/s). Thirdly, the smaller cross-sectional area and similar surface area in the left nasal cavity 4.6–8.2 cm from the nostrils create greater levels of viscous shear.

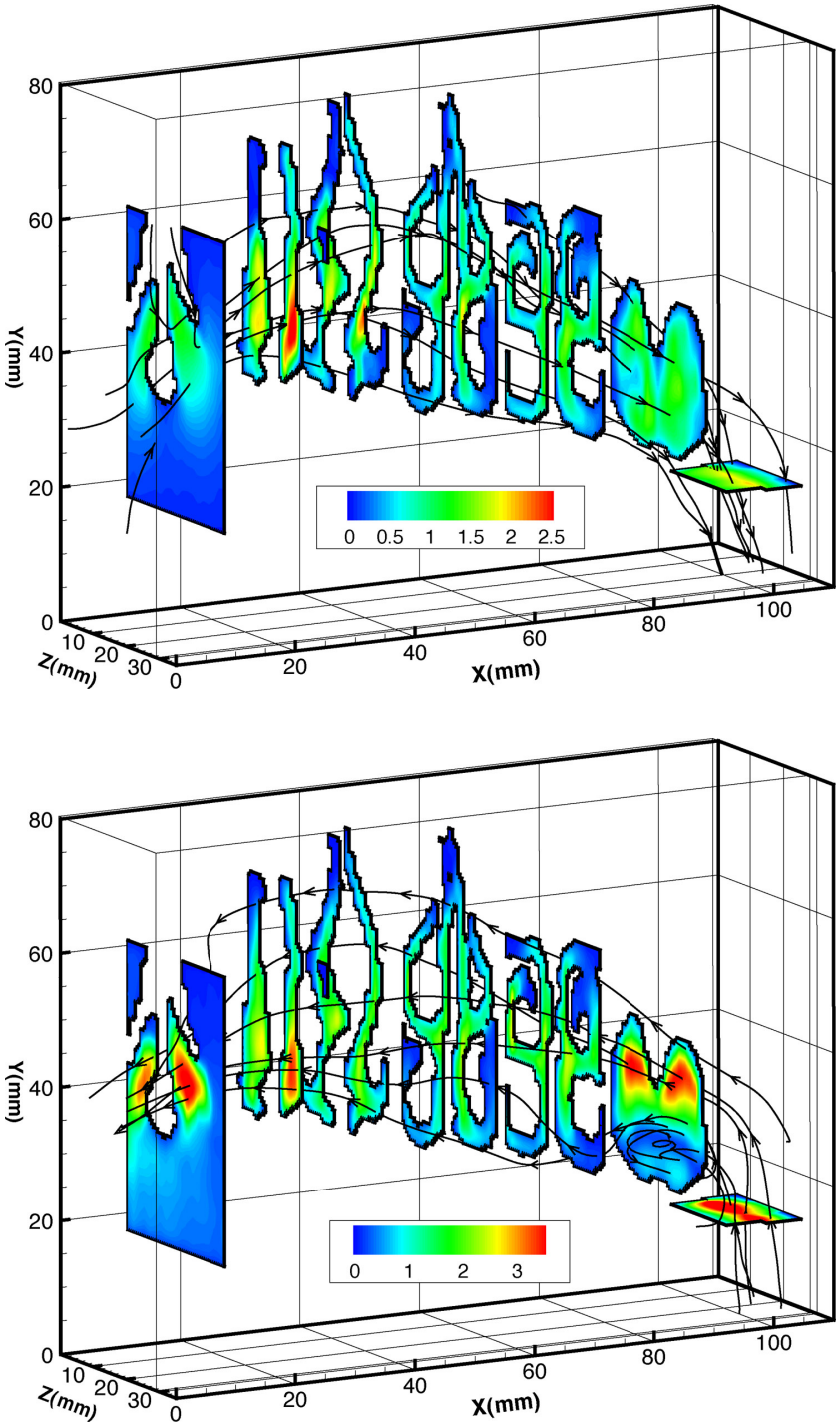

Figure 53. Coronal cross-sections showing the reconstructed 3D velocity field and in vivo scaled absolute velocities (m/s) on a) inspiration and b) expiration.

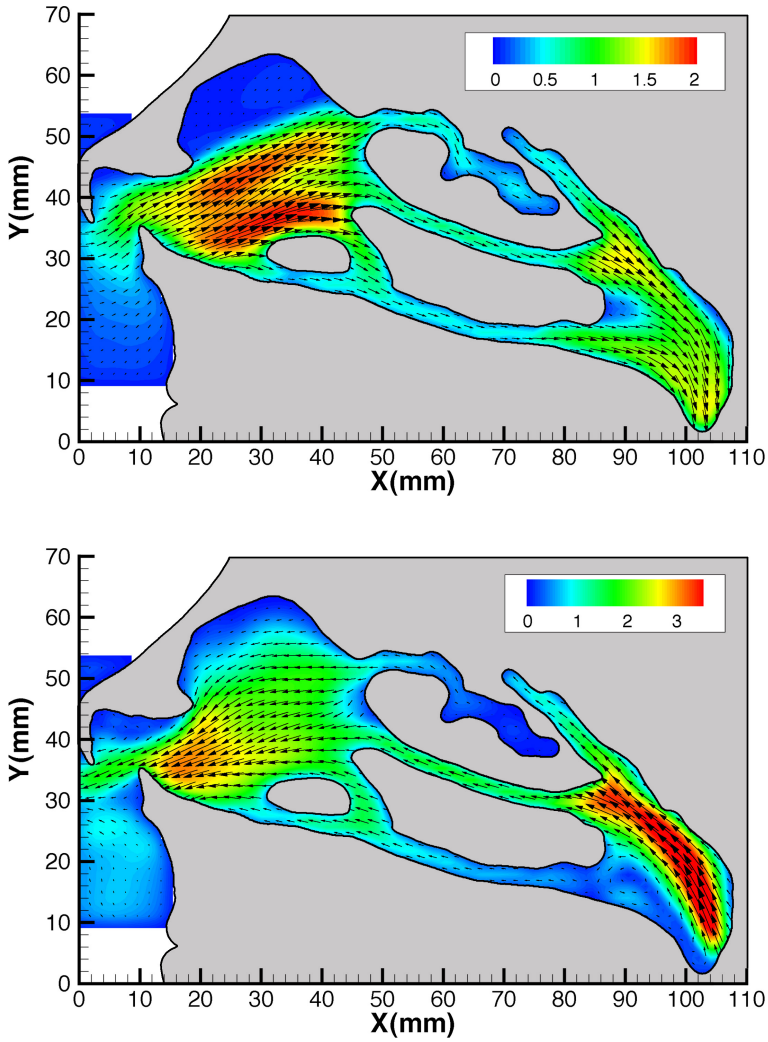

Figure 54. Absolute velocity (m/s) maps through a mid-sagittal cross-section of the left nasal cavity during unassisted breathing on a) inspiration and b) expiration.

Common to both inspiration and expiration were low flows in the inferior meatus and olfactory region as well as a large proportion of flow passing through the middle airway and along the nasal septum, as also witnessed in Chapter 4. It can be seen in Figure 53 that the flow distributions within each choana in the middle coronal cross-section are near identical. On expiration (Figure 54b), a high velocity region on the nasopharynx roof reached 4.2 m/s as the fast flow rising vertically from the velopharynx constriction concentrated on the outside of the near right angle bend from the laryngopharynx. This was significantly faster than the 2.2 m/s measured at the same location in model 1, likely because of the absence of the laryngopharynx geometry in model 1. It was also notably higher than the maximum velocity in either of the nasal valves, which was not surprising given that the cross-sectional area of the velopharynx was less than the combined nasal valve areas. All experimental studies to date have reported the maximum velocity to occur in the nasal valve but each has failed to include accurate velopharynx and nasopharynx geometries. A

low velocity region on the nasopharynx floor recirculates due to viscous shear from the superior flow stream. The expired flow tends to remain superior through the nasal cavity with most of the flow passing through the middle airway and along the nasal septum. In contrast, the flow through the nasopharynx and main cavity on inspiration is distributed vertically more evenly. Inspired flows in the anterior region travel on an upward trajectory, like in model 1, however, the gradient is less steep. This could be a result of the less accurate inflow boundary condition in model 1 or could simply be a result of the anatomical differences between models. The flow separation following the nasal valve in model 2 is more distinct and causes an anticlockwise eddy in the superior region. Air is drawn into the nostrils from wide angles on inspiration and is expired as a horizontal stream of air.

Figure 55 shows the out-of-plane velocity component as the colourmap with positive velocities out of the page. It can be seen that the out-of-plane velocities in the nasal valve are significant and reach up to 36% of the absolute velocity magnitude. Secondary flow is visible in the nasal valve on both inspiration (Figure 55a) and expiration (Figure 55b). Lateral velocities are particularly high at the entrance to the nasopharynx on expiration where the flow has been disturbed by the irregular shape of the laryngopharynx upstream. Figure 56 shows the secondary flow in a reconstructed coronal velocity map through the nasopharynx, where the vectors denote in-plane velocities and the colour contour shows the x velocity component (positive into the page). Secondary flows are induced by the curvature of the nasopharynx, which leads to a centripetal acceleration of the flow toward the posterior wall, a radial pressure gradient and high circumferential velocities. Despite the curved nature of the nasopharynx, Dean vortices (Dean 1928) were absent. The strength of secondary flows are characterised by the Dean number, κ (Equation 17) and the curvature ratio $\delta = a/R$, where a and R are the cross-sectional and curvature radii, respectively. The nasopharynx hydraulic diameter was 18.1 mm and the radius of curvature was estimated to be 14.8 mm (Figure 57), giving a Dean number of 1660. The magnitude of the secondary flow is therefore very high, which is evident in Figure 56. Buchmann (2010) found Dean vortices within an asymmetric carotid artery geometry at Re = 800, δ = 0.104 and κ = 775. The nasopharynx, however, is strongly curved (δ = 0.611) and because the elbow is short the secondary flow may not have reached its fully developed state. Berger et al. (1983) states that in cases where δ is not << 1 the axial flow can separate from the inner bend for even very low Reynolds numbers (~10) and create an entirely different flow pattern from small-Dean number flow. The Reynolds number in the nasopharynx in Figure 56 was 2130 and flow separation and recirculation on the nasopharynx floor are clearly visible in Figures 53b and 56. Furthermore, the disturbed

flow profile entering the nasopharynx differs from the fully developed flows applied to curved sections in other studies where Dean vortices were present (Berger et al. 1983; Buchmann 2010).

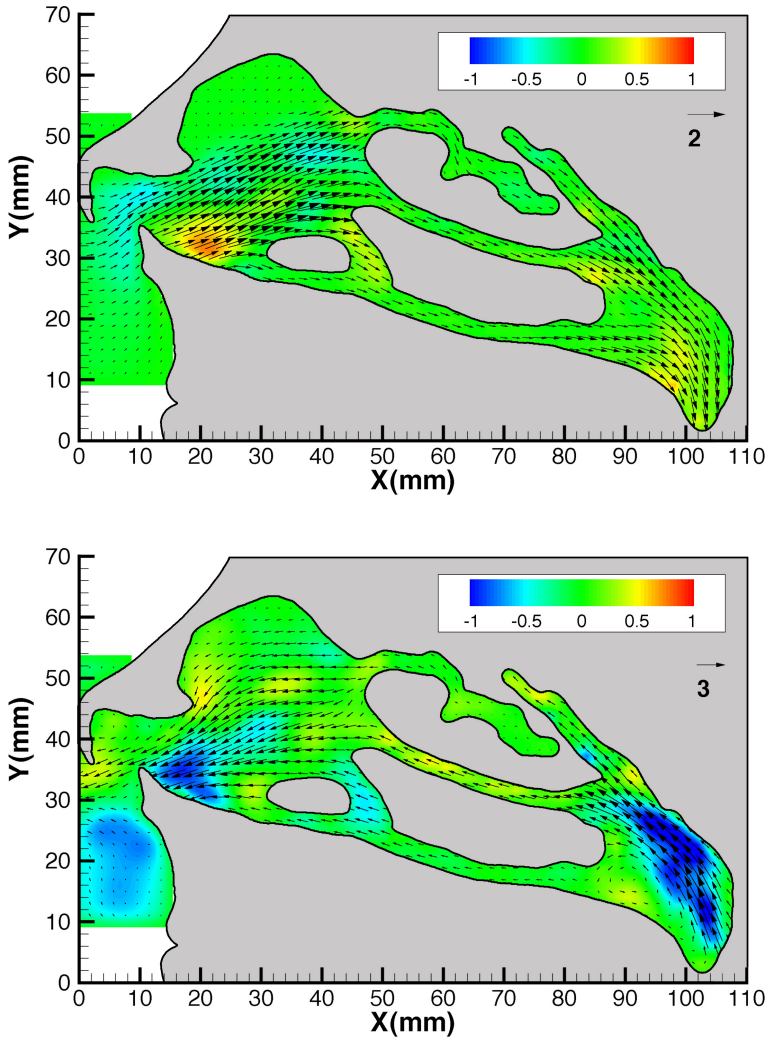

Figure 55. Orthogonal velocity (m/s) component contour during unassisted a inspiration and b expiration (velocities are positive out of the page)

It can be seen in Figure 55 that the out-of-plane component is small in the narrow meati, as they tend to laminate the flow (Churchill et al. 2004). Velocities in the lateral direction are generally the smallest component, and a sagittal laser plane should indeed be used to minimise the loss of seeding particles. To check the validity of the acquired velocities, the area and average velocity of the nasopharynx cross-section shown in Figure 56 was calculated to be 531 mm^2 and -0.92 m/s, respectively. This gave an area averaged flowrate estimate of 29.4 l/min in the expiratory direction, which compared well with the flowrate of 32 ±1.5 l/min indicated on the flowmeter during experiments and gave confidence in the accuracy and correct dimensional scaling of the measurements.

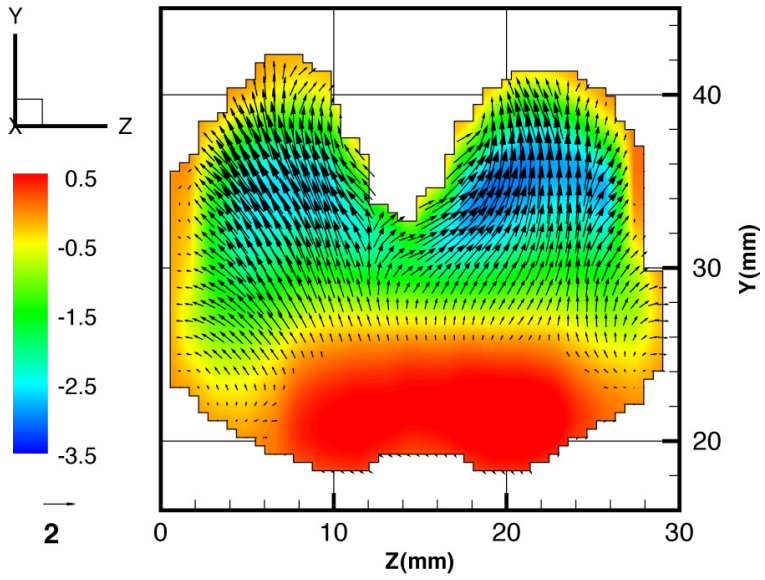

Figure 56. Velocity map through a coronal cross-section of the nasopharynx during natural expiration (where the vectors denote in plane velocities and the colour contour shows the x velocity component (negative out of the page)

$$\kappa = \frac{2a\bar{u}}{\upsilon}\sqrt{\frac{a}{R}} = 2Re\sqrt{\delta} \qquad \textbf{Equation 17}$$

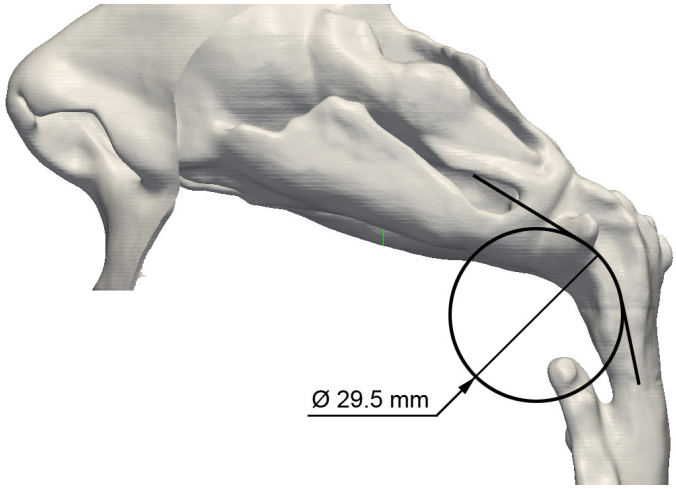

Figure 57. Illustration of the nasopharynx radius of curvature estimation

Figures 58 and 59 illustrate the variations of the maximum absolute, *u, v, w* and average velocities versus distance from the nostrils to give a simplified and more global illustration of the flow through the nasal cavity on inspiration and expiration, respectively. The schematic cross-sections of the nasal cavity shown above the curves give an indication to the geometry at the corresponding distal distance. Further to Figure 55, it can be seen that the *x* velocity component makes up the majority of the absolute velocity throughout the nasal cavity with the exception of the nasopharynx where the flow turns sharply in a vertical (y)

direction towards the lungs. On inspiration, Figure 58 shows the high velocities exiting the nasal valve dissipating over the main nasal cavity and the *v* and w components are again seen to decrease as the turbinates laminate the flow (Churchill et al. 2004). Towards the rear of the nasal cavity the maximum velocity approaches approximately twice the cross-sectional average, which is more representative of a more developed Poiseuille flow profile. Elad et al. (2006) describe the importance of wall shear stress on the health of the nasal epithelium, mucociliary clearance and exchange processes at the wall, and present results showing large spatial variations in wall shear stress. The maximum velocities are high relative to the average velocity in the nasal anterior, and together with the velocity plots suggest there are indeed extremes of both high and low wall shear stress. The most notable feature of the velocity distribution through the nasal cavity on expiration shown in Figure 59 is the relatively constant maximum velocity around the turbinates. The narrow passages appear to restrict the maximum velocity to approximately 2.5 m/s, which would encourage flow over a greater surface area of the nasal cavity and promote exchange processes at the wall.

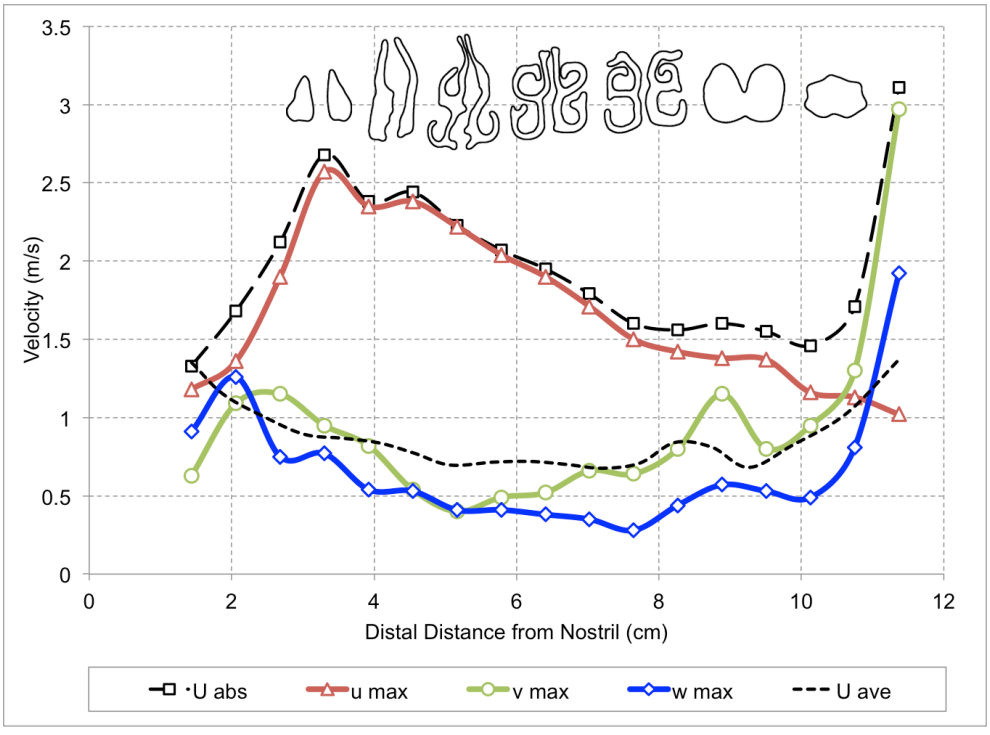

Figure 58. Variations of the maximum absolute, *u*, *v*, *w*, and average velocities through the nasal cavity versus horizontal distance distal of the nostrils during natural breathing inspiration.

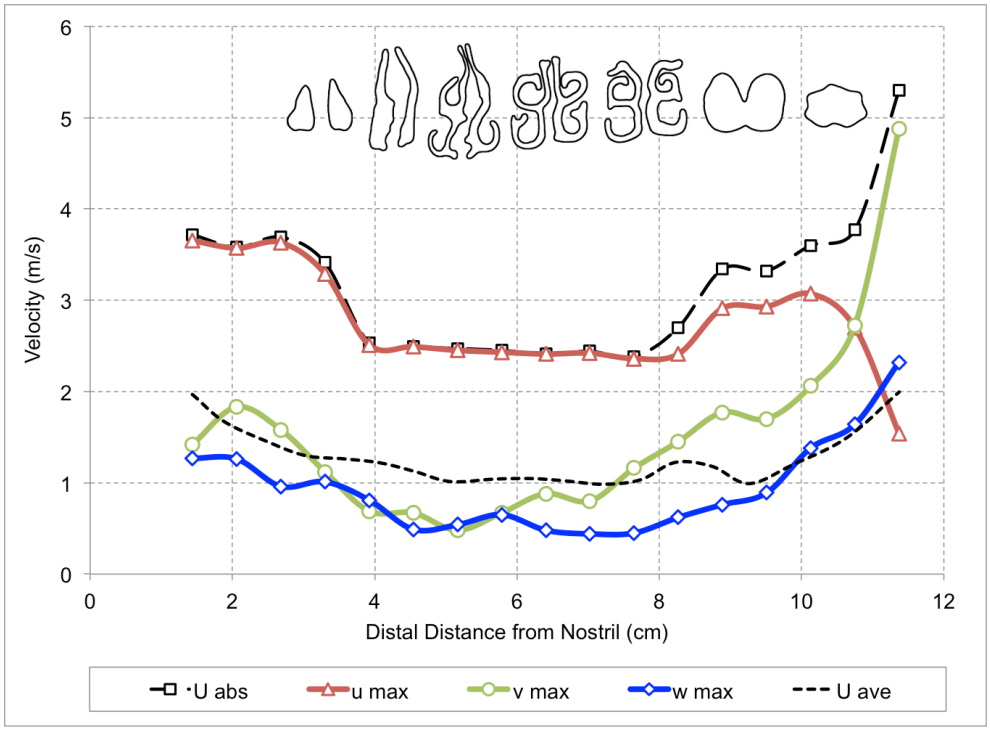

Figure 59. Variations of the maximum absolute, *u*, *v*, *w*, and average velocities through the nasal cavity versus horizontal distance distal of the nostrils during natural breathing expiration.

5.4.2 Cannula Flow

The reconstructed inspiration and expiration velocity fields through the left choana with a cannula flowrate of 30 l/min are plotted in Figure 60 on seven coronal planes and one semi-translucent sagittal plane. Inspiration velocity maps on one sagittal plane for cannula flowrates of 20, 30 and 40 l/min are shown in Figure 61. The cannula jet passes through the upper portion of the nasal valve, separates from the anterior wall at the same location as naturally inspired flow, and strengthens the eddy in the anterior superior region. The rotational speed of this vortex increased with increasing cannula flowrate and, unlike in model 1, where the vortex grew in size with cannula flowrate, here the vortex was confined to the recess posterior of the nasal valve. A second counter-rotating vortex that was not previously observed existed at the anterior end of the middle turbinate below the jet. This vortex consistently spanned the available height underneath the cannula, and at flowrates of 30 and 40 l/min ejected flow out through the nostrils below the prong, whilst flow was entrained into the nasal cavity from above the cannula. Air entrainment, and the fact that it still occurs when cannula flowrate exceeds peak inspiratory demand, is of particular interest clinically because room air dilutes administered levels of humidified and oxygen blended medical gas.

With the cannula resting on the upper lip, the angle and location of the prongs was such that the main flow stream remained towards the cavity roof at same angle as with natural inspiration. Inspired flow with NHF is, however, more concentrated on this upwards path. At a total cannula flowrate of 30 l/min and a single prong area of 15.9 mm^2 the theoretical average velocity across the prong is 15.7 m/s. The maximum measured velocity in the jet at 30 l/min was 17.0 m/s. Maximum velocities at 20 and 40 l/min were 11.5 m/s and 20.8 m/s, respectively. Figure 60a shows inspired flow to pass high through the nasal cavity and exit the nasal cavity attached to the nasopharynx roof. Figure 62 illustrates clearly on one coronal cross-section that this is a modification to the natural breathing pattern where flows are more evenly distributed and prevail through the middle airway. The maximum velocities in the nasopharynx were 2.2, 3.7, and 4.9 m/s at cannula flowrates of 20, 30 and 40 l/min, which were notably higher than 1.6 m/s during natural inspiration. At a cannula flowrate of 40 l/min flow separation and subsequent recirculation are evident off the posterior end of the inferior turbinate in Figure 61c.

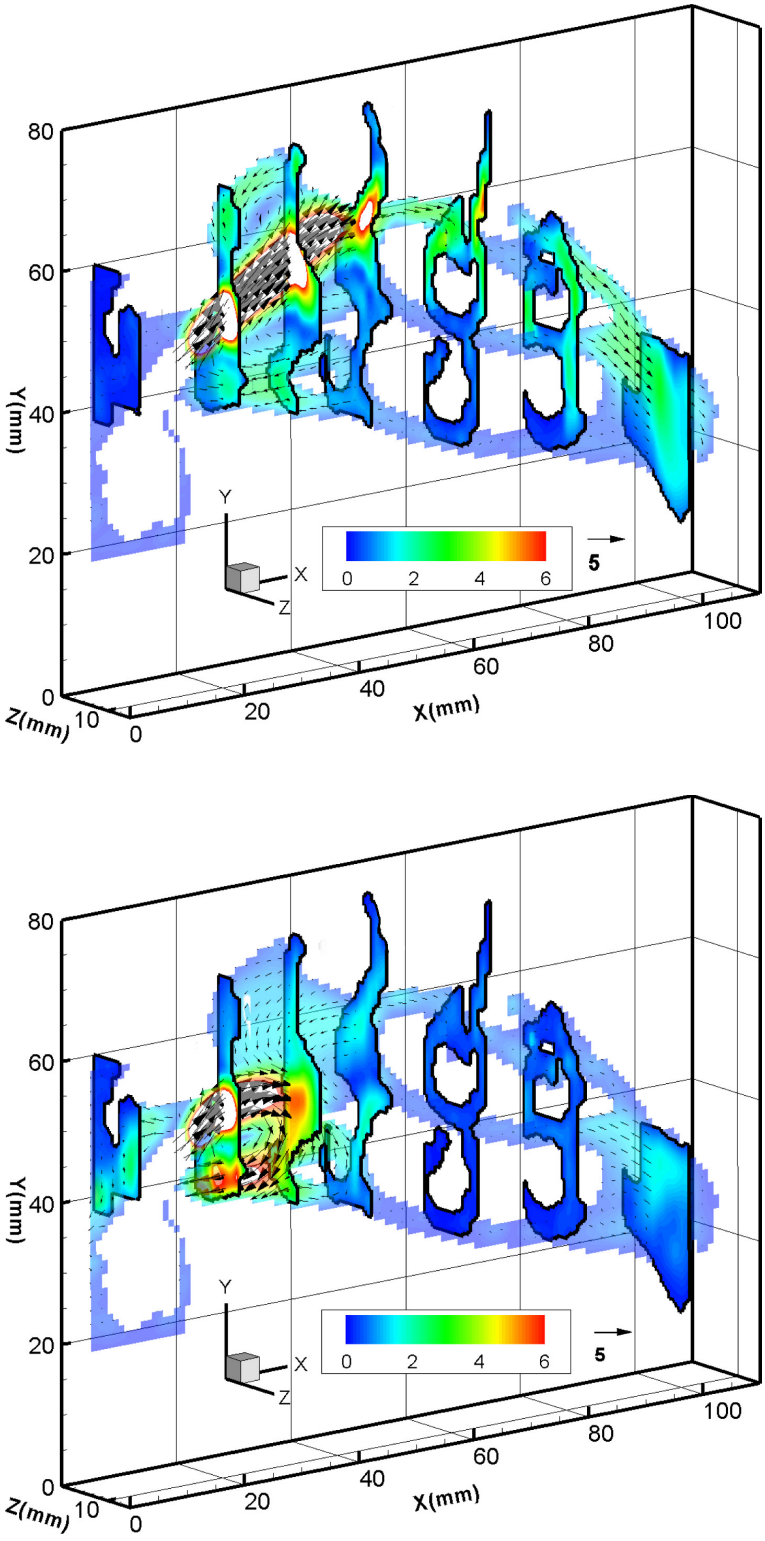

Figure 60. Coronal cross-sections showing the reconstructed 3D velocity field and in vivo scaled absolute velocities (m/s) on a) inspiration and b) expiration with 30 l/min cannula flow

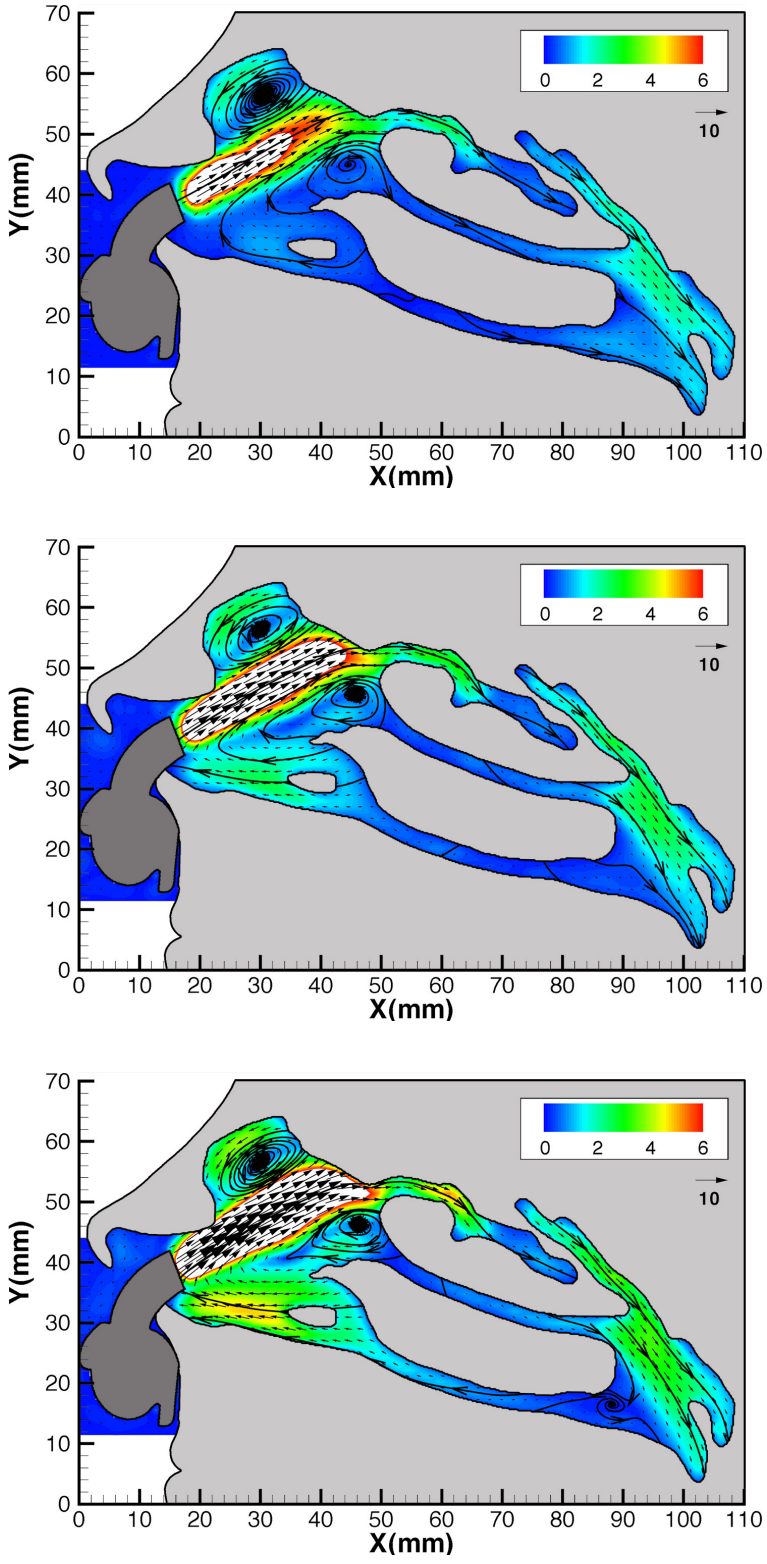

Figure 61. Absolute velocity (m/s) maps through a mid-sagittal cross-section of the left nasal cavity during inspiration with (a) 20 l/min, (b) 30 l/min and (c) 40 l/min cannula flow.

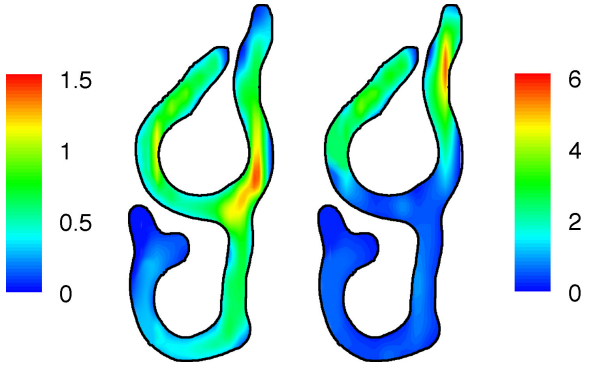

Figure 62. Absolute velocity (m/s) contours on a coronal cross-section of one half of the nasal cavity during (a) natural inspiration and (b) with 30 l/min cannula flow.

The flow pattern on expiration with a cannula flowrate of 30 l/min is shown through the left choana in Figure 60b, and compared with cannula flowrates of 20 and 40 l/min in Figure 63. High velocities were concentrated in the nasal valve and nasal vestibule, where cannula flow was forced to turn 180 degrees by the expired volume to additionally exit through the area available between the cannula prong and nostril. This flow pattern was also present in Chapter 4, however, is observed more distinctly here and the jet curls clockwise underneath the prong for each flowrate. The penetration depth of the jet into the main cavity increases with cannula flowrate, although the radius of curvature is relatively constant. The maximum absolute velocities measured at 20, 30 and 40 l/min were 11.1, 15.1 and 19.8 m/s, which correspond well with the velocities measured on inspiration. In addition to the vortex in the centre of the jet's retreat, a second counter-rotating vortex occurs on the anterior superior end of the inferior turbinate at cannula flowrates of 30 and 40 l/min. A vortex in the same location was observed on inspiration; however, was rotating in a clockwise direction, whilst on expiration the rotation is anticlockwise. Onset of this second vortex in model 1 didn't occur until 40 l/min, and as also evident in Figure 63, increased in strength with cannula flowrate.

The flow profile in the nasopharynx is largely unmodified by NHF, with flow remaining attached to the nasopharynx roof and recirculation on the nasopharynx floor persisting. Note that the velocities in the nasopharynx are lower with NHF because peak expiration flowrate is lower and expiration time is longer. Akin to inspiration, expired flow with NHF remains high through the nasal cavity, whereas, the flow was more evenly distributed during natural expiration as shown by Figure 64. Also common to both inspiration and expiration with NHF are low velocities through the inferior half of the nasal cavity and the presence of counter-rotating vortices (despite being in different locations) that promote mixing. Thinner boundary

layers through the nasal valve and meati are visible in Figures 61 and 63, indicating increased shear stress and therefore increased flow resistance and moisture and heat transfer in these regions.

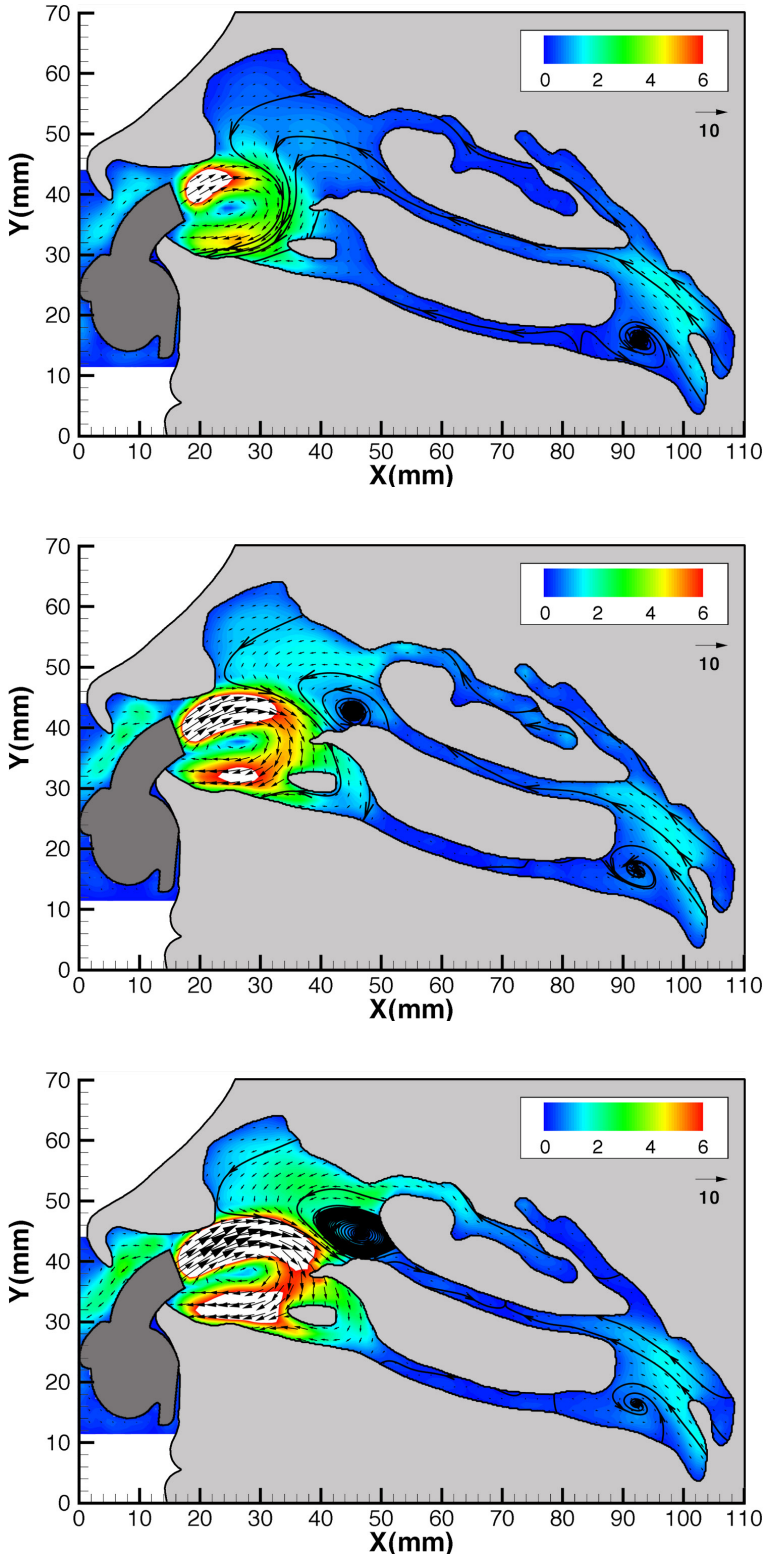

Figure 63. Absolute velocity (m/s) maps through a mid-sagittal cross-section of the left nasal cavity during expiration with (a) 20 l/min, (b) 30 l/min and (c) 40 l/min cannula flow.

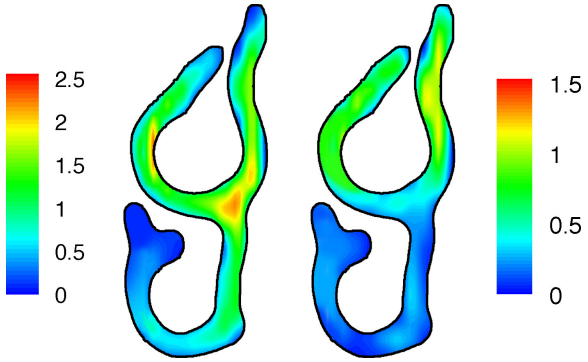

Figure 64. Absolute velocity (m/s) contours on a coronal cross-section of one half of the nasal cavity during (a) natural expiration and (b) with 30 l/min cannula flow.

Figure 65 shows a velocity map with 30 l/min cannula and zero lung flow, which represents the flow pattern at the inflexion points between inspiration and expiration and vice versa assuming quasi-steady flow. Note that the validity of the quasi-steady flow assumption will be discussed in Chapter 6. The cannula jet has an identical trajectory as on inspiration; however, the flow now turns in the nasopharynx as part of a large scale clockwise rotation of the flow in the nasal cavity, where flow travels along the nasal floor and exits through the nose. The maximum cannula jet velocity measured 16.0 m/s and reached 5.9 m/s along the anterior floor. Notably, the maximum jet velocity lies between the maximum jet velocities of 17.0 m/s on inspiration and 15.1 m/s on expiration, alluding to the effect of the breathing pattern on the jet's characteristics. The clockwise vortex that was present at the anterior end of the middle turbinate during inspiration remains without lung flow. A second vortex underneath the cannula jet forms and also rotates in a clockwise direction, separated by a saddle point. The vortex in the recess above the jet is comparable in speed to the same vortex on inspiration.

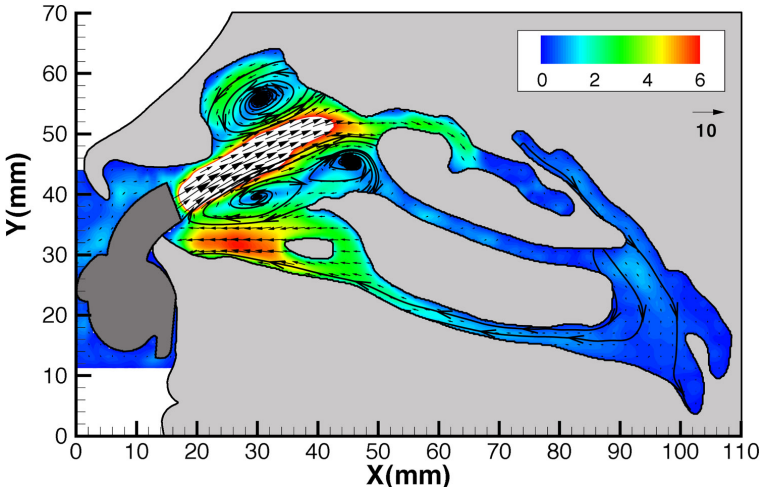

Figure 65. Absolute velocity (m/s) map through a mid-sagittal cross-section of the left nasal cavity with 30 l/min cannula flow and zero lung flow

Figures 66 and 67 illustrate the variations of the maximum absolute, *u, v, w* and average velocities through the nasal cavity with 30 l/min cannula flow on inspiration and expiration, respectively. Juxtaposed are also curves for the maximum absolute velocity during natural breathing. As during natural inspiration, the high velocities in the nasal valve dissipate into the main cavity in Figure 66 due to the increasing cross-sectional area and narrowing of the passages; however, do so at a greater rate. The maximum absolute velocity reaches a minimum in the nasopharynx of 3.0 m/s with NHF, compared with a value of 1.5 m/s during natural inspiration. Considering the natural inspiration flow rate is only 35% lower than during NHF, the cannula jet therefore still has a significant effect on the flow magnitude at the rear of the nasal cavity. The very large difference between the maximum absolute velocities in Figure 66 and the average velocities show the extent to which the cannula jet causes localised concentrations of high velocities.

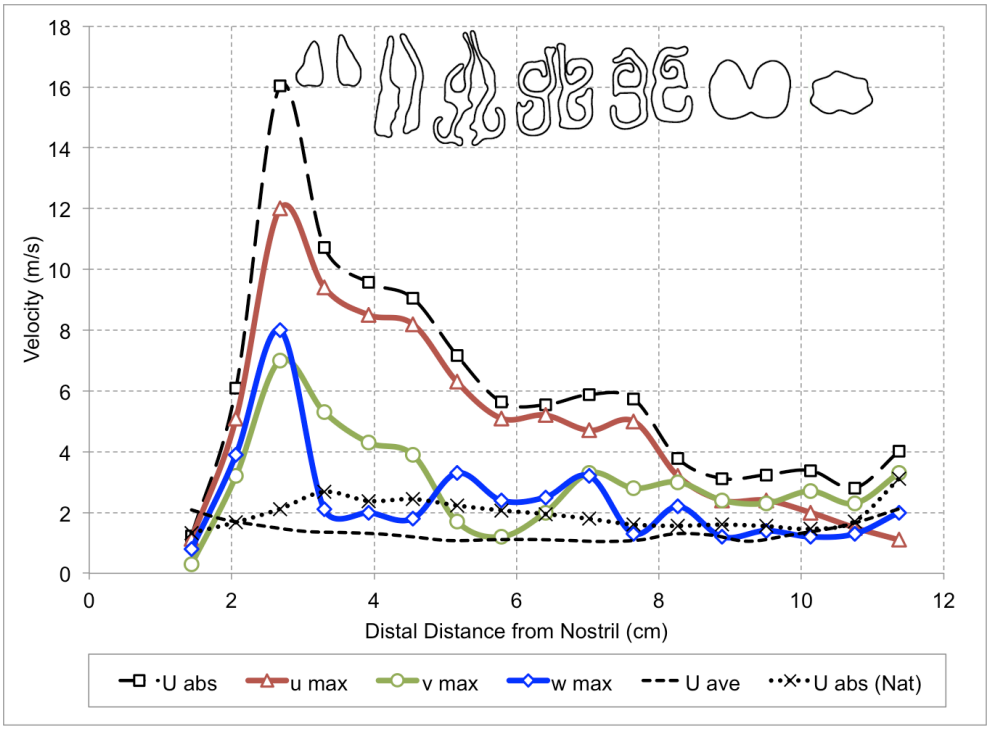

Figure 66. Variations of the maximum absolute, *u*, *v*, *w*, and average velocities through the nasal cavity versus horizontal distance distal of the nostrils during inspiration with NHF.

Figure 67 shows that the high velocities on expiration with NHF are limited to the anterior region where the jet is forced round to retreat, and the large contribution the transverse (z) velocity component makes. Upstream in the main cavity, the velocities are low and relatively constant through the main cavity. The maximum velocity at a distal distance of 7 cm was 140% lower with NHF than during natural expiation, despite the flowrate being only 43% lower. The flow is clearly more evenly distributed over cross-sections of the main cavity with NHF, which is likely due to the large resistance imposed by the cannula as already

discussed. The average and maximum velocities at 7 cm were 0.54 m/s and 1.0 m/s with NHF, which also suggests a more developed flow profile through the main cavity than in the anterior. Elad et al. (2006) consider the benefits of nasal flow stimulating cellular mechanisms on the inner nasal lining, such as mucus secretion from goblet cells. It is possible that NHF flow encouraging flow through more of the nasal cross-section is good for nasal epithelial health.

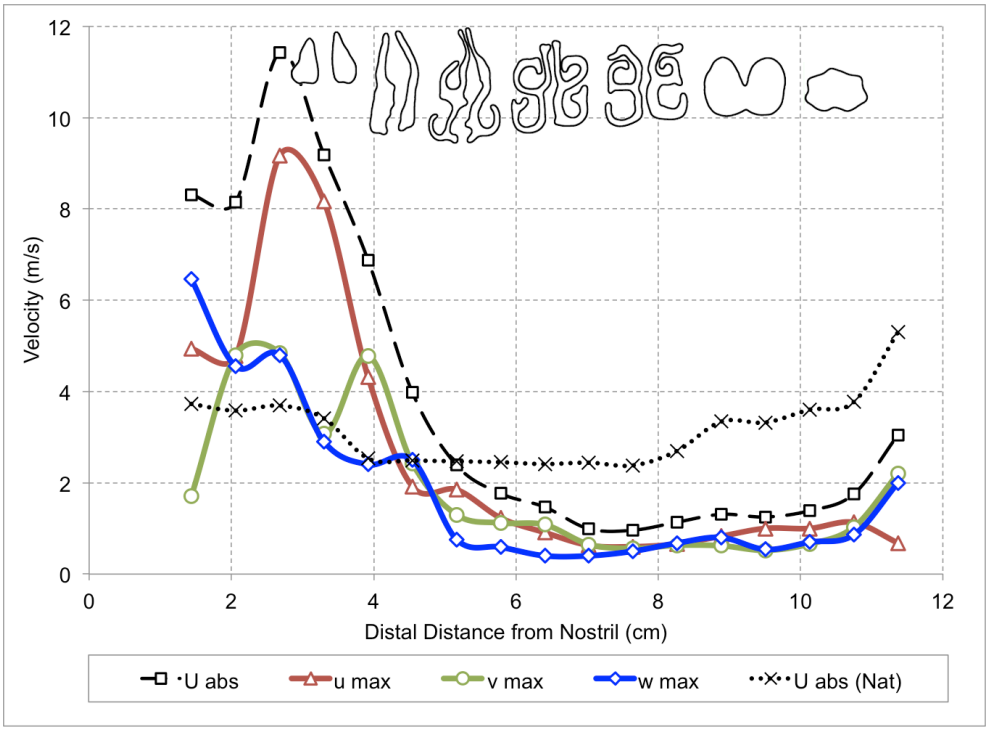

Figure 67. Variations of the maximum absolute, *u*, *v*, *w*, and average velocities through the nasal cavity versus horizontal distance distal of the nostrils during expiration with NHF

5.4.3 Cannula Size

Velocity maps with the large size cannula during inspiration and expiration are shown in Figures 68a and b with a cannula flowrate of 30 l/min. The cannula jet is noticeably wider and slower when compared with the medium cannula, reaching 10.1 m/s on inspiration compared with 17.0 m/s for the same flowrate. The maximum large cannula jet velocity is in correspondence with a theoretical average velocity of 8.9 m/s (prong area 28.2 mm^2). The vortex on the anterior end of the middle turbinate and the associated rotating ejection of air along the anterior nasal floor observed with the medium cannula no longer occurs with the large cannula. Entrainment of air at the nostrils due to a jet pump effect was also absent. Instead, a pair of small counter-rotating vortices was present in a low velocity region under the jet stream. The flow stream

exits the nasal cavity through the nasopharynx in much the same pattern as with the medium cannula; however, a low velocity detached stream joins the flow from the inferior airway.

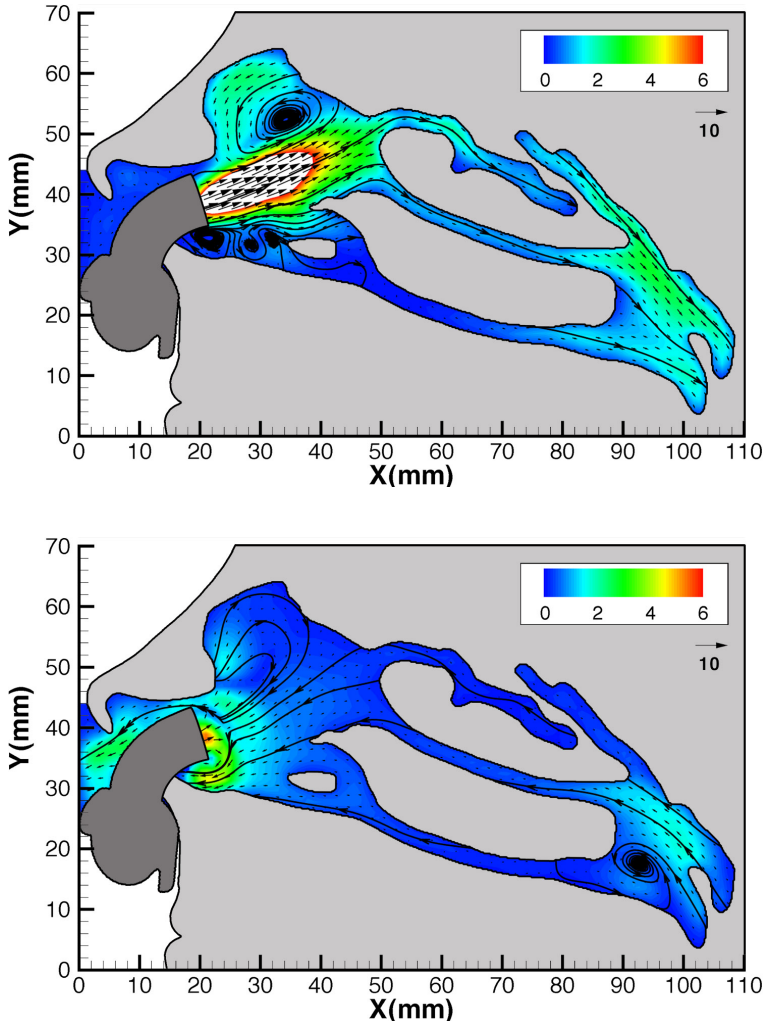

Figure 68. Absolute velocity (m/s) maps through a mid-sagittal cross-section of the left nasal cavity with a large cannula at 30 l/min during (a) inspiration and (b) expiration.

The cannula jet on expiration is reversed immediately upon exiting the prong. There is a stagnation point in line with the center of the prong and the cannula jet is fanned around the prong in three dimensions as shown by the high tangential velocity component at the jet exit in Figure 69. The maximum tangential and absolute velocities were 3.5 m/s and 5.5 m/s, which were both located in the anterior region. It was not possible to measure the jet velocity immediately at the exit because the flow was turned and diverged so quickly and the cross-correlation windows adjacent to the jet exit gained and lost too many particles due to the apparent discontinuity in the flow field.

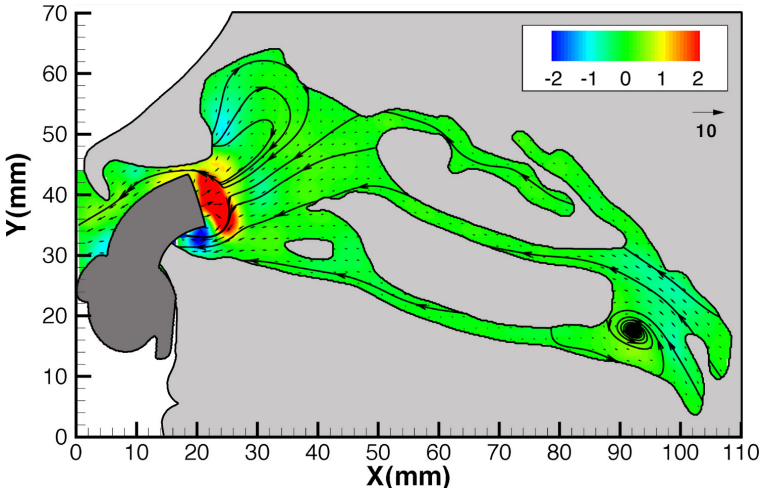

Figure 69. Orthogonal velocity (m/s) component contour with a large cannula at 30 l/min during expiration (velocities are positive out of the page)

5.5 Numerical Comparison

The following section describes numerical simulations that were performed by Stringer et al. (2010) at the University of Auckland in collaboration with the current work. Steady state numerical simulations were conducted for the same natural breathing conditions presented in this chapter using an identical nasal geometry. The results are compared to those obtained with PIV.

5.5.1 Background

There have been relatively few studies that have made direct comparisons between numerical simulations and detailed experimental measurements of nasal flow fields (Doorly et al. 2008c). Keyhani et al. (1995) obtained numerical computed velocity fields that agreed with their experimental hotwire measurements in a 20 times scale unilateral nasal model to within typically 10 to 25%. Mylavarapu et al. (2009) performed pressure and velocity measurements in a stereo-lithography model with an expiratory flowrate of 200 l/min and compared the results with numerical simulations. Mylavarapu et al. employed several different numerical approaches, including large eddy simulation (LES) and steady Reynolds-averaged Navier-Stokes (RANS) with k-ε, standard k-ω, and k-ω shear stress transport (SST) turbulence models. The best agreement with static wall pressure measurements was found with the standard k-ω model, which gave an average error of approximately 20% over all the pressure taps. LES and steady RANS with k-ω SST under-

predicted pressures within roughly a 30% average error. The poorer performance can be explained by the fact that all the simulations were performed with the same mesh. The SST model requires a higher grid resolution at the boundary and LES requires that the grid size be of the same order of magnitude or lower than the estimated Taylor microscale. The number of mesh elements used was not reported in the manuscript.

Doorly et al. (2008c) demonstrated close agreement between PIV and computational predictions of the inspired flow field converging through the nasal vestibule. Horschler et al. (2006a) also compared numerical and PIV results and investigated inspiration and expiration flowrates of 9.5 l/min (Re = 400) and 7.6 l/min (Re = 500), respectively. Although the overall qualitative agreement was described as "satisfactory", a detailed quantitative comparison was not provided and the geometry was heavily simplified. PIV is an ideal experimental tool for validating numerical predictions because PIV results possess a high spatial resolution and can be compared with high-density numerical data fields. Experimental validation of numerical models is necessary in order to ascertain whether the physics of the problem have been modeled correctly.

5.5.2 Numerical Methodology

The nasal geometry was obtained from a CT scan of the actual flow phantom (model 2) and flowrate boundary conditions were applied at the throat using the same steady natural inspiration and expiration flowrates of 22 and 32 l/min. In order to recreate physiological boundary conditions at the nostrils and throat, an expanded rectangular domain was meshed around the external nose and face, and an artificial pipe with an approximate diameter to length ratio of 1:10 was extruded onto the trachea. The appended domain was large enough to capture the region of high-speed flow exiting the nostrils on expiration, whilst small enough not to be excessively computationally expensive. The pipe allowed a simple plug flow boundary condition to be applied to its end without over-defining and restricting the flow profile exiting the larynx. A zero pressure atmospheric boundary condition was applied to the surface of the exterior domain and all the airway surfaces were defined as non-slip walls. A moderate turbulent intensity level of 5% was specified at throat on expiration. Air was assumed to be Newtonian with the same saturated air properties as described in section 4.3 on page 90. A mesh convergence analysis found a mesh with 600,000 nodes gave sufficient accuracy without unnecessary computational expense. Mesh density was highest in the nasal valve area to resolve the high spatial velocity gradients.

Steady state simulations were performed in ANSYS CFX 12.1 by solving the RANS equations with a k-ω SST turbulence model to combine the advantages of the k-ω and k-ε models. The k-ω turbulence model closes the RANS equations using two further equations for the turbulence kinetic energy k and the specific dissipation ω, and performs well in boundary layers (Menter 1994). The k-ε turbulence model closes the RANS equations with equations for kinetic energy and turbulent dissipation rate ε, and has the advantage of being less sensitive to free stream and inlet conditions. The SST turbulence model utilised the k-ω model near no-slip surfaces, such as the solid boundaries in the airways, and the k-ε model in the core of the flow. Liu et al. (2010) described the SST model to be ideal for modeling flow in a complex geometry like the nasal cavity

5.5.3 Results and Discussions

The numerical and experimental results during natural inspiration compared in Figure 70 show convincing agreement in both velocity magnitude and flow topology. Only every tenth vector in the numerical velocity field is shown for clarity. The computationally modeled maximum velocity of 2.2 m/s in the nasal valve was consistent with the corresponding velocity of 2.1 m/s measured by PIV, differing by less than 5%. Similarly, the maximum predicted velocity of the 1.8 m/s at the roof of the nasopharynx just posterior of the middle turbinate was within 12% of the 1.6 m/s obtained experimentally. The average velocities across the numerical and experimental flow fields were 0.9 m/s and 0.7 m/s, respectively. It is clear Figure 70 that there is close agreement with the flow features obtained by the two modalities on inspiration, and Figure 71 shows an equally impressive likeness on expiration. Maximum nasal valve velocities on expiration matched within 4%. There was, however, a discrepancy in regard to the maximum velocity obtained in the nasopharynx. The numerical prediction was 5.4 m/s, whilst PIV measured 4.2 m/s. This

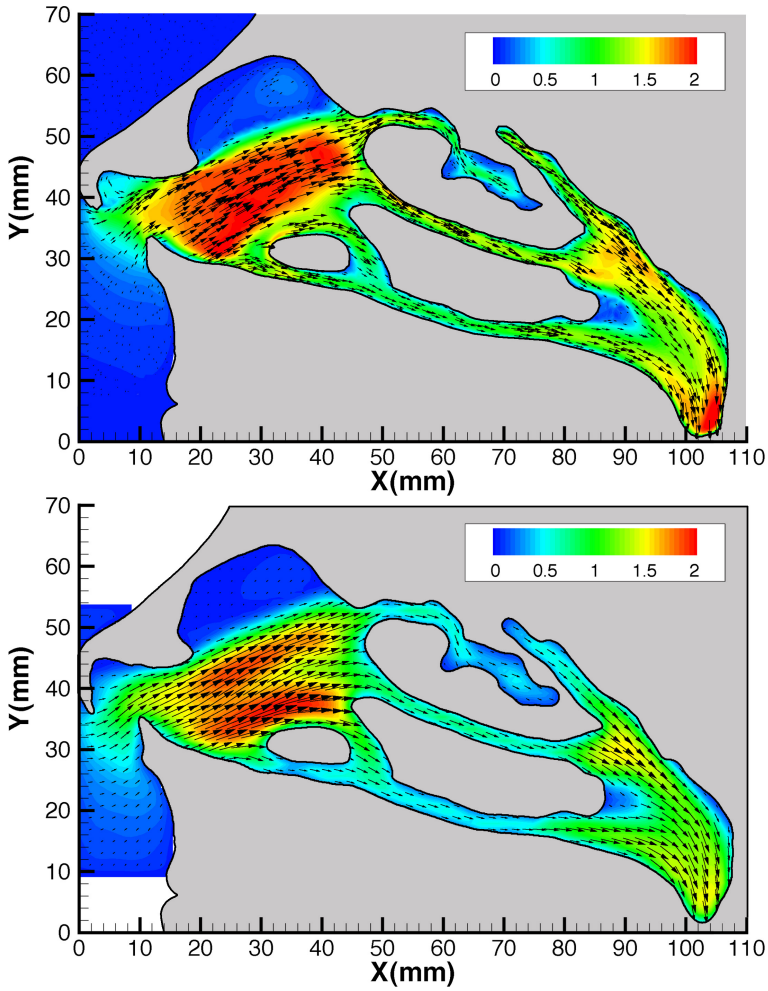

Figure 70. Comparison between (a) computational predictions and (b) PIV measurements of the velocity field through a mid-sagittal cross-section of the left nasal cavity on inspiration.

could possibly be a result of the boundary condition applied in the numerical model and an analysis should be performed in future work to assess the susceptibility of flow in the nasopharynx to the inlet configuration and modeled flow profile at the throat. A summary of the key numerical and experimental velocities is given in Table 16. The numerical model consistently over predicted speed, although it is possible the PIV measurements were lower than the true velocities due to a cross-correlation window's averaging effect, the relatively low magnification, and high velocity gradients. It was not possible to reduce the interrogation window size smaller than 32 × 32 pixel^2 without significantly diminishing the signal to noise ratio. The results presented, however, are considered to be in good agreement and suggest that CFD simulations can be used to accurately compute the flow field in the upper airway.

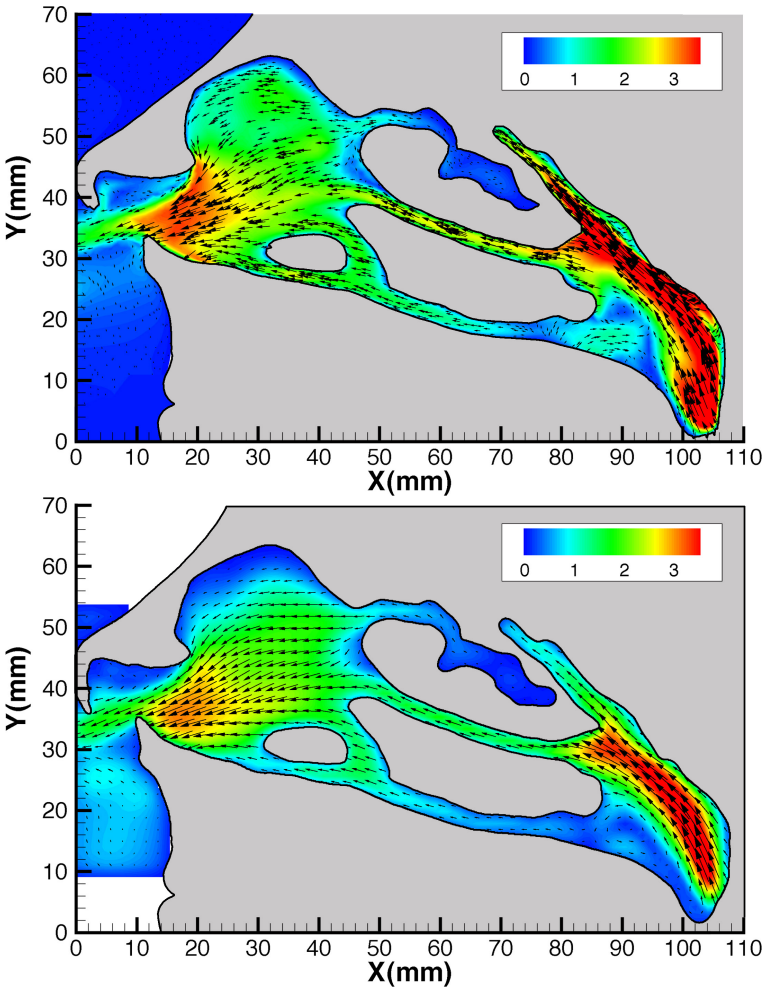

Figure 71. Comparison between (a) computational predictions and (b) PIV measurements of the velocity field through a mid-sagittal cross-section of the left nasal cavity on expiration.

Table 16. Summary of the key Numerical / Experimental absolute velocities (m/s) with percentage deviations given in parentheses.

	Max. Nasal Valve	Max. Nasopharynx	Average
Inspiration	2.2 / 2.1 (5%)	1.8 / 1.6 (12%)	0.9 / 0.7 (23%)
Expiration	3.2 / 3.3 (4%)	5.4 / 4.2 (23%)	1.4 / 1.1 (22%)

5.6 Conclusions

Stereo-PIV was used to measure the flow field in the human nasal cavity during natural breathing and over a range of NHF conditions varying cannula flowrate (20, 30 and 40 l/min) and prong diameter. The same physiological flowrates measured in Chapter 4 were again applied with a quasi-steady flow assumption. Series of time-averaged measurements captured on traversed sagittal planes were reconstructed into velocity volumes. Natural breathing inspiration and expiration maximal velocities of 2.8 m/s and 3.8 m/s, respectively, were located in the right nasal valve. Velocity magnitudes differed appreciably between the left and right sides of the nasal cavity. During natural breathing, the maximum velocity was 33% larger in the right choana on inspiration and 19% higher on expiration. Important contributions to flow resistance through the nasal cavity of features other than the nasal valve have been highlighted. Although the morphology was asymmetric about the nasal septum, the flow tended to behave similarly through the features common to both sides of the nasal cavity. The flow pattern through the nasal cavity is largely two-dimensional; however, lateral velocities have been found to contribute up to 36% of the absolute velocity magnitude in anterior regions. To capture the complete velocity magnitude, a three-component measurement technique such as stereo-PIV or discrete measurement planes aligned parallel to the flow in the nasal cavity anterior with a two-component measurement technique should therefore be used. The highest velocities are located in the sagittal plane: thus, a sagittal light sheet stereo-PIV configuration should be used, as in this study, to minimise the loss of seeding particles. The expiration flowrate of 29.4 l/min calculated from a reconstructed velocity volumes corresponded well with the system prescribed flowrate of 32 l/min.

NHF modifies the flow velocity magnitude and distribution in the nasal cavity significantly, altering the proportion of inspiration and expiration through each meatus and producing jet velocities up to 17.0 m/s for 30 l/min cannula flow. Inspired and expired flows with NHF remain high through the nasal cavity, whereas the main flow stream passes through the middle airway and along the septal wall during both natural inspiration and expiration. Strong recirculating features are created above and below the cannula jet on expiration and significantly strengthened on inspiration. Close agreement between numerical and experimentally measured flow features and velocities suggests that CFD using the k-ω SST turbulence model and 600,000 nodes can be used to accurately compute the flow field in the upper airway and could be employed to investigate a wider range of natural and assisted breathing conditions.

6 Oscillatory Flow by Stereo-PIV

This chapter presents the third and final campaign of PIV measurements conducted in the current work. Instead of applying steady flows with a quasi-steady flow assumption, physiologically accurate oscillatory flows are reproduced in vitro using Reynolds and Womersley number matching and a piston pump driven by a ball screw and stepper motor. Flows are described as oscillatory rather than pulsatile because breathing flows are centred on a zero mean, and pulsatile flow implies a superimposed steady flow component such as in the cardiovascular system. Oscillatory flows during both mouth closed and mouth-open breathing conditions are assessed using models 2 and 3, respectively. The nasal flow pattern created by the small cannula size was additionally investigated.

6.1 Introduction

The Womersley number for quiet breathing was described in section 4.1.1 to be as high as 4, which raised concern on whether or not nasal flows can be modeled as steady and the validity of a quasi-steady assumption. Time resolved stereo-PIV measurements of nasal flows during natural and NHF assisted mouth-closed breathing were therefore undertaken to determine if the distinct flow patterns observed with steady flow measurements also existed with oscillatory flow and how they evolved when the flow alternated between inspiration and expiration. The effect of mouth-open breathing during NHF therapy is of particular interest clinically because it reduces the resistance of the upper airways and subsequently the mean airway pressure. Moreover, air thought to be drawn in though the mouth would dilute administered levels of humidified and oxygen blended medical gas. The amount of flow that enters or exits the mouth on inspiration or expiration had, until the current work, never been measured and was unknown.

Although most investigations to date have assumed nasal flows to be quasi-steady, concurrent studies by Horschler et al. (2010) and Lee et al. (2010) support the conclusion of the current work that the assumption is invalid for natural breathing. Numerical investigations by Horschler et al. and Lee et al. both

describe major differences between steady and unsteady flow simulations, particularly near the transition between inspiration and expiration. Horschler et al. describes a good agreement between steady and unsteady results at high Reynolds numbers ($Re \geq 1500$) and significant discrepancies at low Reynolds number flows. More specifically, major differences were found at increasing mass flux and to a lesser extent on decreasing mass flux. Lee et al.'s comparison of steady and unsteady large eddy simulations revealed sizable differences in expiration phase flow characteristics and temperature profiles. Although the quasi-steady flow assumption was not discussed by Simmen et al. (1999), time dependence is visible in their unsteady flow visualisation results, which employed a piston pump. Schematics symbolising the airflow pattern through the nasal cavity are different at equivalent flowrates either side of peak inspiration and expiration, and turbulence was discussed as being prominent in the acceleration and deceleration phases.

Chung et al. (2006) used planar PIV and a piston pump driven by a cam to measure flows across the breath cycle through a twice scale model of one choana. Lindemann et al. (2005), Ishikawa et al. (2006), Yu et al. (2008), and Zhang et al. (2008) have undertaken numerical simulations of unsteady flows in the nasal cavity; however, as in Chung et al., the validity of a quasi-steady flow assumption was not tested nor flow time dependence discussed. The results of all four of these numerical studies are also unlikely to be reliable because a RANS bases solver was used in each case. Lee et al. (2010) used the LES technique, which has a better capability of treating transient terms in the governing equations correctly. Furthermore, Zhang et al. used a symmetrical sawtooth breath wave profile, which is not physiological.

6.2 Experimental Setup

6.2.1 Pump Design and Construction

A piston pump (Figure 72) driven by a stepper motor and ballscrew was constructed to reproduce physiologically accurate breath waveforms in vitro. The cylinder was an acrylic tube with a nominal bore of 140 mm and the piston head was sealed with two nitrite lip seals arranged back to back. A Rollon Compact 18 series rail and T slider supported the piston rod. A 5 mm pitch Hiwin precision rolled ballscrew and ballnut were used and supported by SBC flange and fixed block style support units at the free and motorized ends, respectively. The net hydrostatic pressure on the piston head created by the flow system prevented any backlash. The stepper motor (Stebon 'F' Series Nema 23, FDL603-370-47) had a step angle

of 1.8°, which translated to an in vitro volume displacement of 0.385 ml per step. This resolution provided a smooth waveform such that there were still 8 steps per second at a flowrate as small as 0.185 l/min (1% of the maximum flow). Labview (http://www.ni.com/labview/) was used to control the stepper motor via a National Instruments 9401 digital module and 9172 CompactDAQ chassis. An optical switch allowed the pump to be automatically returned to home position and hard wired limit switches ensured the piston remained within working bounds.

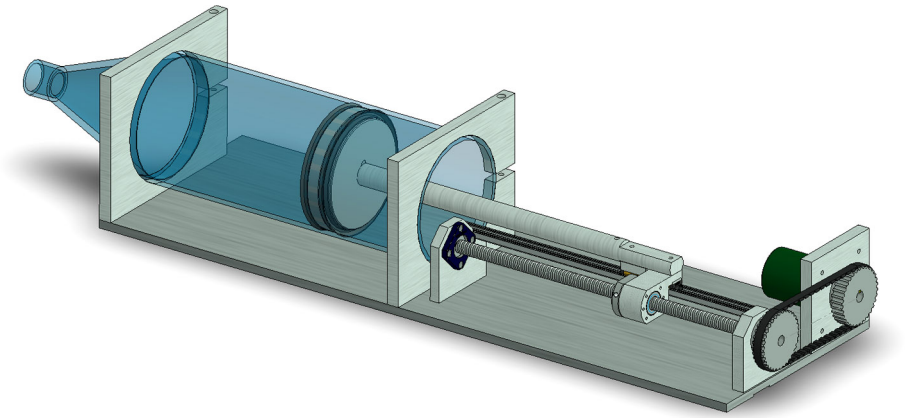

Figure 72. Piston pump devised to produce physiologically accurate breath waveforms.

6.2.2 Flow System

The in vivo natural and NHF breath waveforms measured in section 4.2.3 on page 88 were repeated, averaged over 20 breaths, and fitted to a Fourier series. The Fourier coefficients were obtained in Matlab and subsequently inputted into the Labview programming. Normalized flow and piston displacement waves are shown in Figure 73. Inspiration is considered as positive. In vivo and in vitro dimensional similarity was achieved by scaling the waveform's amplitude (flowrate Q) by Equation 18 to maintain a constant Reynolds number and by scaling the period T to maintain a constant Womersley number by Equation 19. Values for the dimensionless quantities calculated in the nasopharynx based on a measured hydraulic diameter of 15.1 mm (area = 205.3 mm^2, perimeter = 54.4 mm) are given in Table 17 along with the in vivo and corresponding in vitro flow parameters used in experiments. Notable is the fact the Womersley numbers of 1.9 and 1.8 for natural and NHF breathing, respectively are lower than those estimated by Doorly et al. ($\alpha = 3$) and Hahn et al. ($\alpha = 3$) because the breathing rate of the in vivo subject in the current work was athletic and had a natural breathing rate of approximately 11 breaths per minute, which is particularly low (Tobin et al. 1983).

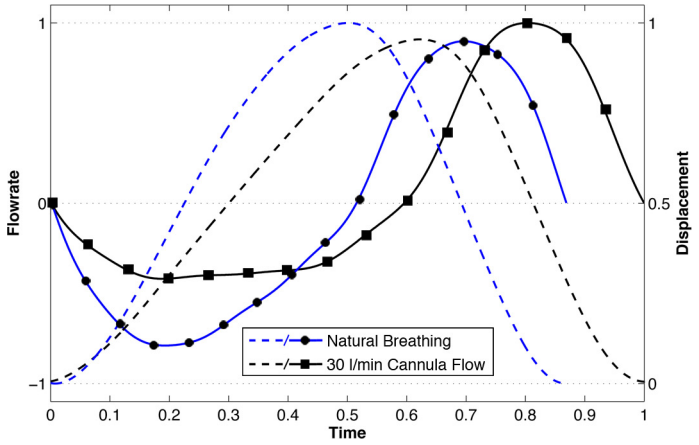

Figure 73. Plot showing normalised flow (solid lines) and piston displacement (dashed lines) waves during natural breathing and with 30 l/min cannula flow. The locations of the 15 measurement times are marked and inspiration is considered positive.

$$Q_{\text{in vitro}} = 1.55 \frac{\upsilon_{\text{in vitro}}}{\upsilon_{\text{in vivo}}} Q_{\text{in vivo}}$$ **Equation 18**

$$T_{\text{in vitro}} = 1.55^2 \frac{\upsilon_{\text{in vivo}}}{\upsilon_{\text{in vitro}}} T_{\text{in vivo}}$$ **Equation 19**

Table 17. Peak in vivo and in vitro flowrates and periods dimensionally scaled by the Reynolds (Re) and Womersley (α) numbers in the nasopharynx

		In vivo		Flow Quantities		In vitro	
		Peak flow (l/min)	Period (s)	Re	α	Peak flow (l/min)	Period (s)
Natural Breathing	Expiration	26.0	5.4	1810	1.9	14.6	35.8
	Inspiration	29.6		2060		16.6	
30 l/min Cannula	Expiration	13.8	6.2	960	1.8	7.7	41.2
	Inspiration	32.9		2290		18.5	

A schematic of the experimental flow system is shown in Figure 74 with model 2. Model 3 was also mounted in a likewise supine position. The system liquid temperature was raised from the constant 25°C used in previous measurements to 32°C, which reduced the viscosity of the working liquid and increased the in vitro period in order to reduce the work requirements of the piston pump motor and increase the effective temporal resolution. Despite the physiological geometries upstream of the regions of interest in both models and the fact that the necessary entrance length for a fully developed inlet condition is almost 40% shorter for an oscillatory flow when compared with a steady flow (Burgmann et al. 2009), the same

length of straight pipe was attached to the models' throat to connect the pump. The increased backpressure required to produce a 30 l/min flowrate through the small cannulae necessitated the use of a pump in addition to the 3 m high header tank that was capable of a dynamic head up to 40 m (single phase PK 60, http://www.pedrollo.co.uk/).

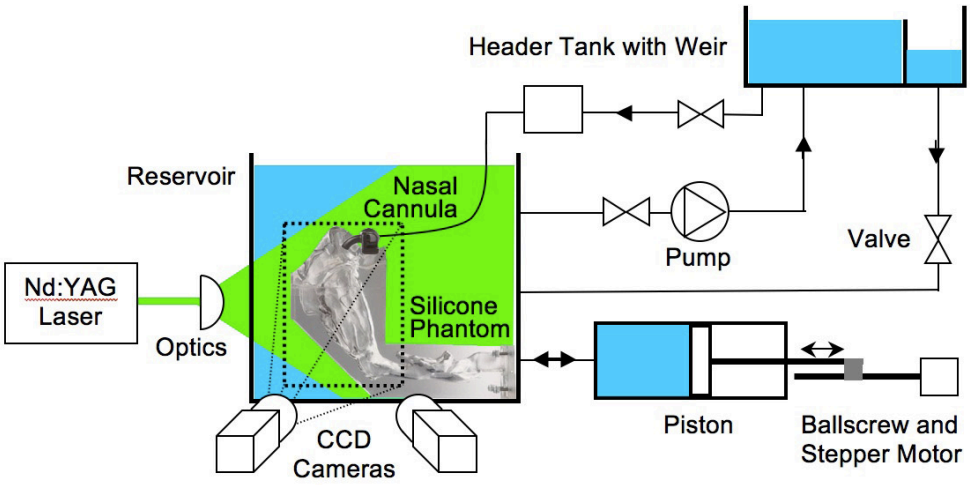

Figure 74. Schematic of the pulsatile flow experimental set-up

6.2.3 PIV

Displacement fields from 10 image pairs at identical phases in the breath cycle were ensemble correlation averaged for two reasons: to increase the strength of the cross-correlation peak and to produce phase-averaged results. Although a larger number of recordings would normally be desired, Figure 75 illustrates the level of convergence obtained when only 10 image pairs were ensembled. Values obtained from ensembling over 9 and 10 image pairs were all within 0.03%. This was considered acceptable because a greater number of recordings would provide diminishingly smaller improvements yet come at a large laboratory time expense. Figure 75 was produced from recordings taken during peak natural inspiration. The maximum absolute velocities measured from one and two image pairs corresponded to noise spikes.

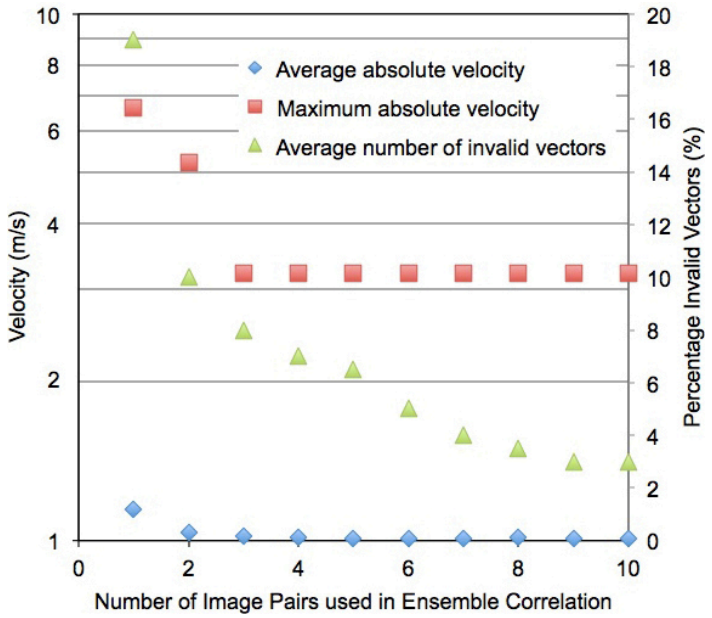

Figure 75. Graph illustrating the convergence of cross-correlation performance and measured velocities when ensembling up to 10 image pairs

At the start of each breath wave, the piston pump's stepper motor controller triggered a BNC 565 pulse/delay generator's burst routine to trigger each laser cavity and camera at the 15 equi-spaced measurement phases illustrated in Figure 73. Due to equipment and time constraints, the time delay between successive exposures was the same for each measurement phase. In order to maximise the resolution of slower phases, the time delay was chosen such that the maximum particle displacement for the peak velocity was about 16 pixels. The time delay was tuned in this way for each measurement location by cross-correlating a test image pair and calculating the required change in time delay to achieve the desired displacement. In model 2, at a cross-section through the centre of the left nasal valve for example, the time delay was 1,200 μs during natural breathing and 500 μs with cannula flow. Towards the outside of the inferior meatus where the flow velocities are slower, time delays in the order of 3,500 and 2,000 μs were used during natural and cannula breathing, respectively. To take advantage of the Lorenz-Mie scatter pattern shown in Figure 22 on page 60, instead of using a symmetrical camera arrangement, the left camera was positioned at a small stereo angle and the right camera orientated at approximately 30° in forward scatter. An overview of the relevant experimental parameters is given in Table 18.

Table 18. Overview of the relevant experimental parameters

		Model 2: Mouth closed	Model 3: Mouth open
Nasal cavity model	Scale	1.55 : 1	
	Dimensions (H × W × D)	250 × 190 × 70 mm	490 × 175 × 85 mm
	Material	Silicone (Sylgard 184)	
Flow	Liquid	~ 60% glycerin, 40% water	
	Properties at 32°C	η = 1.422, μ = 7.41x10^{-3} kg/ms, ρ = 1151 kg/m^3	
	U_{max}	24.8 m/s	7.9 m/s
Calibration target	Dimensions (H × W × D)	200 × 200 × 10 mm	
	Grid spacing	5 × 5 mm	
	Marker Diameter	2.5 mm	
Seeding	Type / Diameter / Density	Hollow glass spheres / 16 μm / 1.1 g/cm^3	
Laser	Type	Nd:YAG, dual cavity	
	Max Power	120 mJ	
	Pulse width	9 ns	
	Thickness	2 mm	
Cameras	Type	CCD	
	Resolution	1600 × 1200, 8 bit	
	Pixel Size	7.4 × 7.4 μm	
Image Properties	Lens focal length	60 mm	
	Viewing angles	-6.4° & 29.1°	-5.1° & 31.0°
	Lens aperture	f = 8 & 11	
	Average magnification	0.116 mm/pixel	0.079 mm/pixel
	Region of interest	133 × 172 mm	118 × 88 mm
	Maximum particle displacement	16 pix	
Stereo PIV analysis	Spatial Resolution	40 × 40 pixel^2	32 × 32 pixel^2
		4.6 × 4.6 mm^2	2.5 × 2.5 mm^2
	Grid Spacing	1.2 mm	0.8 mm
		10 pixel	10 pixel
	# vectors	144 × 111 × 1	111 × 148 × 1
Volume Resolution (full nasal cavity)	Rectangular Domain Dimensions (I × J × K)	20 × 222 × 87	20 × 296 × 72
	Number of sagittal planes	30	24
	Sampling resolution	1.2 × 1.2 × 0.5 mm	0.83 × 0.83 × 0.67 mm

6.3 Description of the Measurements

The range of conditions and regions of interest (ROI) for which 98 stereo-PIV measurement planes were acquired each with 15 breathing phases are overviewed in Figure 76. In model 2 during natural and NHF breathing with a medium size cannula, the phantom was traversed to capture measurements on 30 sagittal slices throughout the entire nasal cavity at 1.5 mm increments. The series of traversed 2D-3C phase averaged velocity maps obtained were again interpolated into 3D-3C volumes. Flow fields throughout the left choana were also measured with the small sized cannula. In model 3, the region of interest was the pharynx (Figure 77) within which 24 measurement planes were recorded. As in Chapter 5 a cannula flowrate of 30 l/min was chosen as the baseline for comparative analysis.

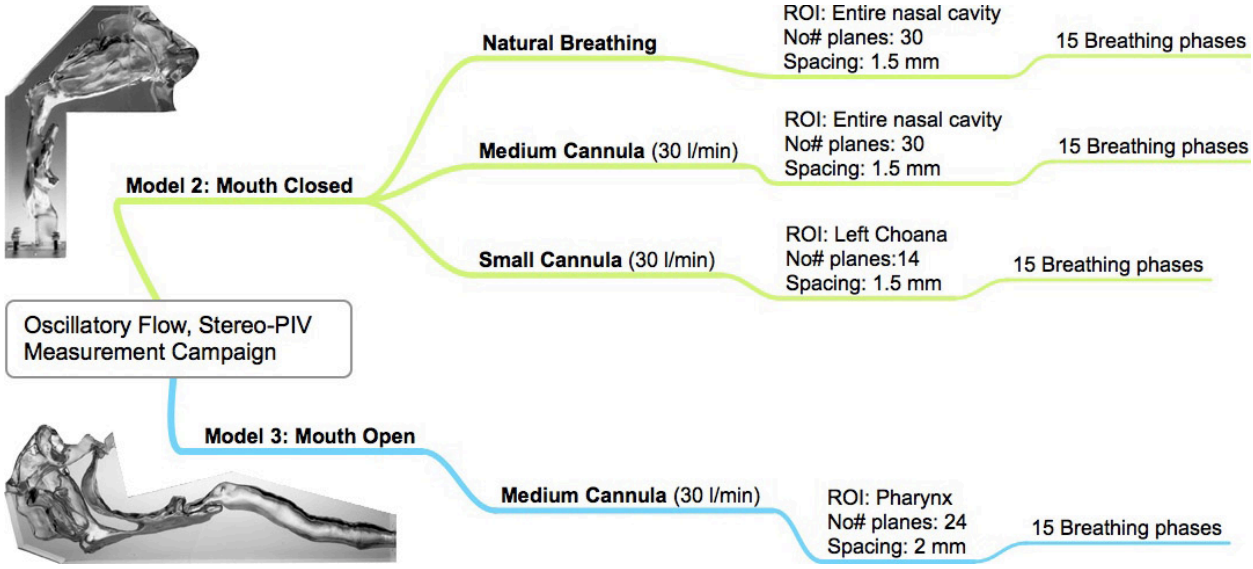

Figure 76. Overview of conditions measured by time resolved stereo-PIV and their respective regions of interest (ROI).

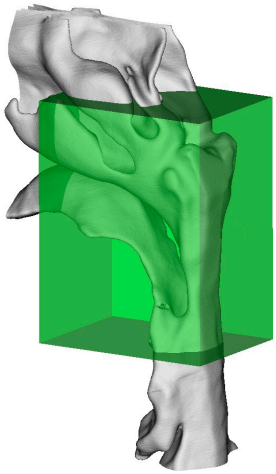

Figure 77. Schematic illustrating the region of interest in the pharynx in model 3.

6.4 Results and Discussions

All velocities shown are in vivo scaled and where applicable, only every third vector is displayed for clarity. Results are shown for 8 of the 15 time steps measured. The corresponding flowrates and temporal locations are given numerically in Table 19 and the temporal evolution of the flow field illustrated in a clockwise direction in Figures 78, 83, 88 and 90. The location of the measurement phases at peak expiration (c), the inflection from expiration to inspiration (e), and peak inspiration (g), differed slightly from the exact values because the measurement phases were equi-spaced. The exact values for these characteristic flows are given in parentheses in Table 19. Phase 'a' was coincident with the beginning of the breath cycle, i.e. the inflexion prior to expiration. In all cases vector lengths denote in-plane velocity magnitude. In-plane and transverse velocities have been capped to 8 m/s and a range of -3 to 3 m/s, respectively to enhance visualization of lower velocities.

Table 19. In vivo flowrates and temporal locations of each measurement phase presented. The exact values at peak flows and the transition from expiration to inspiration are given in parentheses.

Phase	a	b	c	d	e	f	g	h
Natural breathing								
Time (s)	0.00	0.72	1.08 (1.20)	1.80	3.24 (3.21)	3.60	4.32 (4.33)	5.04
Flowrate (l/min)	0.0	-22.1	-25.8 (-26.0)	-22.4	1.07 (0.0)	16.1	29.6 (29.6)	18.6
30 l/min Cannula								
Time (s)	0.00	0.83	1.24 (1.18)	2.48	3.73 (3.71)	4.14	4.97 (5.00)	5.80
Flowrate (l/min)	0.0	-12.4	-13.8 (-13.8)	-12.3	0.35 (0.0)	12.9	32.9 (32.9)	17.6

6.4.1 Natural Breathing

Phase averaged velocity fields for eight phases across the simulated natural breathing cycle are presented in Figure 78. At the transition from inspiration to expiration where the net flowrate is zero (phase a), the maximum velocity in Figure 78a is not zero but 0.39 m/s. This flow stream occurs in the nasal valve and is reminiscent of the jet of inspired air that enters the nasal cavity in Figure 78g. Inertial effects at the transition from inspiration to expiration are therefore significant and flow in the nasal cavity does have

some time dependency. At the measurement phase that represents the transition from expiration to inspiration (e) the actual flowrate was 1.07 l/min and a maximum velocity of 0.30 m/s occurred in the nasal valve. Phase 'e' was taken only three hundredths of a second after the inflection point, and yet the flowrate was already 1.07 l/min because the maximum rate of change of flowrate was high (39.8 l/min s^{-1}). For a nasal valve cross-sectional area of 1.11 cm^2 and a flowrate of 1.07 l/min, the theoretical average velocity across the nasal valve was 0.16 m/s. A maximum velocity of 0.30 m/s was therefore expected assuming the average velocity should be approximately half the maximum velocity, as would be the case for a Poiseuille profile. Given this close agreement, the maximum velocity at zero flow between expiration to inspiration could be extrapolated to be near zero, certainly closer to zero than the 0.39 m/s measured at the transition from inspiration to expiration. This suggests that time dependency and inertial effects are greater at the transition from inspiration to expiration than at the transition for expiration to inspiration, which is consistent with the findings of Horschler et al. (2010) and Lee et al. (2010). In the current study, the largest rate of change of flowrate magnitude occurred at the transition from inspiration to expiration during natural breathing (-52.2 l/min s^{-1}). It was therefore logical to find the largest inertial effects at this point.

During expiration, the flowrate at phase 'b' (-22.1 l/min) is 1.3% lower than the flowrate at phase 'd' (-22.4 l/min); however, the maximum velocity in the nasopharynx at phase 'b' (3.39 m/s) is 9% (0.29 m/s) higher. This inconsistency would not occur if the flow was quasi-steady. Nonetheless, the general flow pattern throughout expiration (Figs. 9b-d) is similar. Figures 9f and 9h correspond to approximately equal inspiration flowrates, 9f occurring before and 9h occurring after the peak flowrate at position 9g. The velocity patterns in Figs. 9f and 9g are very similar in both distribution and magnitude, which would suggest time independence during inspiration. Although the effect of time dependence is largest at flow transitions, Lee et al. (2010) supports the current work's results showing greater time dependence during expiration than on inspiration.

Despite the effects of time dependence during flow transitions and changing flux, the flow patterns at the stationary points of inflexion were visually indistinguishable from the results obtained with steady flows in Chapter 5. Figures 79 and 80 give a comparison at expiration and inspiration, respectively, of the steady and unsteady results obtained at peak flows. The exceptional difference was that the inspired jet passing through the nasal valve in steady conditions had a different flow profile to the more even distribution measured with oscillatory flow. The flow pattern through the entire nasal cavity during peak expiratory and inspiratory phases is shown in Figure 81, where the same flow features discussed in Chapter 5 are visible

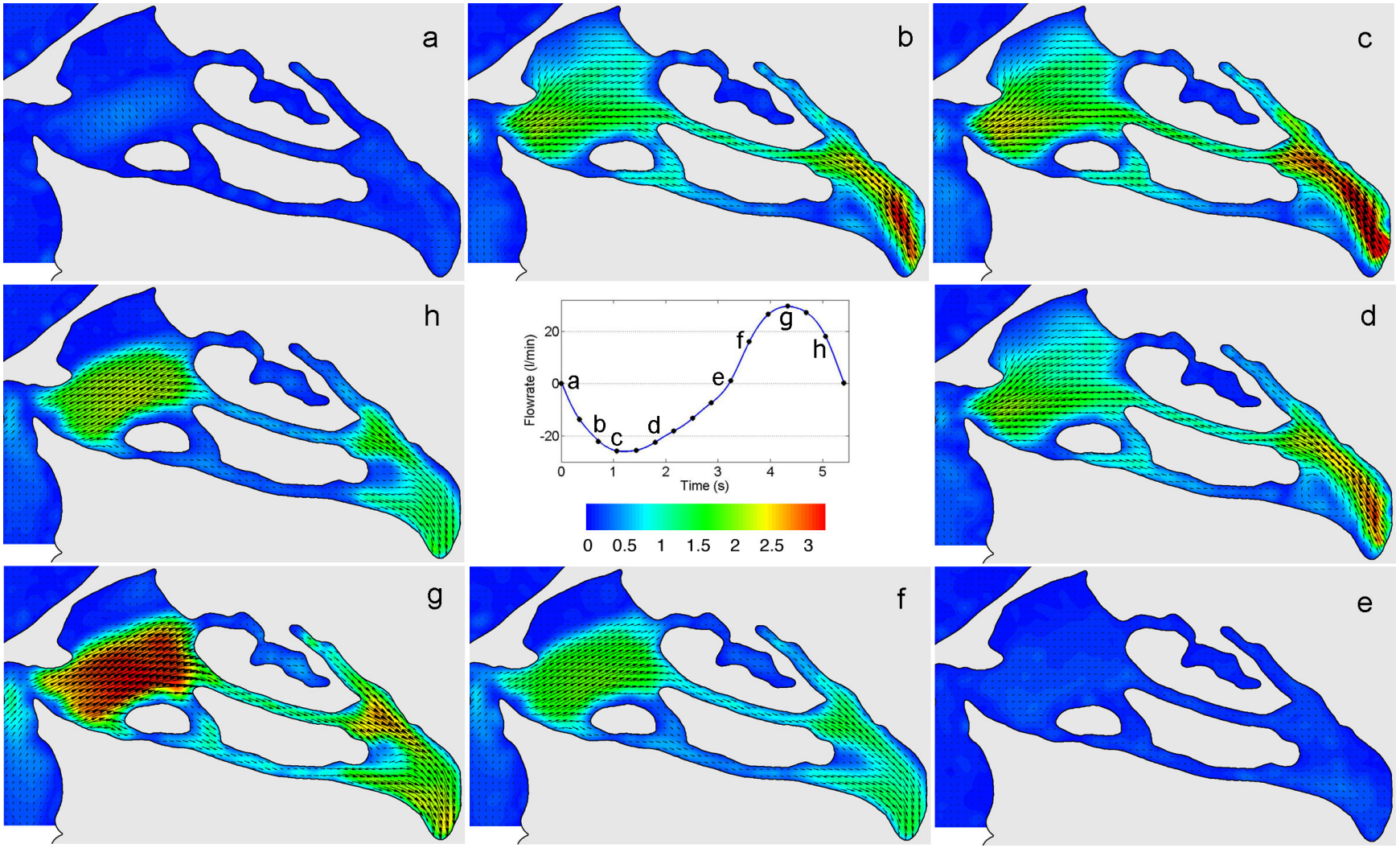

Figure 74. Phase averaged, absolute velocity fields (m/s) through a cross-section of the left nasal valve during natural breathing.

yet presented at a higher resolution. With the colour contours in Figure 81 representing flux velocities, the path of expiratory and inspiratory flows can be clearly seen to pass predominately through the middle airway. Velocity magnitudes again differed appreciably between the left and right sides of the nasal cavity. The maximum velocities in the left and right nasal valves were 2.4 m/s and 3.1 m/s, respectively, during peak expiration (Figure 78c), and 3.3 m/s and 4.3 m/s at peak inspiration (Figure 78g). Flow was biased towards the right nasal cavity on both expiration (63.4%) and inspiration (64.1%). The maximum velocity measured in the nasopharynx during expiration was 3.8 m/s. The out of plane velocity components were largest at peak expiration and peak inspiration, and are shown in the colour contour of Figure 82. Flow entering the nasopharynx is disturbed by the irregular shape of the laryngopharynx upstream, resulting in a maximum lateral velocity of -1.8 m/s. In the nasal valve, maximum lateral velocities of -0.73 m/s and 1.20 m/s occur on peak expiration and inspiration, respectively.

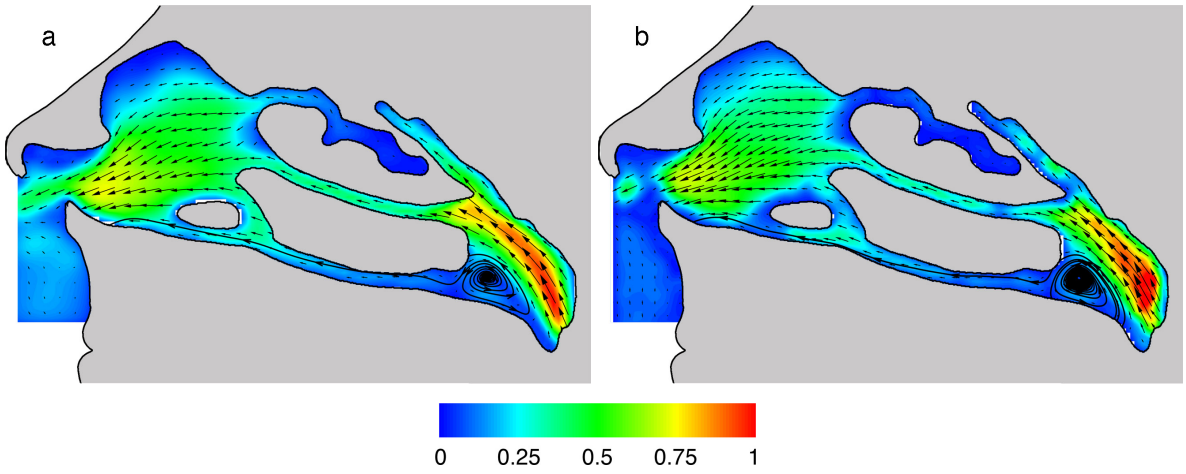

Figure 79. Comparison of steady and unsteady normalised velocity maps (m/s) obtained at peak expiration

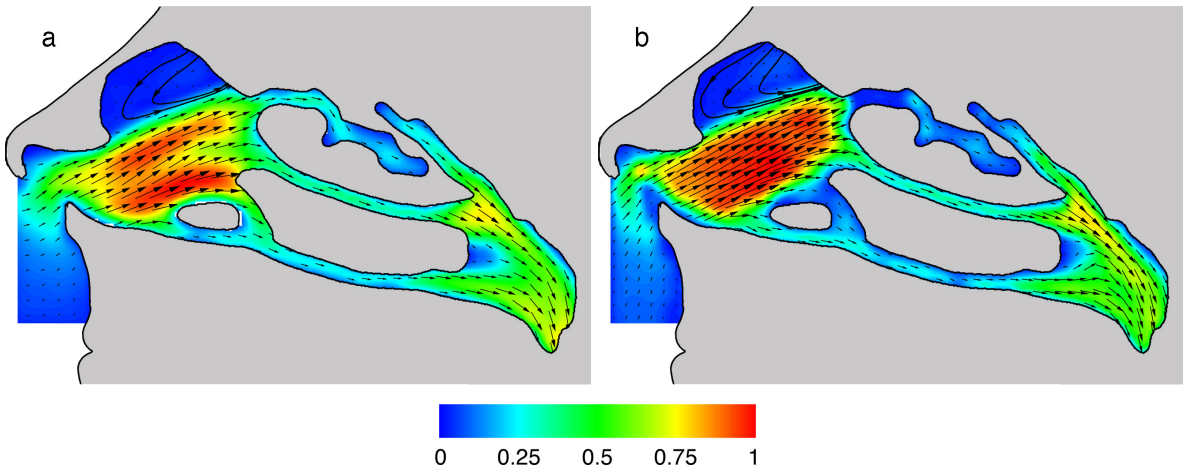

Figure 80. Comparison of steady and unsteady normalised velocity maps (m/s) obtained at peak inspiration

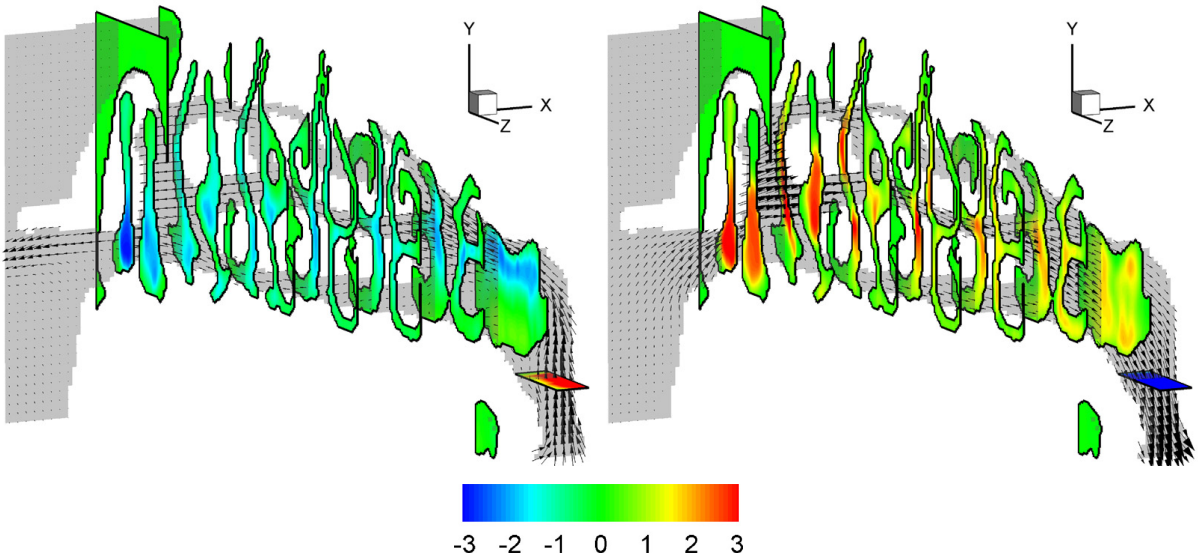

Figure 81. Velocity contours (m/s) displaying x velocities through coronal slices and y velocities through an axial slice of the reconstructed velocity volume during natural (a) peak expiration and (b) peak inspiration (phases c and g respectively).

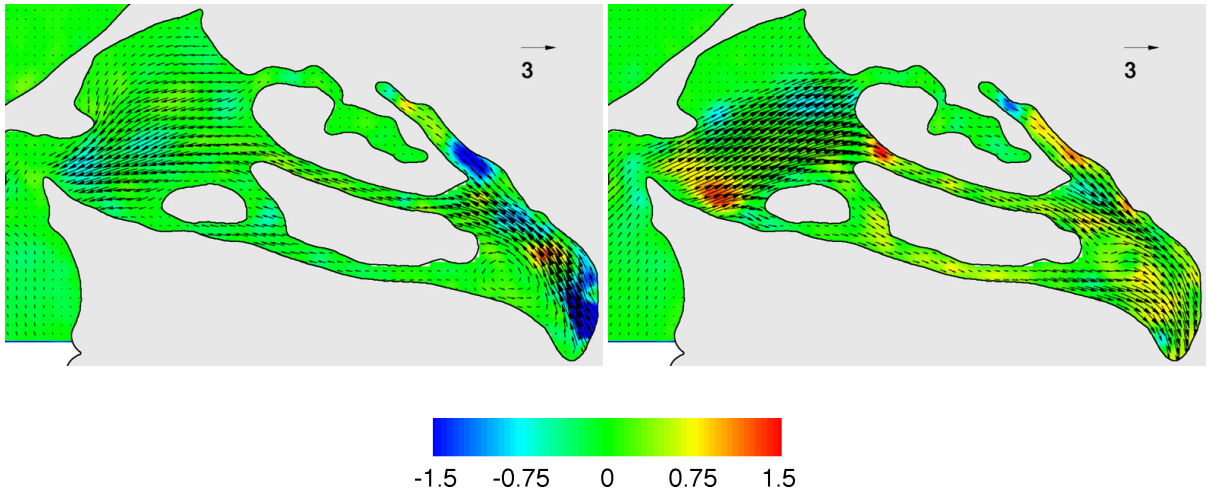

Figure 82. Orthogonal velocity (m/s) component contour during natural (a) expiration and (b) inspiration (velocities are positive out of the page)

6.4.2 Medium Cannula

Phase averaged velocity fields of the cyclical flow in the nasal cavity during breathing with 30 l/min cannula flow are presented in Figure 83 for eight phases. Cross-sections of the reconstructed velocity volume at peak expiration and inspiration are shown in Figure 84. On a preliminary inspection of the results in Figure 83 it was suggested that a quasi-steady assumption is valid for flow in the nasal cavity with NHF. Velocity patterns at equivalent flowrates on opposing slopes such as in Figures 83a and 83e, Figures 83b and 83d, and Figures 83f and 83h were nearly indistinguishable and thus flow time dependence was

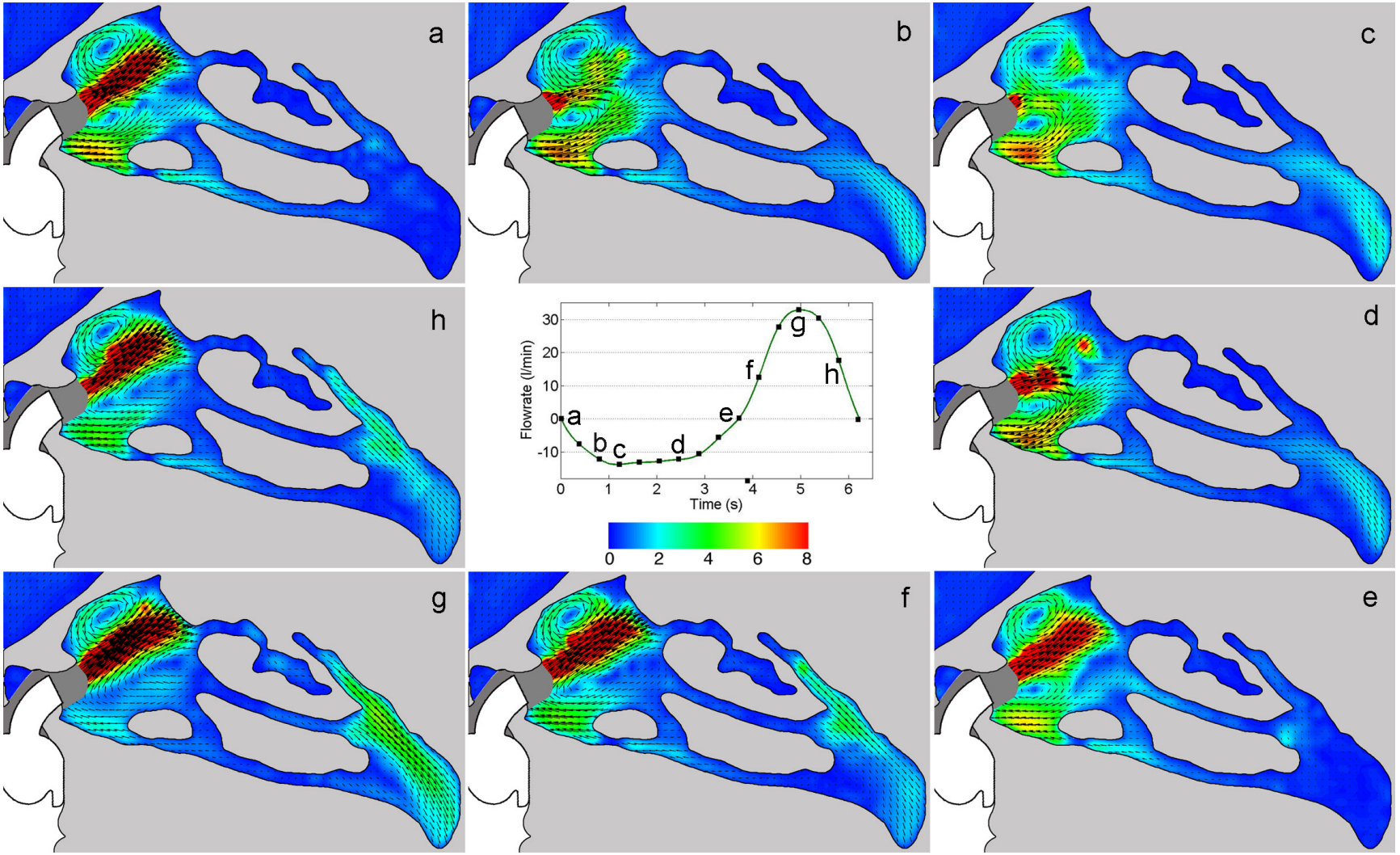

Figure 79. Phase averaged, absolute velocity fields (m/s) through a cross-section of the left choana with a medium cannula at 30 l/min (data unavailable in the dark grey region)

not observed. Convincing evidence to the contrary, however, is given in Figure 85 where the peak expiration results obtained in steady flow conditions are juxtaposed with those obtained with oscillatory flow. The vortex in the anterior recess posterior of the nasal valve created by the high shear of the inspiratory jet persists throughout the entire respiratory cycle, whereas in steady flow conditions expiratory flow flushed out this vortex. The quasi-steady flow assumption is therefore not valid in the nasal cavity on expiration with NHF. During inspiration on the other hand, the strong correspondence shown between the steady and oscillatory results in Figure 86 suggests that a quasi-steady flow assumption during inspiration is valid.

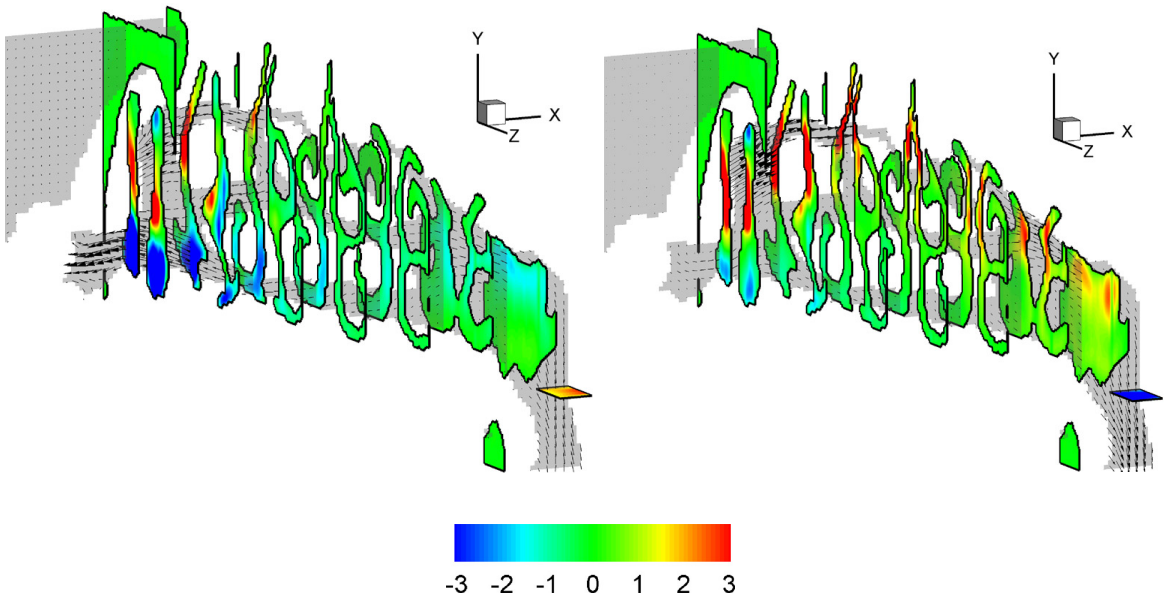

Figure 84. Velocity contours (m/s) displaying x velocities through coronal slices and y velocities through an axial slice of the reconstructed velocity volume at (a) peak expiration (phase 'c') and (b) peak inspiration (phase 'g'), with 30 l/min cannula flow.

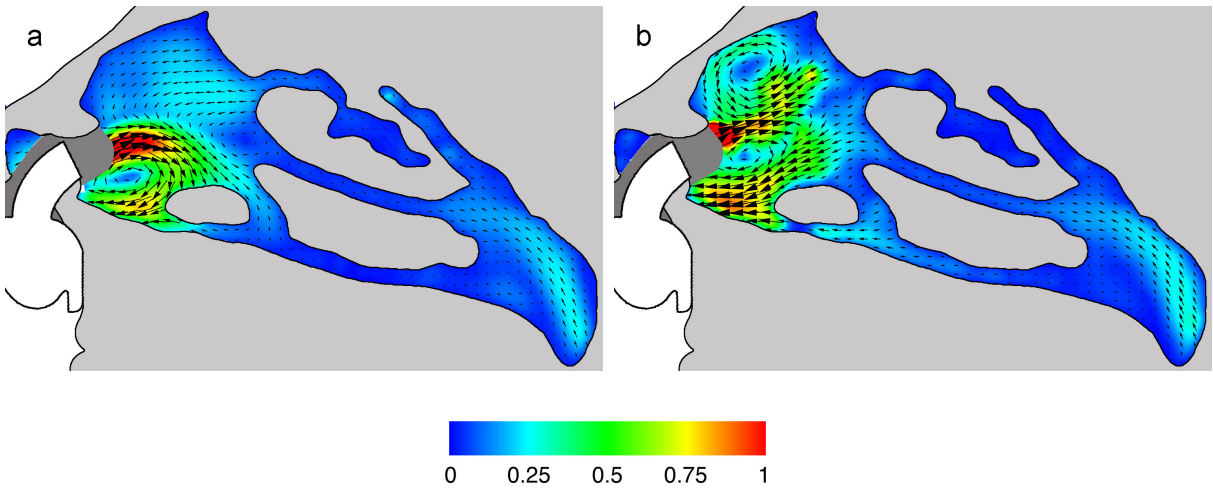

Figure 85. Comparison of a) steady and b) unsteady normalised velocity maps (m/s) obtained at peak expiration with a medium cannula flowrate of 30 l/min

A quasi-steady flow assumption was shown to be inaccurate at the inflection between inspiration and expiration during natural breathing where the rate of change of flowrate was -52.2 l/min s^{-1}. At the inflexion between natural expiration and inspiration where the flow acceleration was 38.3 l/min s^{-1}, a quasi steady flow assumption was shown to be more accurate, although discrepancies were found. With NHF, a quasi-steady flow assumption was found to be credible on inspiration where the flow acceleration and deceleration maximums were 19.6 and -32 l/min s^{-1}. Any attempt to find a relationship between the appropriate usage of a quasi-steady flow assumption with the maximum rate of change of flow was, however, rendered invalid by clear evidence that the assumption is invalid during expiration with NHF when the flow wave was effectively flat and the rate of change of flowrate zero.

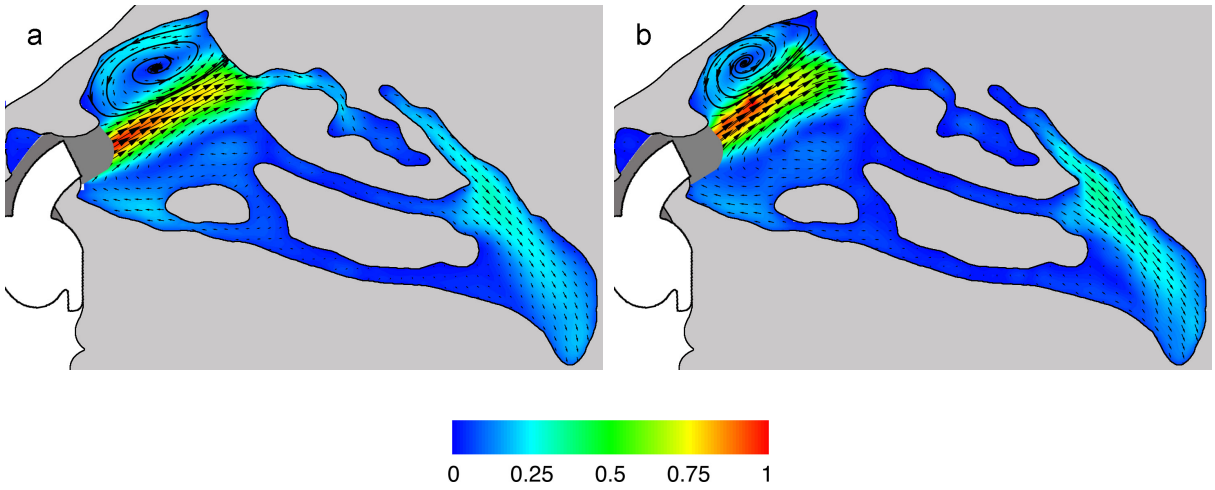

Figure 86. Comparison of a) steady and b) unsteady normalised velocity maps (m/s) obtained at peak inspiration with a medium cannula flowrate of 30 l/min

Dysart et al. (2009) have reviewed the proposed mechanisms by which NHF provides respiratory support. Increased airway oxygen concentrations with NHF have been largely attributed to the suggestion that cannula flow washes out nasopharyngeal dead space. Unlike a fish, where the water enters through the mouth and exits the gills, and all of the fresh water is available for gaseous exchange, approximately 30% of the inspired tidal volume during normal breathing in a human is reused from the previous breath. Anatomical dead space is the volume of gas in the conducting airways that remains in the airways to be re-breathed at the end of expiration and is about 150 ml in an adult male. The in vivo volume of the model 2 geometry is 56.4 ml; therefore, the upper airway contributes a significant portion of the total anatomical deadspace. Although anatomical dead space gas helps to warm and humidify inspired gas through mixing, it reduces the alveolar oxygen concentration and increases the alveolar carbon dioxide concentration. Having already taken part in the exchange of oxygen and carbon dioxide in the lung, the dead space at end-

expiration has a higher fraction of carbon dioxide. Fresh gas introduced by the cannula is thought to wash out the dead space in the nasal cavity and reduce the amount of carbon dioxide recycled back into the lung and contribute to the increase of oxygen fraction seen clinically with NHF (Dysart et al. 2009; Lund et al. 1996). A comparable therapy called tracheal gas insufflation (TGI) delivers air via a tube placed through the nose into the trachea and has been demonstrated by numerous studies to promote CO_2 elimination and enhance oxygen concentrations (Dysart et al. 2009).

Figures 83 and 84 reveal a large-scale clockwise rotation of the flow in the nasal cavity with NHF. In Figure 83, the flow along the nasal cavity floor travels in a forward direction throughout the respiratory cycle. In the third anterior cross-section of Figure 84a, the flow at the top of the nasal cavity is 3.2 m/s and at the bottom is -2.6 m/s. The cannula jet drives the flow backward, through the upper portion of the nasal cavity until the flow turns in the nasopharynx and flows forwards along the nasal cavity floor. The flow is then expelled through the nostrils along the bottom of the nasal valve under the cannula jet. It can be seen in Figure 83 and Figure 84b, that even during peak inspiration, when peak inspiratory demand (32.9 l/min) exceeds the cannula flowrate (30 l/min), air still travels along the nasal floor in a proximal direction and is discharged out the posterior portion of the nostrils. Fresh gas introduced by the cannula flushes the dead space in the nasal cavity, which may reduce the amount of carbon dioxide recycled back into the lung and contribute to the increase of oxygen fraction seen clinically with NHF. Moreover, turbulent mixing generated by the cannula jet (Re = 3730 at 30 l/min) enhances carbon dioxide removal. The current study provides the first visualisation of the washout effect and reinforces the in vivo evaluations outlined in Dysart et al. (2009). In contrast to the nasopharyngeal washout flow pattern predicted by Walsh et al. (2009), flow in an adult nasal cavity with NHF is now known to continuously travel forwards through the lower meatus, discharge through the nostrils below the cannula jet, and be inspiration and expiration dependent.

6.4.3 Small Cannula

Cross-sections of the reconstructed velocity volume at peak expiration and inspiration are shown in Figure 87. Phase averaged velocity fields of the cyclical flow in the nasal cavity with a small cannula at 30 l/min are presented in Figure 88 for eight phases. The overall flow structure is similar to that of the medium cannula; however, forcing the same flowrate through smaller diameter prongs creates a more concentrated and faster jet that causes two key differences. Firstly, the jet emanating from the small cannula is turned to exit the nostrils at a slightly later point in the expiratory period because the small cannula jet has a higher

momentum. This is visible by comparing Figures 83b and 88b. The maximum small cannula jet velocity measured was 19.0 m/s, which occurred in phase 'e' at the closest measurable region to the prong termination. This is lower than the theoretical average velocity exiting the cannula of 23.6 m/s because data was unavailable directly in front of the prong and the jet disperses rapidly in the vertical direction upon exiting the prong, as evident in Figure 87. It is also likely the maximum velocity was biased because the smallest possible interrogation window was 44% of the prong's diameter.

The second key difference is that the vortex under the jet, which was present across the majority of the respiratory cycle with the medium cannula, is instead absent with the small cannula in all but the expiratory phases b–d. Instead the higher speed of the small cannula jet increases the strength of the large-scale clockwise rotation throughout the nasal cavity, which enlarges and moves the centre of the recirculatory feature towards the posterior, much like what was observed at peak inspiration with the medium cannula. During peak inspiration with the small cannula, the forward flow along the nasal floor is indeed distinctly stronger in Figure 87b than in Figure 84b. The stronger rotation of the flow is thought to increase the deadspace washout effect.

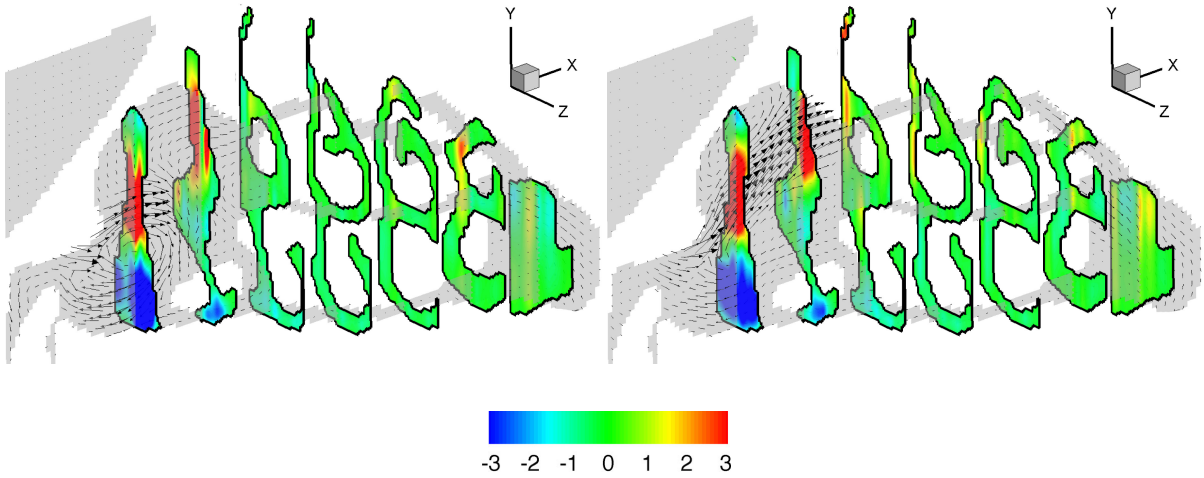

Figure 87. Velocitycontours (m/s) displaying x velocities through coronal slices of the reconstructed velocity volume of the right choana at (a) peak expiration (phase 'c') and (b) peak inspiration (phase 'g'), with a small cannula at 30 l/min

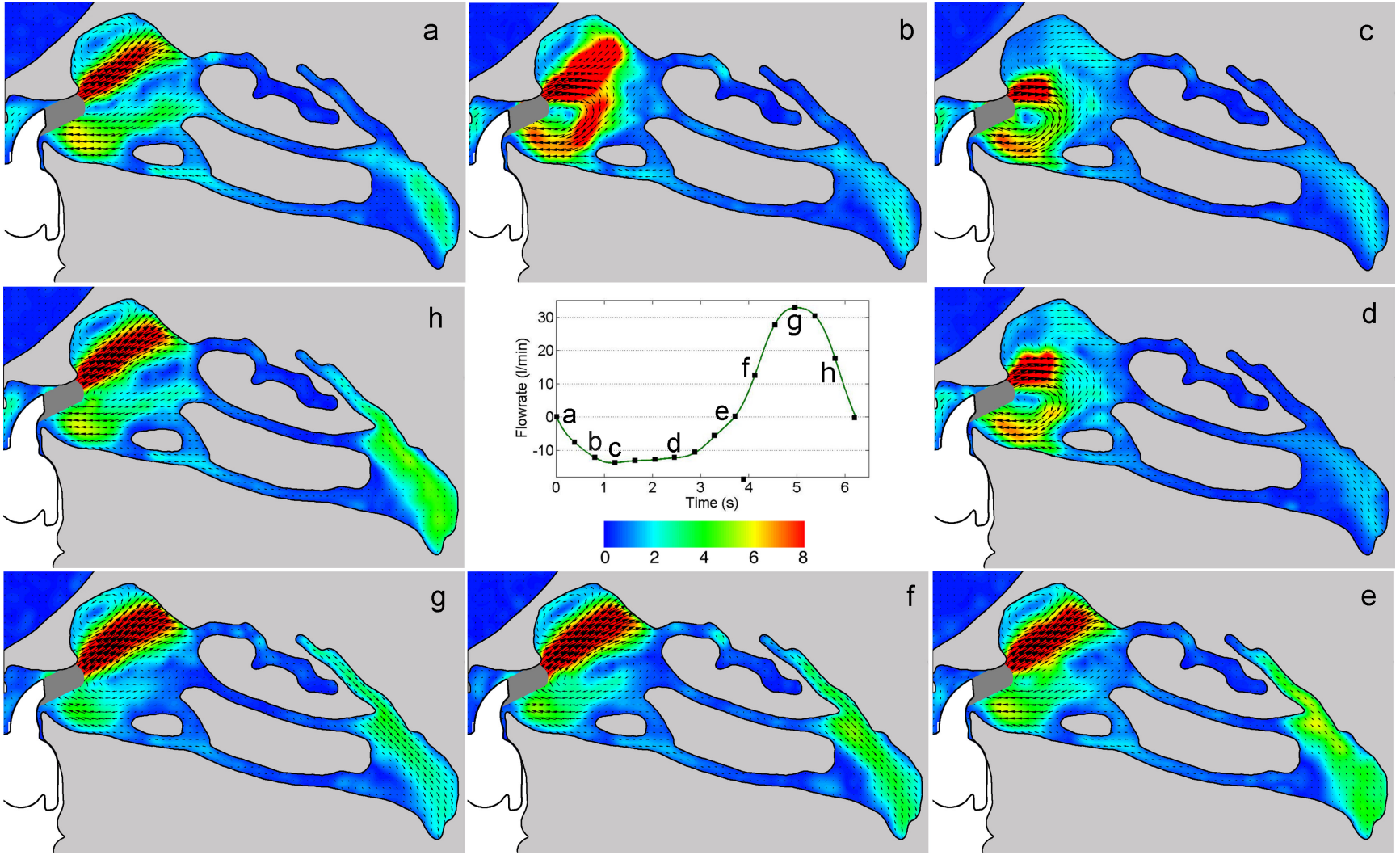

Figure 84. Phase averaged velocity fields (m/s) through a cross-section of the left choana with a small cannula at 30 l/min (data unavailable in the dark grey region)

6.4.4 Mouth Open Measurements

Coronal and axial cross-sections of the reconstructed velocity volume at peak expiration and inspiration are shown in Figure 89. Figure 90 presents eight phase-averaged velocity maps measured across the respiratory cycle on a mid sagittal plane bisecting the pharynx during NHF assisted breathing with 30 l/min cannula flow. The velocity maps are in a vertical orientation with the oral cavity to the left of each image, the nasopharynx in the top right and the termination of the laryngopharynx at the bottom. The flowrates through the nasopharynx, mouth and larynx were quantified by integrating the orthogonal velocity component over the cross-sectional areas illustrated in Figure 89 at each of the 15 time steps measured. The normalised results are presented in Figure 91 with distal (towards the lungs) flowrates considered positive. The actual lung flowrate is a plot of the system prescribed flow wave. The net lung flowrate is the summation of the measured mouth and nasal flowrates by mass conservation, and the measured lung flowrate is the flowrate calculated over the axial cross-section at the throat of the domain. The deviation of the net and measured lung flowrates from the actual lung flowrate gives an indication to the level of error in this flowrate measurement technique. Note that the net lung flowrate has the accumulation of errors from both the measured mouth and nasal flowrates. Each measured flowrate is an under estimate of the actual flowrates because of the limited grid resolution and averaging effect of the correlation windows. The trends, however, are considered to be accurate because the errors are systematic. The leakage flowrate, which is considered negative because it flows in a proximal direction, is calculated by subtracting the known constant flowrate of 30 l/min from the nasal flowrate.

At the beginning of expiration when the net lung flowrate is zero (Figure 90a), flow from the cannula is split between the two possible pathways of turning and exiting through the nostril or travelling through the nasal cavity and pharynx to exit through the mouth. Approximately 40% of the cannula flow exits through the mouth, which suggests that this pathway has a 60% higher resistance. The flow that does exit the mouth is first accelerated through the velopharynx and travels down into the larynx attached to the posterior wall before rising up through the oral cavity on the anterior wall. The maximum velocity in the velopharynx in Figure 90a is 5.3 m/s. The flow separates off the back of the tongue and turns through the oral cavity attached to the roof of the mouth. It is likely that the constriction at the velopharynx has a large associated resistance because the nasal valve is known to result in a large pressure drop during natural breathing and can only be higher with NHF, yet the flow preference is to escape through the nostrils.

At the onset of expiration (Figure 90b), the flow that passes through the nasopharynx is forced out through the mouth, turning through a sharp bend around the soft palette without first descending along the posterior wall into the larynx and ascending along on the posterior wall as was evident in Figure 90a. The same flow pattern as Figure 90b is visible at peak expiration in Figure 90c with flow still separating at the same location off the back of the tongue. At peak expiration, the flow through the nasal cavity reaches a minimum and the leakage flowrate a maximum. All the expired volume exits through the mouth in addition to approximately 22% of the cannula's 30 l/min. It is worth mentioning at this point that during mouth-open breathing the net flow through the nasal cavity is distal throughout the respiratory cycle. In saying that, the large-scale clockwise rotation observed in the nasal cavity during mouth-closed breathing still remains during mouth-open breathing. The flow along the nasal floor in the anterior most cross-sections of Figure 89 can be seen to travel forwards during both peak expiration and inspiration. The fact that the net flow is always distal and that large-scale recirculation persists are important points because this means the nasal cavity is continually being flushed with fresh air by not one but two mechanisms during mouth-open breathing. At peak expiration, of the total flow entering the upper airways from the cannula and lungs, 55% exits through the leakage area, while the remaining 45% exits through the mouth. The percentage of air exiting through the leakage area at peak expiration is therefore 5% lower than the 60% measured at the transition from inspiration to expiration. This is likely because of lower velocities and reduced resistance at the velopharynx, owing to more flow exiting through the mouth. The maximum velocities in Figure 90c are 3.0 m/s in the velopharynx and 6.7 m/s in the oropharynx.

At the transition from expiration to inspiration shown in Figure 90e, the flow from the cannula continues to turn around the soft palette as it had done during expiration. The fact that this flow pattern is different from the flow pattern at the inflexion from inspiration to expiration in Figure 90a, is categorical evidence of flow time dependence and that the quasi-steady flow assumption is not only invalid in the nasal cavity but also in the pharynx during mouth-open breathing. Further evidence to this conclusion is a vortex in the separation region just above the tongue that does not form until the second half of the expiratory period in Figure 90d. Most interesting is the fact that at the two equivalent zero lung flowrate inflexions, a smaller percentage of the cannula flow exits through the mouth at the transition from expiration to inspiration (phase 'e'). At phase 'e', 35% of the cannula flow passed through the nose and exited through the mouth; 5% less than in phase 'a'. The flow pattern in Figure 90e therefore has a greater associated resistance and pressure loss through the pharynx than the flow pattern shown in Figure 90a. The maximum velocity in the velopharynx in Figure 90e of 5.4 m/s is almost identical to the 5.3 m/s measured in Figure 90a; however,

this slightly larger velocity will contribute towards the 5% increase in resistance along with the kinetic energy lost in the vortex on the tongue, which is not present in phase 'a'.

The vortex in the separation region on the tongue persists until the flow entering through the mouth at peak inspiration washes it out. For the 0.7 seconds before and after peak inspiration, inspiratory demand was such that the flow in the mouth reversed and air was drawn in through the mouth. At peak inspiration the flow through the nasal cavity reached a maximum and the leakage flowrate reached a minimum. Of the total peak inspiratory demand, 57% was drawn through the nasal cavity (61% of the cannula flow), 29% entered through the mouth and 14% was unaccounted for due to measurement error. That at least 29% of the flow is drawn in through the mouth is of clinical concern because this dry room air dilutes the heated, humidified and possibly oxygen enriched air supplied by the cannula, and nor does it receive the air-conditioning benefits of passing through the nasal cavity. It is possible this could lead to complaints of dry mouths; however, flow only enters through the mouth for 22% of the respiratory cycle, and warmed and humidified air from the cannula circulated through the nose and mouth for the remainder of the respiratory cycle is likely to replenish mouth moisture levels. The flow that is drawn through the nasal cavity accelerates to a maximum velocity of 7.9 m/s in the velopharynx at peak inspiration (Figure 90g), forms a separation region off the soft palate and merges with the stream of air entering through the mouth, which has a maximum velocity of 2.7 m/s. After peak inspiration in Figure 90h the vertical flow profile through the mouth is much more evenly distributed than before peak inspiration in Figure 90f and the separation region off the tongue does not yet exist.

There are two important points to emphasise regarding the effect of mouth-open breathing on the airway pressures delivered by NHF, remembering the basic concept that the maximum and minimum airway pressures occur at peak expiration and inspiration, respectively. Firstly, the fact that flow exits the mouth at peak expiration can only mean that having the mouth open reduces the upper airway resistance and peak expiratory pressure. Secondly, since air enters the mouth during peak inspiration, the upper airway resistance must again be reduced and the minimum pressure in the lungs made less negative. Mouth-open breathing on inspiration therefore increases the mean airway pressure, whilst on expiration the contribution is towards a lower mean airway pressure. The net result on the overall mean airway pressure will be dependent on a patient's individual anatomy, and breathing pattern, as well as the cannula flowrate. For the conditions measured here it cannot be deduced whether the mean airway pressure is increased or decreased relative to mouth-closed breathing with NHF; however, it can be stated that in model 3 the mean airway pressure with mouth-open breathing and 30 l/min would have been higher than mouth-

closed or mouth-open natural breathing because during the inspiratory phases shown in Figures 90f and 90h the flow was outwards through the mouth. This flow through the mouth has an associated pressure loss that would have increased the pressure in the lower airways and would not have occurred during natural breathing. It must be stated, however, that these conclusions should also be tested in an in vivo environment because the position of the soft palate changes for different modes of breathing and model 3 was constructed with the soft palate in a position for mouth-open breathing with NHF.

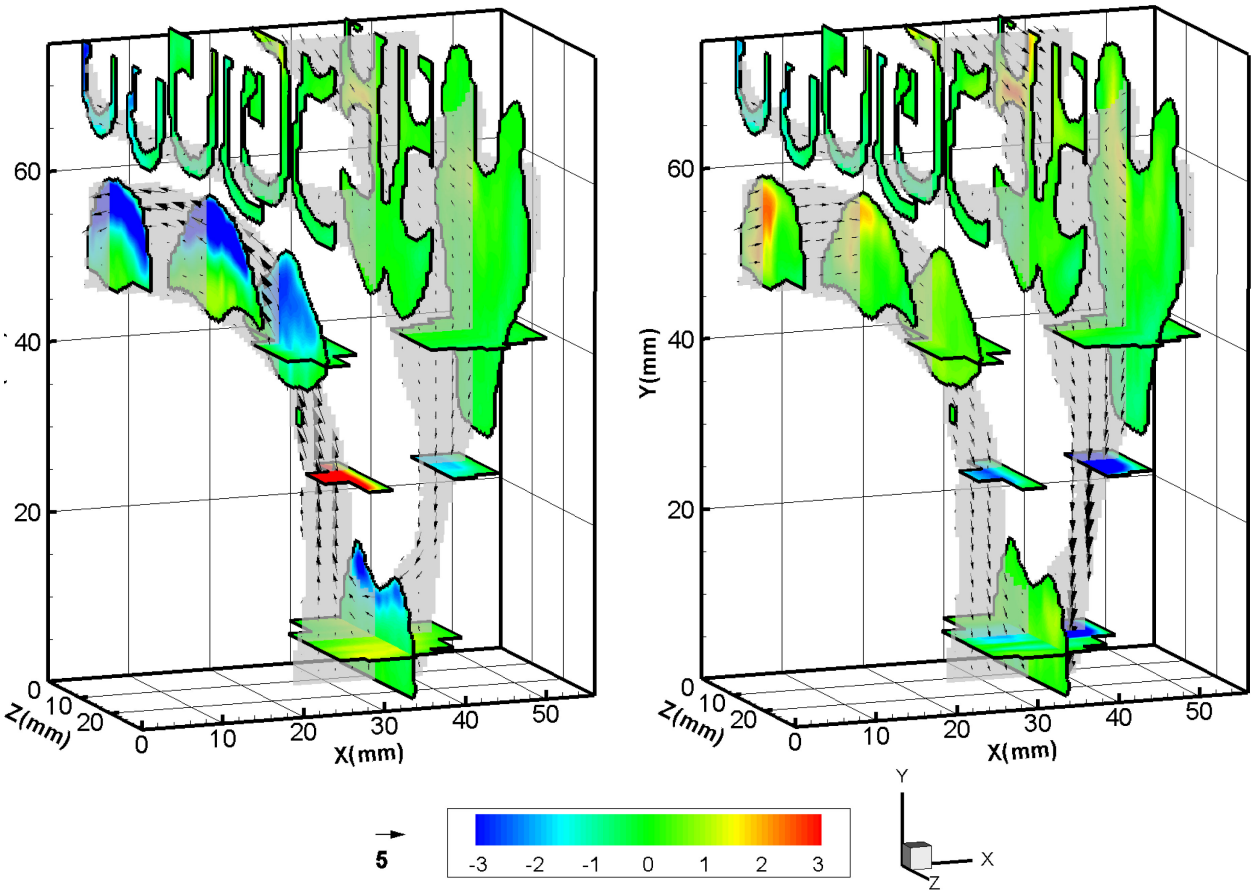

Figure 89. Velocity contours (m/s) displaying x velocities through coronal slices and y velocities through axial slices of the reconstructed velocity volume during natural (a) peak expiration and (b) peak inspiration (phases c and g respectively).

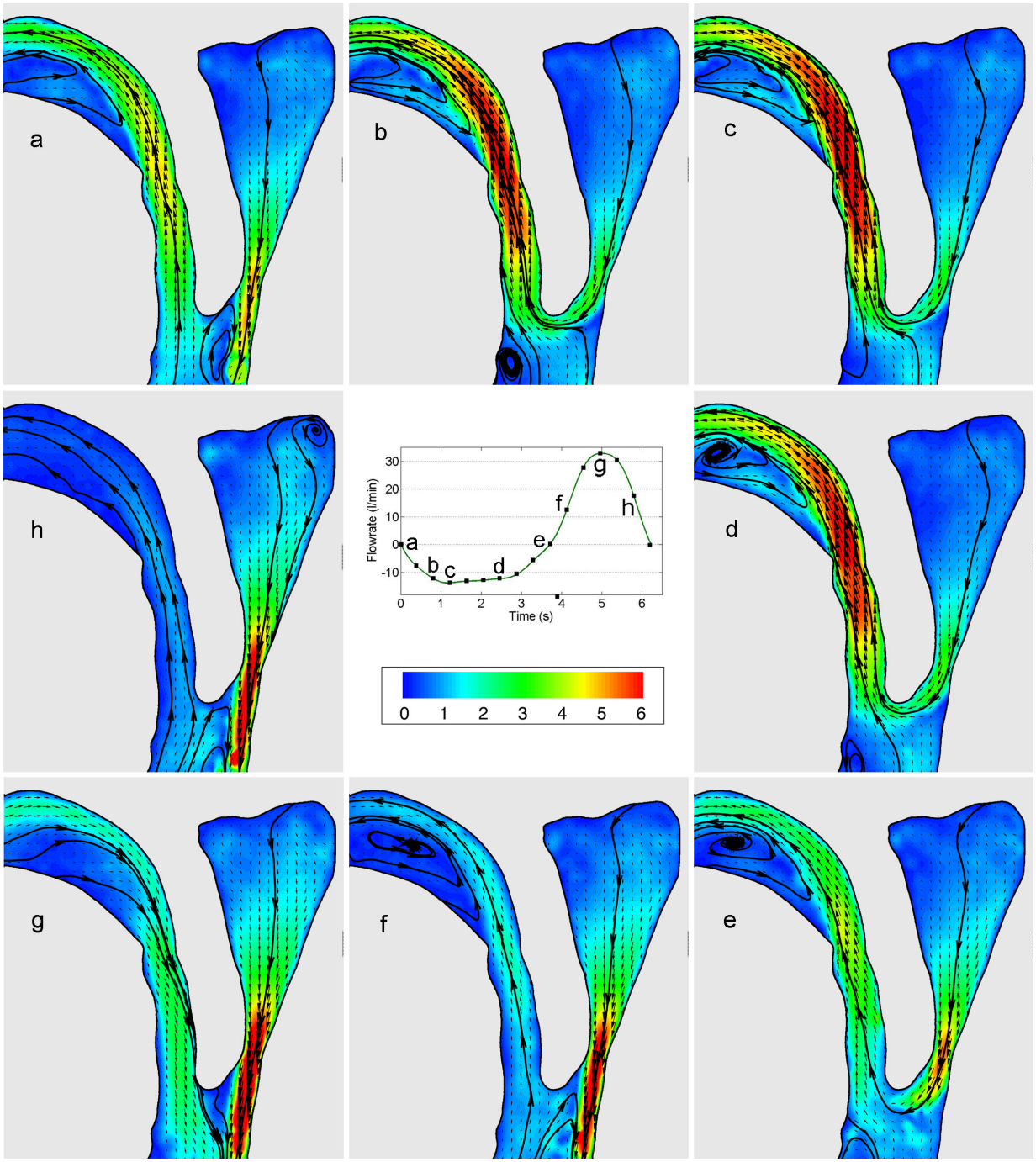

Figure 90. Phase averaged velocity fields (m/s) through a cross-section of the pharynx with a medium cannula at 30 l/min

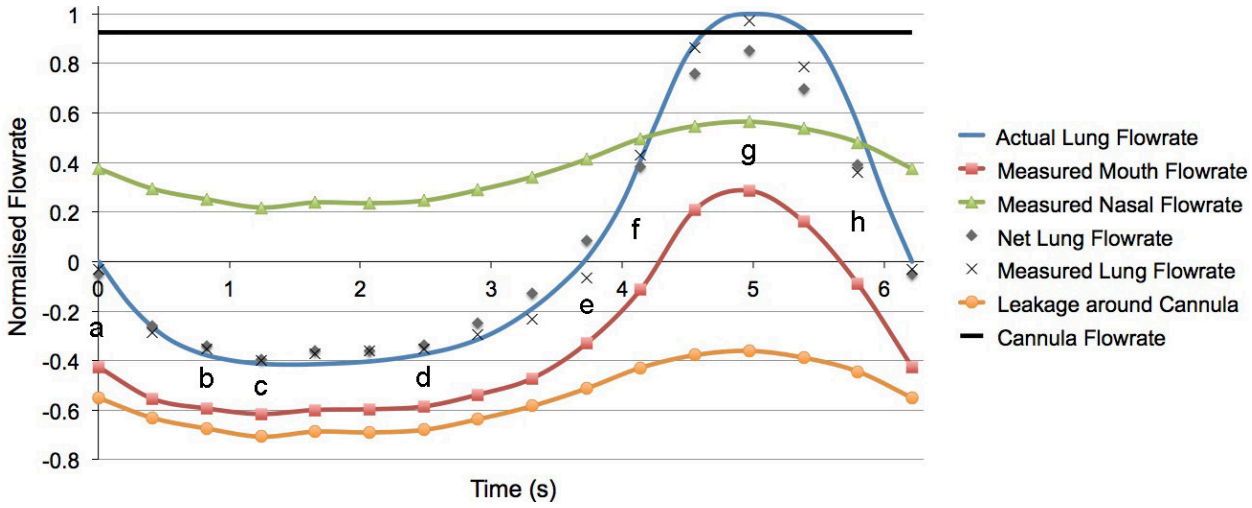

Figure 91. Measured flowrates through the pharynx domain (an inspired flow directions is considered positive).

6.5 Conclusions

Time resolved stereo-PIV has been used to measure the distribution and velocity of the airflow in anatomically accurate nasal cavity models with physiologically correct oscillatory flows during natural and NHF assisted breathing. Measurements were conducted with medium and small cannulae flows of 30 l/min in mouth closed conditions and the flow field throughout the pharynx measured with NHF in a model with the mouth open. In vivo flow measurements were Reynolds and Womersley number matched and applied in vitro. Velocity maps were measured at 15 breath phases and at up to 30 sagittal slices traversed through the complete nasal cavity at 1.5 mm increments. Three dimensional velocity volumes were constructed by interpolating between measurement planes. Despite the Womersley numbers of 1.9 and 1.8 during natural and NHF breathing, respectively, being significantly lower than in other studies where quasi-steady flow has been assumed, results show that a quasi-steady flow assumption for the flow in the nasal cavity is invalid for both natural and NHF breathing. Flow time dependence was particularly evident at the transition between inspiration and expiration during natural breathing, in differences observed between expiratory flow patterns obtained from steady and oscillatory conditions with NHF, and in the pharynx where the flow patterns measured at the two flow inflexions were significantly different. A large-scale recirculatory feature in the nasal cavity during NHF has been found to continuously flush the nasopharyngeal dead space, which may reduce the amount of carbon dioxide recycled back into the lung and increase of oxygen fraction. The flowrates through the mouth and nasal passages during mouth-open breathing were quantified by integrating velocity over cross-sections taken through the reconstructed

velocity volume. The net flow through the nasal cavity was found to travel continuously in distal direction and room air was drawn in through the mouth at peak inspiration. Of the total peak inspiratory demand, 57% was drawn through the nasal cavity (61% of the cannula flow), 29% entered through the mouth and 14% was unaccounted for due to measurement error. At peak expiration, of the total flow entering the upper airways from the cannula and lungs, 55% exits through the leakage area, while the remaining 45% exits through the mouth. Mouth-open breathing with NHF reduces the peak expiratory pressure and raises the minimum inspiratory pressure.

7 Supplementary Investigations

This chapter presents a number of auxiliary projects conducted over the course of the current work that both supplement the PIV measurements and are relevant to NHF. The first project that will be discussed is a series of in vivo pressure and flowrate measurements that were conducted in order to confirm and further eluciate findings found in the literature survey and in PIV measurements. The second project presented discusses stereo-PIV measurements taken within the human vocal tract using methodologies developed for measuring nasal flows. Lastly, a third project included high-speed shadowgraph measurements to determine the presence or absence of airborne droplets in the air exhaled from the nostrils during NHF assisted breathing.

7.1 In Vivo Pressure and Flow Investigations

The series of in vivo pressure and flowrate measurements were conducted with approval from the University of Canterbury Human Ethics Committee (ref. 2007/115).

7.1.1 NHF Generated Pressures

It has been suggested that the elevated airway pressure developed by NHF is predominantly dependent on a relationship between the internal diameter of the nares and cannula's prong diameter (Kahn et al. 2007; Locke et al. 1993; Sreenan et al. 2001). This argument is based on the idea that the leak around the prongs produces the most significant resistance to breathing and small changes in leakage area have a large effect on airway pressures. There have been a very limited number of studies measuring airway pressure during NHF and none have presented nostril areas alongside measured airway pressures. In the current work, a pilot study with 5 volunteers was performed to attempt to find a correlation between airway pressures generated with NHF and nostril area.

Oral cavity pressure measurements were performed across a 15–50 l/min range of NHF flowrates during mouth closed nasal breathing. Cannula flowrates were generated from a tank of medical compressed air and measured using a TSI-4040 flow meter calibrated against a molbox1+™ flow terminal (http://www.dhinstruments.com) incurring an uncertainty of ± 0.1 l/min. A flexible plastic tube with a bore diameter of 2.5 mm was held behind the teeth with pursed lips and connected to a Setra Multi-sense pressure transducer (model 260). The pressure transducer was calibrated with a water manometer (E.Schiltkrecht), which had an uncertainty of ± 0.01 cm H_2O. Sampled voltages over a 0–10 cm H_2O pressure range fitted to a linear line with a maximum deviation of less than 0.02 cm H_2O. For the oral cavity pressure to give an indication of airway pressures, the soft palate was required to be in a neutral position such that oral cavity was open to the upper airways. It was necessary to train each subject to keep their soft palate in a neutral position. Immediate feedback on when the soft palate was in a neutral position or not was given by displaying the oral cavity pressure in real time and ensuring the pressure rose and fell during nasal tidal breathing. Two of the 5 subjects were unable to control the position of their soft palate despite lengthy practice. Mygind et al. (1977) and Foxen et al. (1971) reported from their respective studies that 17 and 25% of patients were unable to relax their soft palate. Measurements of oral cavity pressure with only 3 people were investigated regardless because this was only intended to be a pilot study and clinical methods such as rhinomanometry, which require careful insertion of nasopharyngeal catheters, were not appropriate within a laboratory environment. Pressure measurements were conducted with the medium sized cannula on one female (aged 23 years-old) and two male (aged 23 and 35 years-old) subjects. Conditions represented quiet breathing with each subject at rest and having worn the cannula for at least 5 minutes before measurements were taken at each flowrate. The nostril (external nare) areas of each subject were measured by taking an image normal to each nostril with an in-plane ruler for reference. The nostril area was then traced on the computer, the number of contained pixels measured and converted into mm^2 with the known image magnification squared. The results are displayed in Table 20. Pressure measurements were captured at 100 Hz over 5 breaths and the results averaged to yield mean oral cavity pressures that are indicative of mean upper airway pressures. The results are presented in Figure 92.

Table 20. Nostril sizes for oral cavity pressure measurement subjects

Subject	Age (years)	Nostril Areas (mm^2)			% area occluded by prong
		Left	Right	Average	
Male 1	23	70	70	70	22
Male 2	33	85	79	82	18
Female	23	64	60	62	24

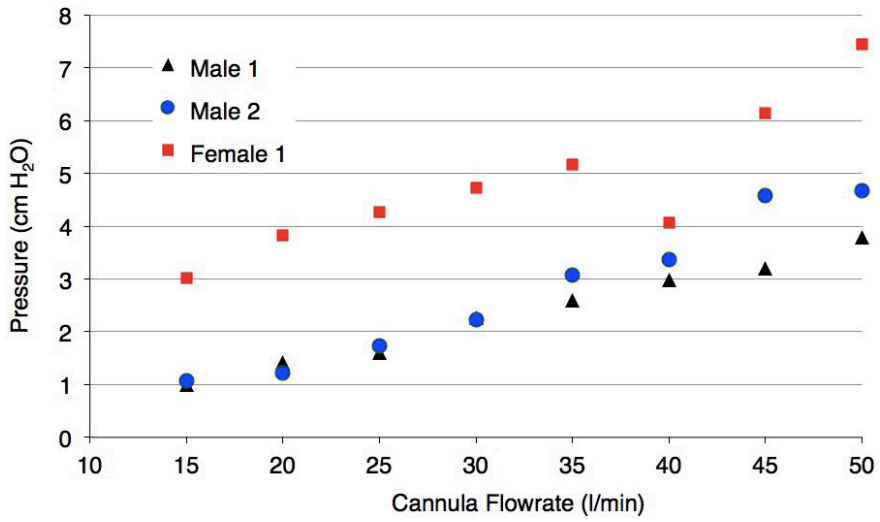

Figure 92. Mean oral cavity pressures measured with a medium cannula at flowrates of 15-50 l/min

It is clear that NHF creates very different airway pressures in different people for a given flowrate. Nevertheless, a positive relationship between airway pressure and cannula flowrate that was approximately linear existed for each subject. It also appears that the gradient of each line, and therefore change in resistance for a given change in cannula flowrate, is approximately constant for each subject. Apparent irregularities in the data for each subject can be attributed to fluctuations in breathing pattern, swallowing, and the position of the soft palate. The pressures of the female are significantly offset from the two male subjects for whom the pressures were more similar. The female did have the smallest nostrils and therefore smallest leakage area so it was expected she would have the highest airway pressures. Male 2 had the largest nostrils, however, it was male 1 who had smaller airway pressures. This discrepancy highlights the fact that there are factors other than nostril size that have a significant effect on the airway pressures developed by NHF. Future studies should be performed in a clinical environment where a nasopharyngeal catheter can be used to avoid issues with controlling the soft palate position. Details such as nostril area, nasal valve area and breathing flowrates should be recorded.

7.1.2 Mouth-Closed and -Open Pressures

It was shown in Chapter 6 that mouth-open breathing must reduce upper airway resistance and therefore lower airway pressures. To determine the degree of reduction relative to mouth-closed breathing pressure measurements were conducted in vivo during mouth-closed and mouth-open breathing on a healthy 23 year-old male. This study was a proof of concept enquiry and again taken in a laboratory environment without such methods as rhinomanometry. A common reference location where both mouth-open and mouth-closed breathing pressures could be compared first needed to be elected. Clearly the mouth could no longer be used and it was difficult to maintain a constant probe location in the nasal vestibule. Due to the confined nature of the nasal vestibule while wearing NHF, it is also likely that such as a probe in the nasal vestibule would have interfered with the flow and pressure fields. An original technique was therefore performed. A Pitot probe was positioned inside the cannula's manifold coaxially in a region of circular cross-section and orientated to measure total pressure using the same calibrated pressure transducer. The total pressure in the manifold was then measured across a 15–50 l/min range of flowrates using the same flow and transducer apparatus described in previous sections 7.1.1. The cannula was then worn during both mouth-closed and mouth-open breathing. Static pressures at the end of the prong in the nasal vestibule during both conditions were inferred by subtracting the total pressure in the manifold at the corresponding cannula flowrates. Pressures were acquired at 100 Hz over 5 breaths and the results averaged to yield mean nasal vestibule pressures. The normalised results for the total pressures in the manifold and inferred nasal vestibule static pressures during mouth-closed and mouth-open breathing are presented in Figure 93.

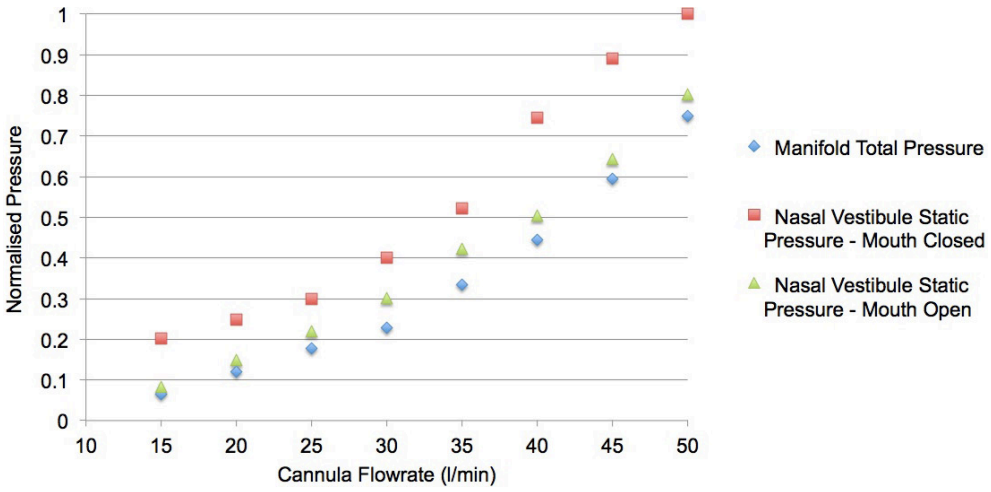

Figure 93. Normalised mean manifold total pressure and inferred nasal vestibule static pressures during mouth closed and mouth-open breathing

The results show that mean nasal vestibule and by extension upper airway pressures, are indeed lower during mouth-open breathing when compared with mouth-closed breathing for a given person and flowrate. The Reynolds numbers of the flow exiting the prong for the lowest and highest cannula flowrates of 15 and 50 l/min are 2110 and 7040. The total pressure in the manifold can be fitted to a second order power curve ($y = 0.0003x^2$) with a R^2 value of 0.995, which is consistent with turbulent flow. The shape of the manifold is complex and it is likely the flow in the manifold at a flowrate of 15 l/min is also unsteady. The pressure in the nasal vestibule also appears to increase proportionally with the square of flowrate, which suggests that the flow in the nasal vestibule is also turbulent. The pressures at 45 and 50 l/min cannula flowrates are lower than what a power law fitted to lower results would predict, which is likely due to the distensibility of the nasal vestibule. The oral cavity pressure measurements shown in Figure 92 depict more of a linear relationship between pressure and cannula flowrate, which indicates that perhaps for the majority of the respiratory cycle, most of the flow through the upper airways is laminar.

7.1.3 Mouth-Open Flowrates

The mouth open results in Chapter 6 also revealed that with a NHF flowrate of 30 l/min the net flow through the nasal cavity was in the inspired direction throughout the respiratory cycle, and outwards flow through the oral cavity prevailed. It was of interest to investigate the effect of cannula flowrate on the amount of air that exited through the oral cavity. The flowrates exiting the mouth with cannula flows from 15 to 50 l/min were measured in the same healthy 23 year-old male by passing orally expired flows through the TSI-4040 flow meter. Flowrates were sampled at 10 Hz for 5 breaths and averaged. The results are shown in Figure 94. The mean flow through the mouth can be seen to generally increase with increasing cannula flowrate, however, it appears to plateau between 40 and 50 l/min cannula flow. The plateau effect is likely to be a result of the compliance of the nasal cavity, i.e. at higher cannula flowrates and higher pressures, a larger proportion of the flow passes through an increasingly distended nasal cavity. The mean flowrate through the mouth measured by stereo-PIV through model 3 in Chapter 6 (Figure 91, page 155) was 10.7 l/min in an expired direction, which compares reasonably well with the 7.5 l/min average shown in Figure 94 for the same 30 l/min cannula flowrate given that the anatomies are different.

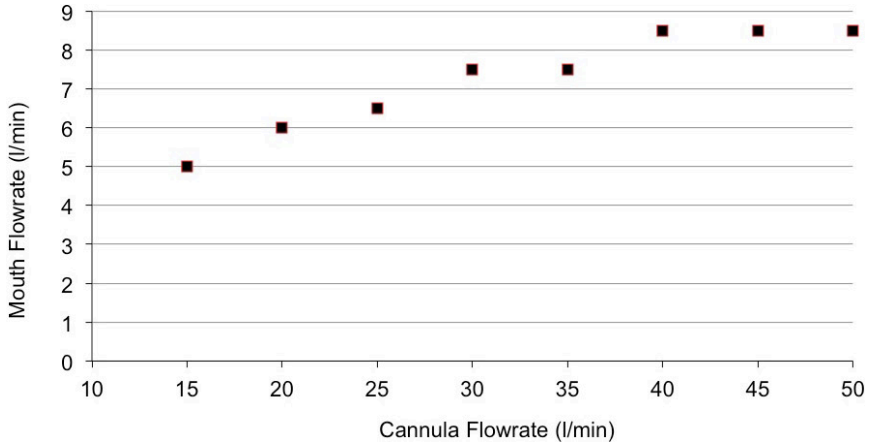

Figure 94. Flowrate exiting through the mouth with a medium cannula at flowrates of 15-50 l/min

7.2 Stereo-PIV Measurements of Articulatory Airflow

7.2.1 Introduction

The structures surrounding the airway, such as the larynx, soft palette (or velum), and tongue change their configuration to make the various sounds that make up speech. These structures are called articulators and are illustrated in Figure 95. The interaction of the airflow and the vocal articulators while speaking is not completely understood. The regions of articulation in the airway are flow obstructions that convert aerodynamic energy into acoustic energy and can be passive (stationary) such as the teeth and hard palette, or active (moving) in the case of the lower lip and tongue. By modifying the positions of the vocal articulators the various sounds that make up speech can be generated. A fricative is a hissing or buzzing consonant that is produced when a steady air stream is forced through a constriction in the oral cavity and the flow state becomes transitional or even turbulent. A three-dimensional computer model that can represent the motion of vocal articulators and simulate the airflow during vowels and consonants has been developed at the University of Auckland's Bioengineering Institute (Lu et al. 2009). The articulator geometries were constructed from Magnetic Resonance Imaging (MRI) scans taken during quiet breathing, and articulatory kinematics were obtained from Electromagnetic Articulography (EMA) and a video of the face. The goal of the current work was to conduct stereo-PIV measurements in the vocal tract in order to experimentally validate the computer model of speech.

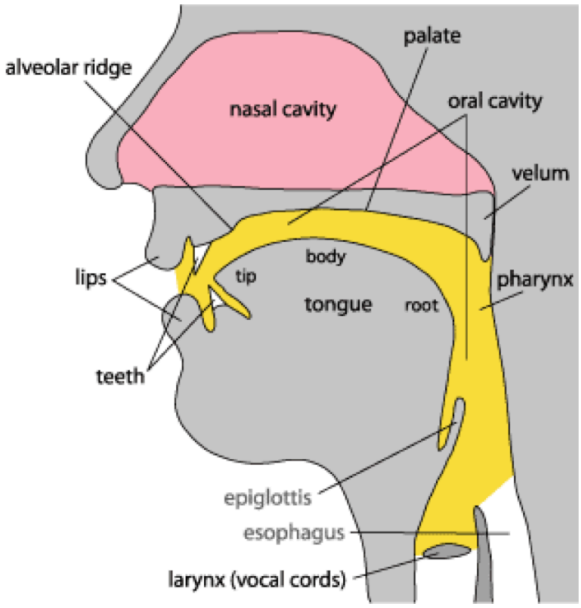

Figure 95. Schematic illustrating the key vocal articulators

7.2.2 Experimental Setup

The techniques discussed in Chapter 2 to manufacture accurate transparent silicone models of the nasal cavity were applied to construct flow phantoms of the vocal tract geometry. Models with simplified geometries representative of the production of 'sh' and 's' fricatives were constructed at 1.55 times scale (Figure 96). For these sounds the soft palette was considered to be closing the nasal cavity. The flow phantoms were submerged in the same reservoir and recirculating flow circuit presented in Figure 50 (page 102) in Chapter 5, again using a refractive index matched working fluid mixture of 39% water and 61% glycerine at 25°C. Steady in vivo expiration flowrates of 12 l/min were applied in vitro using Reynolds number matching (Table 21). Mean flow fields and a reconstructed flow volume were created from ensemble correlation averaging 200 image pairs at 26 sagittal locations traversed in 2 mm increments. Time delays ranged from 330–2000 μs to provide a maximum in-plane displacement of approximately 8 pixels. Iterative cross-correlation was performed to a final window size of 40 × 40 pixel^2 with a grid spacing of 1.4 mm. For details on the PIV apparatus refer to Table 15 on page 104. CT scans of the flow phantoms were taken to enable the accurate production of mask images and provide an identical geometry for numerical simulations. The original and model geometries were compared and the averaged RMS projections between the two surfaces calculated to be 0.50 and 0.57 mm for the 's' and 'sh' models, respectively, which correspond to approximately 2% of the throat diameter (25.4 mm).

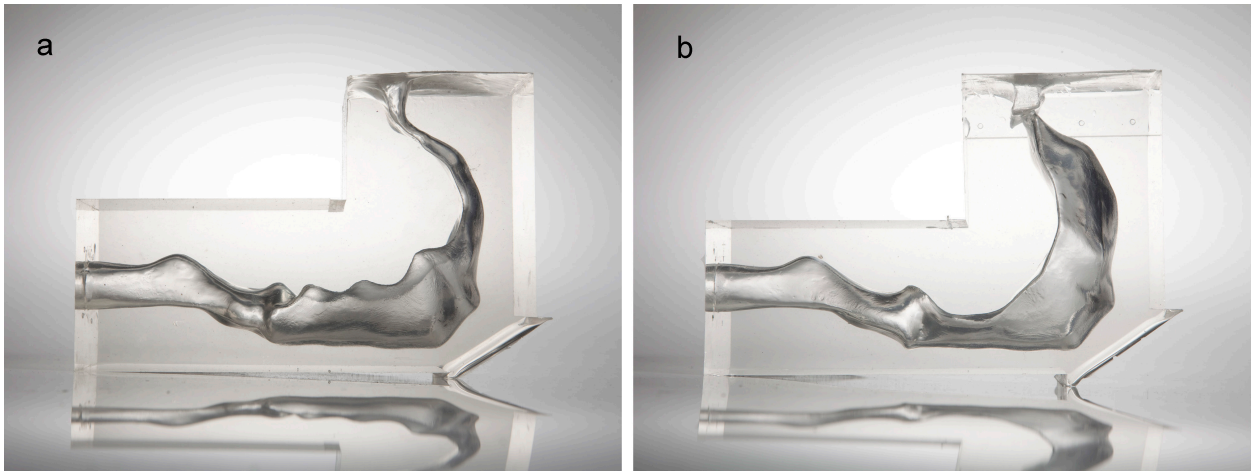

Figure 96. Silicone flow phantoms of the (a) 'sh' and (b) 's' fricative vocal tract geometries

Table 21. Flow in vivo and in vitro flow parameters

In Vivo (Dry Air)		Inlet *Re*	In Vitro (Water/Glycerine at 25°C)			
Flowrate (l/min)	Velocity (m/s)		ρ (kg/m^3)	μ (kg/ms)	Flowrate (l/min)	Velocity (m/s)
12	1.07	1060	1154	9.27×10^{-3}	9.2	0.36

7.2.3 Results and Discussions

Stereo-PIV results are presented for only the 'sh' model because this is an on going project and stereo-PIV measurements within the 's' model and numerical simulations are currently being performed and will be presented together in a journal paper at a later date. Vector lengths denote in-plane velocities and only every third vector is shown for clarity. Figure 97 shows the absolute velocity field through a mid sagittal cross-section of the vocal tract, where the throat of the model is in the right of the image and bends through the oral cavity to the left. The flow accelerates through the constriction above the tongue and exits the model as jet on an inferior trajectory. Self-assurance of this downwards flow can be gained by simply feeling the air direction by hand while producing the 'sh' sound. Flow is entrained from the surroundings into the jet, which interestingly has a maximum velocity of 6.3 m/s that occurs outside of the lips. This velocity is made up largely by the transverse velocity component as evident in Figure 98. Neighbouring planes also show this region of high transverse velocity; thus, mass and momentum appear to be conserved and the velocities genuine. The jet's asymmetry can be explained by the asymmetry of the geometry and it is likely that the solid surface of the reservoir wall in relatively close proximity to the exit resulted in

pressure reflections acting on the jet. The reservoir wall was parallel with a sagittal plane and was separated from the left face of the model by 2 mm, giving only 50 mm between the centre of the mouth's exit and the reservoir wall. The transverse velocity component is very low throughout the internal geometry except for a small region where the flow is disturbed by the irregular geometry of the larynx.

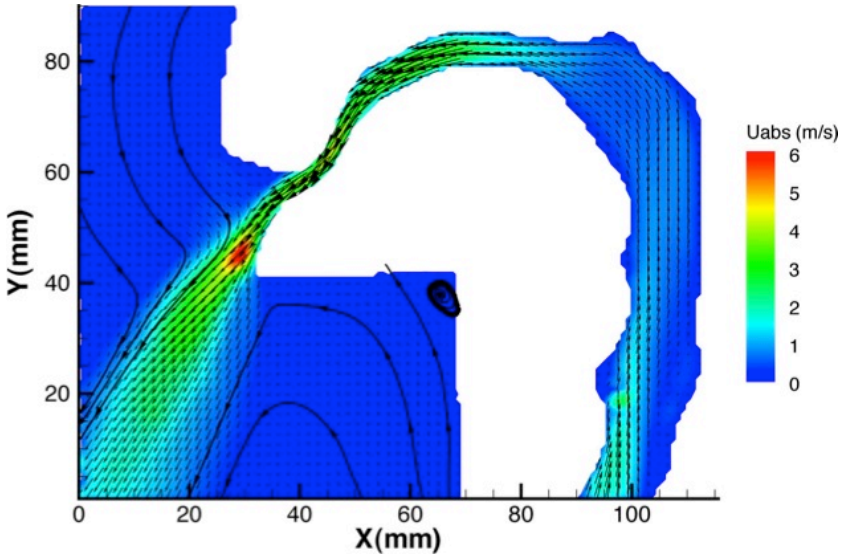

Figure 97. Absolute velocity (m/s) map through a mid-sagittal cross-section of the vocal tract with 12 l/min flow

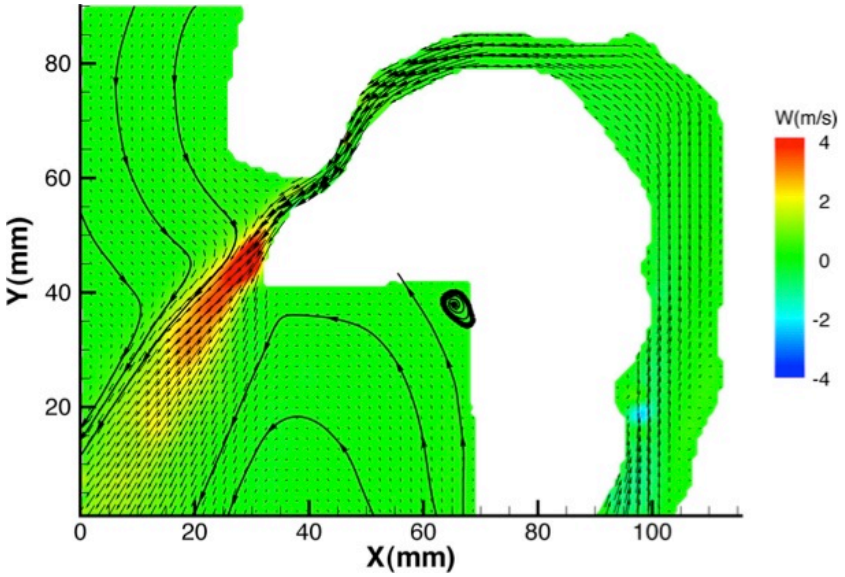

Figure 98. Orthogonal velocity (m/s) component contour through a mid-sagittal cross-section of the vocal tract with 12 l/min flow

Coronal, axial and the mid-sagittal plane cross-sections through the reconstructed velocity volume are shown in Figure 99. The flowrates through 10 coronal and 10 axial cross-sections were calculated by integrating the orthogonal velocity component over each respective cross-sectional area. Calculated

flowrates ranged from 8.3 to 11.3, which compared with the system prescribed flowrate of 12 l/min to varying degrees. The lower flowrates were calculated in the narrower regions of the model where the interrogation windows and 2 mm traversed increments were relatively larger. The width of the model's narrowest region for example was equal to the width of the smallest correlation window, which would have resulted in velocity bias towards zero displacement due to the non-slip boundary condition imposed by the mask images and cross-correlation algorithm. To improve the accuracy of the results in the narrow regions the measurements should be repeated with a higher resolution camera, and/or magnification in order to allow a smaller final interrogation window size.

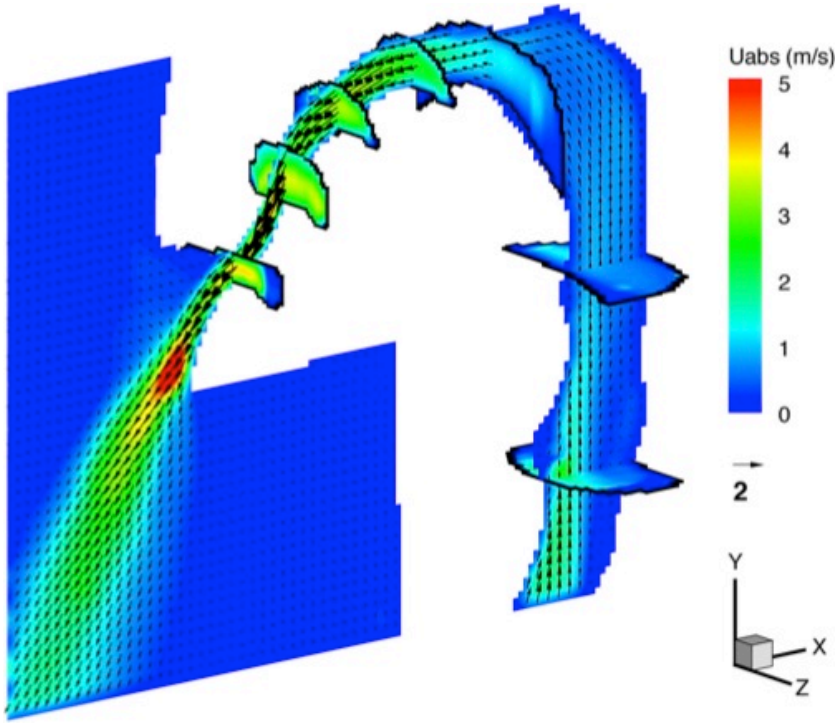

Figure 99. Absolute velocities (m/s) on coronal, axial and the centre sagittal plane cross-sections through the reconstructed 'sh' fricative velocity volume.

7.2.4 Conclusions

Manufacturing methods developed for the construction of nasal models have been successfully applied to produce high quality flow phantoms of vocal tract geometries. The original geometries were reproduced with a spatial accuracy of approximately 2%. Stereo-PIV was used to measure the mean flow field through a vocal tract geometry representative of a 'sh' fricative, employing apparatus and software designed over the duration of this thesis. The results will be used to validate a computer model of speech, in which the flow characteristics will be assessed in detail over a wider range of sounds.

7.3 Airborne Droplet and NHF

7.3.1 Introduction

During the winters of 2008–2009, high dependency units (HDUs) and intensive care units (ICUs) saw a great increase in the rate of admissions of patients suffering from severe viral respiratory infections such as H1N1. NHF has been a widely adopted treatment for patients suffering hypoxemic respiratory failure. The delivery of heated and saturated air inevitably eventuates in condensation forming at the cannula and a high level of moisture in the nasal cavity. Concern was raised as to whether the high velocities and shear rates at the nostrils with NHF created airborne droplets that could transfer contageous respiratory viruses, such as H1NI, from infected patients to hospital staff and nearby patients.

Hui et al. (2009; 2007; 2006) used smoke flow visualisation to study the dispersion of the air exhaled by a human patient simulator wearing a range of respiratory devices. The concentration of air exhaled by patients was found to remain at measureable levels up to at least a 1m radius from the patient. Hui et al. took this distance as the further limit an exhaled particle, being subject to gravity and aerodynamic drag, could travel. Cole and Cook (1998) reviewed the literature on droplet generation and the transport of infectious agents by exhaled particles, noting that coughs generate droplets in the range 0.5–12 μm with a density close to that of water. Chiang et al. (2010) used a laser diffractometer to measure the droplets exhaled by human subjects during quiet breathing, speaking and coughing. They found large numbers of droplets of diameter less than 0.5 μm, and measureable numbers in the range 10 to 100 μm in all cases, but detected no droplets at sizes larger than 100 μm. Simonds et al. (2010) used an optical particle sizer to measure the droplets exhaled by patients wearing a vented mask and nebulizer. In addition to small droplets that appeared to originate from the nebulizer, droplets greater than 10 μm were found and increased in frequency with chest physiotherapy. The air velocities in the nose of a patient receiving NHF differ from those in a cough.

This study seeks to determine if a patient wearing an Optiflow™ cannula is likely to exhale airborne droplets, and how far these might be transported in a hospital ward. In the low ambient humidity of an air-conditioned hospital ward, droplets below a certain size will quickly evaporate rendering the virus inactive. Large droplets will settle out onto surfaces near the infected patient and dry. Droplets in an intermediate size range may be carried by air currents to be inhaled by other patients or staff. Volunteers wearing the Optiflow™ cannula were videoed with a high-magnification, high-speed camera to determine if any

droplets could be seen. Calculations of the trajectory and drying time of selected droplets have been carried out, to determine where they will deposit on surrounding surfaces.

7.3.2 Methodology

Ethics approval for this study was obtained from the Upper South Regional Human Ethics Committee (ref. URB/09/12/064) and the University of Canterbury Human Ethics Committee (ref. 2009/173).

Three healthy male volunteers ranging in age from 30 to 50 years old wore the medium size Fisher and Paykel Healthcare Optiflow™ nasal cannula. Heated and humidified flowrate of 30 l/min were driven by a HC201 air pump (Fisher and Paykel Healthcare) and measured with a TSI-4040 flowmeter. All volunteers spent at least 10 minutes wearing the cannula with 30 l/min flow to become accustomed to it. The subjects breathed with their mouths closed, which during protocol development had been established to be more likely to generate droplets than if the mouth was open. The region immediately below the subject's nostrils was imaged with a Redlake Motion Pro X3 camera at an acquisition rate of 200 frames per second and resolution of 1280 × 1024 pixels^2. The region was backlit with a Sage Action Inc. xenon arc lamp (http://www.sageaction.com) and a diffusing screen of tracing paper. A Nikon RMC Tokina 70–210 mm (55 mm diameter) lens was used with a focal length of 70 mm, a f-number of 22, and was offset from the camera by an image distance of approximately 1.2 m. By Equation 20, this arrangement gave a depth of field t of 17 mm such that shadows cast by droplets across the breadth of one nostril were in focus, where N is the lens' f-number, c is the maximum permissible circle of confusion taken as 1 pixel diameter, v is the image distance and f is the lens' focal length. Calibration by imaging a wire of known diameter showed a magnification of 21.9 μm/pixel. Thus the smallest detectable droplet will have a diameter in the region of 22 μm or less. A silhouette of the nose was cast onto the image frame as a spatial point of reference. The subject wore protective eyeware. Between 600 and 3000 frames were taken in each experiment. The optical layout is illustrated in Figure 100, and Figure 101 shows droplets lying inside the depth of field and unfocussed droplets lying outside.

$$t = 2Nc\frac{v}{f} \qquad \textbf{Equation 20}$$

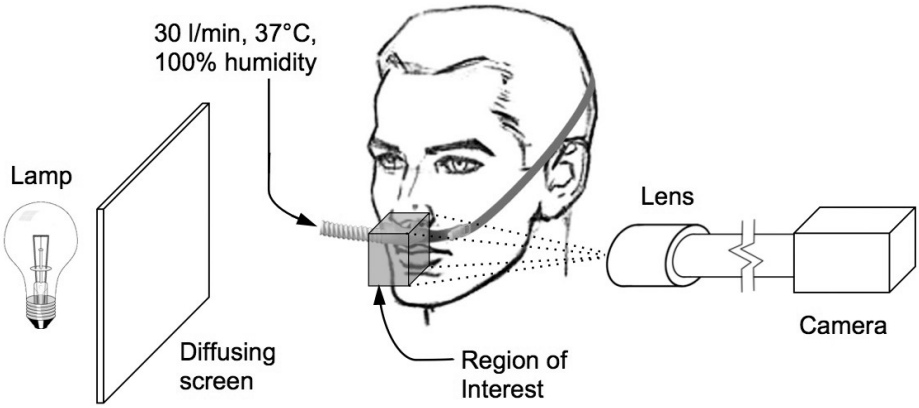

Figure 100. Optical layout

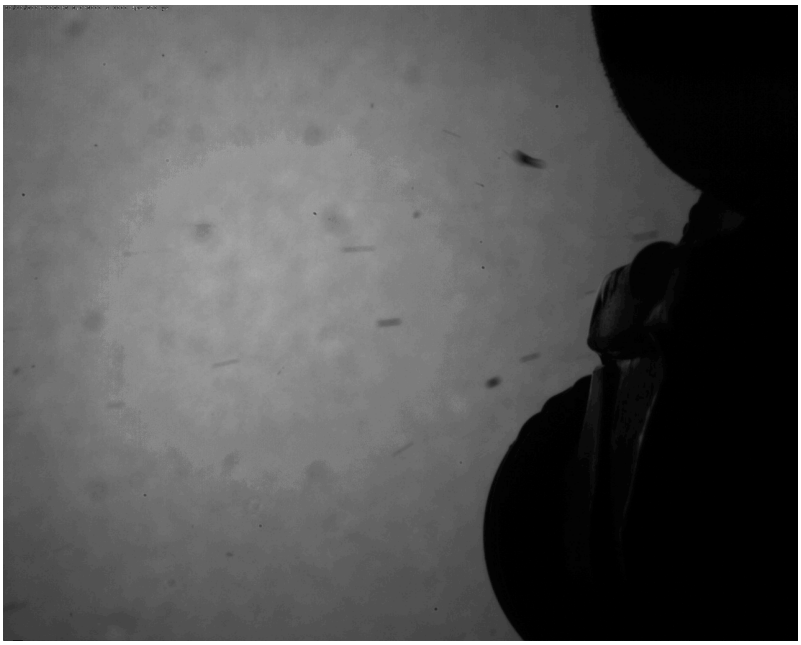

Figure 101. Droplet image during snorting. The tip of the nose is visible in the top right corner.

A chin and forehead rest ensured the subject could consistently place their nose in the field of view. After a few minutes wearing the cannula with the flow on, each subject injected 1 ml of Hamilton AquaeTM fluid into their nasal cavity, using a pipette inserted with the tip just beyond the nasal valve to simulate a worst case accumulation of moisture at the nostril. The subject then replaced the nasal cannula and, holding their breath, placed their nose in the field of view. They then resumed breathing calmly for a few breaths while images were taken. Lastly they exhaled strongly (snorted) for the final few frames of image acquisition. The subject's mouth was closed at all times. In use on the ward, the patient's mouth may be open during exhalation; however, closing the mouth gives the greatest the velocity in the nasal valve and hence the greatest probability of producing airborne droplets.

7.3.3 Results

During steady, quiet breathing, no droplets were observed. Liquid was seen dripping from the nose onto the interface retaining strap but this did not atomise unless the subject snorted. For all subjects, snorting produced many visible droplets (Figure 101). An analysis of the droplet size distribution from one subject is shown in Figure 102. Since the droplet images were streaked due to the exposure time, the size was measured from the minor axis of the droplet image. Droplets measured ranged in size from 22 to 1000 μm. With strong snorting, a bubble of liquid formed at the nose and broke up into smaller droplets. The maximum droplet velocity of 1 m/s was measured from the maximum particle displacements between exposures.

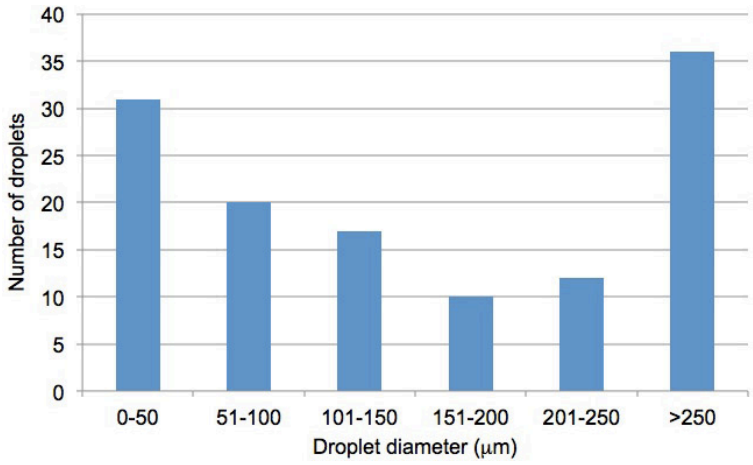

Figure 102. Droplet size distribution, snorting with medium cannula.

7.3.4 Calculations

Using the size distributions presented in Figure 102 and a droplet velocity of 1 m/s, R. Dougherty (a co-author on this work) used the model of Kincaid and Longley (1989) to estimate the lifetime and maximum possible travel distance of evaporating particles. The model considers the heat transfer into the droplet from the surrounding air and the diffusion and convection of vapour away from the droplet surface. The model was programmed in an Excel spreadsheet with a first order explicit time marching scheme. Droplets over a 10–1000 μm range were modeled as spherical drops of pure water emerging from the nose at a temperature of 37°C, a height of 1.5 m above the floor, a trajectory angle of 30 degrees below the horizontal, and an initial velocity of 1 m/s. The drag and gravitational forces on the droplet were calculated, using the drag coefficient correlation from the Goldstein equation (Liao 1998). An upwards

draught of 0.5 m/s was assumed to represent the maximum ventilation current speed in halls and auditoria away from vents in a typical air-conditioned environment (Awbi 2003). The surrounding air was also assumed to have a horizontal velocity component of 0.1 m/s. The direction of air movements were chosen to give an upper limit on the possible range a droplet could travel. The surrounding air was modeled with a dry bulb temperature of 25°C, a relative humidity of 50%, and a sea level pressure of 101325Pa. The results are presented in Table 22.

Table 22. Results of droplet trajectory and evaporation calculations

Droplet initial diameter/ (μm)	Time until strikes ground at 1.5m below nose (s)	Time for complete evaporation (s)	Horizontal distance travelled until complete evaporation or strikes ground (m)
10	Remains airborne until evaporated	0.07	0.08
25	Remains airborne until evaporated	0.9	0.9
100	Remains airborne until evaporated	13	13
200	Remains airborne but reached 1.3m below nose in 20s	43	43
250	3.9	62	<0.5
500	1.21	170	<1
800	0.86	320	<1
1000	0.78	450	<1

7.3.5 Discussions and Conclusions

It can be argued that once a droplet has evaporated any virus that may have been contained in the droplet will be rendered unviable. A droplet smaller than 25 microns will evaporate within one second. During this time the droplet will travel no farther than 1 m from the patient, given the air currents and initial velocity assumed above. Droplets larger than 250 microns are estimated to settle out on the floor in less than 4 seconds and within a 0.5 m radius, providing they do not strike some other surface. Once on a surface they are relatively harmless. The droplets of most interest are in the range of 25 to 250 microns. Droplets in this

size range were predicted to potentially remain airborne for up to 62 seconds and travel up to 43 metres before evaporating.

The experiment simulated a worst-case scenario by assuming a wet nasal mucosa and vigorous nasal snorting to generate droplets. During snorting, it was evident that droplets are produced in the range of 25 to 250 microns with the Optiflow™ cannula under the conditions simulated. Because such high expiration flowrates are uncommon during normal breathing, a limited but potential risk of airborne transmission of viruses is therefore hypothesised. No droplets were observed during quiet breathing. Even though the smallest measurable particle was 20 μm, it can be suggested that during quiet breathing there is no risk of viral transmission via airborne droplets because particles smaller than 25 μm were estimated to travel a maximum distance of only 0.9 m. The limitations of this study are in the limited range of subjects and the limited range of conditions tested. Measurements should be repeated with quantified quiet breathing and snorting flowrates, and during snorting without a cannula to determine whether the presence of the cannula affects the presence and size of snorted droplets.

7.4 Conclusions

A number of auxiliary studies have been performed to supplement the understanding obtained from PIV measurements on the effect of NHF on nasal flows. Stereo-PIV measurements were also performed in the human vocal tract using PIV and model construction methodologies developed for nasal studies, which demonstrates the techniques' flexibility. An approximately linear relationship between airway pressure and cannula flowrate was found for three people, however, the airway pressures generated by a given cannula flowrate varied greatly between subjects. The subject with the smallest nostrils did experience the largest pressures; however, the subject with the largest nostrils did not experience the smallest pressures, which contradicts suggestions in the literature that the most critical factor in determining airway pressure development is the relationship between the respective diameters of the nostril and cannula. In vivo measurements confirmed that upper airway pressures generated by NHF are lower during mouth-open breathing relative to mouth-closed breathing. The average flowrate through the mouth was in the expired direction for all cannula flowrates and increased with increasing cannula flows. The flowrate through the mouth, however, appeared to plateau at cannula flowrates above 40 l/min. The effect of the distensibility of the nasal cavity was evident in the in vivo pressure and flowrate results. Experiments simulating the

worst-case scenario of aerosolised droplet formation with NHF showed that although the transmission of viruses is possible, the risk is limited to snorting. Airborne particles were not generated during normal quiet breathing.

8 Conclusions and Future Work

The flow field in the human nasal cavity has been mapped during natural and NHF assisted breathing with planar- and stereo-PIV in both steady and oscillatory flow conditions. Transparent silicone flow phantoms were manufactured using a method developed using CT scan data and rapid prototyping, and were shown to be the most complete and anatomically accurate in vitro nasal replica models fabricated to date. Physiologically accurate flowrates were measured in vivo and applied in vitro using Reynolds and Womersley number matching. Ensemble correlation averaging and interrogation window refinement, shifting and distortion were employed to produce time and phase averaged velocity maps that contained high velocity gradients and a large dynamic range. Original background subtraction and PIV image mask generation methods have been presented. Measurements were conducted with NHF flowrates between 10–50 l/min and with three different sizes of cannulae. Up to 30 sagittal slices at 1.5 mm spacing were taken through the nasal cavity to enable reconstruction of three dimensional velocity volumes.

During natural breathing, maximal velocities of 2.8 m/s and 3.8 m/s were located in the nasal valve at peak inspiration and expiration, respectively; however, the maximum velocity 4.2 m/s occurred on expiration in the nasopharynx. Velocity magnitudes differed appreciably between the left and right sides of the nasal cavity. During unassisted breathing, the maximum velocity was 33% larger in the right side on inspiration and 19% higher on expiration. Important contributions to flow resistance through the nasal cavity of features other than the nasal valve have been highlighted. Although the morphology was asymmetric about the nasal septum, the flow tended to behave similarly through the features common to both sides of the nasal cavity. The flow pattern through the nasal cavity is largely two-dimensional; however, lateral velocities have been found to contribute up to 36% of the absolute velocity magnitude in anterior regions. To capture the complete velocity magnitude, a three-component measurement technique such as stereo-PIV or discrete measurement planes aligned parallel to the flow in the nasal cavity anterior with a two-component measurement technique should therefore be used. The highest velocities are located in the sagittal plane: thus, a sagittal light sheet stereo-PIV configuration should be used, as in this study, to

minimise the loss of seeding particles. Close agreement was found between numerical and experimental results performed during the same conditions in identical geometries.

NHF modifies the flow velocity magnitude and distribution in the nasal cavity significantly, altering the proportion of inspiration and expiration through each meatus and producing jet velocities up to 20.8 m/s for 40 l/min cannula flow. Inspired and expired flows with NHF remain high through the nasal cavity, whereas the main flow stream passes through the middle airway and along the septal wall during both natural inspiration and expiration. Strong recirculating features are created above and below the cannula jet. Peak inspiration flowrate had a positive relationship with cannula flowrate. Peak expiration flowrate was lower with NHF, and was independent of cannula flowrate.

Despite the current work using lower Womersley numbers than other studies that have modeled nasal flows as steady, the quasi-steady flow assumption for the flow in the nasal cavity has been shown to be invalid for both natural and NHF breathing. Flow time dependence was particularly evident at the transitions between inspiration and expiration in both the nasal cavity and pharynx, and significant discrepancies existed between the results obtained with steady and oscillatory flows at peak expiration with NHF. A large-scale recirculatory feature in the nasal cavity during NHF has been found to continuously flush the nasopharyngeal dead space, which may reduce the amount of carbon dioxide recycled back into the lung and increase oxygen fraction.

The airway pressures generated by a given cannula flowrate for the different subjects varied greatly; however, an approximately linear relationship between airway pressure and cannula flowrate was measured in vivo. Results have shown that the elevated airway pressure developed by NHF cannot be solely determined on a relationship between the internal diameter of the nares and cannula's prong diameter. Although they were not discussed in the thesis, the author and his colleagues have performed further in vitro pressure measurements in an additional life-size silicone flow phantom of the nasal cavity made from the same geometry as model 2 (Jermy et al. 2008). These pressure studies will reveal much clinically useful information.

In vivo and PIV measurements showed that mouth-open breathing with NHF reduces the mean airway pressure. Flow is drawn in through the mouth at peak inspiration while receiving 30 l/min cannula flow, however, the average mouth flow is always in the expiratory direction for any cannula flowrate.

A summary of the most significant original contributions of this research is given below:

- First measurements of the flow field in the nasal cavity with a breathing therapy
- First stereo-PIV measurements in the nasal cavity both with steady or oscillatory flows.
- Most anatomically complete models of the upper airways fabricated to date
- The quasi-steady flow assumption has been proven invalid in the nasal cavity and pharynx
- Nasopharyngeal dead space washout with NHF confirmed

8.1 Future Work

The work presented in this thesis developed a number of novel and versatile methods for PIV measurement of nasal flows and much knowledge has been contributed on both natural and NHF breathing flow patterns. Nevertheless, there remains much potential to extend the current research. Future work should aim to progress the current techniques to even more accurately reproduce in vivo conditions. This section includes thoughts on additional investigations and measurement methodologies conceived for succeeding research.

Although justification for neglecting the compliance of the nasal cavity has been given, an interesting extension of the current research and move towards further realism would be to produce a nasal model incorporating distensible walls and assess any fluid-structure interaction. The walls formed by the turbinates for example would remain rigid, whilst the nasopharynx modeled with compliance. This is a challenging yet achievable endeavor, which has not been undertaken in numerical simulations, let alone in vitro. The negative sacrificial model would be produced and prepared in the same way; however, instead of embedding the model in casting box, the model could be dipped into a bath of silicone and mechanically rotated in three dimensions to promote a uniform wall thickness. Repeating this process will allow the wall thickness to be built progressively. Since the silicone is expensive and because a large volume would be required to immerse the model, once prepared, the silicone should be stored in a fridge or freezer to prolong its pot life. If the negative is heated in an oven to 40°C before commencing coating to allow the air inside the plaster to expand and escape, the coated negative could then be cured at 40°C. This temperature should not significantly weaken the PVA or the integrity of the model and will reduce the build time, possibly allowing the silicone to stay usable for the duration. With each successive layer adding strength and an improved seal of the plaster, the curing temperature could likely be raised. Storing the silicone at a reduced temperature will increase its viscosity, however, this should allow thicker layer applications. It may

even prove advantageous to allow the silicone to set temporarily before commencing coating to increase its viscosity. In the elevated temperature of the oven, the viscosity of the silicone will be reduced prior to setting and the period of rotations should be adjusted accordingly. Once the minimum required wall thickness is obtained at any part of the model, silicone could be painted onto the remaining regions requiring thicker, stiffer walls. The meati are favourably concave in shape and will allow the silicone to be poured into the negative to reproduce the rigid turbinates. It may be necessary to make up more than one batch of silicone because the pot life can only be extended so long; however, because each layer will be thin any mismatch in refractive index would be unlikely to cause corrupting levels of optical distortion. Some of the recent advancements in the area of compliant silicone models made by the author and his colleagues are described in the publications on time-dependent flow field in an elastic pipe (Geoghegan 2010; Geoghegan et al. 2009).

Future investigations should include the study of a larger number and wider range of geometries to ensure the flow features presented are representative amongst a wide population. Recently, attempts have been made at producing standardized nasal cavity geometries by averaging the geometry over a number of subjects (Gambaruto et al. 2009; Liu et al. 2009). Such geometries should be considered as a basis for drawing comparisons between natural and NHF assisted breathing with confidence the results have relevance amongst a large population. Due diligence, however, should be taken with regards to the inevitable simplification of the geometry due to averaging and that it does not neglect certain significant attributes of the flow structure. Having shown close agreement between experimental and numerical results, there is great potential for utilising CFD to investigate a wide range of geometries without incurring the high time and financial expenses associated with constructing patient specific models for PIV measurement. Although the model manufacture method presented has proven its leading performance, further improvements in model accuracy and clarity should still be pursued. New rapid prototyping techniques and materials are continuingly evolving, particularly in the use of transparent materials. The refractive index of the transparent resin used to rapid prototype the cannula models was quoted by the manufacturer as 1.51. Although the models were merely translucent, further improvements in rapid prototyping may allow the direct production of optically clear positive nasal models, eliminating inaccuracies introduced by coating and casting a lost model. Such a material could be refractive index matched with an aqueous solution of tetraline (n = 1.55). Another refractive index matching method envisaged, however, was not implemented, was to take an image of a speckle pattern placed behind the model and cross correlate it with an image of the same in situ speckle pattern without the model in front.

As well as potentially being very accurate, this method could be used to quantify errors in the PIV results due to the distortion created by any refractive index mismatch.

There is potential to extract further information from the velocity fields obtained by the current work. A method called interfacial PIV (iPIV) has been developed (Buchmann 2010) to accurately measure the near wall velocity field and particularly the wall shear stress along non-slip interfaces. Application of this technique within the nasal cavity would increase the accuracy of measurements and allow areas of high wall shear stress causing high viscous pressure losses to be highlighted. Also of interest is quantifying the effect of NHF on wall shear stress magnitude and distribution within the nasal cavity. Computing the vorticity fields in the flow would yield a greater understanding of the fluid mechanics, particularly during the oscillatory phases of the flow. Furthermore, recent work (Charonko et al. 2010; Jaw et al. 2009; Khodarahmi et al. 2010) shows that velocity vector information can be used to derive the pressure field by inversely solving the Navier-Stokes equations. Knowledge of the pressure field during natural and NHF assisted breathing could be used to further elucidate the effect of NHF on pressures in the nasal cavity.

Whether the flow is laminar or turbulent in particular regions of the nasal cavity for given flowrates remains to be substantiated. The results from Chapters 4–6 demonstrated the existence of flow instabilities, however, the investigation of these phenomena was limited because only the time- and phase- averaged flow fields were investigated in the current research. Future studies should compute the instantaneous velocity vector fields and take a sufficient number of image pairs to compute converged turbulence statistics. Moreover, the sampling rate should be increased from the 10 Hz used in the current work by using high-speed imaging. These improvements would allow the role of turbulence in nasal air-conditioning and NHF pressure generation to be identified.

The velocities directly at the exit of the cannula jet proved difficult to acquire because the cannula was effectively a source of seeding particles and their was an apparent discontinuity in the flow field going from a velocity of zero in the cannula mask to maximal jet exit velocities. Cross-correlation windows large enough to capture the high displacements at the cannula exit in the first iteration were too large relative to the diameter of the jet and suffered from strong velocity biases. The cross-correlation algorithm was therefore not able to give an accurate velocity prediction for subsequent iterations with window shifting and iterations. Two methods were implemented to combat this, however, they were not entirely successful and require further development. Firstly, the cross-correlation algorithm was adapted so that a number of iterations would be performed before widow refinement. The velocity predictor for each successive

iteration did converge towards obtaining higher velocities in the jet, however, the signal to noise ratio remained low. Secondly, a grey area in the normally black and white binary mask image was used to specify an area with a non-zero initial velocity predictor to give the correlation algorithm a closer initial velocity prediction to the jet velocity. Again, although the technique was implemented with some success the signal to noise ratio remained low. This could, however, be due to large in and out of plane velocities and loss of seeding particles in this region. Another method that should be investigated for more accurately measuring velocities around the jet exit is the use of cross-correlation windows with different aspect ratios and attempt to align the major axis of an interrogation region with the direction of the jet. It should be re-emphasised that for the current work, the velocities directly at the jet exit were not considered important because it was felt that the velocity magnitude and distribution in this region were predictable and that these high velocities were sacrificed in order to resolve lower velocities in the nasal cavity.

The effect of NHF on the work of breathing should be investigated in future studies. NHF is thought to reduce the metabolic energy cost associated with warming and humidifying inspired gas during normal breathing because air is delivered already at BTPS (Dysart et al. 2009). Saslow et al. (2006) found that the mechanical work of breathing was similar between NHF and nasal CPAP. The mechanical work of breathing with NHF, however, remains to be evaluated with respect to natural breathing. The lung has a non-linear compliance curve and half filled lungs are known to require less muscular effort in breathing (Burton 1994). It is therefore possible that despite the increased resistance imposed by NHF on expiration, the elevated airway pressure produced across the respiratory cycle may reduce the overall work of breathing by distending the lungs and increasing the lungs' functional residual capacity. It has been shown that increased cannula flows reduce the breathing rate and increase oxygen concentrations, therefore it is also possible NHF reduced the work of breathing by reducing the required diaphragmatic work. There are several clinical trials that should be performed to assess the effect of NHF on the work of breathing, breathing patterns, flowrates and airway pressures; however, the conceived protocols for such investigations are confidential to Fisher & Paykel Healthcare.

References

Adrian, R. J. (2005). Twenty years of particle image velocimetry. *Experiments in Fluids, 39*(2), 159-169.

Arbour, P., Bilgen, E., & Girardin, M. (1985). Experimental study of velocity fields in a human nasal fossa by laser anemometry. *Rhinology, 23*(3), 201-207.

Arroyo, M. P., & Greated, C. A. (1991). Stereoscopic particle image velocimetry. *Measurement Science and Technology, 2*(12), 1181-1186.

Awbi, H. B. (2003). *Ventilation of buildings* (2nd ed.). London: Spon Press.

Bailie, N., Hanna, B., Watterson, J., & Gallagher, G. (2006). An overview of numerical modelling of nasal airflow. *Rhinology, 44*(1), 53-57.

Ball, C. G., Uddin, M., & Pollard, A. (2008). Mean flow structures inside the human upper airway. *Flow Turbulence and Combustion, 81*(1-2), 155-188.

Berger, S. A., Talbot, L., & Yao, L. S. (1983). Flow in Curved Pipes. *Annual Review of Fluid Mechanics, 15*(1), 461-512.

Bridger, G. P., & Proctor, D. F. (1970). Maximum nasal inspiratory flow and nasal resistance. *The Annals of otology, rhinology and laryngology, 79*(3), 481-488.

Brown, R. (2008). *Three-dimensional motion capture for the DIET breast cancer imaging system.* University of Canterbury, Christchurch.

Brücker, C., & Park, K. I. (1999). Experimental study of velocity fields in a model of human nasal cavity by DPIV. In *Proceedings of the 1st Int. Symp. Turbulence and Shear Flow Phenomena, Santa Barbara, USA*, September 12-15.

Buchmann, N. A. (2010). *Development of Particle Image Velocimetry for In Vitro Studies of Arterial Haemodynamics.* University of Canterbury, Christchurch.

Burgmann, S., Grosse, S., Schroder, W., Roggenkamp, J., Jansen, S., Graf, F., & Busen, M. (2009). A refractive index-matched facility for fluid-structure interaction studies of pulsatile and oscillating flow in elastic vessels of adjustable compliance. *Experiments in Fluids, 47*(4-5), 865-881.

Burton, R. F. (1994). *Physiology by numbers: An encouragement to quantitative thinking*. Cambridge, UK: Cambridge University Press.

Butler, J. (1960). The work of breathing through the nose. *Clinical Science, 19*, 55-62.

Çakmak, O., Coşkun, M., Çelik, H., Büyüklü, F., & Özlüoglu, L. N. (2003). Value of acoustic rhinometry for measuring nasal valve area. *Laryngoscope, 113*(2), 295-302.

Campbell, E. J., Baker, M. D., & Critessilver, P. (1988). Subjective effects of humidification of oxygen for delivery by nasal cannula - a prospective-study. *Chest, 93*(2), 289-293.

Charonko, J. J., King, C. V., Smith, B. L., & Vlachos, P. P. (2010). Assessment of pressure field calculations from particle image velocimetry measurements. *Measurement Science & Technology, 21*(10), 15.

Chatila, W., Nugent, T., Vance, G., Gaughan, J., & Criner, G. J. (2004). The Effects of High-Flow vs Low-Flow Oxygen on Exercise in Advanced Obstructive Airways Disease*. *Chest*.

Cheng, K., Cheng, Y., Yeh, H., & Swift, D. L. (1995). Deposition of Ultrafine Aerosols in the Head Airways During Natural Breathing and During Simulated Breath Holding Using Replicate Human Upper Airway Casts. *Aerosol Science and Technology, 23*(3), 465-474.

Cheng, Y., Yamada, Y., Yeh, H., & Swift, D. L. (1988). Diffusional Depostion of ultrafine aerosols in a human nasal cavity. *Journal of Aerosol Science, 19*(6), 741-751.

Chiang, M. C. J., Wong, E. Y. L., MacDonald, F., Senthilselvan, A., Lange, C. F., Zayas, G., & King, M. (2010). Rapid Assessment Of Human Respiratory Aerosols, Their volume Concentration, Number And Sizes Of Particles By Laser Diffraction Spectrometry. *Am. J. Respir. Crit. Care Med., 181*(1), A2189-.

Chung, S. K., & Kim, S. K. (2008). Digital particle image velocimetry studies of nasal airflow. *Respiratory Physiology & Neurobiology, 163*(1-3), 111-120.

Chung, S. K., Son, Y. R., Shin, S. J., & Kim, S. K. (2006). Nasal airflow during respiratory cycle. *Am J Rhinol, 20*(4), 379-384.

Churchill, S. E., Shackelford, L. L., Georgi, J. N., & Black, M. T. (2004). Morphological variation and airflow dynamics in the human nose. *Am J Hum Biol, 16*(6), 625-638.

Cole, E. C., & Cook, C. E. (1998). Characterization of infectious aerosols in health care facilities: an aid to effective engineering controls and preventive strategies. *Am J Infect Control, 26*(4), 453-464.

Cole, P. (1982). Upper respiratory airflow. In Proctor, D. F. & Andersen, I. (Eds.), *The nose: upper airway physiology and the atmospheric environment* (pp. 163-185). Amsterdam: Elsevier Biomedical Press.

Cole, P. (2000). Biophysics of Nasal Airflow: A Review. *American journal of Rhinology, 14*(4), 245-249.

Conway, J. H., Fleming, J. S., Perring, S., & Holgate, S. T. (1992). Humidification as an adjunct to chest physiotherapy in aiding tracheobronchial clearance in patients with bronchiectasis. *Respiratory Medicine, 86*(2), 109-114.

Courtiss, E. H., & Goldwyn, R. M. (1983). The effects of nasal surgery on airflow. *Plast Reconstr Surg, 72*(1), 9-21.

Craig, A. B., Dvorak, M., & McIlreath, F. J. (1965). Resistance to airflow through the nose. *Ann Otol Rhinol Laryngol, 74*(3), 589-603.

Croce, C., Fodil, R., Durand, M., & Sbirlea-Apiou, G. (2006). In vitro experiments and numerical simulations of airflow in realistic nasal airway geometry. *Annals of Biomedical Engineering, 34*(6), 997-1007.

Davis, J. C. (1986). *Statistics and Data Analysis in Geology* (Second ed.). New York: John Wiley & Sons.

Daviskas, E., Gonda, I., & Anderson, S. D. (1990). Mathematical modeling of heat and water transport in human respiratory tract. *J. Appl. Physiol., 69*, 362-372.

Dawes, J. D. K. (1952). The course of the nasal airstreams. *The Journal of Laryngology and Otology*.

Dean, W. R. (1928). The stream-line motion of fluid in a curved pipe. (Second paper.). *Philosophical Magazine, 5*(30), 673-695.

Demoule, A., Girou, E., Richard, J. C., Taille, S., & Brochard, L. (2006). Benefits and risks of success or failure of noninvasive ventilation. *Intensive Care Med, 32*(11), 1756-1765.

Doorly, D. J., Taylor, D. J., Franke, P., & Schroter, R. (2008a). Experimental investigation of nasal airflow. *Proceedings of the Institution of Mechanical Engineers, Part H: Journal of Engineering in Medicine, 222*(4), 439-453.

Doorly, D. J., Taylor, D. J., Gambaruto, A. M., Schroter, R. C., & Tolley, N. (2008b). Nasal architecture: form and flow. *Philosophical Transactions of the Royal Society a-Mathematical Physical and Engineering Sciences, 366*(1879), 3225-3246.

Doorly, D. J., Taylor, D. J., & Schroter, R. C. (2008c). Mechanics of airflow in the human nasal airways. *Respir Physiol Neurobiol, 163*(1-3), 100-110.

Drettner, B. (1965). Pressure recordings in the maxillary sinus. *Int. Rhinol., 3*, 1318-1325.

Drettner, B. (1982). The paranasal sinuses. In Proctor, D. F. & Andersen, I. B. (Eds.), *The nose: upper airway physiology and the atmospheric environment* (pp. 145-162). Amsterdam: Elsevier Biomedical Press.

Dring, R. P. (1982). Sizing criteria for laser anemometry particles. *Journal of fluids engineering ASME, 104*(1), 15-17.

Dysart, K., Miller, T. L., Wolfson, M. R., & Shaffer, T. H. (2009). Research in high flow therapy: mechanisms of action. *Respiratory Medicine, 103*(10), 1400-1405.

Eccles, R. (1978). The central rhythm of the nasal cycle. *Acta Oto-Laryngologica, 86*(5-6), 464-468.

Eccles, R. (2000). Nasal airflow in health and disease. *Acta Otolaryngol, 120*(5), 580-595.

Elad, D., Liebenthal, R., Wenig, B. L., & Einav, S. (1993). Analysis of air flow patterns in the human nose. *Med Biol Eng Comput, 31*(6), 585-592.

Elad, D., Naftali, S., Rosenfeld, M., & Wolf, M. (2006). Physical stresses at the air-wall interface of the human nasal cavity during breathing. *J Appl Physiol, 100*(3), 1003-1010.

Elad, D., Wolf, M., & Keck, T. (2008). Air-conditioning in the human nasal cavity. *Respir Physiol Neurobiol.*

Elsinga, G. E., Scarano, F., Wieneke, B., & van Oudheusden, B. W. (2006). Tomographic particle image velocimetry. *Experiments in Fluids, 41*(6), 933-947.

Farley, R. D., & Patel, K. R. (1988). Comparison of air warming in human airway with thermodynamic model. *Med. Biol. Eng. Comput., 26*, 628-632.

Finck, M., Hanel, D., & Wlokas, I. (2007). Simulation of nasal flow by lattice Boltzmann methods. *Comput Biol Med, 37*(6), 739-749.

Fischer, R. (1969). Quoted in Mlynski (2000).

Foxen, E. H. M., Preston, T. D., & Lack, J. A. (1971). The assessment of nasal air-flow. A review of past and present methods. *Journal of Laryngology and Otology, 85*, 811-825.

Francke, G. (1893). Quoted by Parker (1901).

Gallagher, M. W., & McEwan, I. K. (1996). Insights into grain entrainment using particle image velocimetry. In *Proceedings of the 8th Int. Symp. on Applications of Laser Techniques to Fluid Mechanics, Lisbon*.

Gambaruto, A. A., Taylor, D. J., & Doorly, D. J. (2009). Modelling nasal airflow using a Fourier descriptor representation of geometry. *International Journal for Numerical Methods in Fluids, 59*(11), 1259-1283.

Garcia, G. J. M., Mitchell, G., Bailie, N., Thornhill, D., Watterson, J., & Kimbell, J. S. (2007). Visualization of nasal airflow patterns in a patient affected with atrophic rhinitis using particle image velocimetry. In *Proceedings of the Third International Conference on Optical and Laser Diagnostics, London, UK*.

Gehring, J. M., Garlick, S. R., Wheatley, J. R., & Amis, T. C. (2000). Nasal resistance and flow resistive work of nasal breathing during exercise: effects of a nasal dilator strip. *J Appl Physiol, 89*(3), 1114-1122.

Geoghegan, P. H. (2010). SPIV and image correlation measurements of surface displacement during pulsatile flow in models of compliant, stenosed arteries. In *Proceedings of the 15th international symposium on applciations of laser techniques to fluid mechanics, Lisbon, Portugal*, July 5-8.

Geoghegan, P. H., Jermy, M., Buchmann, N. A., Spence, C. J. T., & Freitag, T. (2009). Experimental investigation of flow in a compliant tube using particle image velocimetry. In *Proceedings of the 8th International Symposium on Particle Image Velocimetry, Melbourne, Australia*, August 25-28.

Gertner, R., Podoshin, L., & Fradis, M. (1984). A simple method of measuring the nasal airway in clinical work. *J Laryngol Otol, 98*(4), 351-355.

Girardin, M., Bilgen, E., & Arbour, P. (1983). Experimental study of velocity fields in a human nasal fossa by laser anemometry. *Ann Otol Rhinol Laryngol, 92*(3 Pt 1), 231-236.

Good News Bible: Today's English Version. (1976). Wellington: The Bible society in New Zealand.

Goodale, J. L. (1896). An Experimental Study of the Respiratory Functions of the Nose. *Boston Med Surg J 135*, 457-460.

Grgic, B., Finlay, W. H., & Heenan, A. F. (2004). Regional aerosol deposition and flow measurements in an idealized mouth and throat. *Journal of Aerosol Science, 35*(1), 21-32.

Groves, N., & Tobin, A. (2007). High flow nasal oxygen generates positive airway pressure in adult volunteers. *Australian Critical Care, 20*(4), 126-131.

Hahn, I., Scherer, P. W., & Mozell, M. M. (1993). Velocity profiles measured for airflow through a large-scale model of the human. *J Appl Physiol, 75*(5), 2273-2287.

Hasegawa, M., & Kern, E. B. (1978). Variations in nasal resistance in man: a rhinomanometric study of the nasal cycle in 50 human subjects. *Rhinology, 16*(1), 19-29.

Heenan, A. F., Matida, E., Pollard, A., & Finlay, W. H. (2003). Experimental measurements and computational modeling of the flow field in an idealized human oropharynx. *Experiments in Fluids, 35*(1), 70-84.

Hentschel, B., Horschler, I., Schirski, M., Bischof, C., & Kuhlen, T. (2006). Visualization of Human Nasal Cavity Flows. In *Proceedings of the 12th International Symposium on FLow Visualization, Göttingen, Germany*, September 10-14.

Hess, M. M., Lamprecht, J., & Horlitz, S. (1992). Experimental study of airflow in the main nasal cavity of the human using a nose. *Laryngorhinootologie, 71*(9), 468-471.

Honkanen, M., & Nobach, H. (2005). Background extraction from double-frame PIV images. *Experiments in Fluids, 38*(3), 348-362.

Hopkins, L. M., Kelly, J. T., Wexler, A. S., & Prasad, A. K. (2000). Particle image velocimetry measurements in complex geometries. *Experiments in Fluids, 29*(1), 91-95.

Hornung, D. E., Leopold, D. A., Youngentob, S. L., Sheehe, P. R., Gagne, G. M., Thomas, F. D., & Mozell, M. M. (1987). Airflow patterns in a human nasal model. *Arch Otolaryngol Head Neck Surg, 113*(2), 169-172.

Horschler, I., Brücker, C., Schroder, W., & Meinke, M. (2006a). Investigation of the impact of the geometry on the nose flow. *European Journal of Mechanics - B/Fluids, 25*(4), 471-490.

Horschler, I., Schroder, W., & Meinke, M. (2006b). Comparison of steady and unsteady nasal cavity flow solutions for the complete respiration cycle. *Comput.Fluid Dyn. J., 15*(3), 354-377.

Horschler, I., Schroder, W., & Meinke, M. (2010). On the assumption of steadiness of nasal cavity flow. *Journal of Biomechanics, 43*(6), 1081-1085.

Huang, H. T., Fiedler, H. E., & Wang, J. J. (1993). Limitation and improvement of PIV. Part 2: particle image distortion, a novel technique hybrid digital tracking method. *Experiments in Fluids, 15*(4), 263-273.

Hui, D. S., Chow, B. K., Chu, L. C., Ng, S. S., Hall, S. D., Gin, T., & Chan, M. T. (2009). Exhaled air and aerosolized droplet dispersion during application of a jet nebulizer. *Chest, 135*(3), 648-654.

Hui, D. S., Hall, S. D., Chan, M. T., Chow, B. K., Ng, S. S., Gin, T., & Sung, J. J. (2007). Exhaled air dispersion during oxygen delivery via a simple oxygen mask. *Chest, 132*(2), 540-546.

Hui, D. S., Ip, M., Tang, J. W., Wong, A. L., Chan, M. T., Hall, S. D., Chan, P. K., & Sung, J. J. (2006). Airflows around oxygen masks: A potential source of infection? *Chest, 130*(3), 822-826.

Hulst, v. d. (1957). *Light scattering by small particles*. New York: John Wiley & Sons, Inc.

Isabey, D., & Chang, H. K. (1981). Steady and unsteady pressure-flow relationships in central airways. *Journal of Applied Physiology, 51*(5), 1338-1348.

Ishikawa, S., Nakayama, T., Watanabe, M., & Matsuzawa, T. (2006). Visualization of flow resistance in physiological nasal respiration - Analysis of velocity and vorticities using numerical simulation. *Archives Of Otolaryngology-Head & Neck Surgery, 132*(11), 1203-1209.

Jackson, L. E. (1999). Controversies in the management of inferior turbinate hypertropy: a comprehensive review. *Plats Reconstr Surg, 103*, 300-312.

Jaw, S. Y., Chen, J. H., & Wu, P. C. (2009). Measurement of Pressure Distribution from PIV Experiments. *Journal of Visualization, 12*(1), 27-35.

Jeong, S.-J., Kim, W.-S., & Sung, S.-J. (2007). Numerical investigation on the flow characteristics and aerodynamic force of the upper airway of patient with obstructive sleep apnea using computational fluid dynamics. *Medical Engineering & Physics, 29*(6), 637-651.

Jermy, M. C., Buchmann, N. A., Spence, C. J. T., Nguyen, C. V., & David, T. (2008, 3-4 December). PIV measurements of human Human Blood and Upper Airway flows Flow in scaled Scaled Models. In Proceedings of the *Fifth Australian Conference on Laser Diagnostics in Fluid Mechanics and Combustion*, Perth.

Kahn, D. J., Courtney, S. E., Steele, A. M., & Habib, R. H. (2007). Unpredictability of Delivered Bubble Nasal Continuous Positive Airway Pressure Role of Bias Flow Magnitude and Nares-Prong Air Leaks. *Pediatric Research 62*(3), 343-347.

Keane, R. D., & Adrian, R. J. (1990). Optimization of particle image velocimeters: Part 1, double pulsed systems. *Meas Sci Technol, 1*(11), 1202-1215.

Keck, T., Leiacker, R., Riechelmann, H., & Rettinger, G. (2000). Temperature profile in the nasal cavity. *Laryngoscope, 110*(4), 651-654.

Kelly, J. T., Prasad, A. K., & Wexler, A. S. (2000). Detailed flow patterns in the nasal cavity. *Journal of Applied Physiology, 89*(1), 323-337.

Kelly, M. G., McGarvey, L. P. A., Heaney, L. G., & Elborn, J. S. (2001). Nasal septal perforation and oxygen cannulae. *Hospital Medicine, 62*(4), 248-248.

Keyhani, K., Scherer, P. W., & Mozell, M. M. (1995). Numerical simulation of airflow in the human nasal cavity. *J Biomech Eng, 117*(4), 429-441.

Khodarahmi, I., Shakeri, M., Sharp, M., & Amini, A. A. (2010). Using PIV to determine relative pressures in a stenotic phantom under steady flow based on the Pressure-Poisson equation. *Conf Proc IEEE Eng Med Biol Soc, 1*, 2594-2597.

Khoo, B. C., Chew, T. C., Heng, P. S., & Kong, H. K. (1992). Turbulence characterisation of a confined jet using PIV. *Experiments in Fluids, 13*, 350-356.

Kim, J. K., Yoon, J. H., Kim, C. H., Nam, T. W., Shim, D. B., & Shin, H. A. (2006). Particle image velocimetry measurements for the study of nasal airflow. *Acta Oto-Laryngologica, 126*(3), 282-287.

Kim, S. K., & Chung, S. K. (2004). An investigation on airflow in disordered nasal cavity and its corrected models by tomographic PIV. *Measurement Science and Technology, 15*(6), 1090-1096.

Kim, S. K., & Haw, J. R. (2004). An investigation on airflow in pathological nasal airway by PIV. *Journal of Visualization, 7*(4), 341-348.

Kincaid, D. C., & Longley, T. S. (1989). A water droplet evaporation and temperature model. *Transactions of the Asae, 32*(2), 457-463.

Knight, L. C., Eccles, R., & Reilly, M. (1991). Cyclical changes in nasal airway resistance and middle ear pressures. *Acta Oto-Laryngologica, 111*(4), 769-775.

Konno, A. (1969). Air flow and resistance in the nasal cavity. 1. Observation on nasal airflow, using the model made from nasal and nasopharyngeal casts of the human body. *Nippon Jibiinkoka Gakkai Kaiho, 72*(1), 36-48.

Kubicka, Z. J., Limauro, J., & Darnall, R. A. (2008). Heated, humidified high-flow nasal cannula therapy: yet another way to deliver continuous positive airway pressure? *Pediatrics, 121*(1), 82-88.

Laine, M. T., Huggare, J. A., & Ruoppi, P. (1994). A modification of the pressure-flow technique for measuring breathing of cold air. *Am J Orthod Dentofacial Orthop, 105*(3), 265-269.

Lampland, A. L., Plumm, B., Meyers, P. A., Worwa, C. T., & Mammel, M. C. (2008). Observational Study of Humidified High-Flow Nasal Cannula Compared with Nasal Continuous Positive Airway Pressure. *J Pediatr*.

Lee, J.-H., Na, Y., Kim, S.-K., & Chung, S.-K. (2010). Unsteady flow characteristics through a human nasal airway. *Respiratory Physiology & Neurobiology, 172*(3), 136-146.

Levine, S. C., Levine, H., Jacobs, G., & Kasick, J. (1986). A technique to model the nasal airway for aerodynamic study. *Otolaryngol Head Neck Surg, 95*(4), 442-449.

Liao, S. (1998). On the 8th-order drag coefficient formula of a sphere in a uniform stream: A simplified description. *Communications in Nonlinear Science and Numerical Simulation, 3*(4), 256-260.

Lindemann, J., Brambs, H. J., Keck, T., Wiesmiller, K. M., Rettinger, G., & Pless, D. (2005). Numerical simulation of intranasal airflow after radical sinus surgery. *Am J Otolaryngol, 26*(3), 175-180.

Lindemann, J., Keck, T., Wiesmiller, K., Sander, B., Brambs, H. J., Rettinger, G., & Pless, D. (2006). Nasal air temperature and airflow during respiration in numerical simulation based on multislice computed tomography scan. *American Journal of Rhinology, 20*(2), 219-223.

Liu, Y., Johnson, M. R., Matida, E. A., Kherani, S., & Marsan, J. (2009). Creation of a standardized geometry of the human nasal cavity. *J Appl Physiol, 106*, 784-795.

Liu, Y., Matida, E. A., & Johnson, M. R. (2010). Experimental measurements and computational modeling of aerosol deposition in the Carleton-Civic standardized human nasal cavity. *Journal of Aerosol Science, 41*(6), 569-586.

Locke, R. G., Wolfson, M. R., Shaffer, T. H., & Rubenstein, S. D. (1993). Inadvertent administration of positive end-distending pressure during nasal cannula flow. *Pediatrics, 91*(1), 135-138.

Lu, X. B., Thorpe, W. C., Foster, K., & Hunter, P. J. (2009). From experiments to articulatory motion—A three dimensional talking head model. In *Proceedings of the the 10th Ann. Conf. of the International Speech Communication Association, Brighton, United Kingdom*, 6-10 September.

Lund, J., Holm-Knudsen, R. J., Nielsen, J., & Foge Jensen, P. B. (1996). Nasal cannula versus Hudson face mask in oxygen therapy. *Journal of the Danish Medical Association, 158(28)*, 4077-4079.

Masing, H. (1967a). Experimentelle Untersuchungen über den Strömungsverlauf im Nasenmodell. *Arch. Klein. Exp. Ohren-, Nasen- u. Kehlkopf-Heilk., 189*, 371-381.

Masing, H. (1967b). Experimentelle Untersuchungen über die Strömung im Nasenmodell. *Arch. Klin. Exp. Ohren-, Nasen- Kehlkophheilk, 189*, 59-70.

Meissner, H. H., Santiago, S. M., Koyal, S. N., Riemer, A., Stein, M., Goldman, M. D., & Williams, A. J. (1999). Characteristics of nasal airflow and the effect of a nasal dilator in normal human subjects. *Respiration Physiology, 115*(1), 95-101.

Melling, A. (1997). Tracer particles and seeding for particle image velocimetry. *Measurement Science and Technology., 8*, 1406-1416.

Meng, H., & Hussain, F. (1991). Holographic particle velccimetry: a 3D measurement technique for vortex interactions, coherent structures and turbulence. *Fluid Dyn Res, 8*, 33-52.

Menter, F. R. (1994). 2-Equation eddy-viscosity turbulence models for engineering applications. *Aiaa Journal, 32*(8), 1598-1605.

Mink, P. J. (1920). *Physiologie der oberen Luftwege*. Leipzig: Verlag Vogel.

Mlynski, G. (2000). Airflow and conditioning of respiratory air. *Laryngorhinootologie, 79*(11), 636-638.

Mlynski, G., Grützenmacher, S., Mlynski, B., & Koch, B. (1993). Modelluntersuchungen zur Muschelchirurgie. *Laryngorhinootologie, 72*, 614-617.

Mlynski, G., Grutzenmacher, S., Plontke, S., Grutzmacher, W., Mlynski, B., & Lang, C. (2000). A method for studying nasal air flow by means of fluid dynamics experiments. *Zeitschrift fur Medizinische Physik, 10*(3), 207-214.

Moore, S. M. (2007). *Computational 3D Modelling of Hemodynamics in the Circle of Willis.* University of Canterbury, Christchurch.

. *Morbidity & Mortality: 2007 Chart Book on Cadiovascular, Lung, and Blood Diseases*. (2007).

Mosges, R., Buchner, B., Kleiner, M., Freitas, R., Horschler, I., & Schroder, W. (2010). Computational Fluid Dynamics Analysis of Nasal Flow. *B-Ent, 6*(3), 161-165.

Müller-Wittig, W. K., Mlynski, G., & Weinhold, I. (2002). Nasal airllow diagnosis - comparison of experimental studies and computer simulations. *Medicine Meets Virtual Reality 02/10: Digital Upgrades*.

Mygind, N., & Dahl, R. (1998). Anatomy, physiology and function of the nasal cavities in health and disease. *Advanced Drug Delivery Reviews, 29*(1-2), 3-12.

Mygind, N., Johnson, N. J., & Thomson, J. (1977). Intranasal allergen challenge during corticosteroid treatment. *Clinical Allergy, 7*, 69-74.

Mylavarapu, G., Murugappan, S., Mihaescu, M., Kalra, M., Khosla, S., & Gutmark, E. (2009). Validation of computational fluid dynamics methodology used for human upper airway flow simulations. *Journal of Biomechanics, 42*(10), 1553-1559.

Naftali, S., Rosenfeld, M., Wolf, M., & Elad, D. (2005). The air-conditioning capacity of the human nose. *Ann Biomed Eng, 33*(4), 545-553.

Naftali, S., Schroter, R. C., Shiner, R. J., & Elad, D. (1998). Transport phenomena in the human nasal cavity: a computational model. *Ann Biomed Eng, 26*(5), 831-839.

Naito, K., & Iwata, S. (1997). Current advances in rhinomanometry. *Eur Arch Otorhinolaryngol, 254*, 309-312.

Naito, K., Iwata, S., Kondo, M., & Ohoka, E. (1989). Human respiratory airflow through an artificial nasal model: pressure/flow relationship. *Auris nasus larynx, 16*(2), 89-97.

Nobach, H., & Honkanen, M. (2005). Two-dimensional Gaussian regression for sub-pixel displacement estimation in particle image velocimetry or particle position estimation in particle tracking velocimetry. *Experiments in Fluids, 38*(4), 511-515.

Nunn, J. F. (1993). *Nunn's Applied Respiratory Physiology* (4th ed.). Oxford, UK: Butterworth-Heinemann.

Ochs, M., Nyengaard, J. R., Jung, A., Knudsen, L., Voigt, M., Wahlers, T., Richter, J., & Gundersen, H. J. G. (2004). The Number of Alveoli in the Human Lung. *Am. J. Respir. Crit. Care Med., 169*(1), 120-124.

Park, K. I., Brücker, C., & Limberg, W. (1997). Experimental study of velocity fields in a model of human nasal cavity by DPIV. In *Proceedings of the 7th Int. Conf. on Laser Anemometry - Advances and Applications, Karlsruhe, Germany*.

Parker, C. A. (1901). Some observations and remarks on the air currents in nasal respiration. *J Laryngol Rhinol Otol, 16*, 345-355.

Paulsen, E. (1882). Experimentelle untersuchungen uber Stromungen der Luft in der Nasenhohle. *Sitzungsber Akad. Wiss., 85*, 352.

Pereira, F., & Gharib, M. (2002). Defocusing digital particle image velocimetry and the three-dimensional characterization of two-phase flows. *Measurement Science & Technology, 13*(5), 683-694.

Petruson, B. (1988). Improvement of the nasal airflow by the nasal dilator Nozovent. *Rhinology, 26*(4), 289-292.

Prasad, A. K. (2000). Stereoscopic particle image velocimetry. *Experiments in Fluids, 29*(2), 103-116.

Prasad, A. K., & Jensen, K. (1995). Scheimpflug stereocamera for particle image velocimetry in liquid flows. *Applied Optics, 34*(30), 7092-7099.

Principato, J. J., & Ozenberger, J. M. (1970). Cyclical changes in nasal resistance. *Arch Otolaryngol, 91*(1), 71-77.

Proctor, D. F. (1982). *The nose: upper airway physiology and the atmospheric environment*. Amsterdam: Elsevier Biomedical Press.

Proetz, A. W. (1941). *Essays on the Applied Physiology of the Nose*. St. Louis: Annals Publishing Co.

Proetz, A. W. (1951). Air currents in the upper respiratory tract and their clinical importance. *Annals of Otology Rhinology and Laryngology, 60*(2), 439-467.

Raffel, M., Willert, C. E., & Kompenhans, J. (1998). *Particle Image Velocimetry - A Practical Guide*. Berlin-Heidelburg: Springer-Verlag.

Rappai, M., Collop, N., Kemp, S., & deShazo, R. (2003). The nose and sleep-disordered breathing: what we know and what we do not know. *Chest, 124*(6), 2309-2323.

Ritter, F. N. (1970). Vasculature of the nose. *Ann Otol Rhinol Laryngol, 79*, 468-474.

Robertson, N. J., McCarthy, L. S., Hamilton, P. A., & Moss, A. L. H. (1996). Nasal deformities resulting from flow driver continuous positive airway pressure. *Archives of Disease in Childhood, 75*(3), F209-F212.

Santiago-Diez de Bonilla, J., McCaffrey, T. V., & Kern, E. B. (1986). The nasal valve: a rhinomanometric evaluation of maximum nasal inspiratory flow and pressure curves. *The Annals of otology, rhinology, and laryngology, 95*(3 Pt 1), 229-232.

Saslow, J. G., Aghai, Z. H., Nakhla, T. A., Hart, J. J., Lawrysh, R., Stahl, G. E., & Pyon, K. H. (2006). Work of breathing using high-flow nasal cannula in preterm infants. *Journal of Perinatology, 26*(8), 476-480.

Scarano, F. (2002). Iterative image deformation methods in PIV. *Meas. Sci. Technol., 13*, R1-R19.

Scarano, F., & Riethmuller, M. L. (2000). Advances in iterative multigrid PIV image processing. *Experiments in Fluids, 29*, S51-60.

Scherer, P. W., Hahn, II, & Mozell, M. M. (1989). The biophysics of nasal air-flow. *Otolaryngologic Clinics of North America, 22*(2), 265-278.

Schiedeler, J. (1938). Quoted by Dawes (1952).

Schreck, S., Sullivan, K. J., Ho, C. M., & Chang, H. K. (1993). Correlations between flow resistance and geometry in a model of the human nose. *J Appl Physiol, 75*(4), 1767-1775.

Schroeter, J. D., Kimbell, J. S., & Asgharian, B. (2006). Analysis of particle deposition in the turbinate and olfactory regions using a human nasal computational fluid dynamics model. *J Aerosol Med, 19*(3), 301-313.

Schroter, R. C., & Watkins, N. V. (1989). Respiratory heat exchange in mammals. *Respir. Physiol., 78*, 357-368.

Shepard, J. W., Jr., & Burger, C. D. (1990). Nasal and oral flow-volume loops in normal subjects and patients with obstructive sleep apnea. *The American review of respiratory disease, 142*(6 Pt 1), 1288-1293.

Shevrygin, B. V. (1973). The movement of air to the olfactory region of the nose in man. *Fiziol Zh, 19*, 247-249.

Simmen, D., Scherrer, J. L., Moe, K., & Heinz, B. (1999). A dynamic and direct visualization model for the study of nasal airflow. *Arch Otolaryngol Head Neck Surg, 125*(9), 1015-1021.

Simonds, A. K., Hanak, A., Chatwin, M., Morrell, M., Hall, A., Parker, K. H., Siggers, J. H., & Dickinson, R. J. (2010). Evaluation of droplet dispersion during non-invasive ventilation, oxygen therapy, nebuliser treatment and chest physiotherapy in clinical practice: implications for management of pandemic influenza and other airborne infections. *Health Technol Assess, 14*(46), 131-172.

Soloff, S. M., Adrian, R. J., & Liu, Z. C. (1997). Distortion compensation for generalized stereoscopic particle image velocimetry. *Measurement Science and Technology, 8*(12), 1441-1454.

Spence, C. J. T., Buchmann, N. A., & Jermy, M. (2011). Unsteady Flow in the Nasal Cavity with High Flow Therapy measured by Stereoscopic PIV. *Experiments in Fluids*, 1-11.

Spence, C. J. T., Buchmann, N. A., & Jermy, M. C. (2008, 1-4 July). Particle image velocimetry measurements of nasal cavity flow with high flow humidified nasal interface. In Proceedings of the *13th Int. Symp. Flow Visualization*, Nice.

Spence, C. J. T., Buchmann, N. A., Jermy, M. C., & Moore, S. M. (2010). Stereoscopic PIV measurements of flow in the nasal cavity with high flow therapy. *Experiments in Fluids, 50*(4), 1005-1017.

Spence, K. L., Murphy, D., Kilian, C., McGonigle, R., & Kilani, R. A. (2007). High-flow nasal cannula as a device to provide continuous positive airway pressure in infants. *J Perinatol, 27*(12), 772-775.

Sreenan, C., Lemke, R. P., Hudson-Mason, A., & Osiovich, H. (2001). High-flow nasal cannulae in the management of apnea of prematurity: a comparison with conventional nasal continuous positive airway pressure. *Pediatrics, 107*(5), 1081-1083.

Stitou, A., & Reithmuller, M. L. (2001). Extension of PIV to super resolution using PTV. *Measurement Science & Technology, 12*, 1398-1403.

Stringer, N. M., Cater, J. E., Eaton-Evans, J., & White, C. (2010). *Numerical Comparison of Air Flow Patterns in the Nasal Airways of Adults and Neonates.* The University of Auckland, Auckland.

Stuiver, M. (1958). *Biophysics of the sense of smell.* Univ. Groningen, Groningen, Germany.

Subramaniam, R. P., Richardson, R. B., Morgan, K. T., Kimbell, J. S., & Guilmette, R. A. (1998). Computational fluid dynamics simulations of inspiratory airflow in the human nose and nasopharynx. *Inhalation Toxicology, 10*(5), 473-502.

Sulsenti, G., & Palma, P. (1996). Tailored nasal surgery for normalization of nasal resistance. *Facial Plast Surg, 12*(4), 333-345.

Swift, D. L., & Proctor, D. F. (1977). Access of air to the respiratory tract. In Brain, J. D., Proctor, D. F. & Reid, L. M. (Eds.), *Respiratory Defense Mechanisms* (pp. 63-90). New York: Dekker.

Takahashi, K. (1922). Quoted by Dawes (1952).

Taylor, D. J., Doorly, D. J., & Schroter, R. C. (2010). Inflow boundary profile prescription for numerical simulation of nasal airflow. *Journal of the Royal Society Interface, 7*(44), 515-527.

Tiep, B., & Barnett, M. (2002). High flow nasal vs. high flow mask oxygen delivery: tracheal gas concentrations through a head. *Respir Care*.

Tobin, M. J., Chadha, T. S., Jenouri, G., Birch, S. J., Gazeroglu, H. B., & Sackner, M. A. (1983). Breathing Patterns: 1. Normal subjects. *Chest, 84*, 202-206.

Tonndorf, J. (1939). Quoted in Mlynski (2000).

Triep, M., Brucker, C., & Schroder, W. (2005). High-speed PIV measurements of the flow downstream of a dynamic mechanical model of the human vocal folds. *Experiments in Fluids, 39*(2), 232-245.

Ursella, S., Mazzone, M., Portale, G., Conti, G., Antonelli, M., & Gentiloni Silveri, N. (2007). The use of non-invasive ventilation in the treatment of acute cardiogenic pulmonary edema. *European review for medical and pharmacological sciences, 11*(3), 193-205.

Verin, E., Tardif, C., Buffet, X., Marie, J. P., Lacoume, Y., Andrieu-Guitrancourt, J., & Pasquis, P. (2002). Comparison between anatomy and resistance of upper airway in normal subjects, snorers and OSAS patients. *Respiration Physiology, 129*(3), 335-343.

Versteeg, H., & Hargrave, G. (2001). Inhaled air and aerosol particle flow characteristics in a model of the human upper airway. In *Proceedings of the Proceedings of the 4th International Symposium on Particle Image Velocimetry, Göttingen, Germany*, September 17-19.

Walsh, B. K., Brooks, T. M., & Grenier, B. M. (2009). Oxygen therapy in the neonatal care environment. *Respiratory care, 54*(9), 1193-1202.

Weber, Z. J., Preston, C. B., & Wright, P. G. (1981). Resistance to nasal airflow related to changes in head posture. *Am J Orthod, 80*(5), 536-545.

Weibel, E. R. (1989). Lung Morphometry and Models in Respiratory Physiology. In Chang, H. K. & Paiva, M. (Eds.), *Respiratory Physiology: An Analytical Approach*. New York: Marcle Dekker, Inc.

Wen, J., Inthavong, K., Tu, J., & Wang, S. (2008). Numerical simulations for detailed airflow dynamics in a human nasal cavity. *Respir Physiol Neurobiol, 161*(2), 125-135.

Westerweel, J. (1993). *Digital particle image velocimetry - Theory and application.* Delft University, Netherlands, Delft.

Westerweel, J. (1994). Efficient detection of spurious vectors in particle image velocimetry data. *Experiments in Fluids, 16*(3), 236-247.

Westerweel, J. (1997). Fundamentals of digital particle image velocimetry. *Meas. Sci. Technol., 8*, 1379-1392.

Westerweel, J. (2008). On velocity gradients in PIV interrogation. *Experiments in Fluids, 44*(5), 831-842.

Westerweel, J., Dabiri, D., & Gharib, M. (1997). The effect of a discrete offset on the accuracy of cross-correlation analysis of digital PIV recordings. *Experiments in Fluids, 23*, 20-28.

Westerweel, J., & Scarano, F. (2005). Universal outlier detection for PIV data. *Experiments in Fluids, 39*(6), 1096-1100.

Wieneke, B. (2005). Stereo-PIV using self-calibration on particle images. *Experiments in Fluids, 39*(2), 267-280.

Wilkinson, D. J., Andersen, C. C., Smith, K., & Holberton, J. (2008). Pharyngeal pressure with high-flow nasal cannulae in premature infants. *J Perinatol, 28*(1), 42-47.

Willert, C. (1997). Stereoscopic digital particle image velocimetry for application in wind tunnel flows. *Measurement Science and Technology, 8*(12), 1465-1479.

Willert, C., & Gharib, M. (1991). Digital particle image velocimetry. *Experiments in Fluids, 10*(4), 181-193.

Willert, C., & Gharib, M. (1992). Three-dimensional particle imaging with a single camera. *Experiments in Fluids, 12*, 353-358.

William, E. L., & Harvey, E. C. (1987). Marching cubes: A high resolution 3D surface construction algorithm. *SIGGRAPH Comput. Graph., 21*(4), 163-169.

Williams, A. B., Ritchie, J. E., & Gerard, C. (2006). Evaluation of a high flow nasal oxygen delivery system: gas analysis and pharyngeal pressures. In *Proceedings of the European Society of Intensive Care Medicine 19th Annual Congress, Barcelona, Spain*, 24-27 September.

Williams, R., Rankin, N., Smith, T., Galler, D., & Seakins, P. (1996). Relationship between the humidity and temperature of inspired gas and the function of the airway mucosa. *Critical Care Medicine, 24*(11), 1920-1929.

Wolf, M., Naftali, S., Schroter, R. C., & Elad, D. (2004). Air-conditioning characteristics of the human nose. *J Laryngol Otol, 118*(2), 87-92.

Womersley, J. R. (1955). Method for the Calculation of Velocity, Rate of Flow and Viscous Drag in Arteries When the Pressure Gradient Is Known. *Journal of Physiology-London, 127*(3), 553-563.

Yu, S., Liu, Y., Sun, X., & Li, S. (2008). Influence of nasal structure on the distribution of airflow in nasal cavity. *Rhinology, 46*(2), 137-143.

Zhang, J., Liu, Y., Sun, X., Yu, S., & Yu, C. (2008). Computational fluid dynamics simulations of respiratory airflow in human nasal cavity and its characteristic dimension study. *Acta Mechanica Sinica/Lixue Xuebao, 24*(2), 223-228.

Zwaardemaker, M. (1889). Quoted by M. Uddstromer. *in Acta Otolayngologiea*, Supplement 42, p. 69,1940.

Zwartz, G. J., & Guilmette, R. A. (2001). Effect of flow rate on particle deposition in a replica of a human nasal airway. *Inhal Toxicol, 13*(2), 109-127.

Appendix A – Previous Nasal Models

Flow Visualisation Models

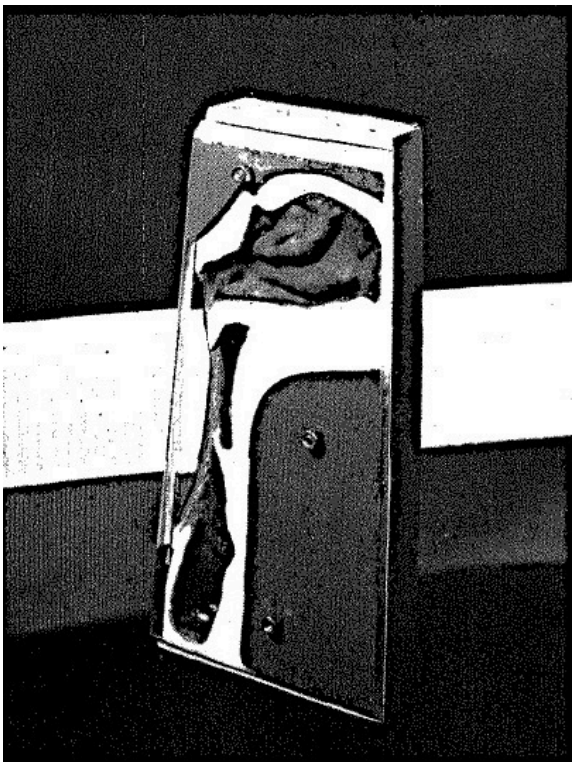

(Proetz 1951)

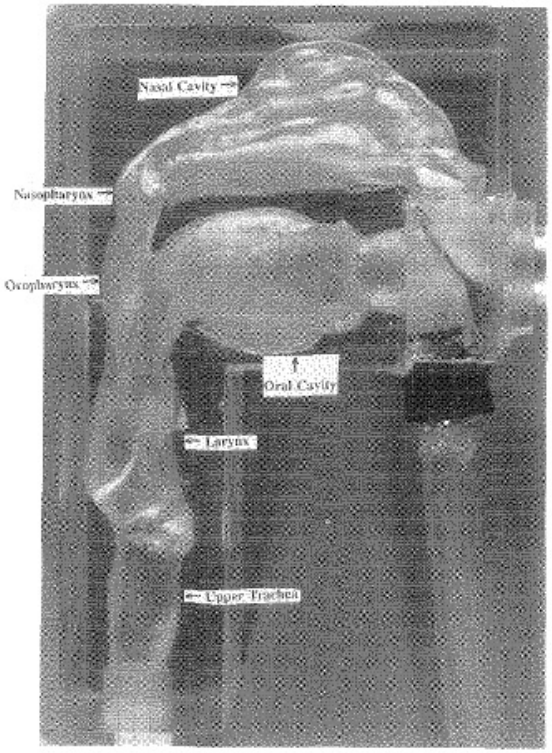

(K. Cheng et al. 1995; Y. Cheng et al. 1988)

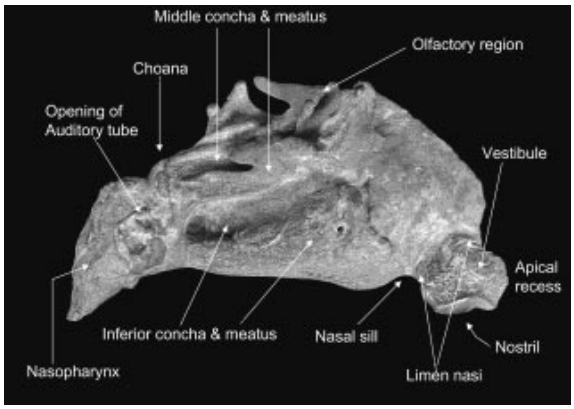

(Churchill et al. 2004)

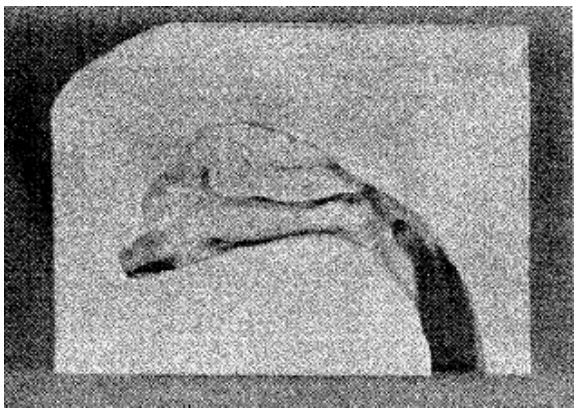

(Konno 1969),

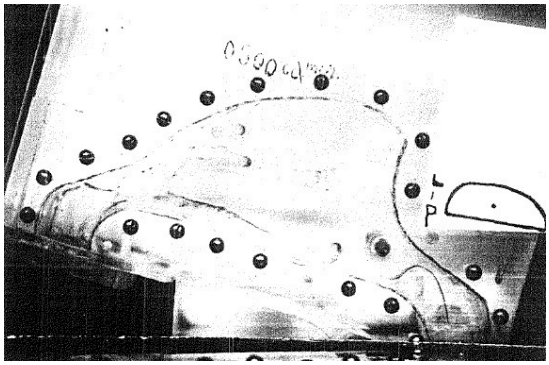

(Swift & Proctor 1977),

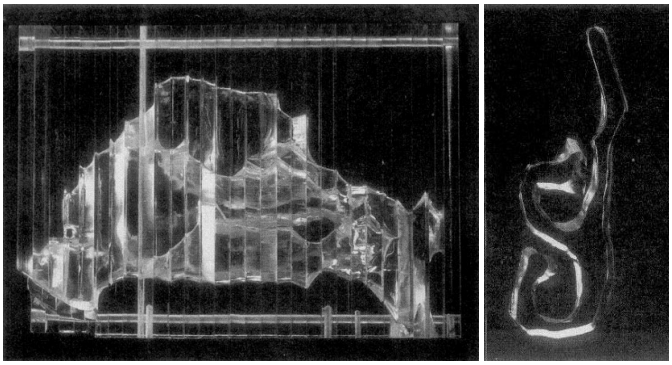

(Schreck et al. 1993)

PIV Models

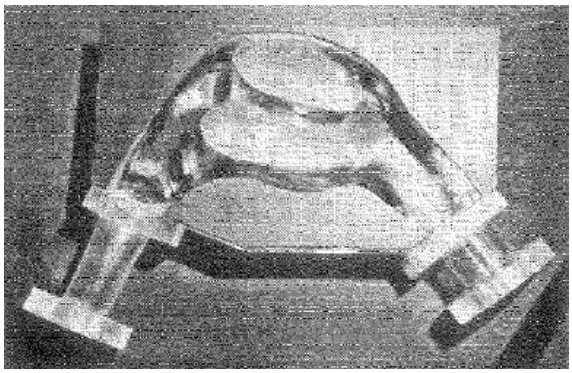

(Brücker & Park 1999; Park et al. 1997)

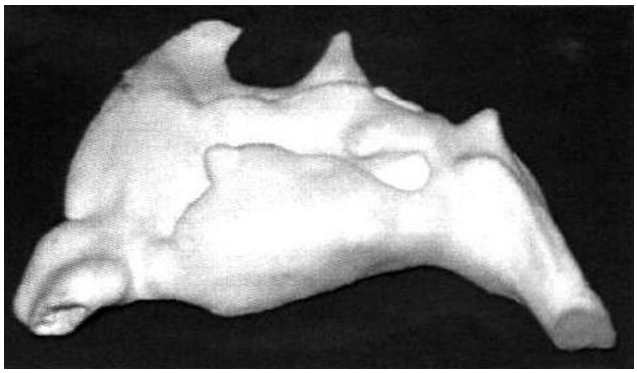

(J. K. Kim et al. 2006; S. K. Kim & Haw 2004)

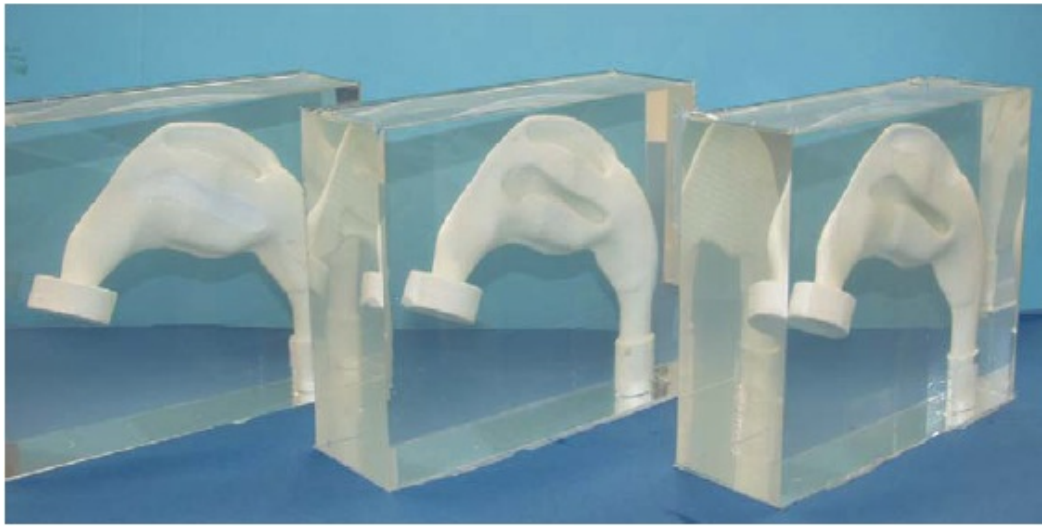

(Horschler et al. 2006a)

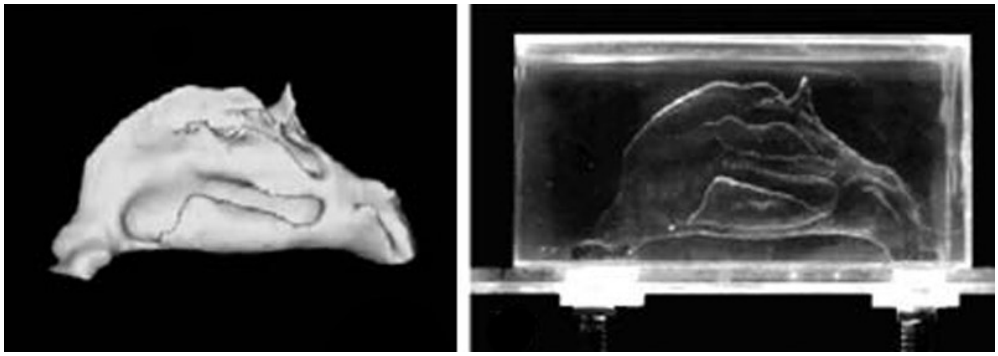

(Chung & Kim 2008; Chung et al. 2006)

(Garcia et al. 2007)

(Doorly et al. 2008a)

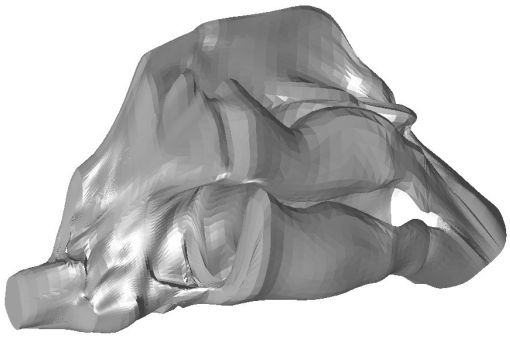

(Hopkins et al. 2000; J. T. Kelly et al. 2000)